

REPORT DOCUMENTATION PAGE				Form Approved OMB No. 0704-0188	
Public reporting burden for this collection of information is estimated to average 1 hour per response, including the time for reviewing instructions, searching existing data sources, gathering and maintaining the data needed, and completing and reviewing the collection of information. Send comments regarding this burden estimate or any other aspect of this collection of information, including suggestions for reducing the burden, to Department of Defense, Washington Headquarters Services, Directorate for Information Operations and Reports (0704-0188), 1215 Jefferson Davis Highway, Suite 1204, Arlington, VA 22202-4302. Respondents should be aware that notwithstanding any other provision of law, no person shall be subject to any penalty for failing to comply with a collection of information if it does not display a currently valid OMB control number. <b>PLEASE DO NOT RETURN YOUR FORM TO THE ABOVE ADDRESS.</b>					
<b>1. REPORT DATE (DD-MM-YYYY)</b> 30-05-2006		<b>2. REPORT TYPE</b> Final Report		<b>3. DATES COVERED (From – To)</b> 01-Mar-03 - 06-Jun-06	
<b>4. TITLE AND SUBTITLE</b>  Conjugated Polymer Solar Cells			<b>5a. CONTRACT NUMBER</b> ISTC Registration No: 2666		
			<b>5b. GRANT NUMBER</b>		
			<b>5c. PROGRAM ELEMENT NUMBER</b>		
<b>6. AUTHOR(S)</b>  Dr. Dmitri Paraschuk			<b>5d. PROJECT NUMBER</b>		
			<b>5d. TASK NUMBER</b>		
			<b>5e. WORK UNIT NUMBER</b>		
<b>7. PERFORMING ORGANIZATION NAME(S) AND ADDRESS(ES)</b> Moscow State University Vorob'evy gori Moscow 119899 Russia				<b>8. PERFORMING ORGANIZATION REPORT NUMBER</b>  N/A	
<b>9. SPONSORING/MONITORING AGENCY NAME(S) AND ADDRESS(ES)</b>  EOARD PSC 821 BOX 14 FPO 09421-0014				<b>10. SPONSOR/MONITOR'S ACRONYM(S)</b>	
				<b>11. SPONSOR/MONITOR'S REPORT NUMBER(S)</b> ISTC 02-7005	
<b>12. DISTRIBUTION/AVAILABILITY STATEMENT</b>  Approved for public release; distribution is unlimited.					
<b>13. SUPPLEMENTARY NOTES</b>					
<b>14. ABSTRACT</b>  This report results from a contract tasking Moscow State University as follows: Conjugated polymers are promising materials for many photonics applications, in particular, for photovoltaic and solar cell devices. This project will study the possibility to use conjugated polymers as active media in solar cell applications. The potential advantages of conjugated polymers solar cells (CPSC) are: the electronic properties of conjugated polymers can be tuned to match the solar spectrum, the intrinsic absorption index of some conjugated polymers could be higher than silicon for large part of the solar spectrum, large area thin films on flexible substrates could be prepared, and the production cost could be lower than for inorganic solar cells. At the same time, the known disadvantages of CPSC are: free carriers are not excited directly under solar irradiation, the mobility of free charges is low and very different for opposite polarity, low stability of conjugated polymers to oxidation and photo-oxidation. This project will use poly-para-phenylene-vinylene, vacuum deposited poly-para-phenylene and their donor-acceptor complexes to realize the advantages of CPSC and to neutralize their drawbacks. The goals of the project are to find a class of conjugated materials most promising for solar cell applications and then to study CPSC prototypes, which will be optimized for high efficiency.					
<b>15. SUBJECT TERMS</b> EOARD, Materials, Plastics					
<b>16. SECURITY CLASSIFICATION OF:</b>			<b>17. LIMITATION OF ABSTRACT</b> UL	<b>18. NUMBER OF PAGES</b>  141	<b>19a. NAME OF RESPONSIBLE PERSON</b> MATTHEW MORGAN, Lt Col, USAF
<b>a. REPORT</b> UNCLAS	<b>b. ABSTRACT</b> UNCLAS	<b>c. THIS PAGE</b> UNCLAS			<b>19b. TELEPHONE NUMBER</b> (Include area code) +44 (0)20 7514 4505

ISTC 2666P

**Final  
Project Technical Report  
of ISTC 2666P**

**Conjugated Polymer Solar Cells**  
(From 1 March 2003 to 28 February 2006 for 36 months)

**Dmitry Yurievich Paraschuk  
(Project Manager)  
International Laser Center of Moscow State University**

May 2006

## List of Contents

1	INTRODUCTION.....	5
1.1	Possibilities of polymer CTCs for photovoltaics (motivation) .....	6
1.2	Previous studies on ground-state CTCs .....	8
2	METHODS .....	10
2.1	Optical absorption spectroscopy .....	10
2.2	Light scattering/absorption technique .....	10
2.3	Evaluation of complex refraction index .....	11
2.4	Microscopy.....	12
2.5	Differential scanning calorimetry (DSC) and thermal gravimetry analysis (TGA).....	12
2.6	Photoluminescence (PL) spectroscopy .....	12
2.7	Raman and FTIR-absorption spectroscopy .....	13
2.8	Photoinduced absorption spectroscopy (PIA).....	13
2.8.1	Visible and near-IR PIA .....	13
2.8.2	Mid-IR (PIA-FTIR).....	14
2.9	Photodegradation studies .....	14
2.10	Time-of-flight (TOF) mobility measurements .....	15
2.11	Surface photovoltage technique .....	15
2.12	Photoelectric methods .....	16
3	SAMPLES AND THEIR CHARACTERIZATION.....	18
3.1	Polymers .....	18
3.1.1	Choice of polymer and solvents .....	18
3.1.2	Film preparation methods .....	21
3.1.2.1	Spin-casting, dip-coating, and drop-casting.....	21
3.1.2.2	Slow solvent evaporation method.....	23
3.1.2.3	Hole drift mobility in MEH-PPV films prepared by drop-casting and SSE .....	26
3.1.2.4	AFM characterization of pristine MEH-PPV films .....	27
3.1.2.5	Absorption and refraction.....	29
3.1.2.6	Conclusion .....	29
3.2	Acceptors .....	30
3.3	MEH-PPV/acceptor blends.....	31
3.3.1	Microscopy .....	32
3.3.2	Transmission maps of MEH-PPV/acceptor blends at 633 nm .....	37
3.3.3	Vibrational analysis.....	38
3.3.3.1	Pristine materials.....	38
3.3.3.2	Blends .....	41
3.3.4	Samples for photoelectric studies.....	44
3.4	Polyhexylthiophene/acceptor blends .....	46
3.4.1	Absorption spectra.....	48
3.4.2	Photoluminescence .....	49
3.4.3	PHT/BuDDF blends .....	50
3.4.4	Discussion.....	52
3.5	Polyfluorene as a possible donor for CTC .....	53
3.6	Other types of complexes with MEH-PPV .....	57
4	RESULTS .....	59
4.1	Evidence of conjugated polymer CTC.....	59
4.1.1	MEH-PPV/TNF and MEH-PPV/DNAQ films .....	59
4.1.1.1	Absorption spectra .....	59
4.1.1.2	Vibrational spectroscopy data.....	60

4.1.1.3	DSC data .....	62
4.1.2	MEH-PPV/TNF solution .....	62
4.1.3	CTCs of MEH-PPV with various fluorene acceptors .....	63
4.1.4	Discussion .....	65
4.2	CTC properties in the ground-state .....	66
4.2.1	Modeling possible donor-acceptor geometry of CTCs .....	66
4.2.2	Thermal analysis of MEH-PPV/TNF blends .....	67
4.2.2.1	DSC of MEH-PPV, TNF, and MEH-PPV/TNF .....	67
4.2.2.2	DSC of MEH-PPV/DNAQ blends .....	70
4.2.2.3	Isothermal TGA analysis of MEH-PPV/TNF blends .....	70
4.2.2.4	Dynamic TGA analysis: improving stability of donor/acceptor blends .....	71
4.2.2.5	Mass-spectra of pristine MEH-PPV and MEH-PPV/TNF blends .....	73
4.2.3	Light absorption and scattering in MEH-PPV/acceptor blends .....	74
4.2.3.1	MEH-PPV/TNF blends .....	74
4.2.3.2	MEH-PPV/DNAQ blends .....	76
4.2.3.3	Conclusion .....	77
4.2.4	Raman studies of blends with different MEH-PPV/acceptor ratio .....	77
4.2.4.1	MEH-PPV/TNF blends .....	78
4.2.4.2	MEH-PPV/DNAQ blends .....	79
4.2.5	How are MEH-PPV properties changed in its CTC? .....	80
4.2.5.1	Optical absorption shift .....	80
4.2.5.2	Changes in vibrational spectra .....	80
4.2.5.3	Discussion .....	82
4.2.6	Summary .....	83
4.3	Photoexcited states in donor-acceptor blends with ground-state CT interaction .....	83
4.3.1	Photoluminescence .....	83
4.3.1.1	MEH-PPV/TNF and MEH/PPV/DNAQ films .....	83
4.3.1.2	MEH-PPV/TNF solutions .....	84
4.3.1.3	Discussion .....	85
4.3.2	Photoinduced absorption spectroscopy .....	85
4.3.2.1	Identification of polaron states .....	86
4.3.2.2	Direct photoexcitation of CTC .....	89
4.3.2.3	Varying donor-acceptor ratio, solvents, and temperature .....	90
4.3.2.4	Photoinduced absorption FTIR spectroscopy .....	92
4.3.2.5	Summary .....	95
4.3.3	Surface photovoltage spectroscopy .....	95
4.3.4	Charge drift mobilities in MEH-PPV/TNF and MEH-PPV/DNAQ films .....	96
4.3.5	Photoelectric data .....	97
4.3.6	Enhancing photooxidation stability of MEH-PPV in donor-acceptor blends .....	99
4.3.6.1	FTIR data .....	100
4.3.6.2	Optical absorption .....	103
4.3.6.3	Discussion .....	104
4.4	Ternary blends .....	104
4.4.1	Photoinduced charge generation .....	104
4.4.2	Photoelectric data .....	106
4.5	MEH-PPV/DNAQ and MEH-PPV/polyDNAQ blends .....	108
4.5.1	Absorption, light scattering, and Raman data .....	108
4.5.2	Photoluminescence .....	111
4.5.3	Photoinduced absorption spectroscopy .....	111
4.5.4	Photoelectric data .....	113
4.5.5	MEH-PPV/DNAQ and MEH-PPV/polyDNAQ: summary .....	114

4.6	MEH-PPV/Pt <sub>0.75</sub> C <sub>60</sub> composites .....	115
4.6.1	Samples .....	115
4.6.2	Microscopy, absorption, and scattering data .....	116
4.6.3	Photoluminescence quenching data .....	117
4.6.4	Photoinduced absorption data .....	118
4.6.5	Photoelectric data .....	120
4.6.6	Summary .....	121
5	DISCUSSION AND IMPLICATIONS .....	122
6	CONCLUSIONS .....	125
7	ACKNOWLEDGMENT .....	127
8	REFERENCES .....	128
9	PUBLICATIONS .....	130
9.1	Published papers .....	130
9.2	Conference presentations .....	132
9.3	Theses and Dissertations .....	141

# 1 INTRODUCTION

*The three following parts (objective, expected results, and technical approach) were copied from the initial proposal with minor changes.*

Conjugated polymers are promising materials for many photonic, electronic and optoelectronic applications, in particular, for solar cells. Basic advantages of conjugated polymers for solar cells are as follows:

- their absorption coefficient is typically higher than that of Si,
- their optical absorption spectrum can be tuned to match the solar spectrum,
- large area thin films on flexible substrates could be prepared,
- the production cost could be lower than that of inorganic solar cells.

At the same time, the known disadvantages of pristine conjugated polymers are:

- the quantum yield of free charges is far below than unity under optical excitation,
- the mobility of free charges is too low,
- low stability of conjugated polymers to oxidation and photo-oxidation,
- the absorption spectrum of the best polymers used for solar cells does not match the solar spectrum (low-band gap polymers are needed).

## OBJECTIVE

The main objective of the project was to study conjugated polymer ground-state charge-transfer complexes (CTC) with different acceptors/donors as an active medium of polymer solar cells in order to realize the advantages of conjugated polymers and to neutralize their drawbacks. In particular, it was planned to study CTCs using as a donor a soluble poly-para-phenylene-vinylene (PPV). It was supposed that polymer CTCs could give a possibility to increase the polymer solar cell efficiency due to tuning their absorption spectrum to the solar spectrum. The project goals were to demonstrate the possibility of improving the photovoltaic properties of conjugated polymers using polymer CTCs.

## EXPECTED RESULTS

We planned to perform a well-directed search of low-molecular acceptors for conjugated polymers, to find optimal parameters of the compositions, and to study solar cells based on conjugated polymer CTCs. In the course of the project, polymer solar cells should be prepared and studied. It was planned:

- to prepare CTC films based on conjugated polymers with different donors/acceptors,
- to study structural properties of the films,
- to evaluate the efficiency of free carrier generation under photoexcitation,
- to study mechanisms of free carrier transport and degradation,
- to measure current–voltage characteristics under photoexcitation,
- to investigate the efficiency of the photovoltaic effect as a function of photon energy,
- to evaluate the influence of defects and disorder on solar cell characteristics,
- to estimate the long-term stability of polymer solar cells in laboratory conditions.

As a result, it was expected that the most essential factors responsible for the polymer solar cell efficiency should be investigated and the possibility to control them should be demonstrated. Recommendations concerning charge transfer (CT) complexes based on conjugated polymers as solar cell working layers should be given.

## TECHNICAL APPROACH

The ICP team was responsible for preparation of samples and the MSU team was responsible for their optical studies. It was planned that ICP team prepared samples (conjugated polymer films/solutions, CPSC prototypes), characterized them (optical absorption and vibrational spectra,, structural properties, stability in ambient conditions etc.), prepared and assembled solar cell samples. Then, both teams should study the samples using the following methods and techniques:

- fluorescence spectroscopy,
- NIR-VIS photoinduced absorption spectroscopy under CW laser excitation,
- CW photoexcitation spectroscopy (the photoinduced absorption signals as a function of photon energy is studied),
- photovoltaic measurements.

The data should be measured as a function of various photoexcitation parameters (pump intensity and photon energy, temperature, pump modulation frequency, external electric field parameters) and sample properties (donor/acceptor type, dopant content, morphology, defects, etc.). To maximize the solar cell efficiency based on conjugated polymer CTCs, it was necessary to study the following series of states and processes in our samples: incident photon — exciton state — exciton diffusion — charge carrier generation — charge carrier transport. Therefore, one needed to evaluate exciton transport properties and the dissociation probability into free carriers, and then to estimate the free carrier mobility and lifetime.

Other possible channels of photon energy conversion that do not contribute to the photovoltaic effect (exciton recombination, free carrier recombination, trapping etc.) should be analyzed and afterwards, possibly, be suppressed. The spectroscopic data obtained should be used to modify the sample preparation routine.

Several types of polymer solar cell prototypes should be studied. As reference samples, working layers made of an undoped conjugated polymer (oligomer) between two electrodes was planned to be studied. In other samples, working layers made of polymer (oligomer) CTC of different composition should be used. Multilayer prototypes should be studied, in particular, with additional transport layers for increasing photoconversion efficiency.

## **1.1 Possibilities of polymer CTCs for photovoltaics (motivation)**

In this section, we review possibilities of ground-state charge-transfer complexes (CTC) of conjugated polymers for photovoltaics and previous studies on ground-state CTCs.

### **Extension of optical absorption**

As is well known for small aromatic conjugated molecules, they can easily form intermolecular CTCs in the electronic ground state with a molecule having higher electron affinity. Such CTCs were widely studied in the 1950-60s and their properties were successfully interpreted in the framework of the Mulliken model of weak CT interaction suggesting mixing of the ground-state wavefunctions. These CTCs usually have characteristic optical absorption in the visible range corresponding to a CT band. It would be important to obtain a CTC of a conjugated polymer because it would give a possibility to extend the photosensitivity into the red and near infra-red spectral regions.

### **Facilitation of the charge separation using CTC**

In a photovoltaic material, charge separation must follow photon absorption. As generally accepted for organic materials, photons generate mainly excitons, which can efficiently dissociate into free electron-hole pairs in donor-acceptor blends. For that, an exciton generated at the donor (acceptor) has to diffuse to the donor-acceptor interface where charge separation occurs. In a CTC, donor-acceptor interaction in the electronic ground state implies that charge separation can start immediately after photon absorption since the CT absorption formally corresponds to electron

transfer directly from the donor to the acceptor. Therefore, a direct path from an absorbed photon to a pair of separated charges is possible, in contrast to materials usually used in organic photovoltaics, which require the stage of diffusion of photoexcitations.

### Phase separation and CT interaction

A promising approach in organic photovoltaics is using a bulk heterojunction in which photoexcitations dissociate into mobile charges throughout a donor-acceptor blend. The peculiarities of donor-acceptor phase separation at the nanoscale are known to be of great importance for solar cell performance. As a CTC implies donor-acceptor attraction, the ground-state CT interaction could be a factor influencing the donor-acceptor phase separation (Fig. 1) and possibly could give a way to control it. Note that earlier attempts of linking covalently the donor (polymer) and acceptor (fullerene) in a double-cable structure to optimize the donor-acceptor interpenetrating network did not lead to better solar cell performance.

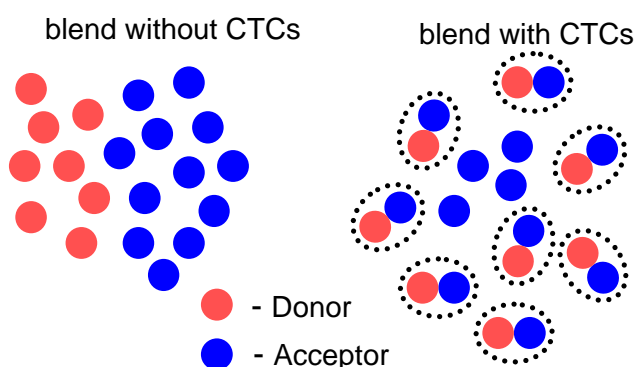


Fig. 1. Donor-acceptor blend with (right) and without (left) ground-state CT interaction (right).

### Anisotropy effects

For a conjugated chain, both the optical absorption and the charge transport are most efficient along its axis. In the solar cell geometry, where light passes through a thin photoactive layer between two electrodes, the optimal orientation of the conjugated chains for the optical absorption is parallel to the electrodes and for the charge transport between the electrodes is perpendicular to them. In fact, mainly the in-plane chains absorb the light, but the out-of-plane chains should provide charge transport. However, as known from studies of small conjugated molecule CTCs, the dipole transition moment of the CT absorption can be oriented perpendicular to the transition moment of the individual donor or acceptor. Therefore, with CTCs, the charge transport direction and the transition dipole moment can be oriented differently giving a possibility to improve the efficiency of solar cells (Fig. 2).



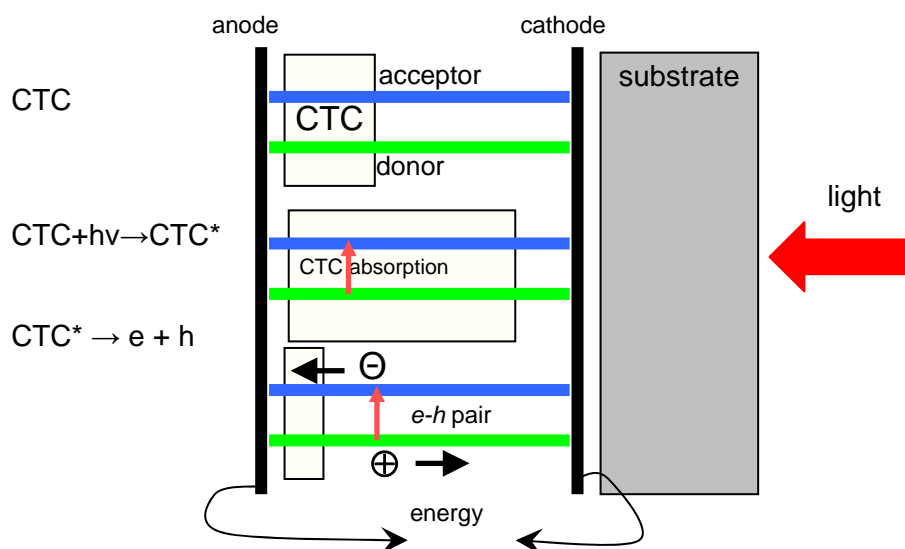


Fig. 2. An idealized solar cell using CTC between aligned donor and acceptor polymer chains illustrating that intrachain charge transport and transition dipole moment are oriented perpendicular for better performance.

Thus, in this project, we were motivated by attractive potentialities of intermolecular CTCs, which are summarized in Fig. 3.

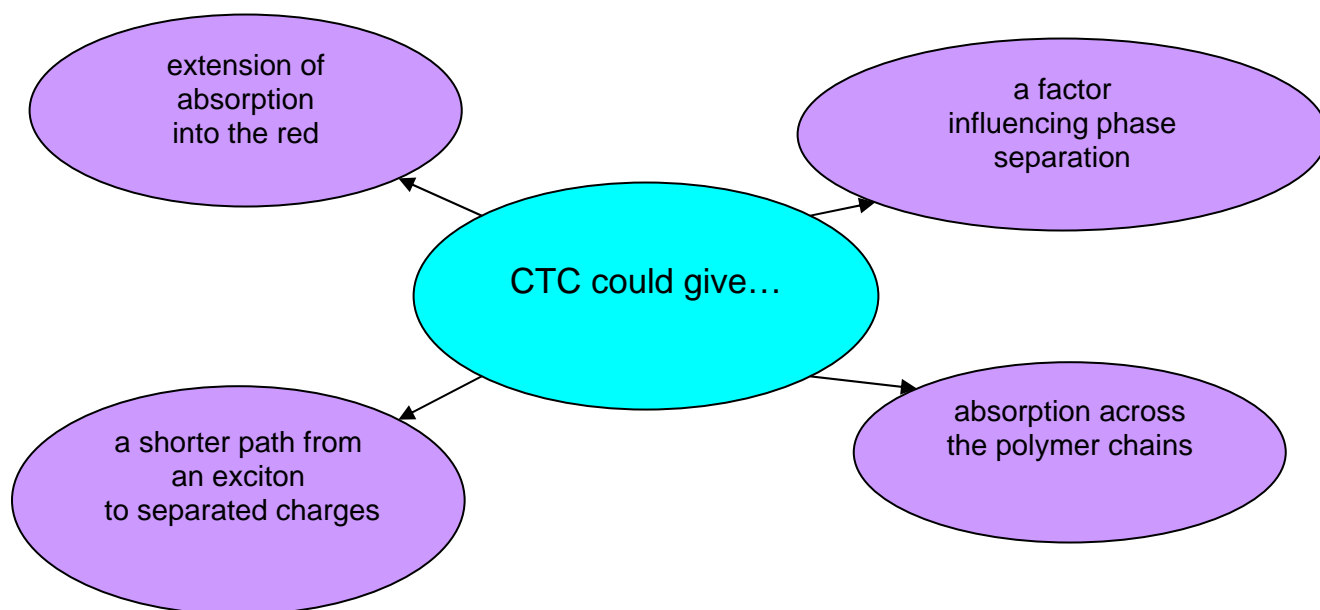


Fig. 3. Attractive potentialities of ground-state CTCs for polymer solar cells.

## 1.2 Previous studies on ground-state CTCs

When we started the project, there was no reliable evidence for noticeable intermolecular CT interaction of a  $\pi$ -conjugated polymer chain in the electronic ground state although a number of types of donor-acceptor blends and bilayers of  $\pi$ -conjugated polymers with low-molecular and high-molecular acceptors (including fullerenes and nanotubes) had been studied. It is generally accepted

that donor-acceptor blends of conjugated polymers and organic electronic acceptors, e.g. MEH-PPV/C<sub>60</sub>, MEH-PPV/ tetracyanoquinodimethane (TCNQ), etc., do not usually demonstrate ground-state CT. There was the only paper [1] claiming that poly(3-alkylthiophene) forms a CTC with molecular oxygen. However, we believe that the results of this paper should be interpreted rather as doping of the polymer by oxygen since their EPR and conductivity data indicated the presence of unpaired charges. On the other hand, intramolecular CT complexes have recently been reported for polythiophene [2], where weak CT occurs from a polymer unit cell to the covalently bonded acceptor molecule.

Nevertheless, it was reported [3] that short oligothiophenes and oligo-paraphenylenes can form a CTC with TCNQ. It is unclear why long conjugated molecules do not form CTCs with various acceptors including such a strong electronic acceptor as TCNQ. At the same time, as was recently shown, relatively large  $\pi$ -conjugated molecules phthalocyanine and fullerene can also form a ground-state CTC [4,5]. Moreover, this CTC absorbs in the near IR (1.4 eV) generating the photocurrent. Thus, it was demonstrated that CTCs could give a new route for developing wide spectrum organic photovoltaic cells.

Note that non-conjugated polymers demonstrate CT interaction in the electronic ground state, e.g., polyvinylcarbazole CTCs have been thoroughly studied since the 1970s. Moreover, such CTCs are used in electrophotography to provide the photosensitivity in the infrared range. This illustrates that polymer CTCs are able to generate free mobile charges and therefore have a potential for photovoltaics further motivating our study on conjugated polymer CTCs.

## 2 METHODS

### 2.1 Optical absorption spectroscopy

Absorption spectra of spin-cast films were usually recorded using a UV-vis Hitachi 300 or Shimadzu UV-3101PC spectrophotometers. As donor-acceptor blended films could have noticeable light scattering, which could contribute in the measured optical density in the optical gap of the polymer, we also used a home-made spectrometer collecting a large part of the scattered light. In addition, this spectrometer allowed measuring absorption spectra of optically-thick drop-cast films whose optical density was typically higher than 2.

Fig. 4 shows the optical schematic of the spectrometer. We used monochromators MSD-1 (Lomo) for films and MDR-4 (Lomo). As a light source we used a 60 W halogen lamp with back reflector. Absorption spectra were measured in the range of 400-900 nm. Liquid samples (solutions) were placed into a specially made cell with thickness of liquid 0.1 mm. The sample was set right behind the exit slit of the monochromator (see Fig. 4). For light collection a wide-aperture silicon photodiode (PD) was used. It was set immediately after the sample at a distance of about 2 mm to collect the light scattered in the solid angle  $2\pi$  sr. The PD signal was measured by a lock-in detector.

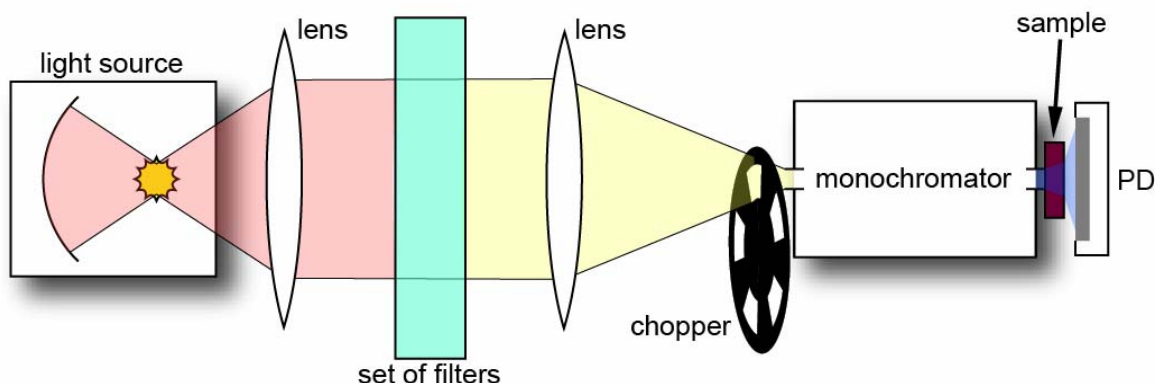


Fig. 4. Optical schematic of the spectrometer collecting the light scattered in  $2\pi$  sr.

A disadvantage of our optical scheme (Fig. 4) is that a luminescent sample could increase the signal measured by the PD. This could result in some underestimation of the sample's optical density in the spectral range of high absorption of the sample. This could be noticeable only for pristine MEH-PPV samples.

### 2.2 Light scattering/absorption technique

Ground-state CT interaction in films of MEH-PPV/TNF and MEH-PPV/DNAQ blends results in optical absorption tails in the bandgap of MEH-PPV, i.e., below 2 eV. However, it is difficult to determine the contribution of true optical absorption in these tails using a common spectrophotometer that measures the film transmission in which both the light absorption and scattering can contribute noticeably. In fact, increasing the acceptor content in the blend could lead to rising light scattering at optical inhomogeneities resulting from donor-acceptor phase separation. Thus, the amount of light scattered in the blends contains information about phase separation and should be taken into account in measuring the optical density of the blends especially in the spectral region of their low absorption.

We developed a simple method to measure light scattering in polymer films and to characterize phase separation effects. We evaluated the amount of light both scattered and

absorbed in thin polymer films measuring their optical transmission at a few laser wavelengths. We used a collimated laser beam and a wide-aperture photodetector with or without a small dump blocking the straight laser beam as shown in Fig. 5. The photodetector collects the major part of the scattered light transmitted by the film. Then, making some assumptions about the scattering indicatrix, we calculated the scattering and absorption coefficients. This technique has been applied for study of donor-acceptor blends in combination with usual optical microscopy and absorption spectroscopy.

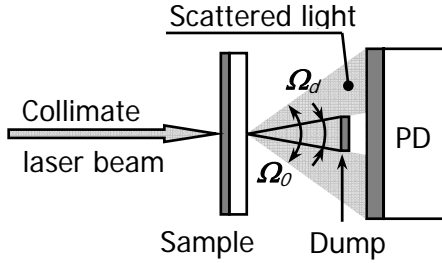


Fig. 5. Schematic diagram of experiment,  $\Omega_0 \approx 0.25$  sr,  $\Omega_d < \Omega_0$ .

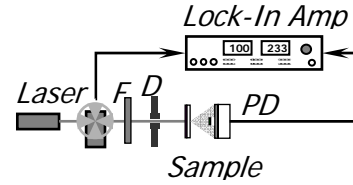


Fig. 6. Experimental setup.

Fig. 6 shows the experimental setup. A collimated 1-mm diameter laser beam from a continuous wave laser passes through a 0.5-mm diameter aperture ( $D$ ) to adjust the beam diameter to the dump one. We used a number of lasers emitting at wavelengths of 633, 670, 810, and 946 nm. The incident laser beam is attenuated by neutral filters ( $F$ ) down to 0.1 mW (Fig. 6). Then, the laser beam illuminates *Sample* from the side of a polymer film. The major part of the scattered light is collected by a Si photodetector ( $PD$ ) with 12-mm diameter of the photosensitive area. The laser beam is modulated by a mechanical chopper. The  $PD$  signal is measured using a lock-in amplifier (Stanford Research SR-830) at a modulation frequency of 120 Hz.

### 2.3 Evaluation of complex refractive index

We developed a simple method to measure complex refractive index  $n$  of MEH-PPV films. We were motivated to find a correlation between complex refractive index of polymer film and film preparation procedure. In addition, we could evaluate the film thicknesses.

To measure  $\text{Re}(n)$ ,  $\text{Im}(n)$ , and  $d$  for the polymer film on a substrate, we assembled an optical set-up allowing us to measure the light intensity reflected from the film-air and film-glass interfaces, and also transmitted by the film. All the measurements are done under nearly normal incidence. From these three magnitudes and the known  $n$  of the substrate, one can calculate  $\text{Re}(n)$ ,  $\text{Im}(n)$ , and  $d$  using the Frenel's formulas. Our measurements were done at the wavelength  $\lambda=532$  nm corresponding to the strong optical absorption of MEH-PPV. Interference effects in the polymer films were taken into account. We determined complex  $n$  and  $d$  for MEH-PPV films prepared by drop-casting and slow solvent elimination (SSE) methods from chlorobenzene, toluene, and cyclohexanone solutions.

Experimental setup is shown on Fig. 7. The laser beam is split in two ones  $I1$  and  $I2$ . The measurement was done in two steps. We closed beam  $I2$  and measured the intensity of beam  $I1$  transmitted and reflected by the film, using photodetector  $PD1$  and  $PD2$ , respectively. Then, we closed beam  $I1$  and measured the signals of  $PD1$  and  $PD2$ . The beams coincided on the sample with 0.5 mm accuracy. We used wide-aperture  $PD1$  and  $PD2$  for collecting all the reflected or transmitted light including a possible scattering contribution.

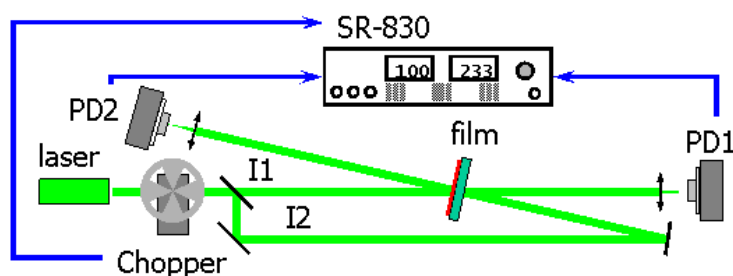


Fig. 7. Experimental setup for measuring complex  $n$ , and  $d$ .

## 2.4 Microscopy

AFM images were recorded using “Femtoscan online” (ATC, <http://www.femtoscan.net>) or “Smena” (NT-MDT, [http://ru.ntmdt.ru/Products/Scanning\\_Probe\\_Microscopes/product6.html](http://ru.ntmdt.ru/Products/Scanning_Probe_Microscopes/product6.html)) instruments in the contact or tapping mode. Cantilevers Veeco (0,06 n/m) were used.

Microphotographs of polymer films were taken using a CARL ZEISS microscope and a NIKON COOLPIX 4500 camera in the transmitted light unless otherwise mentioned.

## 2.5 Differential scanning calorimetry (DSC) and thermal gravimetry analysis (TGA)

Thermal analysis of polymer films has been accomplished by TGA and DSC methods with the aid of Perkin-Elmer Series 7 Analysers. The DSC analyzer was calibrated by Indium and Zink metals melting standards. All the experiments (if not indicated separately) have been performed at 10 K/min heating rate with samples positioned in aluminium hermetically sealed pans. DSC traces acquired for samples were automatically corrected by the instrument for the instrumental baseline recorded beforehand for empty aluminium pans throughout the temperature region of interest. The TGA analyzer was calibrated by measuring Curie points for alumel, perkallor and nickel metals magnetic standards. TGA experiments have been performed at 10 K/min heating rate in oxygen flow atmosphere (gas discharge rate of ca. 100 cm<sup>3</sup>/min).

## 2.6 Photoluminescence (PL) spectroscopy

PL spectroscopy is commonly used to study photoexcited states in polymer donor-acceptor blends. The PL intensity gives information about the lifetime of the lowest dipole-allowed exciton photoexcited either at the donor or the acceptor. As a rule, the exciton lifetime is strongly decreased upon adding an acceptor to the donor (conjugated polymer) due to electron or energy transfer from the donor to the acceptor.

The PL spectra were recorded using a home-made set-up including a monochromator, a Si-photodetector, and a lock-in amplifier (Fig. 8). The spectral response of this set-up was corrected using a spectrally calibrated tungsten lamp with ribbon emitter (VNIOFI, Moscow). For optically thin samples (spin-cast and dip-coated films) at 532 nm, the PL values were normalized to the pump absorption. The backscattering geometry at a laser excitation wavelength of 532 nm was used with typical excitation power  $\sim 5$  mW/cm<sup>2</sup> to reduce photodegradation. PL data were measured at laboratory ambient conditions, in vacuo ( $\sim 10^{-2}$  Torr), or under nitrogen flow in the temperature range 90–350 K. To take into account the possible photodegradation effect, we recorded a set of PL spectra successively and compared them. For pristine MEH-PPV films in ambient atmosphere showing the highest PL photodegradation effect, it could decrease our PL signal by less than 10–15%. PL photodegradation tests were made in separate measurements. To evaluate the rate of PL photodegradation, we recorded the peak PL signal at 580–600 nm as a function of exposure at

intensity 80 mW/cm<sup>2</sup> in ambient room conditions using for excitation chopped laser radiation at 532 nm. As well for PL studies we used a Shimadzu fluorimeter (PR-5000). The PL data from this fluorimeter are presented without spectral calibration.

The **PL quantum yield** was measured at room temperature using a reference sample method. We used Rhodamine101 (R101) as a reference material which PL spectrum is overlapped with that of MEH-PPV. We prepared a number of highly diluted R101 solutions in methanol to obtain the linear dependence of PL intensity on their optical density and so to eliminate PL quenching in concentrated solutions. After that the PL spectra of R101 solutions and MEH-PPV (solutions and films) were measured in the backscattering geometry and normalized to the optical density of the samples. The PL quantum yield for films was measured in a pumped vacuum cell. The quantum yield was calculated from the integrated PL spectra and measured optical density. Reflection losses and solid angle correction due to difference in the refractive index of the samples were taken into account.

The **PL quenching data** for MEH-PPV/acceptor blends were measured in the following way. PL spectra were recorded in ambient conditions for excitation wavelength 532 nm at intensity up to 40 mW/cm<sup>2</sup> depending on the PL signal. The films were optically thick at 532 nm to avoid normalizing to the absorbed pump. The PL spectra were measured in 2-4 different points on the sample. In the blends with low acceptor content, possible PL degradation was checked in repeated measurements.

## 2.7 Raman and FTIR-absorption spectroscopy

### *FTIR spectra*

IR transmission and Raman spectra of free standing films were recorded at room temperature with 2 cm<sup>-1</sup> resolution using a Perkin-Elmer FTIR (Model 1720-X) spectrophotometer furnished with a NIR-FT Raman attachment. The back-scattering geometry and a liquid nitrogen cooled InGaAs detector were used for acquiring Raman spectra at excitation wavelength 1064 nm. FTIR transmission spectra for films prepared by drop-casting on BaF<sub>2</sub> substrates were also recorded at room temperature with 2 cm<sup>-1</sup> resolution using a FTIR Analyzer or a Infracum FT-801 spectrometer with a MG-32A photodetector from Simex (Novosibirsk).

### *Raman spectra at visible excitation*

Raman spectra for excitation at 670 nm were recorded in the range 800–1200 cm<sup>-1</sup> using a double monochromator and a photomultiplier (Hamamatsu R2949, spectral range 200–900 nm) operating in the photon counting mode. A home-made thermoelectric cooler working at –10 °C for the R2949 was constructed. As a Raman excitation laser, we designed an external cavity GaInP/AlGaInP diode laser in the Littrow configuration based on a multimode commercial laser diode and diffractive grating with the output power more than 50 mW at the wavelength 670 nm and the FWHM linewidth less than 3 cm<sup>-1</sup>. The 180° and 90°-scattering geometries were used.

## 2.8 Photoinduced absorption spectroscopy (PIA)

PIA spectroscopy is a well-known technique to probe long-lived photoexcited states in conjugated polymers. Essentially that PIA can reveal whether the photoexcited states are charge or neutral providing information about their lifetime and recombination mechanisms. In the project, we used two types of PIA techniques covering the spectral ranges 0.6–2 eV and 0.1–0.5 eV. All the PIA studies were done on drop-cast films.

### 2.8.1 Visible and near-IR PIA

Fig. 8 shows the optical schematic of our visible and near-IR PIA spectrometer. The pump beam was mechanically chopped, and the PIA signal in the probe channel was processed by a lock-in amplifier (SR-830) at the frequency of modulation. In the probe channel we used a tungsten-halogen lamp, a monochromator and a solid-state photodetector. A Si-photodetector and thermoelectrically cooled InGaAs-photodetector were used covering the range 400–1900 nm. As a pump source we used a cw Nd:YAG laser with an intracavity optical doubler (532 nm), diode lasers (670, 810 nm) and light emitting diodes (490, 630 nm). Measurements were conducted for pump intensity 0.1–30 W/cm<sup>2</sup> and chopping frequency 5–2000 Hz. We typically used a chopping frequency of 75 Hz unless otherwise mentioned. For pristine MEH-PPV films the PL was subtracted from the measured PIA signal. For low temperature measurements a nitrogen flow cryostat was used.

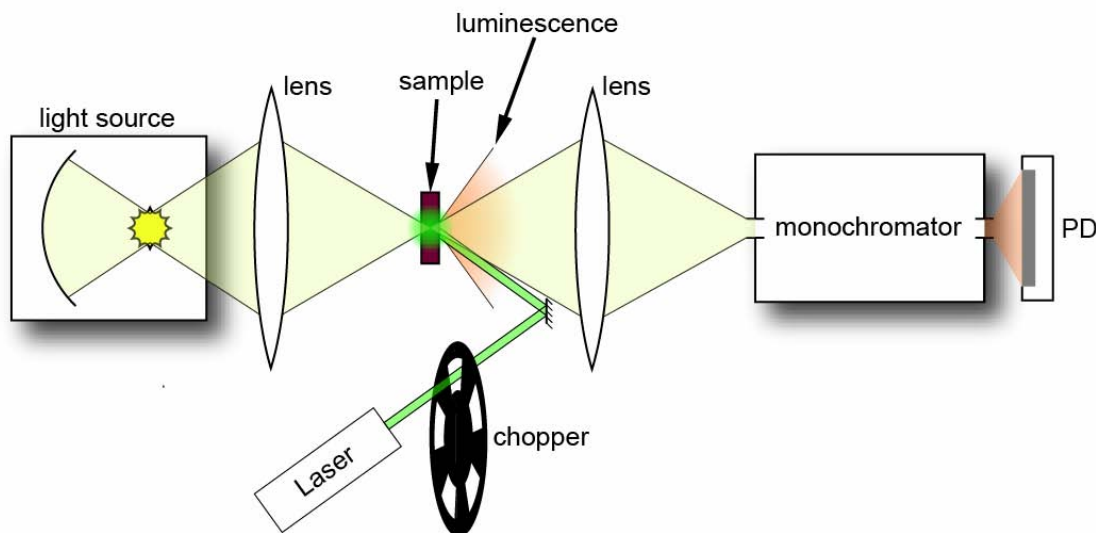


Fig. 8. Optical schematic of PIA and PL spectrometer.

### 2.8.2 Mid-IR (PIA-FTIR)

Experiments were carried out using Infracum FT-801 spectrometer with a MG-32A photodetector in ambient conditions with resolution of 6 cm<sup>-1</sup>. PIA-FTIR spectra were measured by accumulating IR transmission spectra with and without illumination during the equal time intervals (16 or 32 sec). The data were averaged over large numbers of “light/dark” cycles to reach appropriate signal-to-noise ratio that usually took a few hours. Polymer films on BaF<sub>2</sub> substrates were illuminated by a second harmonic of Nd:YAG CW laser (wavelength 532 nm, intensity 60 mW/cm<sup>2</sup>) in ambient laboratory conditions. To check a substrate heating effect, the following experiment was performed. We placed in the sample unit of the spectrometer a sample and a clear BaF<sub>2</sub> substrate heated up to 60°C and recorded the absorption spectra until it got cold to room temperature. Heating affects the BaF<sub>2</sub> absorption below 1000 cm<sup>-1</sup> that makes the heating effect readily observable.

## 2.9 Photodegradation studies

Drop-cast polymer films on BaF<sub>2</sub> substrates were exposed to cw laser radiation at 532 nm with an intensity of 330 mW/cm<sup>2</sup> (second harmonic of a CW Nd:YAG laser) for a time period up to 6 hours from the side of air-film interface. The laser beam diameter was ~7 mm. FTIR measurements were carried out by using an Infracum FT-810 spectrometer (Simex). Transmission spectra were recorded with 1 cm<sup>-1</sup> resolution.

Evolution of the UV-vis absorption spectra of spin-cast polymer films on glass substrates was recorded under irradiation with broad-band light by using a collimated 80-mm diameter beam from a 1000 W xenon lamp. The IR radiation was blocked by water filters.

All the photodegradation studies were performed at ambient laboratory conditions.

## 2.10 Time-of-flight (TOF) mobility measurements

The charge carrier drift mobility in polymer films was measured by a conventional time-of-flight (TOF) technique at room temperature. Polymer films were deposited on ITO-coated glass substrates by drop-casting or SSE. Then an Al layer was thermally deposited on the polymer film. The charge carriers were generated by illumination through the ITO side with a 20 ns pulse of a xenon lamp (Xenon Corp., Model-437B) with an appropriate filter. All requirements for a small signal mode of the TOF technique were fulfilled. The current transients were recorded with a digital oscilloscope (Tektronix TDS 340A). The transit time  $T$  is related to the drift mobility as  $\mu = d/F T$ , where  $F$  is the applied electric field and  $d$  the film thickness.

## 2.11 Surface photovoltage technique

Spatial charge separation is an important step in photovoltaics. Generation of the separated charges can be probed indirectly by pure optical methods as photoinduced absorption spectroscopy or more directly by photoelectric methods as current-voltage characteristics. However, in the latter, interfaces at the electric contacts of the device unavoidably contribute to the measured signal complicating extraction of information about spatial separation of photoinduced charges. On the other hand, surface photovoltage (SPV) probes spatially separated charges without electrical contact. SPV technique was initially developed and is commonly applied to study charge separation in inorganic semiconductors.

Fig. 9 shows the scheme of the SPV technique. The SPV was measured using lock-in technique in the capacitor arrangement with a thin mica layer used as a spacer between the semi-transparent Cr electrode and the sample surface. A quartz-prism monochromator equipped with a tungsten-halogen lamp was used as the light source in the spectral range 0.5–4 eV. MEH-PPV/TNF films with different component ratios were drop- and spin-cast from chlorobenzene solution on ITO/glass substrates.

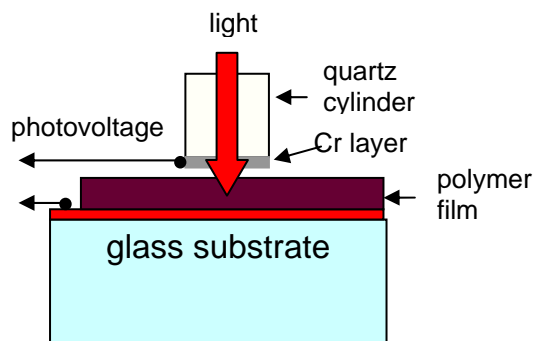


Fig. 9. Scheme of SPV technique. Light from the monochromator goes through a quartz cylinder of 5 mm diameter.



## 2.12 Photoelectric methods

For photoelectric studies, solar cell samples (photodiodes) were prepared according to the procedure described below in Sec. 3.3.4. Samples were not encapsulated. A typical sample is shown in Fig. 10 (bottom right).

Fig. 10 (top) describes the measurement scheme. To make photoelectric measurements, we have developed a computer-controlled device consisting of a preamplifier, ADC, and bias voltage generator. Device electrodes implemented mechanical contact to sample ones as seen in Fig. 10 (bottom left) showing a sample under measurement. Photodiode samples were illuminated from the glass plate side (Fig. 10, bottom left). Active area determined by a top circular aluminum contact ( $\sim 5 \text{ mm}^2$ ) was illuminated homogeneously in all experiments. Optical density of the photodiodes was no more than unity. All photoelectric studies were done in ambient conditions in a couple of days after sputtering.

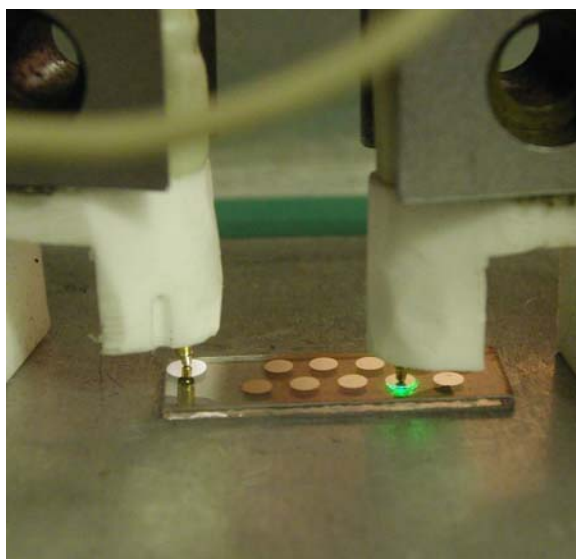
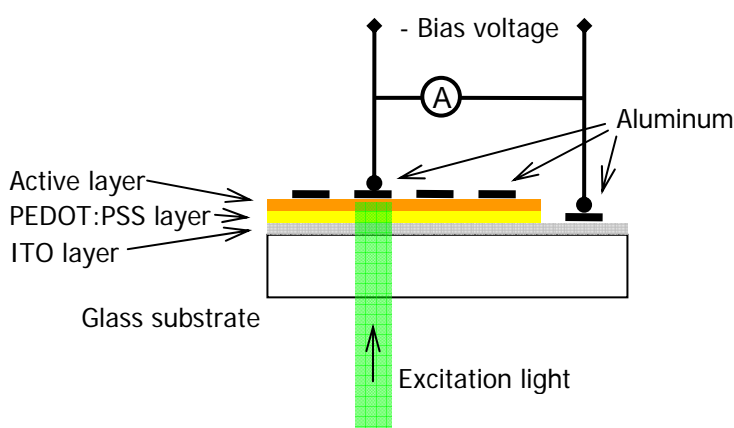


Fig. 10. Sandwich-type sample: structure, current measurement, illumination. Top: schematic model; bottom left: a sample during photoelectric experiment; bottom right: sample's photo (10x30 mm, diameter of top electrodes is 2.5 mm).

We have studied photodiodes with a bulk heterojunction active layer composing of MEH-PPV/acceptor blends with different donor/acceptor ratios. Photodiodes with pristine MEH-PPV active

layer also has been studied as reference samples. Most of the photoelectric measurements have been implemented using several top contacts or even several samples if necessary to verify reliability of results.

#### *Current-to-voltage characteristics*

Current-to-voltage characteristics of the photodiodes were measured within  $-2...+2$  V bias voltage range in dark and under illumination. Radiation from a tungsten-halogen lamp corrected by a glass filter (SZS-5) was used as a solar simulator. Light intensity on the sample surface was  $100 \text{ mW/cm}^2$ .

#### *Photocurrent excitation spectra*

Photodiodes were illuminated from the glass plate side by light from a tungsten-halogen lamp dispersed by a monochromator (a ZHS-18 glass filter was used to suppress higher diffraction orders). The optical radiation was chopped at  $\sim 70$  Hz with intensity on the sample surface being less than  $0.5 \text{ mW/cm}^2$ . The preamplified photocurrent was measured by a lock-in amplifier (SR-830). Photocurrent excitation spectra were measured within 500–700 nm region at several bias voltages ( $-1.0...+1.5$  V) and then corrected by the incident spectra. Results are presented in the form of external quantum efficiency (EQE), i.e. the probability of appearance of an elementary charge at contacts per one incident photon.

## 3 SAMPLES AND THEIR CHARACTERIZATION

More than 550 samples including pristine conjugated polymer films, polymer/acceptor blended films and solutions, photodiodes etc. were prepared in the course of project by the ICP team. A major part of them was studied by the MSU team.

### 3.1 Polymers

Photophysical properties of conjugated polymer films strongly relate to their morphology at the nanoscale. Moreover, recent improvements in performance of polymer solar cells have been realized mainly by optimizing the nanomorphology of the active layer [7]. Therefore, the choice of the optimal method of polymer film preparation is essential. We were motivated by the following point: processing of conjugated polymers from a raw polymer to a device should be conducted in conditions as close as possible to those of the thermodynamic equilibrium. Polymer macromolecules should have an opportunity to form a suitable conformation in which the most stable morphology could be realized. The processing usually includes the following stages:

1. Raw polymer dissolution.
2. Transition into the solid phase.
3. Normalization (for example, annealing).

It is known that the polymer conformation in solution strongly depends on solvent type and solute concentration [8]. Essentially that the polymer conformation in the solid phase can inherit some features from that of solution [9]. Transition into the solid phase determines mainly the morphology although annealing could erase all the differences resulted from the previous processing stages. In the course of the project, we have evaluated several preparation methods: spin-casting, dip-coating, drop-casting, and slow solvent evaporation (SSE) for different solvents. We were guided by the following spectroscopic criteria:

- steepness and position of the absorption edge;
- width, vibrational structure of the whole lowest absorption band;
- position, width, and fine structure of the PL spectrum;
- the PL quantum yield and PL excitation spectrum shape;
- the PL degradation rate.

More red-shifted PL and absorption spectra were considered as indicators of higher degree of  $\pi$ -conjugation or/and interchain interaction in the films. The narrower the PL and the absorption spectrum, the narrower distribution in conjugated length and the less undesired aggregation. At the same time, the less intensive PL fine structure, the less undesired aggregation can be expected. In addition, the less intensity of vibronic bands in PL and absorption (unless inhomogeneous broadening does not smear the spectra), the longer conjugated length can be suggested as higher electron delocalization should result in weaker vibronic sidebands [10]. And finally, higher PL quantum yield, flatter PL excitation spectrum, and lower PL degradation rate were also considered as signatures of more optimal nanomorphology.

#### 3.1.1 Choice of polymer and solvents

As a basic polymer, poly[2-methoxy-5-(2'-ethylhexyloxy)-1,4-phenylene vinylene] (MEH-PPV) from Sigma-Aldrich (product number 53,651-2, MW=125000 g/mol, MFCD03093943, <http://www.sigmaaldrich.com/catalog/search/ProductDetail/ALDRICH/536512>) was chosen. MEH-PPV is an archetypical model polymer (Fig. 11), for which a lot of information is available in the literature. Poly(3-hexyl-thiophene) (PHT) and poly(9,9-bis(2-ethylhexyl)-fluorene-2,7-diyl) (PF2/6) were also

studied, see Sec. 3.5 and Sec. 3.4, correspondingly. All these polymers are soluble in common organic solvents owing to bulky substituents attached to the conjugated backbone.

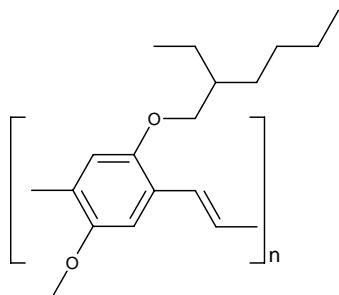


Fig. 11. Chemical structure of MEH-PPV.

For polymer solar cells, polymer films of thickness  $\sim 100$  nm with an optimal morphology should be prepared. Therefore, the next steps were selection of optimal solvents and methods of thin films preparation. Characterization of polymer films was based on microscopy images (optical and AFM) and optical spectra (absorption and PL).

After analysis of the literature data, we selected the following solvents for MEH-PPV:

- Chlorobenzene,
- Toluene,
- Cyclohexanone.

The following factors were taken into account:

- The solvent should be “good” in the following sense: interaction between the solvent molecules and the polymer chains should be higher than that of between the polymer chains.
- The solvent must have the boiling temperature in the range  $100\text{--}170^\circ\text{C}$ . A lower boiling temperature may give low quality films due to too high speed of solvent evaporation. On the other hand, a higher boiling temperature results in too long time of sample drying.
- Solvents with different dielectric constants are desirable because it might be a factor for CTC formation.

MEH-PPV solutions were prepared for concentration in the range  $0.1\text{--}5$  g/l and dissolving time in the range  $30\text{--}180$  min at  $60^\circ\text{C}$ . For each solvent a set of films was prepared by dip-coating and drop-casting. Then, for each set of films microscopy images, optical absorption, and PL spectra were recorded and analyzed.

Fig. 12 shows room temperature optical absorption and PL spectra for films prepared from three different solvents by dip-coating. It is seen that cyclohexanone results in a smoother optical absorption edge and a broader PL spectrum. These features are commonly attributed to a broader distribution of conjugation lengths of chromophores and lumonophores, respectively. The PL spectra in Fig. 12 vary in the position and width indicating the difference in conjugation length distribution and interchain interaction of luminescent species. Redder optical spectra are usually assigned to a longer conjugation length or/and more pronounced interchain interactions. Chlorobenzene dip-coated films have a narrower and bluer PL spectrum implying a narrower distribution in conjugation length and a less effect of interchain interactions.

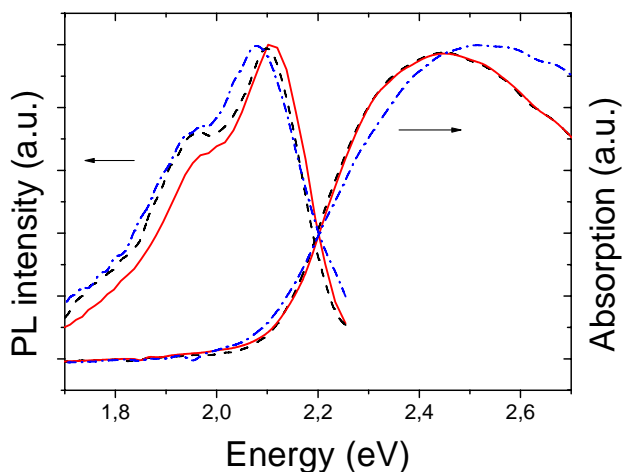


Fig. 12 Normalized absorption and PL spectra of MEH-PPV films at 300 K prepared from toluene (dash line), chlorobenzene (solid line), and cyclohexanone (dash-dot line) by dip-coating.

Fig. 13 demonstrates PL spectra of drop-cast films prepared from different solvents and recorded at 100 and 300 K. At both temperatures, the positions of PL bands change in the range 10–20 meV (2–4 nm) for different solvents. At 100 K, the PL spectra show a ~15 meV (20 nm) red shift and become finer structured. The finer structure, the less inhomogeneous broadening, and the red shift indicates increasing the conjugation length with cooling. The difference between solvents is seen clearer at 100 K (Fig. 13, right): toluene results in redder PL that usually assigned to more pronounced interchain interaction.

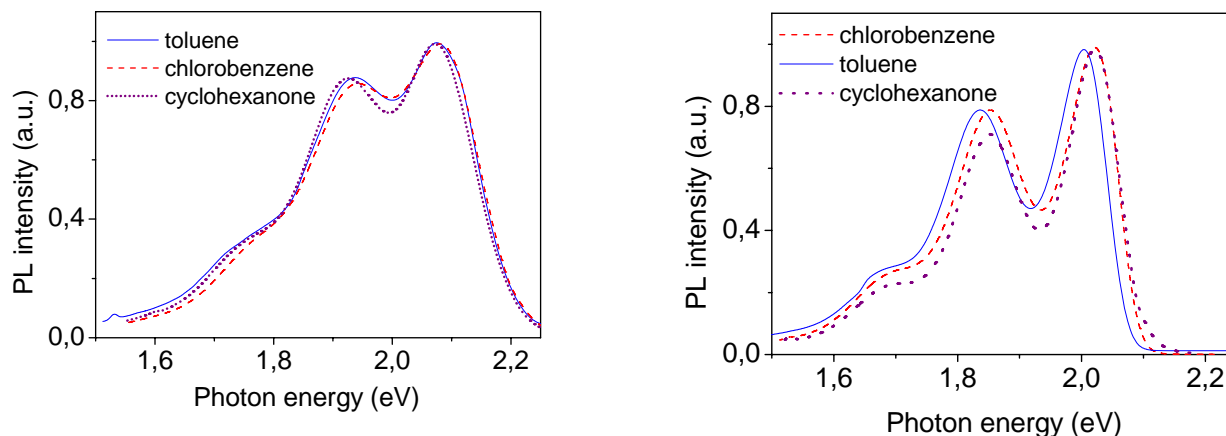


Fig. 13. PL spectra of drop-cast films prepared from different solvents at 300 K (left) and at 100 K (right).

Practical evaluation of the solvents can be summarized as follows. Toluene and chlorobenzene are “good”. MEH-PPV is dissolved readily, does not form gel, and forms quite homogeneous films. The boiling temperature is optimal for film preparation. Cyclohexanone is “satisfactory” because its higher boiling temperature impedes sample drying.

Taking into account the above optical data, chlorobenzene and toluene were chosen as basic solvents for MEH-PPV film preparation. Note that chlorobenzene is considered as the optimal solvent for bulk heterojunction PPV/fullerene polymer solar cells. In a number of cases, other solvents (tetrahydrofuran, dichloroethane, and iodobenzene) were used as well, in particular, for preparation of donor-acceptor blends and for the SSE preparation method.

### 3.1.2 Film preparation methods

#### 3.1.2.1 *Spin-casting, dip-coating, and drop-casting*

We have evaluated several commonly used preparation methods of polymer films:

- spin-casting (an appropriate amount of solution is dropped onto a horizontally aligned substrate that then is being spun up),
- dip-coating (immersing a substrate into polymer solution),
- drop-casting (an appropriate amount of solution is dropped onto a horizontally aligned fixed substrate).

These methods differ from each other by the time of solvent elimination during solidification. It is reasonable to expect that the longer this time, the more thermodynamically stable and ordered morphology could be realized. Such morphology implies a higher degree of interchain interaction and a higher concentration of longer conjugated lengths. Among these three methods, drop-casting provides the longest solvent elimination time, and spin-casting gives the shortest one. The films were prepared in the air atmosphere. For comparison of the film preparation methods, we were guided by the criteria mentioned in the beginning of this section.

Fig. 14 compares absorption and PL spectra of films prepared from the same chlorobenzene solution by spin-casting, dip-coating, and drop-casting. It is seen that the spin-coating gives a bluer absorption spectrum than the dip-coating suggesting a shorter conjugation length of the chromophores for the former. On the other hand, the PL position is the same for the spin-cast and dip-coated films (Fig. 14) implying the same conjugated length of the luminophores. Nevertheless, the nominally 01 vibronic sideband in PL is weaker making the whole PL spectrum narrower for the dip-coated film. Therefore, according to the spectroscopic criteria stated above, we conclude that the dip-coating is more preferable than the spin-casting.

This conclusion is supported by PL data shown in Fig. 15 that compares spectra of MEH-PPV films prepared by different methods from tetrahydrofuran. It is seen that generally the longer solvent elimination time, the redder PL is observed. Again, the spin-casting results in the bluest PL, which gradually shifts to the red in the following sequence: dip-coating, drop-casting, SSE. The reddest PL in the SSE film implies the longest conjugation length. At the same time, a feature at 1.9 eV for the SSE film (Fig. 15) is reasonably to assign to aggregates. The SSE method is discussed in the next section.

Comparing spin-casting, dip-coating, and drop-casting; the latter results in the reddest PL as follows from Fig. 14 and Fig. 15 suggesting the longest conjugated length. The same was observed for the toluene films (for example, cf. Fig. 12 and Fig. 13, left). Moreover, comparing the PL spectra in Fig. 12 and Fig. 13, left, one can see that the difference in PL position for films prepared from different solvents is less for the drop-cast films (Fig. 13, left) than for the dip-coated films (Fig. 12). This possibly indicates that drop-cast films are less sensitive to the polymer conformation in solution. These observations probably imply more optimal and stable morphology in drop-cast films. Note that reliable absorption spectra for drop-cast films are difficult to measure due to their high optical density.

We compared the PL photodegradation rate of MEH-PPV films prepared by different methods and from different solvents. For all the films studied we observed that the PL intensity essentially drops after a characteristic exposure of  $\sim 20 \text{ J/cm}^2$ . We did not find any clear correlation of the PL photodegradation rate with the preparation method including the SSE.

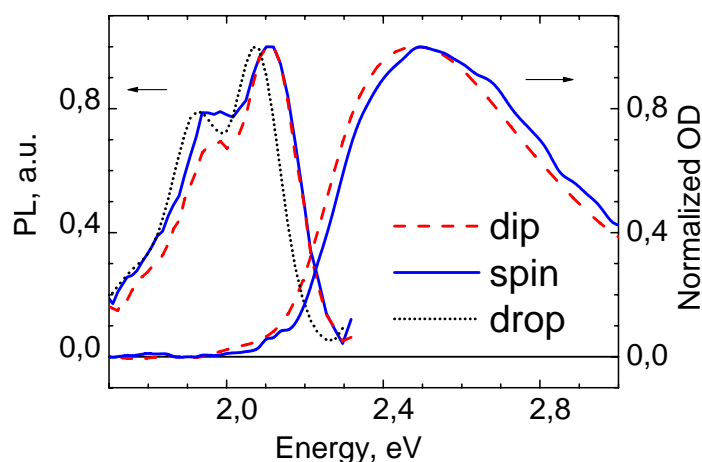


Fig. 14. Normalized PL and absorption spectra of MEH-PPV films prepared by the different methods from the same chlorobenzene solution (2 g/l). The spinning rate was 1000 rpm. PL excitation was at 532 nm.

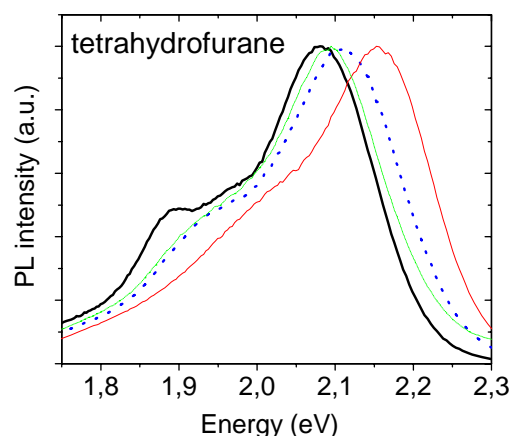


Fig. 15. Normalized PL spectra of MEH-PPV films prepared from tetrahydrofuran (right) by SSE (thick solid); drop-casting (dash-dotted); dip-coating (dotted); spin-casting (thin solid). The solution with concentration 2 g/l was used in all the methods except the SSE (1 g/l). The excitation wavelength was 500 nm. The spectra were not corrected for the instrument response.

Thus, the drop-casting seems to result in more optimal and stable morphology than with dip-coating and spin-casting. However the thickness of drop-cast films typically is high (300–1000 nm) and strongly varies over the film that is hardly acceptable for solar cells fabrication and other studies for which film's thickness is an essential parameter. Nevertheless, we used drop-casting in the project in a number of studies (see below). Spin-casting gives films with the bluest spectra PL and absorption that suggests less optimal (ordered) morphology. On the other hand, spin-casting is commonly used since it can give very homogeneous films with thickness to be controlled in a wide range by varying the spinning rate. As follows from our studies, dip-coating possibly results in more preferable morphology. But we could not make homogeneous dip-coated films (see Fig. 16, middle) that would need special equipment, which was unavailable. Accordingly, in the project we used mainly spin- and drop-casting, which are described and referenced to the spectroscopy methods in the next two paragraphs.

### *Spin-casting*

We used spin-casting mainly for fabrication of polymer solar cells and recording optical absorption spectra of the films. The spinning rate was gradually increased up to the maximum (typically 1500 rpm if otherwise mentioned) and was kept at maximum during 90 sec. Typical thicknesses of spin-cast MEH-PPV films prepared from solutions on glass substrates with polymer concentration 1–5 g/l. Thickness of a film spin-cast from a chlorobenzene solution (5 g/l) was 60 nm that was measured with AFM (see Sec. 3.3.1). This thickness corresponds to the optical density 0.77. Fig. 16 (left) shows a typical film photo.

### *Drop-casting*

In a major part of optical studies it was more convenient to work with drop-cast films since they are much thicker than spin-cast or dip-coated films. Pristine and donor-acceptor blended films prepared by drop-casting have a typical thickness in the range 300-1000 nm (measured with AFM, see Sec. 3.3.1) that was necessary for Raman and FTIR studies to have sufficient signal-to-noise ratio. Drop-cast films were optically thick in the spectral range of MEH-PPV absorption ( $>2$  eV) that was convenient for PL quenching and PIA studies to have almost all pump radiation to be absorbed in the film; and therefore any film thickness effect could be neglected. Drop-cast films were also suitable to measure the optical absorption in the optical gap of MEH-PPV in studies of CT interaction in donor-acceptor blends. Drop-cast films were also used in TOF studies. Drop-casting was performed on a substrate made of glass or BaF<sub>2</sub>. Note that drop-cast films were non-homogeneous in thickness typically varying by a few hundred nanometers overall the film's surface as follows from our AFM and optical absorption data. A photo of a typical drop-cast film is shown Fig. 16 (right).

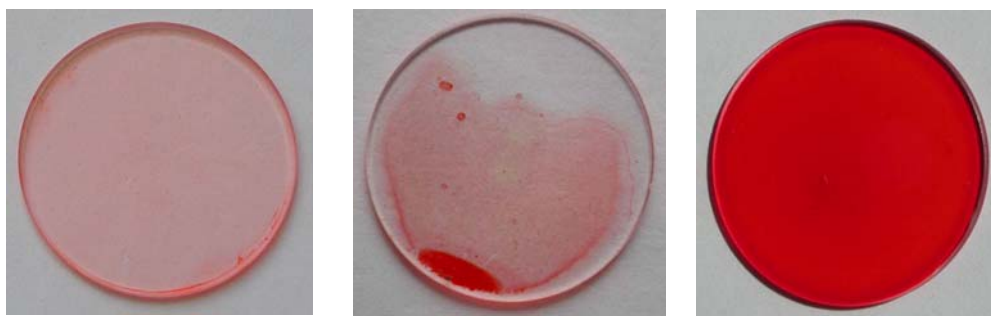


Fig. 16. Photos of a spin-cast (left), dip-coated (middle), and drop-cast (right) films prepared from chlorobenzene (2 g/l.)

#### **3.1.2.2 Slow solvent evaporation method**

Our above PL data imply that the longer solvent evaporation time during solidification, the more optimal film morphology could be realized. Motivated by further increasing the solvent evaporation time, we have developed possibly a new method of polymer film preparation. In this method, very slow ( $\sim 10$ -20 days) solvent evaporation (SSE) under ambient conditions from a vessel with the polymer solution is realized with a substrate being placed on its bottom. The SSE method is expected to provide nearly equilibrium conditions for polymer film formation. Below we compare the PL properties of SSE and drop-cast films since they have more similar preparation conditions than those of dip-coated or spin-cast films. The thickness of the SSE films was about that of drop-cast films or some higher.

As seen in Fig. 15, the PL of the SSE film is reddest showing a more enhanced fine structure than those of films prepared by the other methods. Fig. 17 compares PL spectra of drop-cast and SSE films. They are very close in position and shape, however the SSE films have somewhat redder and more structured PL spectra indicating longer conjugated chain lengths and their narrower distribution in length. Fig. 18 shows absorption edge, PL and PL excitation (PLE) spectra of a SSE film prepared from toluene. A relatively flat PLE spectrum implies that all the conjugation chains contribute to PL almost equally.

As follows from Fig. 17, the PL position in the SSE film is less sensitive to temperature than that in the drop-cast film. Moreover, Fig. 19 shows that the temperature dependence of PL intensity is smoother for the SSE film than for the drop-cast film. These observations indicate that luminophores in the SSE films are less sensitive to temperature than those in the drop-cast films.

The PL quantum yield (QE) of MEH-PPV solution and films was measured relative to a diluted Rhodamine 101 methanol solution and corrected for the corresponding refractive index factor (to take into account the difference in the detection solid angles). For samples from chlorobenzene, the



PL QE 30% was measured for the MEH-PPV solution,  $\approx 20\%$  was evaluated for a SSE film at 300 K (supposing its refractive index to be 1.9) and 20% lower than that for a dip-coated film. It is important that the red-shifted PL in the SSE films is at least as efficient as the PL in the dip-coated films. Therefore, PL can be red shifted and quite efficient in the SSE films indicating that enhanced interchain interaction expected in them does not decrease the PL efficiency.

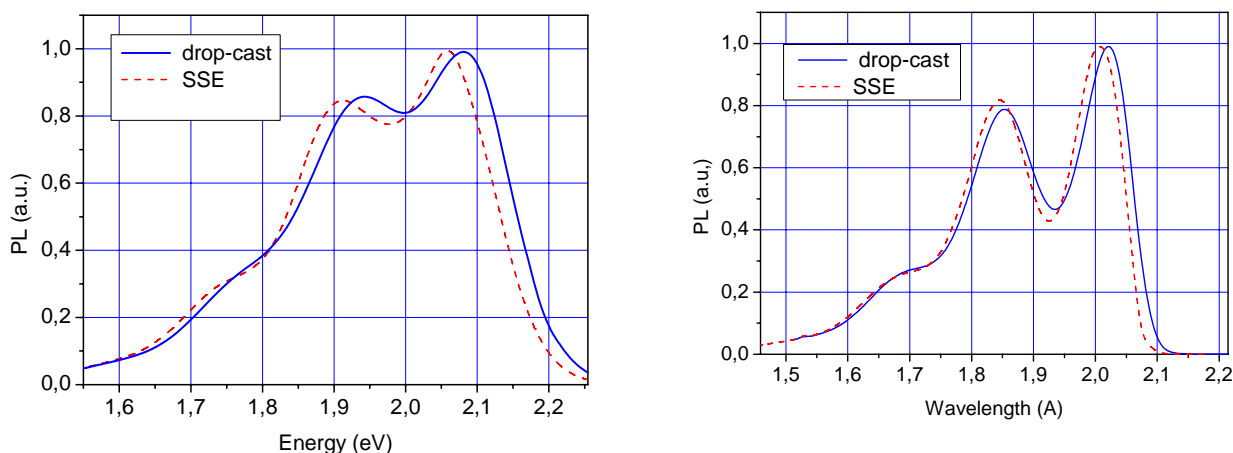


Fig. 17 Normalized PL spectra of MEH-PPV films prepared from chlorobenzene by SSE (dashed) and drop casting (solid) methods at 300 K (left) and at 100 K (right). The polymer concentration in solution was 2 g/l.

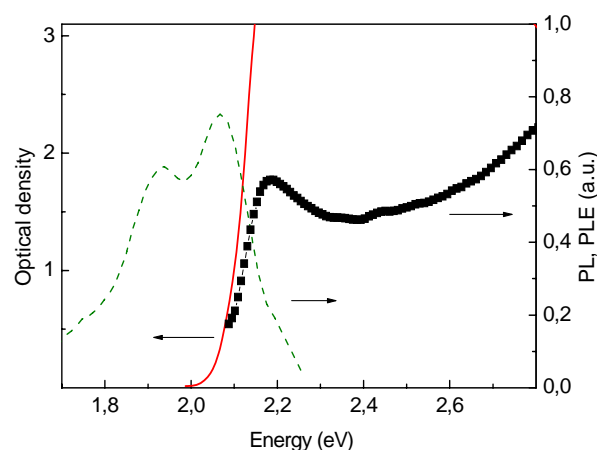


Fig. 18 Absorption edge, PL, and PLE spectra of the SSE film prepared from toluene with concentration 0.5 g/l. PLE was recorded at 600 nm and corrected for the instrument response and the film absorption. The optical density of the SSE film for spectral range  $>2.1$  eV was too high to be measured by the spectrophotometer.

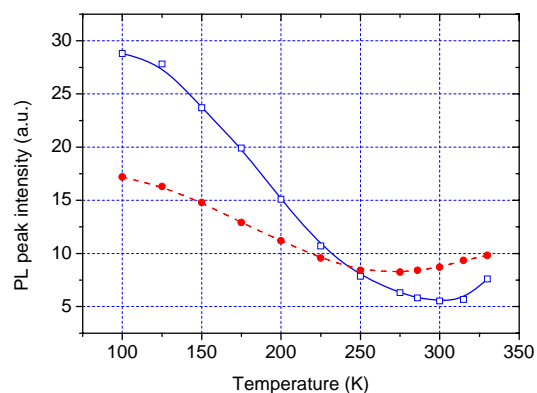


Fig. 19 Temperature dependence of peak PL intensity for drop-cast (solid, at 613 nm) and SSE (dashed, at 620 nm) films of MEH-PPV prepared from chlorobenzene. The absolute PL intensities for these films should not be compared.

Furthermore, we have observed a noticeable difference in PL spectra of drop-cast and SSE films after long term storing. Fig. 20 compares PL spectra of drop-cast and SSE MEH-PPV films

recorded after preparation and long-term storing. The PL spectrum of the drop-cast film is red shifted after storing with some increase in intensity at the long-wavelength shoulder (Fig. 20, left). According to the literature data, red shifted PL is usually associated with unfavorable aggregation leading to decreasing the PL efficiency. At the same time, the PL of the SSE film (Fig. 20, right) does not show any shift after two months. Moreover, a clear fine structure appears after storing implying more homogeneous structure of luminophores. These observations suggest that the SSE method and drop-casting give different film nanomorphologies evolving after preparation in distinct ways.

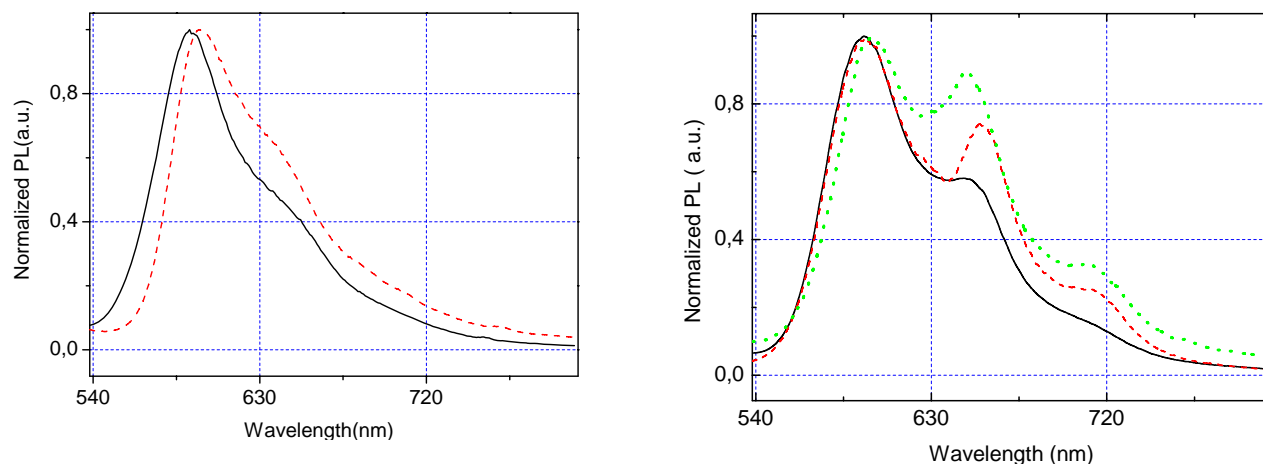


Fig. 20 PL spectra of MEH-PPV films prepared from toluene by drop casting (left) and SSE (right). Dashed lines correspond to the spectra recorded 2 months later, dotted line — 4 months after film preparation. Both samples were stored in the same conditions. Spectra were not corrected for the instrument response.

#### *Possibilities of the SSE method*

We have found that the SSE method allows us to prepare films with strongly different structural and optical properties varying concentration, solvent, and time of solvent elimination. As an example of different film structures, Fig. 21 presents microscope photos of the SSE films with nearly amorphous (left) and highly crystalline (right) structures.

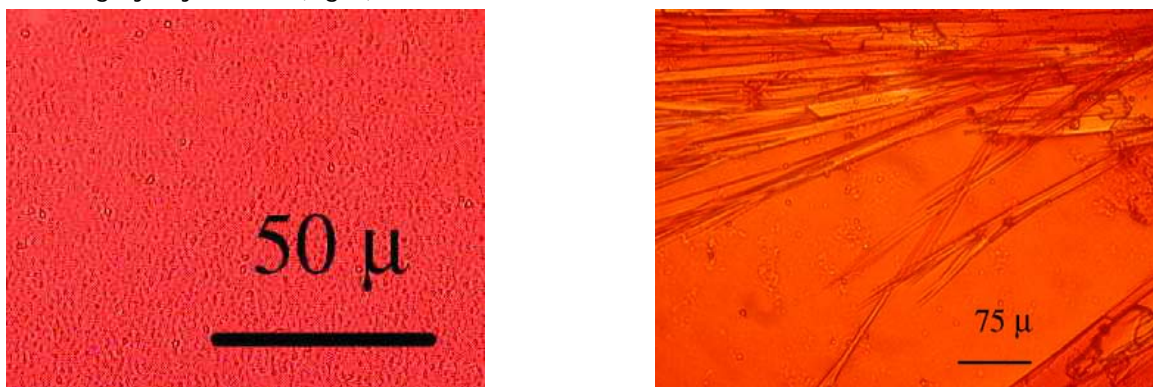


Fig. 21 Microphotographs of MEH-PPV films prepared from chlorobenzene (left) and iodobenzene (right) solutions by the SSE method.

However, we found that the use of solutions with concentration below a certain value (for example,  $\sim 0.1$  g/l from toluene) results in low quality SSE films with inhomogeneous structure and low stability. In particular, the PL and optical absorption spectra of samples obtained from 0.01 g/l

solution became broader. In contrast, the PL and absorption spectra of films prepared from solutions with concentration in the range 0.5–2 g/l show only slightly differences.

It is essential that the SSE method allows us to prepare films with strongly different optical properties varying concentration, solvent, and time of solvent elimination. Fig. 22 shows the PL spectra of three SSE samples prepared from toluene and chlorobenzene. If sample 1 demonstrates the PL spectrum typical for MEH-PPV films with characteristic vibrational structure, the other two are essentially different in the shape and spectral position. For example, the PL of sample 2 is considerably red shifted and has a clear fine structure. We suggest that the bands at 1.9 and 1.72 eV are from a small fraction of specially ordered macromolecules. The band at 2.1 eV is probably from the rest of conjugated fragments of MEH-PPV. Essentially, that although the absorption edge in sample 2 starts at 2.1 eV as in usual MEH-PPV films a small absorption peak at 1.9 eV is clearly observed (Fig. 22). We suggest that the two PL low-energy bands (1.72 and 1.9 eV) and the band at 2.1 eV in sample 2 correspond to different electronic states. In fact, we observed the bands at 1.72 and 1.9 eV excited by red laser pump at 1.96 eV (633 nm) where the optical absorption is very low (see Fig. 22). Moreover, the PL quantum yields for pump at 633 and 532 nm calculated per absorbed photon were close. These data suggest that PL at 1.9 and 1.72 eV arises due to efficient energy migration from the high-energy chromophores to the low-energy luminophores. At the same time, the PL quantum yield for sample 2 was a few times lower than that of standard MEH-PPV films. At this point, the origin of the low energy PL bands is not clear, for example, they may appear from aggregated chains or from long conjugated chains.

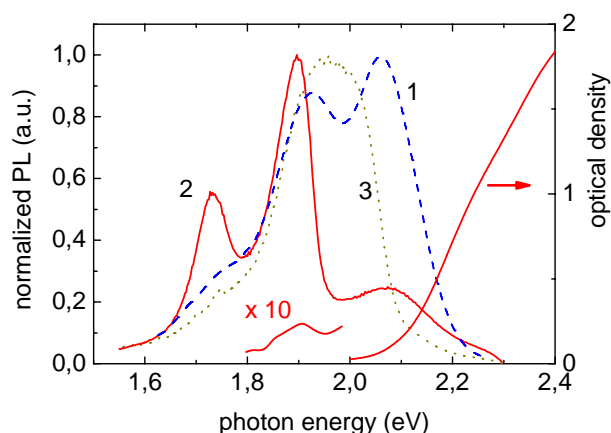


Fig. 22 PL spectra of the SSE MEH-PPV films: (1) from 0.5 g/l solution in toluene; (2) from 0,01 g/l solution in toluene; (3) from 1 g/l solution in chlorobenzene. The excitation wavelengths were 540, 450 and 500 nm, respectively. The absorption spectrum of sample 2 is also shown with enlarged scale in the range 1.8–2 eV.

### 3.1.2.3 Hole drift mobility in MEH-PPV films prepared by drop-casting and SSE

For photoelectric applications, the charge mobility is one of the most essential parameters of the polymer working layers. Hole drift mobility in MEH-PPV films prepared by drop-casting and SSE has been measured using the time-of-flight (TOF) technique (see Sec. 2.10) at room temperature. The films were prepared from the same chlorobenzene solution with concentration 2 g/l. The film thicknesses were about 1  $\mu\text{m}$ . Transient currents have been found to show non-dispersed and dispersed behavior in SSE and drop-cast films, respectively (Fig. 23). Fig. 24 compares the field dependence of the hole drift mobility in both types of films. As seen in Fig. 24, the hole mobility in the SSE film ranges from  $2.2 \cdot 10^{-6}$  to  $7.0 \cdot 10^{-6} \text{ cm}^2 \text{V}^{-1} \text{s}^{-1}$  rising as the applied electric field increases from  $4.2 \cdot 10^4$  to  $2.9 \cdot 10^5 \text{ V/cm}$ . The mobility in the drop-cast film is lower by a factor of 4-5 in this electric field range. This difference was observed for different SSE and drop-cast films.

The higher hole mobility in the SSE films suggests that charge carrier transport sites are more uniformly distributed in the SSE films and these sites form a more efficient network for hole transport with less deep trapping. From our TOF data one may suggest that conjugated segments of

MEH-PPV, serving as transport sites, are packed more favorably in the SSE film than in drop-cast one in order to afford enhanced intermolecular electron transfer. Indeed, such closely packed MEH-PPV molecules form order domains with more perfect morphology [11]. Within an ordered domain, the microscopic mobility was found to increase. Alternatively, an interface between the ordered and disordered domains can be a charge trap. So, the more interfaces between the ordered and disordered domains, the lower drift mobility. One can suppose that the size of the ordered domain is larger; and therefore the content of these interfaces is lower in the SSE films than in the drop-cast ones. This can explain the higher mobility in the SSE films.

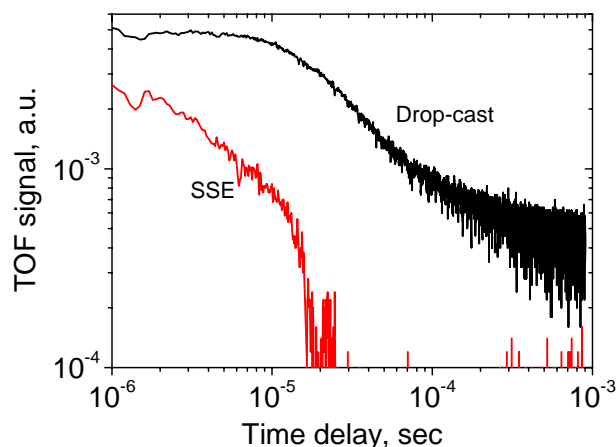


Fig. 23. Time-of-flight signal in SSE and drop-cast films prepared from chlorobenzene.

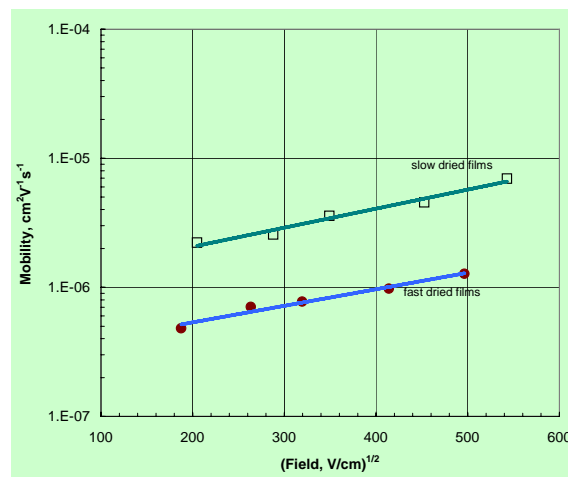


Fig. 24 Hole drift mobility in MEH-PPV films prepared by drop-casting (lower line) and SSE (upper line) as a function of the applied electric field.

#### 3.1.2.4 AFM characterization of pristine MEH-PPV films

MEH-PPV films prepared by spin- and drop-casting, dip-coating, and SSE from chlorobenzene were studied by AFM in the contact mode. Table 1 summarizes our AFM data. Fig. 25 and Fig. 26 show typical AFM images of spin-cast and SSE films, correspondingly.

Method of film preparation	Roughness, nm	Typical size of circular topographic features (diameter x height), nm	Film thickness, nm
Spin-casting at 1500 rpm	0,7	150x5	~25
Dip-coating	1,1	140x12	<15
Drop-casting	1,8	200x15	not available
SSE	1,7	400x6	not available

Table 1. Summary of AFM data for pristine MEH-PPV films prepared from chlorobenzene.

Note that the SSE method allows us to prepare quite flat films with low height of topographic features characteristic of spin-cast films (Table 1). We suppose that small craters (Fig. 26) form due to evaporation of tiny drops of solvent incorporated in the film during film drying.

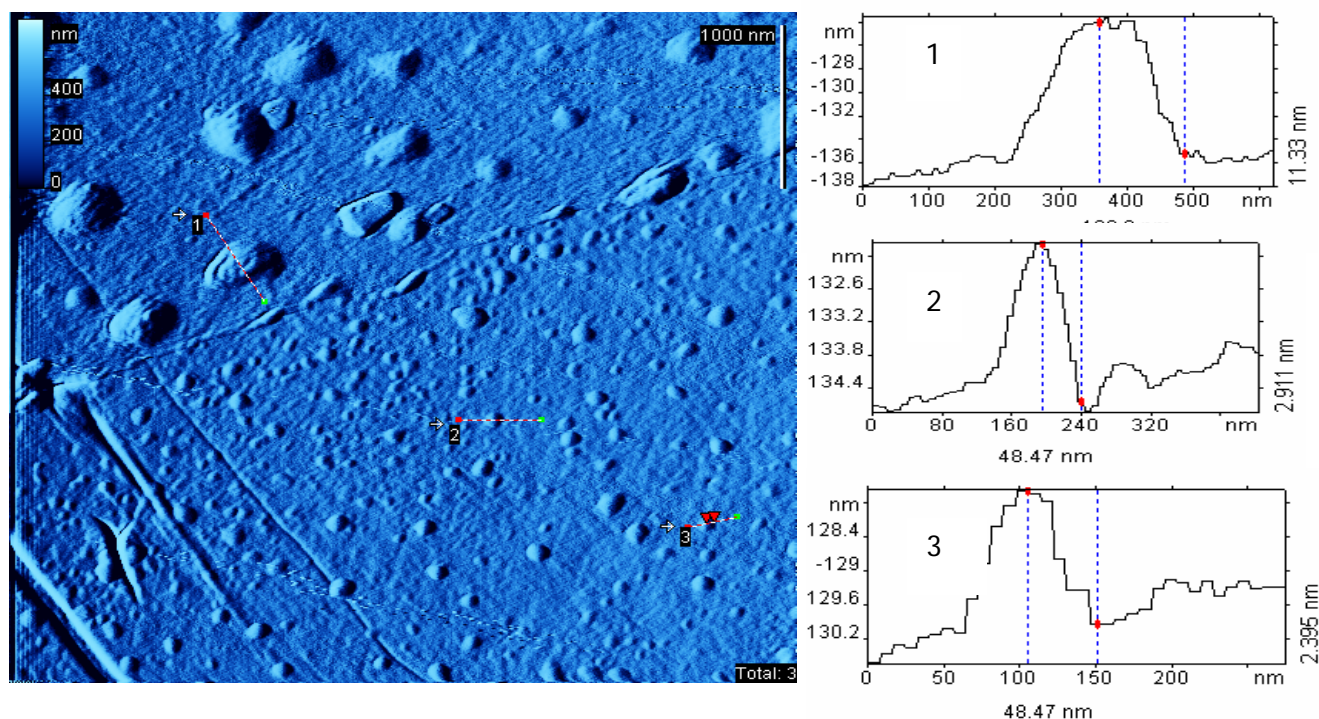


Fig. 25. Topography and typical cross-sections of MEH-PPV film prepared by spin-casting at 1500 rpm from chlorobenzene.

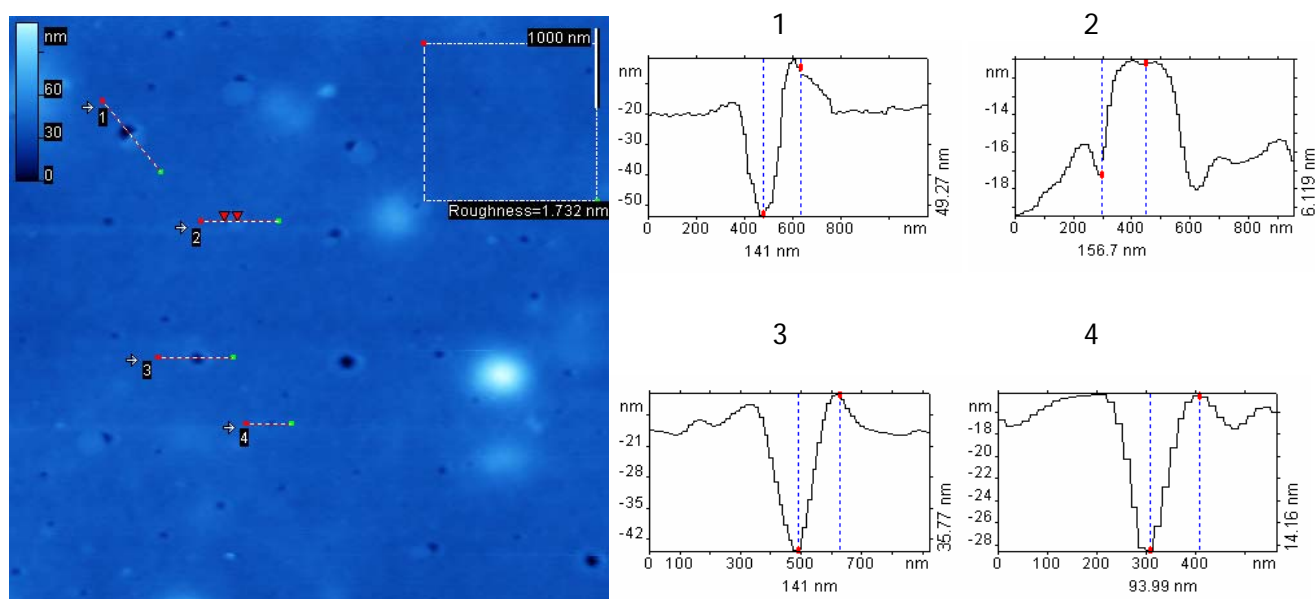


Fig. 26. Topography and typical cross-sections of a MEH-PPV film prepared by SSE from chlorobenzene.



### 3.1.2.5 Absorption and refraction

We measured complex refractive index  $n$  of MEH-PPV films using the technique described in Sec. 2.3. We studied pristine MEH-PPV films prepared by different methods (spin-casting, drop-casting, dip-coating, and SSE) and different solvents (chlorobenzene, toluene, and cyclohexanone). We have not found any correlation between  $n$  and either the preparation method or solvent. Fig. 27 shows results for a set of films prepared by drop-casting and SSE from different solvents. It is seen that  $\text{Re}(n)$  varies in the range 1.45–2.1, and  $\text{Im}(n)$  varies in the range 0.2–0.85. We are not sure that the observed scattering of our data reflects the true difference in film's refractive index. Possibly, the method has an intrinsic flaw, e.g., it suggests that the complex  $n$  of the film is identical at its two interfaces (air/film and substrate/film). Maybe this suggestion is not correct as solidification conditions, which are known to influence the film's nanomorphology and therefore optical properties, are somewhat different at these two interfaces. Nevertheless, as follows from Fig. 27, the typical absorption coefficient of MEH-PPV in the absorption maximum at 500 nm is  $1.5 \pm 0.3 \cdot 10^5 \text{ cm}^{-1}$ , which is in good correspondence with the literature data.

We evaluated the absorption coefficient of the polymer films by another way. The thickness of the films was measured using AFM and their optical density was obtained from the optical absorption spectra. The peak absorption coefficient of drop-cast and spin-cast pristine MEH-PPV films was  $0.9 \pm 0.1 \cdot 10^5$  and  $1 \pm 0.1 \cdot 10^5 \text{ cm}^{-1}$  at 500 nm, respectively. These values are within the range of those shown in Fig. 27. Thus, our findings suggest that the optical parameters of pristine MEH-PPV films do not depend on the preparation methods within our experimental error.

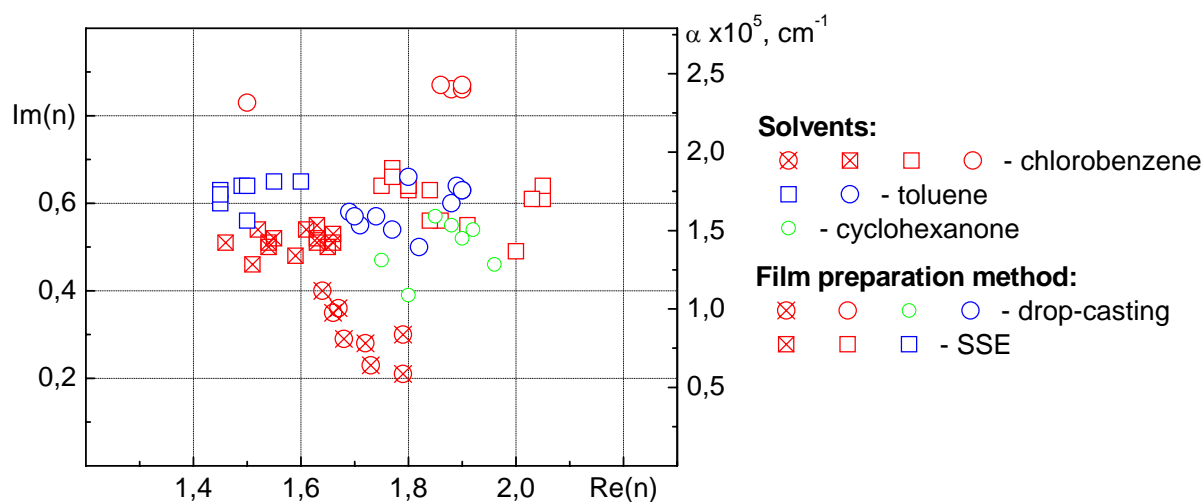


Fig. 27. Complex refractive index of MEH-PPV films at 532 nm. The symbols of the same color and shape correspond to different points on the same film. The right vertical axis shows the absorption coefficient calculated as  $\alpha = 1.18 \times 4\pi \text{Im}(n)/\lambda$  for the MEH-PPV absorption maximum at 500 nm. The factor 1.18 takes into account the difference in the optical absorption of spin-cast MEH-PPV films at 532 and 500 nm.

### 3.1.2.6 Conclusion

Thus, we analyzed four methods of polymer film preparation (dip-coating, spin-casting, drop casting, and SSE) differing from each other by the time of solvent elimination during solidification. Our studies on MEH-PPV suggest that the longer this time, the more optimal morphology is realized corresponding to longer conjugated chains of chromophores and luminophores, a narrower

distribution in conjugated lengths, more effective energy migration and charge transport. The best methods in this sense seem to be drop-casting and SSE. Among the latter, the SSE is the best since the hole mobility in the SSE films is shown to be a few times higher than in the drop-cast films. At the same time, the PL quantum yield in the SSE films can be as high as in the films prepared by other methods. However, practically, the used drop-casting and SSE methods have a drawback: the film thickness is difficult to make thin (~100 nm) and homogeneous. In addition, the SSE takes a lot of time for solidification. As a result, we used spin-casting for recording absorption spectra and photoelectric studies, i.e., solar cells prototypes; in all other studies we used drop-casting.

## 3.2 Acceptors

At the beginning, the preliminary screening of organic acceptors was fulfilled. We were guided by the magnitude of the electron affinity and topological compatibility with the MEH-PPV structure. We also supposed that longer acceptor molecules are more optimal for CTC interaction with conjugated chains. More than 10 organic compounds such as TCNQ, TCNE, chloranil, 1,5-dinitroantraquinone (DNAQ), 2,4,7-trinitrofluorenone (TNF), etc. were studied. We also used fullerene ( $C_{60}$ ) as an acceptor, which is commonly considered not to form any CTC with PPV-type and other conjugated polymers. We used MEH-PPV/ $C_{60}$  blends as well-studied reference samples for comparison with the effect of other acceptors.

Molecular acceptors (TNF, DNAQ, etc.) were used as received from Russian suppliers (purity no less than 99%). They are highly soluble in polar solvents such as chlorobenzene, tetrahydrofuran etc.

Absorption and PL were recorded for MEH-PPV/acceptor blends both in solutions and films. If an acceptor resulted in noticeable change of the pristine MEH-PPV spectra, we studied this MEH-PPV/acceptor blend in detail. Table 2 describes acceptors that we thoroughly studied in blends with polymers. The experimental data and more detailed data on the acceptors are given in the following sections.

We have found that among the acceptors studied TNF results in most pronounced changes of absorption and vibrational spectra of MEH-PPV in MEH-PPV/TNF blends indicating a noticeable ground-state interaction. Because of this, we have studied blends of MEH-PPV with ten various acceptors of the fluorene series whose EAs are expected to be about or higher than the TNF EA. The list of the fluorene acceptors and their EAs are given below in Table 8 of Sec.4.1.3.

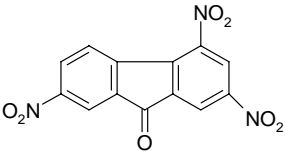
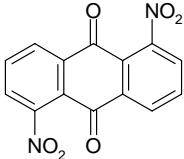
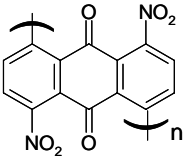

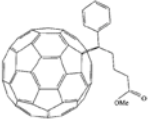
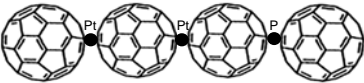
Code	Formula	EA. eV	$E_{\text{red}}$ , V vs Ag/AgCl	See Section
TNF		2.2	-0.32	4.1, 4.2, 4.3, 4.4
DNAQ		1.9 (calculated at AM3 level)	-0.74 (taken as that of polyDNAQ)	4.1, 4.2, 4.3, 4.4, 4.5
polyDNAQ			-0.74	4.5
C <sub>60</sub>		2.7	-0.6	4.3, 4.4, 4.6
PCBM			-0.69	4.4
Pt <sub>0.75</sub> C <sub>60</sub>		Not available	Not available	4.6

Table 2. Acceptors, their EAs and first reduction potentials from literature data. The last column indicates section numbers of the report.

### 3.3 MEH-PPV/acceptor blends

Polymer/acceptor blends were prepared from mixtures of measured volumes of polymer and acceptor solutions. The polymer/acceptor molar ratio was varied from 1:0.0001 to 1:2. The blends were prepared in the same solvent and typically with the same concentrations of the individual components. Polymer solutions (in chlorobenzene, toluene, cyclohexanone etc.) were prepared by dissolving an appropriate amount of the polymer into the measured quantity of solvent and stirring for 60–90 min at 50°C in ultrasonic bath. Spin-casting, drop-casting, and SSE methods were used for film preparation (see Sec. 3.1.2). All the preparation steps were performed in ambient laboratory conditions.

Chlorobenzene was chosen as a basic solvent for blends. We were motivated that it is one of the best solvents for MEH-PPV resulting in an extended polymer conformation in solution. This open, extended conformation was expected to be favorable for interaction with acceptor molecules. On the



other hand, we also studied blended films prepared from toluene or cyclohexanone. All these three solvents allowed preparation of neat homogeneous films. Using optical absorption and vibrational spectroscopy, we did not notice any essential difference in the properties of films prepared from different solvents. On the other hand, our experience suggests that the PIA data on MEH-PPV/TNF blends can be sensitive to the solvent type and peculiarities of the film preparation method (see Sec. 4.3.2.3).

### 3.3.1 Microscopy

The major part of the results on CTCs was obtained on MEH-PPV/TNF and MEH-PPV/DNAQ blended films. Their characterization is given below. Characterization studies of MEH-PPV blends with a series of fluorene acceptors are described below in Sec. 4.1.3.

MEH-PPV/TNF and MEH-PPV/DNAQ blends form visually homogeneous films for molar acceptor/donor ratio less than unity. Photos of typical 1:1 MEH-PPV/TNF and MEH-PPV/DNAQ are shown below in Fig. 70.

Fig. 28 depicts optical microscopy images of drop-cast MEH-PPV/TNF (left) and MEH-PPV/DNAQ (right) films with 1:1 molar ratio of the components. At this ratio a noticeable part of acceptor forms separate features that can be assigned to acceptor crystallites. At acceptor content in the blend 0.5 and lower, any visible features are not observed visually or using optical microscopy as illustrated in Fig. 29 (see also Fig. 96 and Fig. 99).

In 1:1 MEH-PPV/TNF films, TNF crystallizes in tree-like structures (Fig. 28, left) covering the overall film's surface ( $\sim 1\text{--}4\text{ cm}^2$ ) with a characteristic spot in the central part of the film. The width of the branches is varied in the range  $5\text{--}30\text{ }\mu\text{m}$ . The smallest spot is seen as a center of the tree-like structure in (Fig. 28, left). This spot appears only in the chlorobenzene films as a result of evaporation of the residue solvent during solidification, and it has a lower concentration of the TNF phase. This spot typically has a size in the range  $0.1\text{--}5\text{ mm}$  depending on the peculiarities of the film preparation method (the largest spot is shown below in Fig. 121). Remarkably that our PIA data were sensitive to the presence of this spot (see Sec. 4.3.2.3). MEH-PPV/TNF films prepared from cyclohexanone or toluene also showed TNF crystallites. However, they formed completely different structures as compared with that shown in Fig. 28 (left). For example, in cyclohexanone TNF was aggregated in separated features like those shown in Fig. 28 (right)

DNAQ in blends with MEH-PPV forms large separate features with a typical size of  $\sim 20\text{ }\mu\text{m}$  clearly visible in Fig. 28 (right).

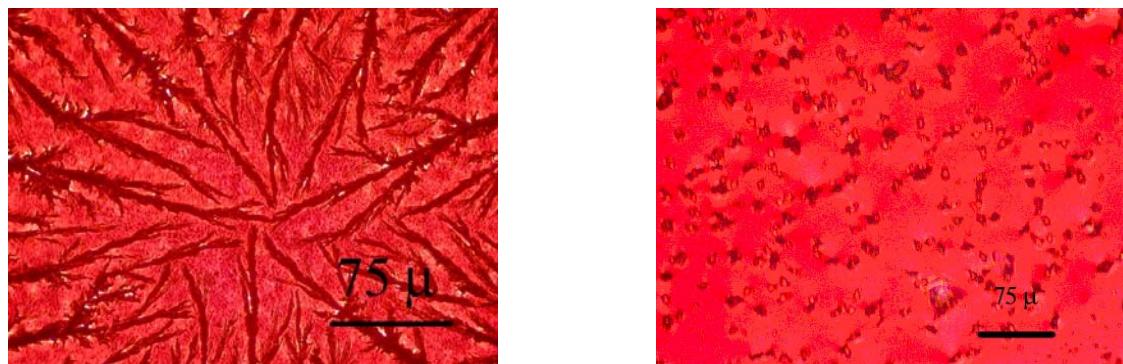


Fig. 28. Optical microscopy images of 1:1 MEH-PPV/TNF (left) and 1:1 MEH-PPV/DNAQ (right) drop-cast film prepared from chlorobenzene.



Fig. 29. Microphotograph of 1:0.2 MEH-PPV/TNF film drop-cast from chlorobenzene.

MEH-PPV/acceptor blended films were characterized by AFM. MEH-PPV/TNF films with different MEH-PPV/TNF molar ratios were studied. Films were spin-cast at 1500 rpm on glass substrates from chlorobenzene solution prepared by mixing MEH-PPV and TNF individual solutions of 2 g/l concentrations. AFM images were recorded on the “Femtoscan online” instrument and processed using its built-in filters (slope correction, median filtering etc.). To increase the contrast of topographic images, they were highlighted. Roughness was calculated on  $2 \times 2 \mu\text{m}$  regions not containing large topographic features.

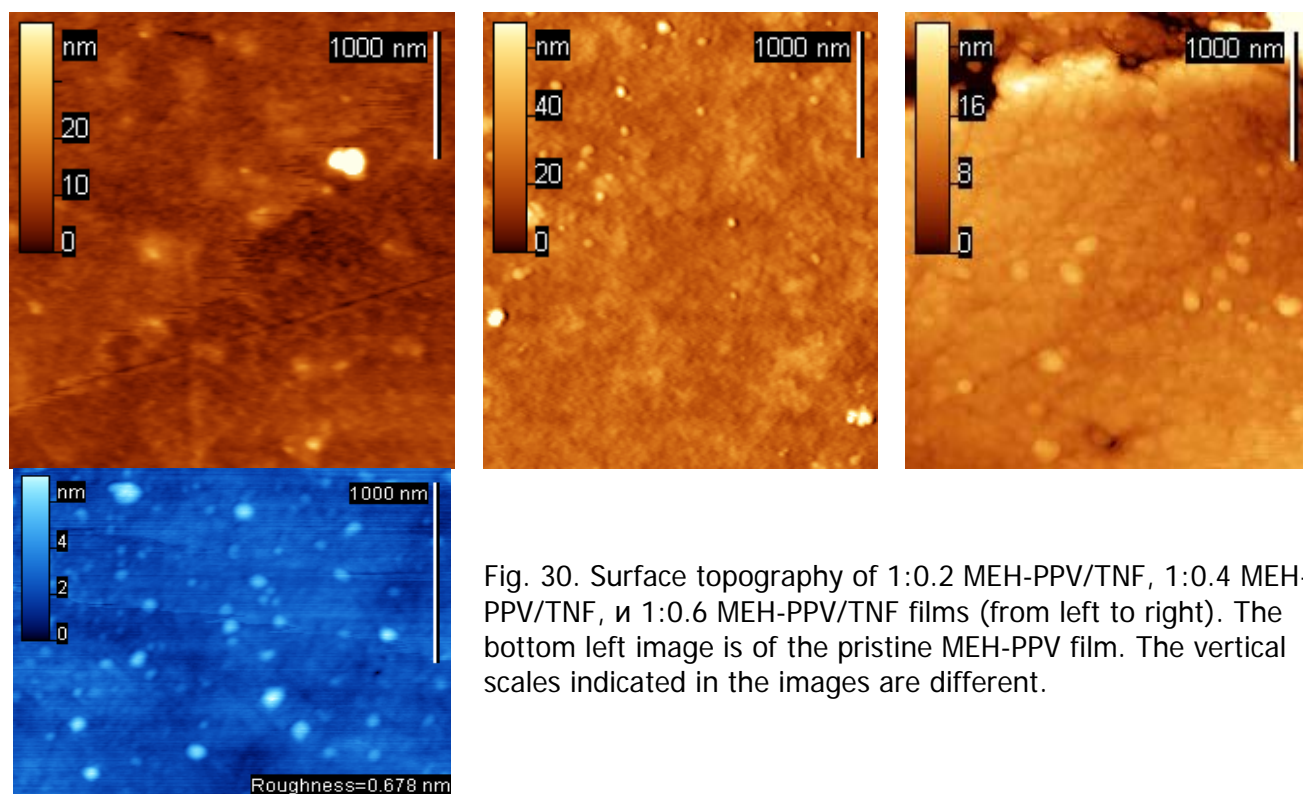


Fig. 30. Surface topography of 1:0.2 MEH-PPV/TNF, 1:0.4 MEH-PPV/TNF, и 1:0.6 MEH-PPV/TNF films (from left to right). The bottom left image is of the pristine MEH-PPV film. The vertical scales indicated in the images are different.

Fig. 30 compares topographies of the samples with different TNF content. It is seen that increasing TNF content results in a less smooth surface with characteristic topographic features. Their number grows with increasing the TNF content. Table 3 summarizes the results comparing AFM data for the blends and the pristine MEH-PPV. Fig. 31, Fig. 32, and Fig. 32 show AFM images with typical cross-sections of the topographic features for the blended films with 1:0.2, 1:0.4, and 1:0.6 MEH-PPV/TNF ratios, respectively. The 1:0.2 MEH-PPV/TNF film had a smooth amorphous surface with small islands in the form of a plateau of 5–6 nm height. The surface of the 1:0.4 MEH-PPV/TNF film looks like consisting of these islands. The 1:0.6 MEH-PPV/TNF film had a surface possibly consisting of layered structures. Note that the roughness of the latter sample was less than

that of the former (Table 3). AFM image of a 1:1 MEH-PPV/TNF spin-cast film deposited on a PEDOT:PSS layer is shown below in Fig. 48. In this sample with highest content of TNF, it forms separated features in the form of plateau with width x height 500x50 nm. Thus, the typical width and height of TNF features grow with increase its content in the blend.

Sample	Figure	Roughness, nm	Comment
pristine MEH-PPV	Fig. 30 (bottom left)	0.67	the smoothest surface
1:0.2 MEH-PPV/TNF	Fig. 31	$2.1 \pm 0.8$	smooth surface; a number of globular features with height 6–20 nm and of elevated regions at height 6 nm
1:0.4 MEH-PPV/TNF	Fig. 32	$3.9 \pm 0.6$	less smooth surface; a number of crystal-like features with size x height $\sim 30 \times 5$ nm
1:0.6 MEH-PPV/TNF	Fig. 33	$1.9 \pm 0.9$	relatively smooth surface (cf. with the 1:0.4 film); a lot of globular structures with height 6–8 nm; layered structures with width x height 500–1000 x 20 nm
1:1 MEH-PPV/TNF	Fig. 48	n/a	isolated features in the form of plateau with width x height 500x50 nm (cast on PEDOT:PSS layer at a somewhat different coating procedure)

Table 3. Summary of AFM characterization for MEH-PPV/TNF films spin-cast at 1500 rpm from chlorobenzene.

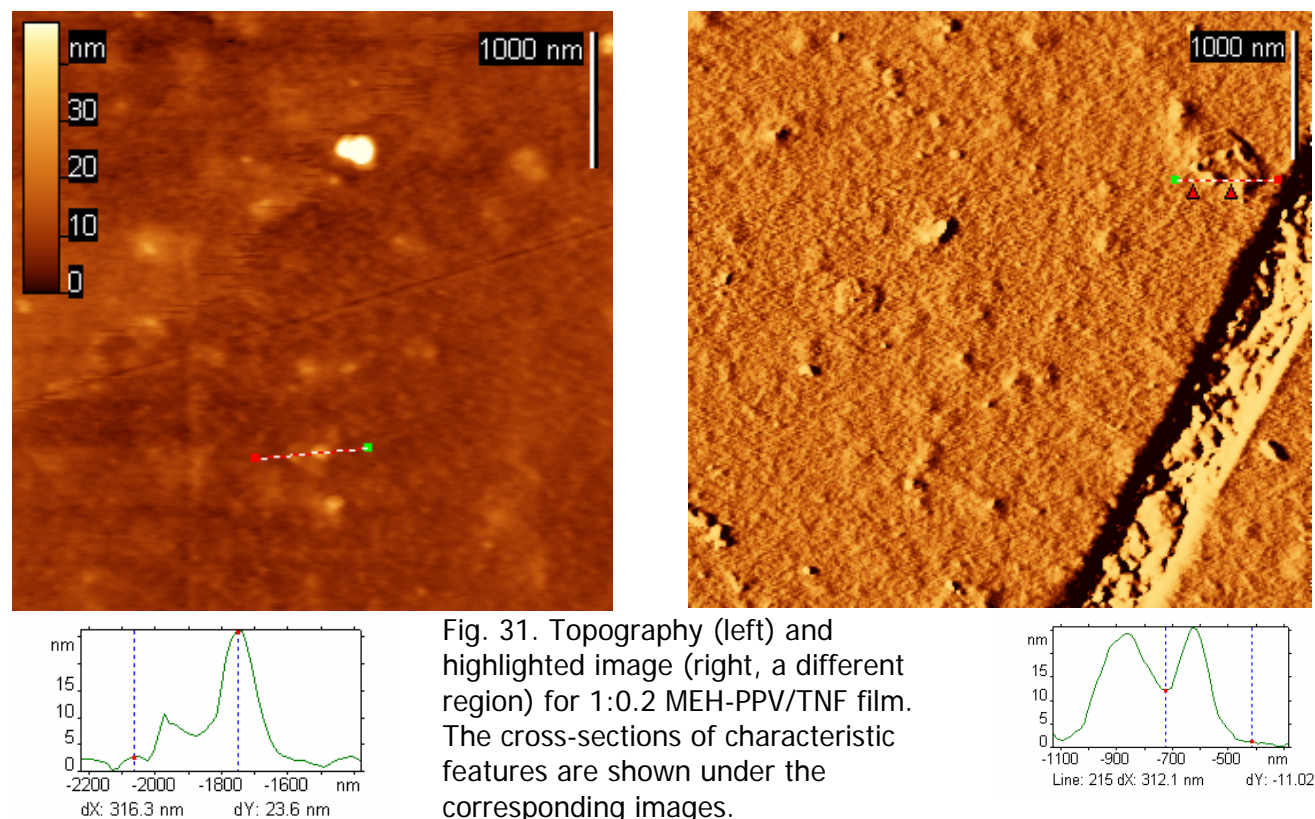


Fig. 31. Topography (left) and highlighted image (right, a different region) for 1:0.2 MEH-PPV/TNF film. The cross-sections of characteristic features are shown under the corresponding images.



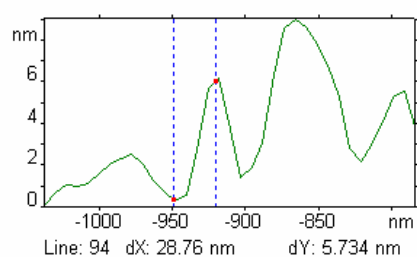
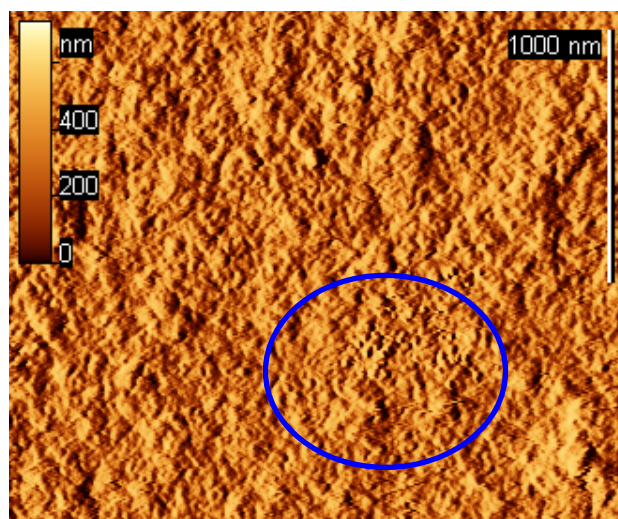
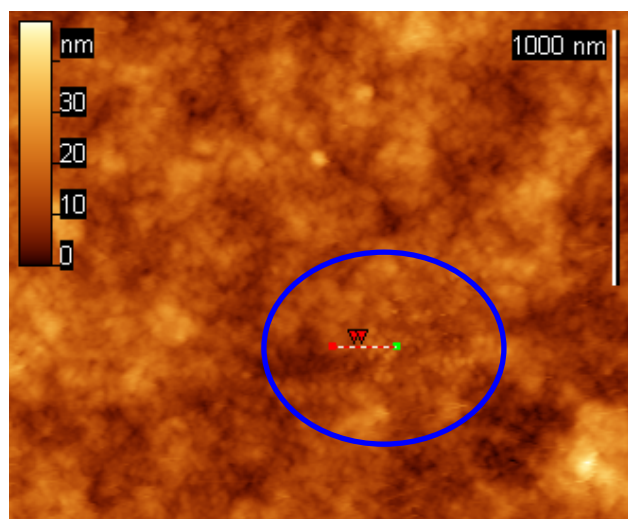


Fig. 32. Topography (left) and highlighted image (right) of the same region for 1:0.4 MEH-PPV/TNF film. Ovals indicate typical crystal-like features with size  $\sim 30$  nm and height 5 nm. The cross-section of such a structure is shown in the bottom left.

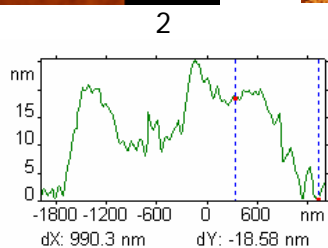
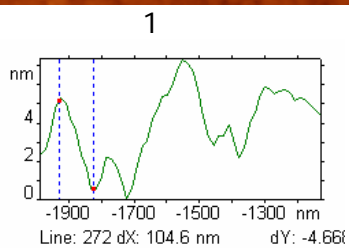
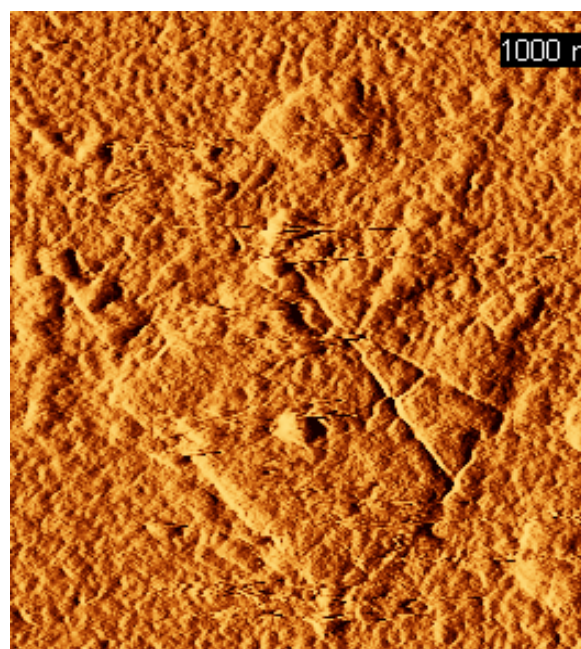
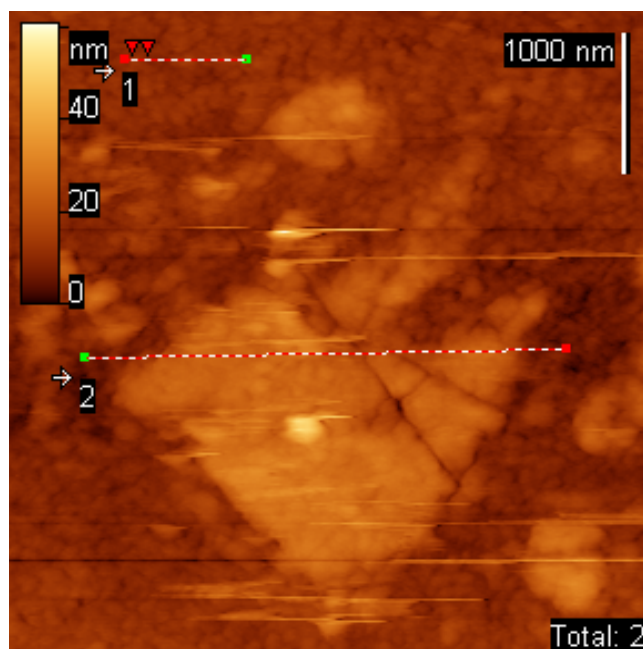


Fig. 33. Characteristic region of the 1:0.6 MEH-PPV/TNF film with an elevated layer of  $\sim 15$  nm thickness (cross-section 2 on the left). Globular structures have a typical height of 5 nm (cross-section 1 on the left.).

Fig. 34 shows an AFM image of a 1:1 MEH-PPV/DNAQ spin-cast film. Analogously to MEH-PPV/TNF films, the surface is relatively smooth (see also Fig. 49) with topographic features that can be assigned to DNAQ crystallites with a typical size of 500 nm.

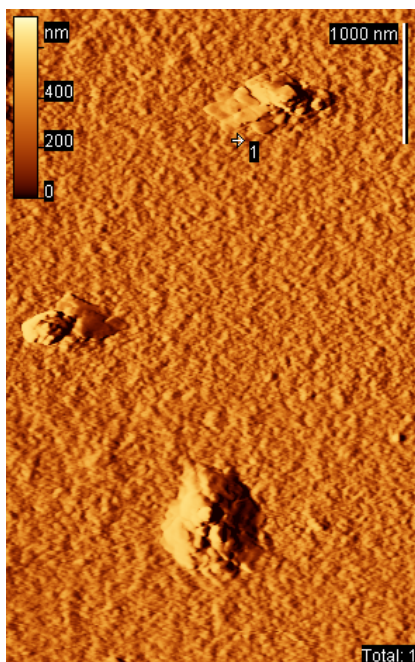


Fig. 34. AFM image of 1:1 MEH-PPV/DNAQ spin-cast from chlorobenzene at 1500 rpm. Concentration of the individual components in solution was 1 g/l.

Fig. 35 illustrates a thickness evaluation procedure using AFM for a relatively thick MEH-PPV drop-cast film. Thicknesses of various spin- and drop-cast films were evaluated by this way.

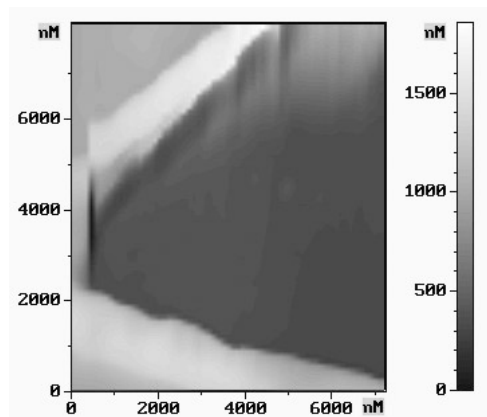


Fig. 35. AFM cross-section of a scratched film for evaluation film thickness. The sample is a MEH-PPV film drop-cast from dichloroethane on a glass substrate. The thickness is  $\approx 700$  nm. The corresponding part of the film's image is shown on the bottom left. The measurement was done on "Smena" NT-MDT

To evaluate how the film thickness depends of the acceptor content, we measured thickness of three films with MEH-PPV:TNF ratios 1:0 (pristine), 1:0.33, and 1:1 prepared from chlorobenzene solution at 1500 rpm on glass substrates. The initial concentration of solutions with the individual components was 5 g/l. The film thickness in surface regions not containing large TNF features was typically 50–60 nm, and therefore it does not show any clear dependence on the TNF content. Note that the polymer concentration in the blended solution decreased by half with increasing the TNF content up to 1:1. This should result in decreasing the film's thickness if we assume that mainly MEH-PPV forms the film. Because of this, a more accurate measurement of film thickness versus the acceptor content probably should be performed for films cast from solutions with the same polymer concentration. This has not been done.

### 3.3.2 Transmission maps of MEH-PPV/acceptor blends at 633 nm

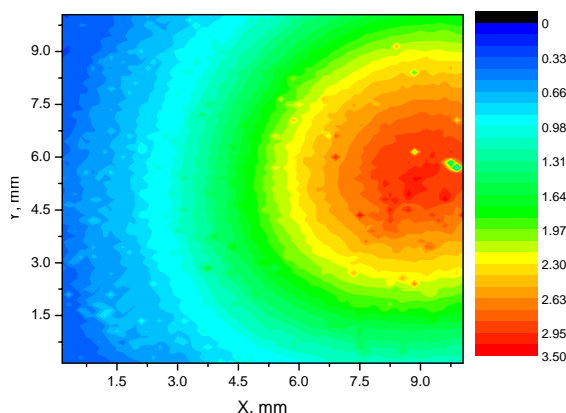


Fig. 36 Transmission map of MEH-PPV:TNF film (molar ratio 1:0.33) drop-cast from chlorobenzene (10x10 mm, resolution 0.15 mm). The color code in Fig. 37–Fig. 39 corresponds to the measured optical density at 633 nm.

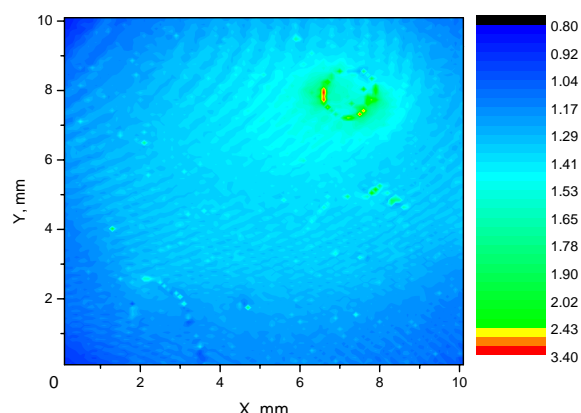


Fig. 37 Transmission map of MEH-PPV:TNF film (molar ratio 1:0.3) prepared by SSE from chlorobenzene (10x10 mm, resolution 0.1 mm).

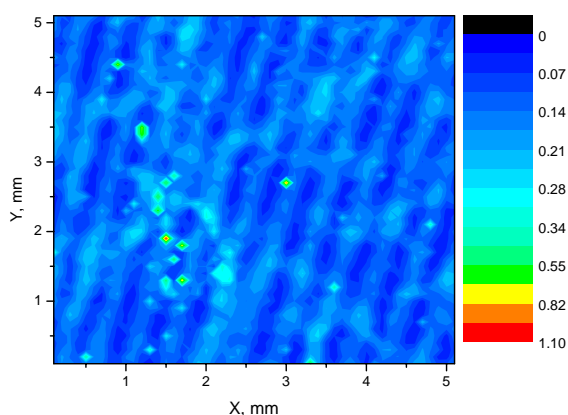


Fig. 38 Transmission map of MEH-PPV:C<sub>60</sub> film (molar ratio 1:1) spin-cast from chlorobenzene (5x5 mm, resolution 0.1 mm).

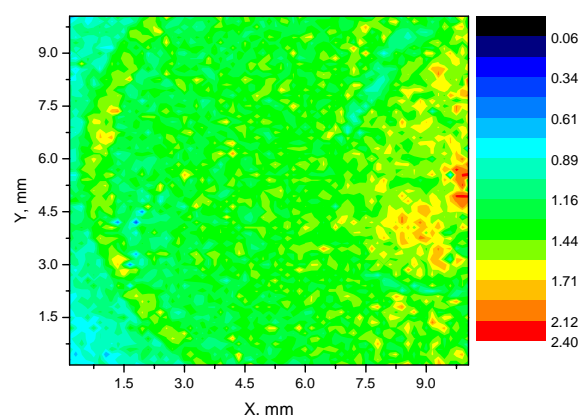


Fig. 39 Transmission map of MEH-PPV:TNF film (molar ratio 1:2) drop-cast from chlorobenzene (10x10 mm, resolution 0.15 mm).



We have observed that drop-cast MEH-PPV/TNF and MEH-PPV/DNAQ films, in which the acceptor molar fraction exceeds some value ( $\sim 0.3$ – $0.4$ ), have noticeable lateral inhomogeneity in light scattering and film thickness over their aperture. The former could be seen visually indicating the uncomplexed acceptor phase, the latter was observed using AFM.

To evaluate the lateral homogeneity, the optical transmittance in films of MEH-PPV/acceptor blends at 633 nm was measured over the sample area with 0.1–0.15 mm resolution. MEH-PPV/acceptor blend films prepared by spin-casting, drop-casting and SSE methods have been studied. As an acceptor we used TNF, DNAQ, polyDNAQ, and  $C_{60}$ . In donor-acceptor blends with ground-state CT interaction, i.e., in MEH-PPV/TNF, MEH-PPV/DNAQ, the measured signal is determined by both scattering and CTC absorption (see Sec. 4.2.3), whereas in MEH-PPV/ $C_{60}$  and MEH-PPV/polyDNAQ films the signal was dominated mainly by light scattering. Transmission maps of MEH-PPV/TNF films with nearly optimal donor/acceptor ratio prepared by drop-casting and SSE are shown in Fig. 36 and Fig. 37, respectively. The signal here is determined mainly by the CTC absorption at 633 nm. Fig. 36 shows that the drop-cast film has the central spot with maximum thickness, which decreases smoothly to the edges over three times. The SSE film has the similar but more homogeneous structure: a wider central spot and about 50% thickness change to the edges (Fig. 37). Almost all the films are characterized by wave-like thickness changes (stripes) with the amplitude of about 0.1 OD and period of 0.3–1.0 mm. Spin-cast films have the average thickness no more than 100 nm, which is approximately equal over the sample area, but such stripes may amount more than half of the average film thickness (Fig. 38). Films with high acceptor/donor molar ratio show rather inhomogeneous transmission maps caused probably by scattering at the uncomplexed acceptor (Fig. 39).

### 3.3.3 Vibrational analysis

#### 3.3.3.1 Pristine materials

If a CTC forms in a MEH-PPV/acceptor blend, one can expect to observe non-additive bands in the IR absorption spectra associated with ground state CT. To monitor possible changes of vibrational bands in the blends, we recorded vibrational spectra of the pristine materials.

Fig. 40 shows FTIR transmission spectra of pristine MEH-PPV and TNF films. Fig. 41 shows FTIR transmission spectra of pristine MEH-PPV and DNAQ. Raman spectra of TNF and DNAQ are also plotted. As seen in Fig. 40 and Fig. 41, there are a number of well-separated IR bands in both the MEH-PPV and the acceptors that might be used for identification ground-state CT. Furthermore, most of the bands of the pristine materials are assigned. Assignment of the observed IR bands in pristine MEH-PPV to vibrations of the polymer backbone is shown in Table 4. Assignment of the most intensive characteristic bands of TNF and DNAQ is listed in Table 5.

As seen in Fig. 40 and Fig. 41, C=O and NO<sub>2</sub> groups of both acceptors give intensive IR bands. The C=O Raman bands are intensive for both acceptors. We noted that NO<sub>2</sub> and other bands in the pristine acceptors were quite sensitive to the method of sample preparation. Shift of a few wavenumbers, noticeable changes in fine structure and intensity of NO<sub>2</sub> and some other acceptor bands were typically observed for different acceptor samples (powders, drop-cast samples prepared in slightly different ways, etc.). This is indicative of a polymorphic structure of TNF and DNAQ, which can be sensitive to the sample preparation details. Because of this, the most acceptor bands hardly can be used for identification of ground-state CT in blends with polymers. It seems that only the C=O band could be a reference for monitoring partial electron transfer to the acceptor as follows from our vibrational studies. In fact, the C=O band is quite sensitive to the electron density in the conjugated backbone of the acceptors (see Fig. 76 below) and is clearly seen both in the Raman and the IR spectra (Fig. 40 and Fig. 41). At the same time, our experience suggests that the C=O band is less sensitive to peculiarities of sample preparation than the NO<sub>2</sub> bands.

Note that carbonyl bands are typically observed in IR spectra of pristine MEH-PPV (bands at 1680 and 1730  $\text{cm}^{-1}$  in Fig. 40 and Fig. 41). They appear and grow with film's aging or photooxidation. We used these bands to monitor photooxidation of pristine MEH-PPV and MEH-PPV/acceptor blends (see Sec. 4.3.6).

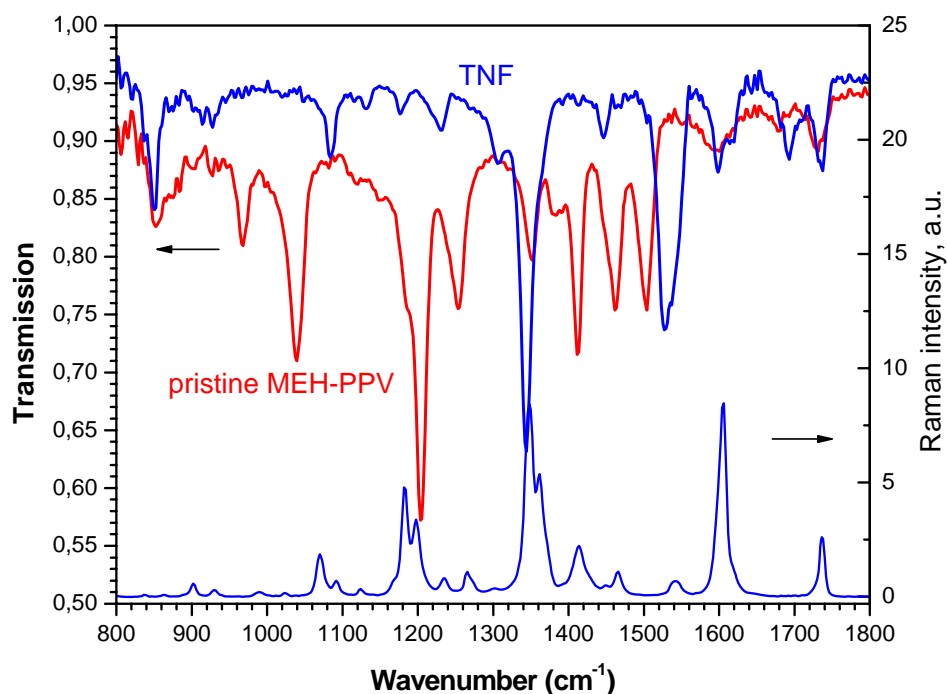


Fig. 40. IR transmission spectra of pristine MEH-PPV and TNF films drop-cast from chlorobenzene on  $\text{BaF}_2$  substrates. Raman spectrum of pristine TNF is also shown (recorded with excitation at 1064 nm).

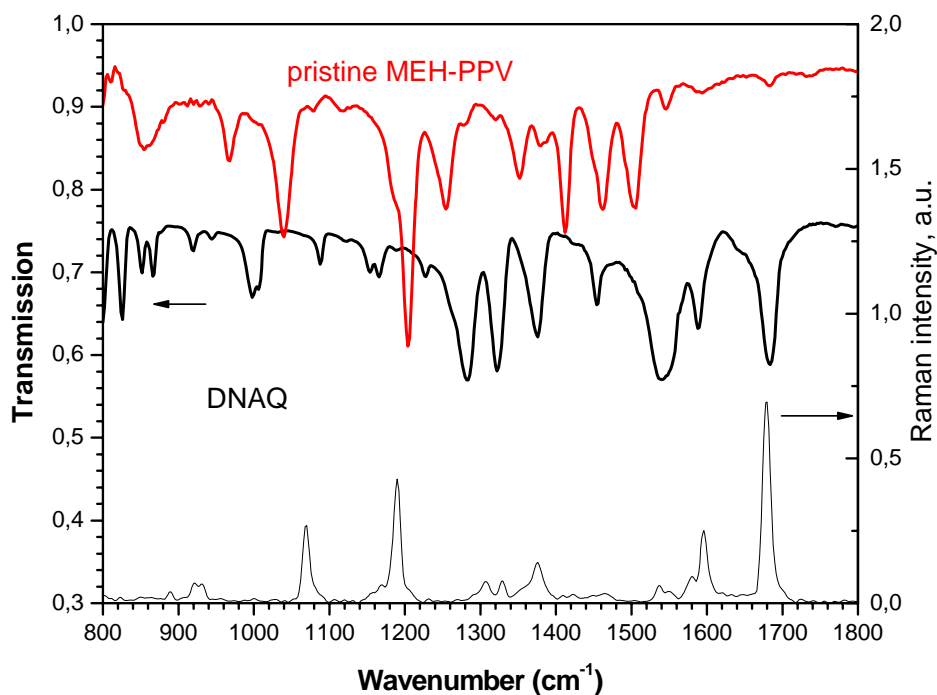


Fig. 41. IR and Raman spectra of DNAQ powder. The IR MEH-PPV spectrum is also plotted for comparison.



Wavenumber (cm <sup>-1</sup> )	Type of vibration
852	Out of plane phenyl CH-wag
966*	Trans-double bond CH-wag (vinyl group)
1039	Alkyl oxygen stretch
1203	Phenyl oxygen stretch
1352	Symmetric alkyl CH <sub>2</sub> deformation
1412	Semicircular phenyl stretch
1462	Antisymmetric phenyl stretch
1504*	Semicircular phenyl stretch (C—C aromatic)
1595	Aromatic stretching
1680, 1730*	Carbonyl bands of oxidized chains

Table 4. Assignment of the most intensive MEH-PPV IR vibrational bands. Asterisks mark characteristic bands used in our studies.

Wavenumber (cm <sup>-1</sup> )		Type of vibration
TNF	DNAQ	
	1282	CC stretch
	1322	CC stretch
1343–1347	1377	Asym. NO <sub>2</sub> stretch
1530–1550	1540	Sym. NO <sub>2</sub> stretch
1730–1735	1683	C=O stretch

Table 5. Assignment of characteristic TNF and DNAQ-PPV IR vibrational bands.

As commonly accepted, conjugated polymers and fullerenes do not interact in blends in their electronic ground state. As we used C<sub>60</sub> as a reference acceptor, we plot in Fig. 42 IR transmission spectra of our pristine MEH-PPV film and of a thin C<sub>60</sub> film on a silicon substrate. C<sub>60</sub> has four IR-active vibrational modes 526.5, 576.5, 1181.9, and 1428.6 cm<sup>-1</sup>, and the two latter are seen Fig. 42.

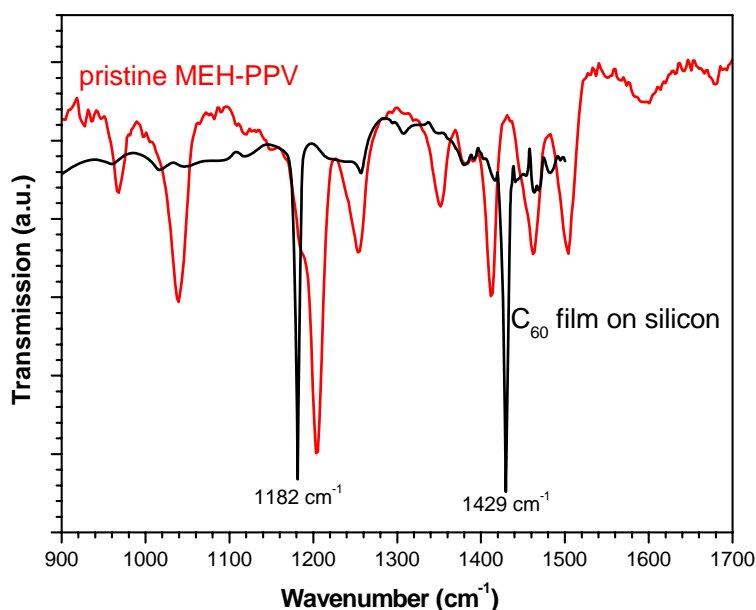


Fig. 42. IR transmission spectra of pristine MEH-PPV and C<sub>60</sub> films. In this region only two IR-active vibrational modes are clearly visible for C<sub>60</sub> [12].

Fig. 43 demonstrates a typical Raman spectrum of a pristine MEH-PPV film drop-cast from chlorobenzene recorded at room temperature with excitation at 670 nm. The spectrum shows 7

bands characteristic of vibrations of the PPV conjugated backbone with peaks/features at 1626, 1582, 1558, 1310, 1283, 1111, and 966  $\text{cm}^{-1}$ . Exactly the same frequencies were observed for excitation at 1064 nm. In our studies of the MEH-PPV/acceptor blends, we investigated only two characteristic Raman vibrations: carbon-carbon (CC) stretching of the phenyl ring at 1582  $\text{cm}^{-1}$  and out-of-plane wag of vinylene CH at 966  $\text{cm}^{-1}$ . The latter mode is schematically shown below in Fig. 102.

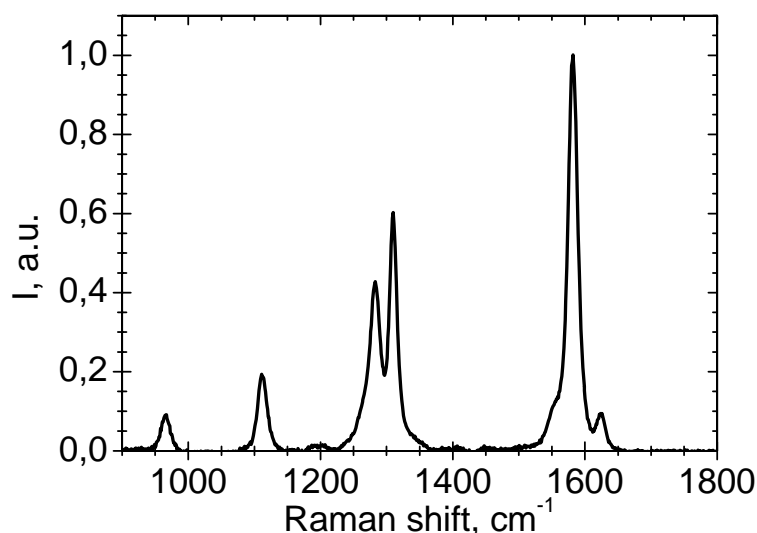


Fig. 43. Raman spectrum of pristine MEH-PPV film recorded at excitation wavelength 670 nm.

### 3.3.3.2 Blends

#### *MEH-PPV/TNF blends*

We observed that a number of MEH-PPV IR absorption bands considerably change their intensity in the MEH-PPV/TNF blend demonstrating non-additive behavior. To see this effect more clearly, we show in Fig. 44 FTIR spectra of a 1:1 MEH-PPV/TNF films and jointly recorded TNF and MEH-PPV films. For the latter we put in the spectrometer two closely spaced films on  $\text{BaF}_2$  substrates and checked the independency of the joint spectra on the order of the samples and the film/substrate interfaces. The same spectrum was obtained from separately recorded MEH-PPV and TNF spectra after their numerical superposition. As follows from Fig. 44, the IR spectrum of MEH-PPV/TNF is not a simple superposition of the two components that might be a result of noticeable mixing of the ground state electronic wave functions of MEH-PPV and TNF. The non-additive bands are listed in Table 6.

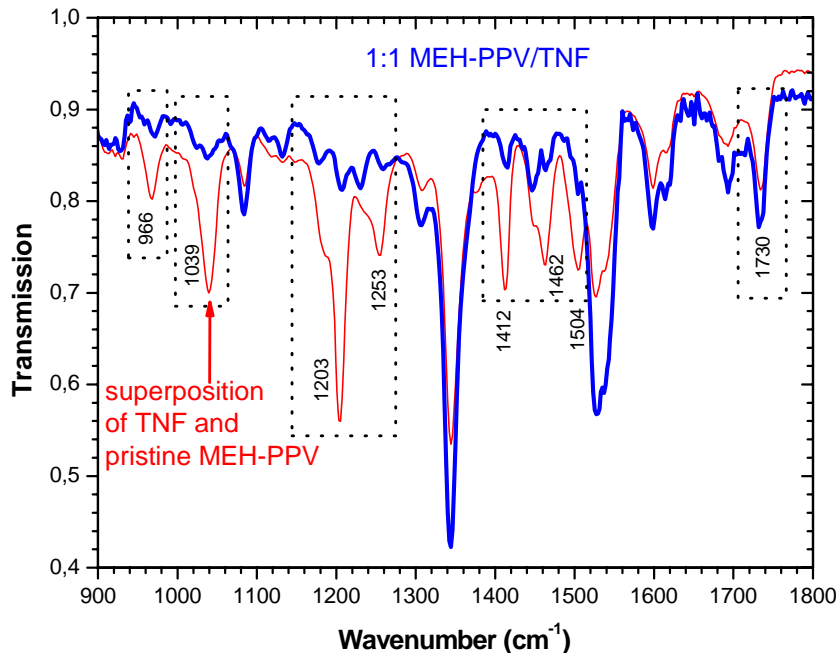


Fig. 44. IR spectra of 1:1 MEH-PPV/TNF film (thick line) and jointly recorded TNF and pristine MEH-PPV films (thin line). Non-additive regions are shown in frames.

Wavenumber (cm <sup>-1</sup> )		Type of vibration	Change in the blend
MEH-PPV	TNF		
966*		CH vinylene wag	Blue shift by 4 cm <sup>-1</sup>
1039		Alkyl oxygen stretch	Strong decrease in intensity
1203		Phenyl oxygen stretch	Very strong decrease in intensity
1253		?	Strong decrease in intensity
1412		Semicircular phenyl stretch	Decrease in intensity, shift to 1416 cm <sup>-1</sup>
1462		Antisymmetric phenyl stretch	Decrease in intensity
1504		Semicircular phenyl stretch (C—C aromatic)	Decrease in intensity
	1730*	C=O stretch	Red shift by ~2 cm <sup>-1</sup>

Table 6. Non-additive IR bands in MEH-PPV/TNF blends. Asterisks mark bands to be assigned to CTC (see below Sec. 4.1.1.2).

#### MEH-PPV/ DNAQ blends

Analogously, we observed that a number of DNAQ bands considerably change their intensity in the MEH-PPV/DNAQ blend demonstrating non-additive behavior. To see this effect more clearly, we show in Fig. 45 FTIR spectra of a 1:1 MEH-PPV/DNAQ film and superposition of DNAQ and MEH-PPV. For the latter we multiplied the separately recorded spectra of DNAQ and MEH-PPV. Fig. 45 shows that intensities of DNAQ bands at 920, 1000, 1376, 1588, and 1684 cm<sup>-1</sup> noticeably decrease in the blend. Therefore, the IR spectrum of MEH-PPV/DANQ also is not a simple superposition of the two components that may evidence for a ground-state CTC between MEH-PPV and DNAQ.

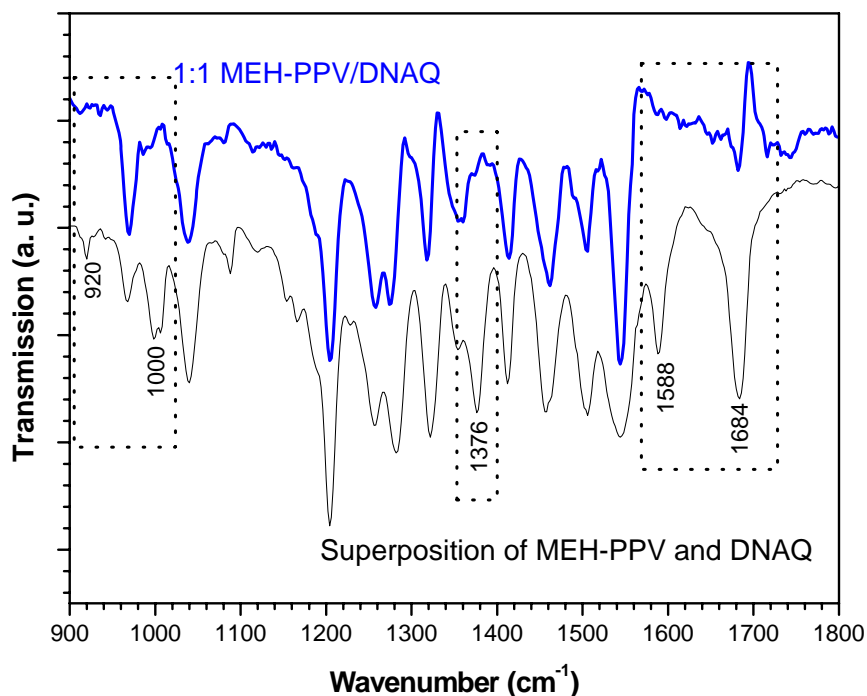


Fig. 45. IR spectra of 1:1 MEH-PPV/DNAQ film (thick line) and superposition of DNAQ and pristine MEH-PPV film (thin line). Non-additive regions are shown in frames.

#### MEH-PPV/C<sub>60</sub> blends

IR transmission spectra of MEH-PPV and MEH-PPV/C<sub>60</sub> with different content of C<sub>60</sub> are compared in Fig. 46. Addition of C<sub>60</sub> into MEH-PPV does not result in any change of MEH-PPV IR modes in the spectral range 900–1700 cm<sup>-1</sup>. In this range, only two characteristic IR modes of C<sub>60</sub> can be observed as peaks or shoulders (1182, 1429 cm<sup>-1</sup>) superimposed on the MEH-PPV bands. The relative intensity of these two peaks depends on the C<sub>60</sub> amount added into the MEH-PPV (Fig. 46). Thus, the IR spectrum of MEH-PPV/C<sub>60</sub> is a simple superposition of the two components, implying relatively weak mixing of their ground state electronic wave functions. Note that this fact is well known (for example, see [19]).

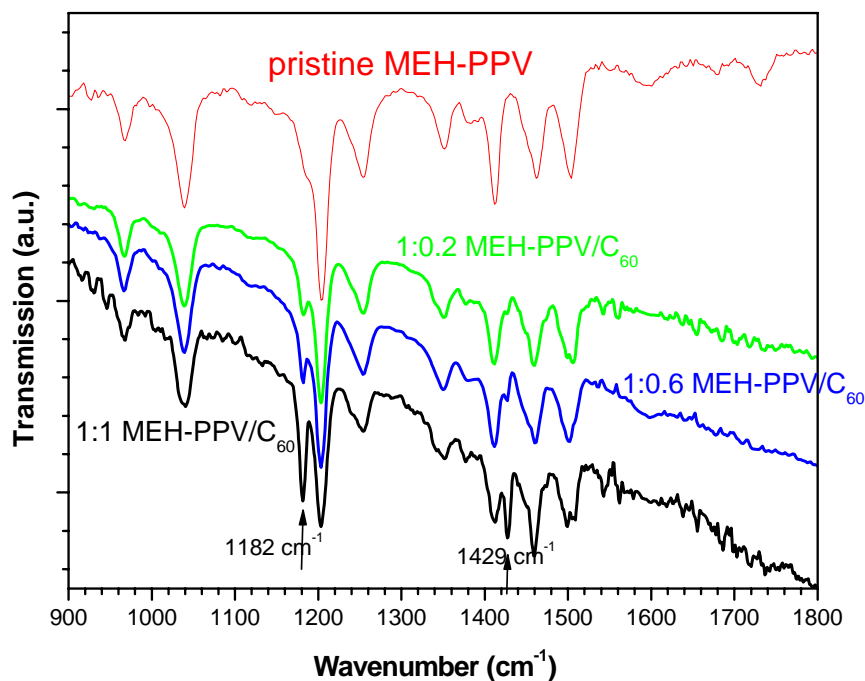


Fig. 46. IR spectra of MEH-PPV and MEH-PPV/C<sub>60</sub> films. Arrows indicate C<sub>60</sub> bands.

## Summary

IR transmission spectra of MEH-PPV/TNF and MEH-PPV/DNAQ blended films possibly indicate noticeable ground-state interaction that might be assigned to CTC. A few MEH-PPV bands are changed in the MEH-PPV/TNF blend, and similarly a few DNAQ bands are changed in the MEH-PPV/DNAQ blend. On the other hand, MEH-PPV/C<sub>60</sub> blends do not show any essential non-additive features and therefore ground-state interaction. However, other reasons of the observed non-additivity are quite possible. Indeed, as noted above, local environment of the acceptor species in the polymer matrix could be essentially changed in the blend compared with the pristine acceptor samples. Because of this, the changes in the IR vibration bands listed in Table 6 can not be conclusive evidence of ground-state donor-acceptor CT. Nevertheless, we have observed that two bands, namely at 966 cm<sup>-1</sup> for MEH-PPV and at 1730 cm<sup>-1</sup> for TNF, reveal themselves in the corresponding Raman spectra showing a behavior that we assign to CTC (see Sec. 4.1.1.2, 4.2.4, 4.2.5.2).

### 3.3.4 Samples for photoelectric studies

We fabricated photodiodes with bulk heterojunction active layer composing of a MEH-PPV/acceptor blend. Photodiodes with pristine MEH-PPV active layer also were made as reference samples. The following acceptors were used: TNF, DNAQ, pDNAQ, PtC<sub>60</sub>, and C<sub>60</sub>. The two latter acceptor was used as a reference as MEH-PPV/C<sub>60</sub> that were studied by many other teams. We also prepared bulk heterojunction photodiodes with an active layer in the form of a ternary blend (MEH-PPV/ DNAQ/C<sub>60</sub> and MEH-PPV/DNAQ/ PCBM).

Sandwich-type samples for photovoltaic measurements were prepared using ITO-covered substrates (MERK, 30x10x1 mm, <12 Ω/□ surface resistance). The ITO surface has a typical roughness of 3 nm rms (10 nm peak-to-peak) with a characteristic size of topographic features of 200–300 nm. Substrates were washed in ultrasonic bath in aqueous detergent solution and finally rinsed in isopropyl alcohol. A PEDOT:PSS layer was deposited onto the ITO-side by spin coating and was dried in air at 60°C. Then an active layer was spin-cast onto the PEDOT:PSS from MEH-PPV/acceptor chlorobenzene solution unless otherwise mentioned. The latter was prepared by mixing pristine MEH-PPV solution (2–5 g/l) with acceptor solution (2–5 g/l). The MEH-PPV:acceptor ratio was varied between 1:0 (pristine) and 1:1.

The spin-casting procedure was as follows: first 7 seconds the spinning rate was increased from 0 to the maximum, and during the following 33 seconds it was kept at this level. Typically the maximum spinning rate was 1000 rpm, and it always was in the range 500–1500 rpm.

All the preparation steps were performed at ambient laboratory conditions. Each batch of four samples was stored for 3 days in vacuum, and then Al contacts were thermally sputtered onto the active layer. Samples were not encapsulated. Photoelectric measurements were started immediately after Al deposition. Photos of a typical sample are shown in Fig. 10 above.

Representative solar cell samples were characterized by AFM on a “Smena” NT-MDT instrument to evaluate the surface topography of the layers and their thickness. Fig. 47 demonstrates typical cross-sections of our solar cell samples. The PEDOT:PSS layer was 100–150 nm thick, the active one was 30–80 nm thick, and the Al one was ≈50 nm thick. The working layer thickness depended on the spinning rate and the MEH-PPV concentration in solution.

Fig. 48 plots an AFM image of 1:1 MEH-PPV/TNF working layer spin-cast from chlorobenzene. As for spin-cast MEH-PPV/TNF films with the lower TNF content (see Fig. 30, Fig. 31, Fig. 32, and Fig. 33), the major part of the film's surface is relatively smooth, but the characteristic TNF features in the form of plateau with width x height 500x50 nm are observed (Fig. 48).

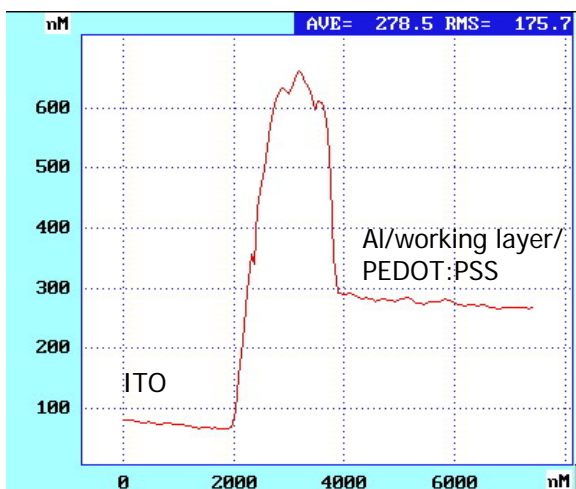
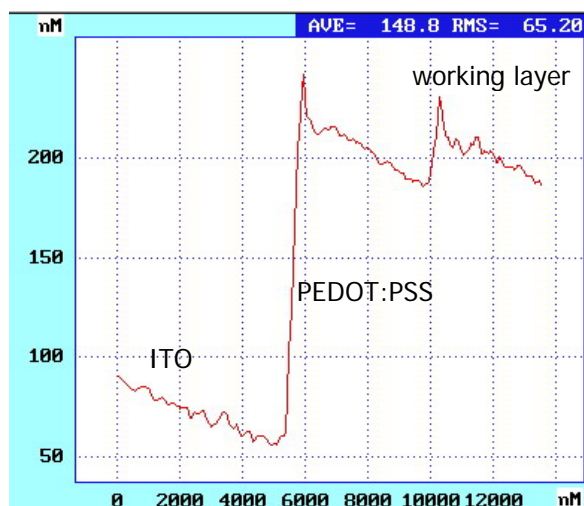


Fig. 47. AFM cross-sections of a scratched solar cell sample. Left: Cross-section between Al electrodes: the PEDOT:PSS layer (thickness 150 nm) covered by the working layer (thickness 30 nm). The working layer was deposited at 1500 rpm. Right: Cross-section of the sandwich Al/working layer/PEDOT:PSS layers.

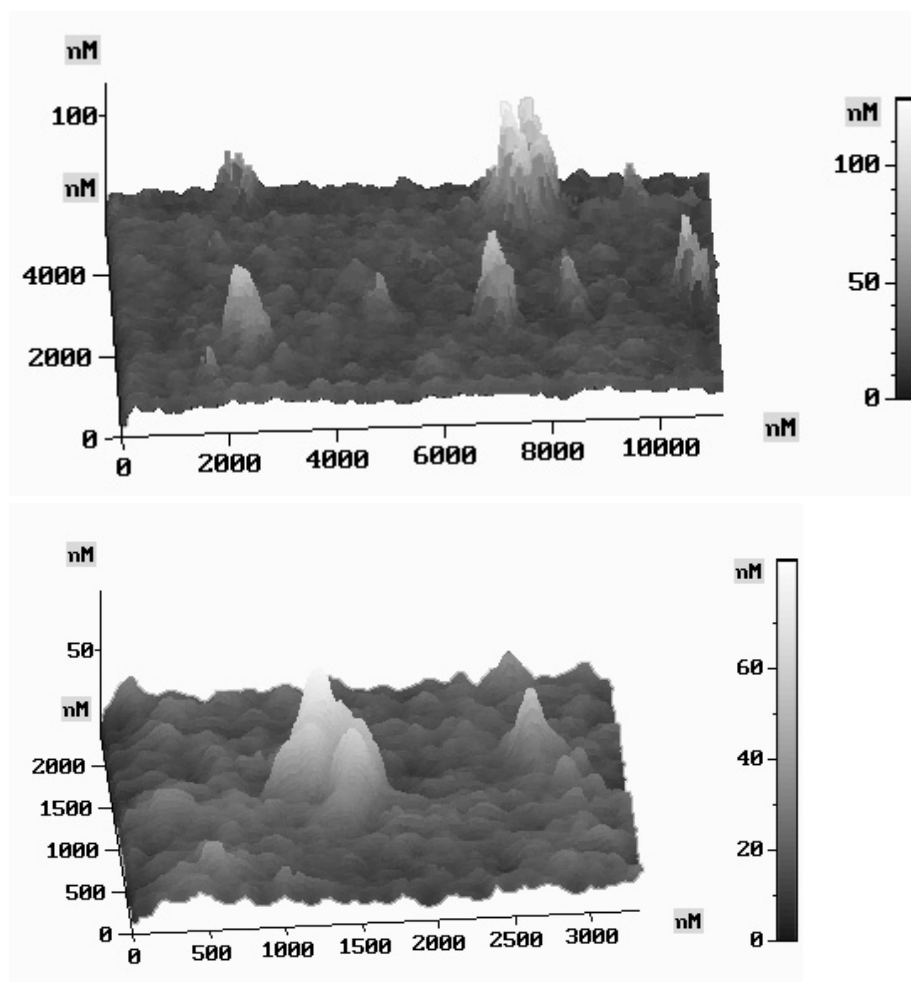


Fig. 48. AFM image of a solar cell sample between Al electrodes with 1:1 MEH-PPV/TNF working layer spin-cast at 1500 rpm from chlorobenzene. Concentration of the individual components in solution was 2.5 g/l. Top: region 6x16  $\mu\text{m}$ ; bottom: enlarged feature.

Fig. 49 shows a  $1.5 \times 3 \mu\text{m}$  region of a 1:1 MEH-PPV/DNAQ working layer spin-cast from chlorobenzene. This region of the film does not contain separate acceptor features (cf. with Fig. 34), and its topography is similar to that of MEH-PPV/TNF films (Fig. 48).

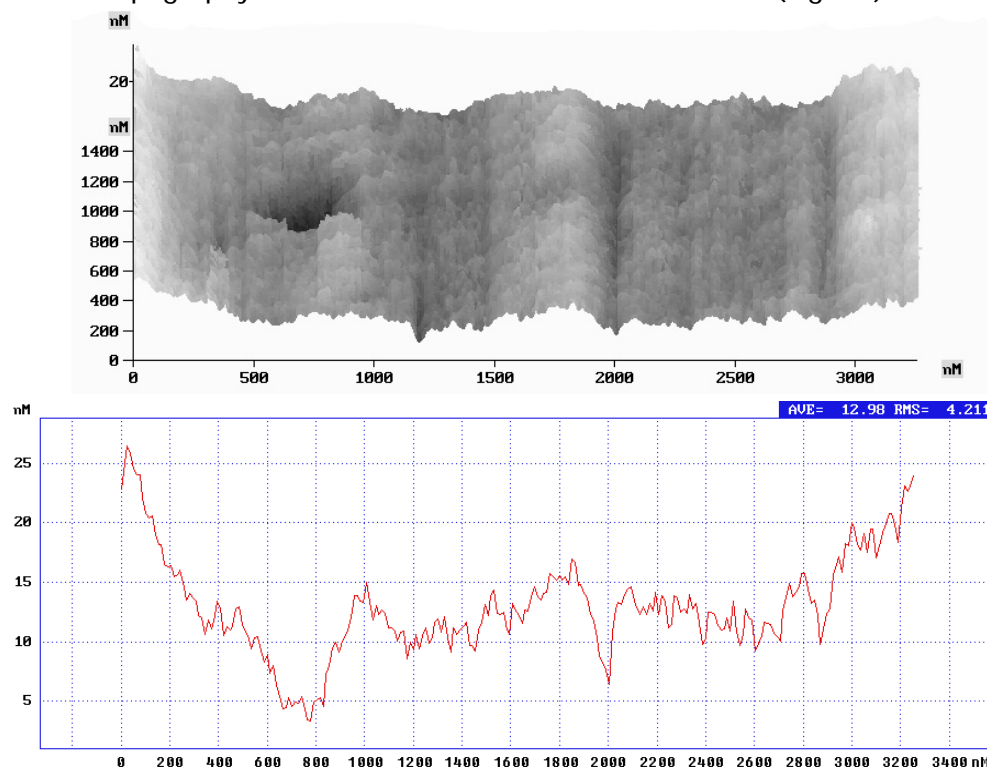


Fig. 49. AFM data for a solar cell sample between Al electrodes with 1:1 MEH-PPV/DNAQ working layer spin-cast at 1000 rpm from chlorobenzene. Concentration of the individual components in solution was 2.5 g/l.

The solar cell samples were studied by photoelectric methods (Sec. 2.12); the results are presented below in Sec. 4.3.5, 4.5.4, 4.4.2, 4.6.5, and 4.5.4.

### 3.4 Polyhexylthiophene/acceptor blends

Soluble polythiophenes are promising materials for polymer solar cells, e.g., the most efficient cells are based on poly(3-hexylthiophene) (PHT). Because of this, it would be important to find organic acceptors that could give a ground-state CTC with PHT (Fig. 50). The issue to be studied was whether PHT can form a ground-state intermolecular CTC with an organic acceptor.

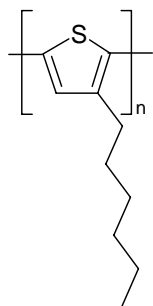
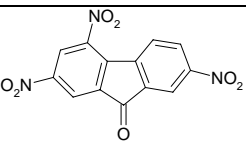
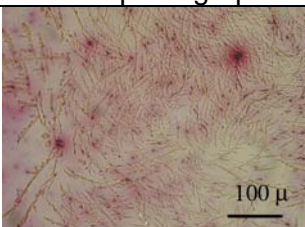
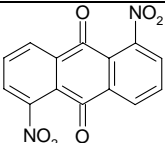
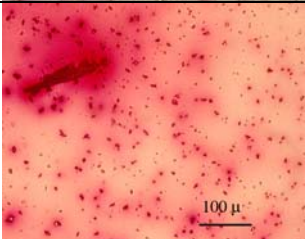
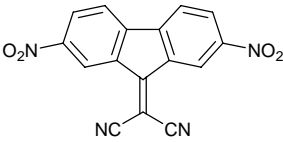
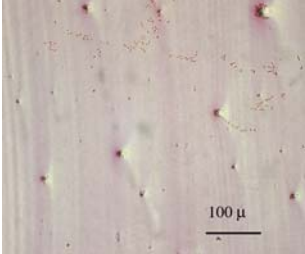
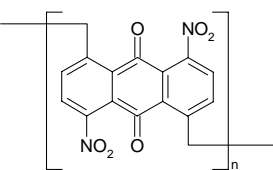
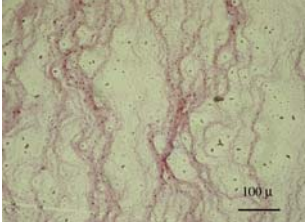
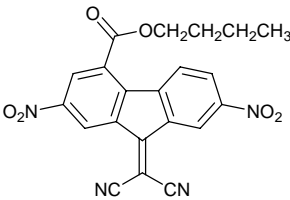
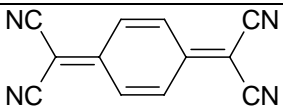
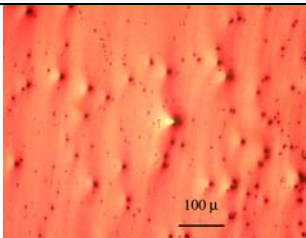


Fig. 50. Chemical structure of PHT.

PHT was obtained from Rieke Metals, Inc., item #4002 (MW~40000 g/mol, 98.5% regioregular, <http://riekemetals.thomasnet.com/item/cialty-conducting-polymers-product-numbers->

[4000-s-/cialty-conducting-polymers-product-numbers-4000-s-/4002?&seo=1](#)). PHT/acceptor films were prepared by spin- and drop-casting from chlorobenzene.

First of all, we prepared blended films and recorded their optical absorption and PL spectra using the same acceptors as for MEH-PPV. The motivation for this preliminary study was to find acceptors allowing formation of relatively homogeneous blended films and giving the most noticeable changes in the optical spectra as compared with the pristine PHT. The list of the acceptors used is shown in Table 7.

#	Acceptor	Abbrev.	Formula	Microphotograph
1	2,4,7-Trinitrofluorenone	TNF		
2	1,5-Dinitroanthraquinone	DNAQ		
3	9-Dicyanomethylene-2,7-dinitrofluorene	DDF		
4	Poly(4,8-dinitroanthraquinone-1,5-diyl)	polyDNAQ		
5	(Butyloxy)-(9-Dicyanomethylene-2,7-dinitrofluorene)-one	BuDDF		See Fig. 53 below
6	Tetracyanoquinodimethane	TCNQ		



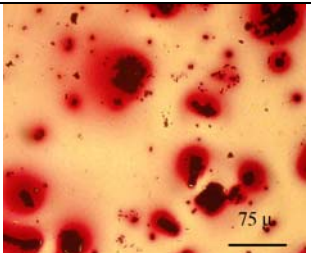
7	Tetracyanobenzene	TCB	<chem>N#Cc1cc(C#N)cc(C#N)c1#N</chem> 
---	-------------------	-----	---

Table 7. List, abbreviations, and formulas of acceptors for PHT. The color in the images does not correlate with the color of the films. Films were prepared by drop- or spin casting from chlorobenzene.

Pristine PHT films were visually highly homogeneous and had low light scattering. However, most PHT/acceptor blends studied demonstrated a noticeable increase in light scattering and did not show any change in color. In some PHT/acceptor blends (e.g. PHT/TCB) strong phase separation was observed as seen in Table 7.

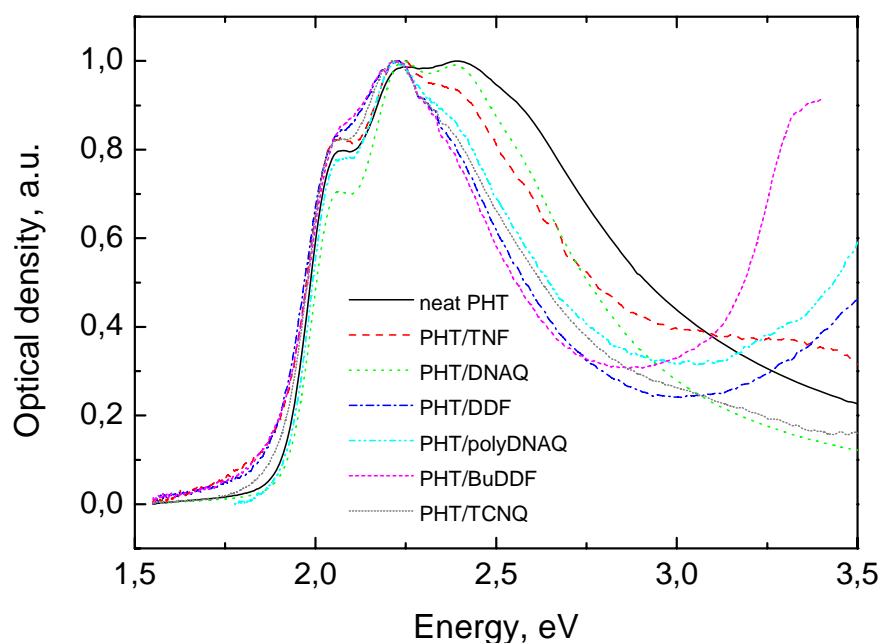


Fig. 51. Normalized absorption spectra of 1:0.4 PHT/acceptor blends. Spectra were corrected to the zero absorbance at 1.55 eV and then normalized for better comparison. Pristine PHT, PHT/TNF, PHT/DNAQ blends were prepared by drop-casting, other blends were prepared by spin-casting from chlorobenzene. The initial concentration of the components in the individual solutions was 2 g/l.

### 3.4.1 Absorption spectra

Fig. 51 shows absorption spectra of PHT/acceptor films. It is seen that addition of acceptor noticeably modifies the spectra. Note that all the acceptors absorb in the UV. As one can see in Fig. 51, introduction of acceptor in the PHT matrix can result in: (i) change in the shape of the main PHT absorption band and (ii) an absorption tail below the PHT bandgap. Consider these observations in detail:

- (i) Remarkably that if for MEH-PPV/acceptor blends we observed a red shift of the whole MEH-PPV absorption band in the blends (see Fig. 71 and Fig. 80), the PHT vibrational sidebands do not show any shifts. As seen in Fig. 51, the effect of acceptor on the PHT absorption band is a redistribution of the oscillator strength between the vibrational sidebands, with the high energy tail (from 2.2 to 3 eV) decreasing. This behavior could be explained assuming that the acceptor added results in changing the ratio between the regioregular and the regiorandom domains of PHT. In fact, the low-energy fine-structured part of the PHT absorption ( $<2.5$  eV) is known to be of the regioregular phase, whereas its higher energy part is of the regiorandom one with the absorption onset at  $\sim 2$  eV. Furthermore, such an acceptor as polyDNAQ, which does not give a noticeable CTC with MEH-PPV (see Sec. 4.5.1), results in similar modification of the PHT absorption as the other acceptors (one can expect that it will not form a CTC with PHT as well). Hence, the observed changes of the PHT absorption in the blends can not be unambiguously assigned to CTC formation in PHT/acceptor blends.
- (ii) On the other hand, the enhanced subgap absorption observed most clearly for TNF, BuDDF, and DDF (Fig. 51) could be a CTC signature. However, it should bear in mind that the subgap absorption tails can stem from PHT crystallites as well. Moreover, the light scattering can mimic the true absorption in the blends as discussed in Sec. 4.2.3.

### 3.4.2 Photoluminescence

Fig. 52 compares PL in pristine PHT with PL in PHT/TCNQ and PHT/BuDDF blends. Pristine PHT films have quite weak PL in the range 1.6–2 eV. However, the PHT PL is not quenched completely in the blends as seen in Fig. 52. At the same time, PL in the blends is characteristic of the acceptors emitting just below their absorption edge at  $\sim 4$  eV. A similar behavior, i.e., very weak PHT PL and considerably higher acceptor PL, was observed in other PHT/acceptor blends. The presence of the acceptor PL in the blends indicates that the photoexcited acceptor does not transfer efficiently either energy or charge to the donor (PHT) as could be expected for acceptor molecules well dispersed in the PHT matrix. This implies noticeable donor-acceptor phase separation in the blends resulting in PL of the acceptor crystallites. Indeed, phase separation was observed at the microscale for different PHT/acceptor blends (see Table 7). On the other hand, the PHT PL is not completely quenched in the blends as well. This implies that the PHT/acceptor blends contain regions of intact PHT as well as intact acceptor. Therefore, even if a CTC forms in PHT/acceptor blends, it involves only a part of both the PHT and acceptor species. This is in contrast with MEH-PPV/acceptor blends (see Sec. 4.2).

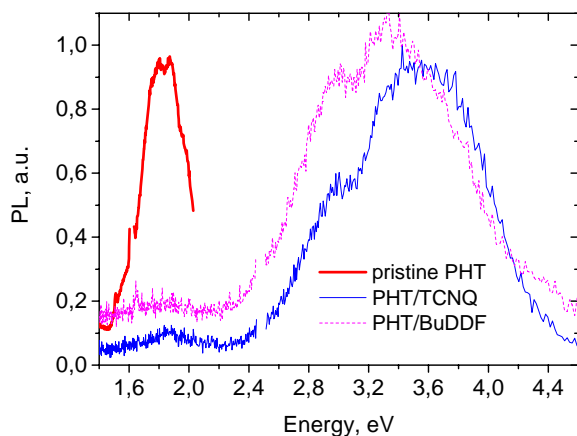


Fig. 52 Normalized PL spectra of pristine PHT (thick solid), PHT/TCNQ (thin solid), PHT/BuDDF (dashed) cast from chlorobenzene, PHT:acceptor=1:0.4. Excitation wavelength was 260 nm for the blends and 500 nm for the pristine PHT.

Thus, the optical absorption data in PHT/acceptor blends are highly ambiguous as an indicator of ground-state CTC. Because of this, we chose the PHT/BuDDF blend for further studies, as it gives the most prominent changes in the optical absorption of the blend as compared with the pristine PHT (Fig. 51). In addition, PHT/BuDDF blended films show better optical homogeneity than the others (cf. images in Table 7 and Fig. 53) making the PHT/BuDDF absorption spectra less sensitive to scattering at the phase separated acceptor species.

### 3.4.3 PHT/BuDDF blends

To identify a possible CTC in PHT/BuDDF blends (Fig. 53), in addition to the optical absorption data, we used vibrational spectroscopy that was done for MEH-PPV/acceptor blends (see Sec. 4.1.1.2). DSC was also used to identify possible donor-acceptor interaction in PHT/BuDDF blends. PHT/BuDDF blends with molar ratio of components varied from 1:0.05 up to 1:1 were studied.

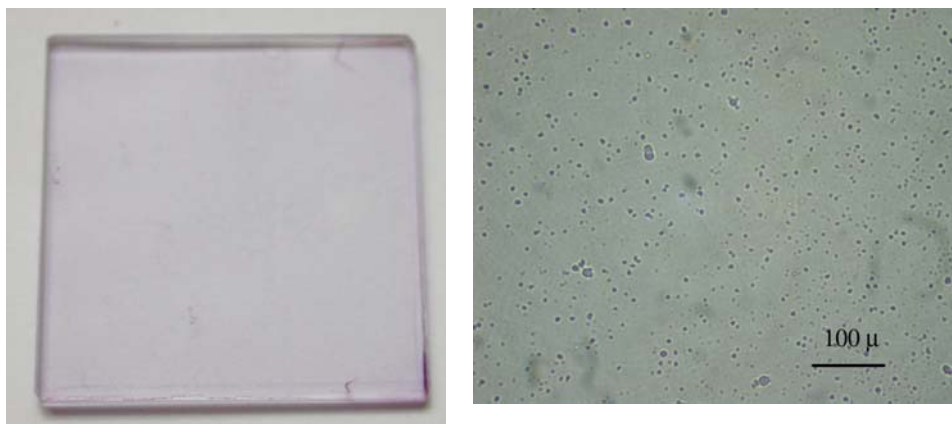


Fig. 53. Photo (left) and microphoto (right) of 1:0.5 PHT/BuDDF film spin-cast from chlorobenzene.

#### *Vibrational spectroscopy*

To find evidence of CTC in PHT/BuDDF blends, we investigated their Raman and FTIR spectra. Analogously to the case of MEH-PPV/TNF and MEH-PPV/DNAQ blends (Sec. 4.1.1.2), we have found that the vibrational spectra of the PHT/BuDDF blends could not be embodied by formal summing the spectra of the neat components. Rather, a few characteristic valence and deformational bands in the FTIR spectra of PHT/BuDDF blends have exhibited specific shifts and/or intensity changes depending on the molar ratio of the components.

Fig. 54 presents characteristic FTIR data. In particular, behavior of the  $\text{-C}\equiv\text{N}$  stretch vibration of BuDDF (Fig. 54a) could evidence that it participates in the CTC formation with PHT conjugated backbone by virtue of furnishing its aromatic system. Partial CT from the polymer backbone to the acceptor aromatic system can make valence vibrations of the  $\text{-C}\equiv\text{N}$  electron-accepting group of BuDDF softer. A similar softening effect for the fluorenone  $\text{C=O}$  group was observed in MEH-PPV/TNF blends (see Sec. 4.1.1.2). Accordingly, for the 1/0.05 PHT/BuDDF blend, where almost exhaustive involvement of the acceptor into interaction with the PHT is expected, the  $\text{-C}\equiv\text{N}$  stretch band shows the largest red shift relative to the intact BuDDF (Fig. 54a). However, the higher partial loads of BuDDF in the blend, the higher contribution of the unbound acceptor becomes, and the  $\text{-C}\equiv\text{N}$  stretch band in the IR spectra becomes progressively closer to that characteristic of the neat BuDDF (Fig. 54a).

Fig. 54b demonstrates non-additive behavior of PHT deformation modes in the PHT/BuDDF blends. The broadening and the blue shifts of the band assignable to the interannular bond rotation

in PHT, which is normally located at  $820\text{ cm}^{-1}$  (Fig. 54b), may reflect the gradual amplification of twisting of the conjugated segments, growth of the quasi-ordered PHT phase contribution, and some loss in the PHT crystalline phase.

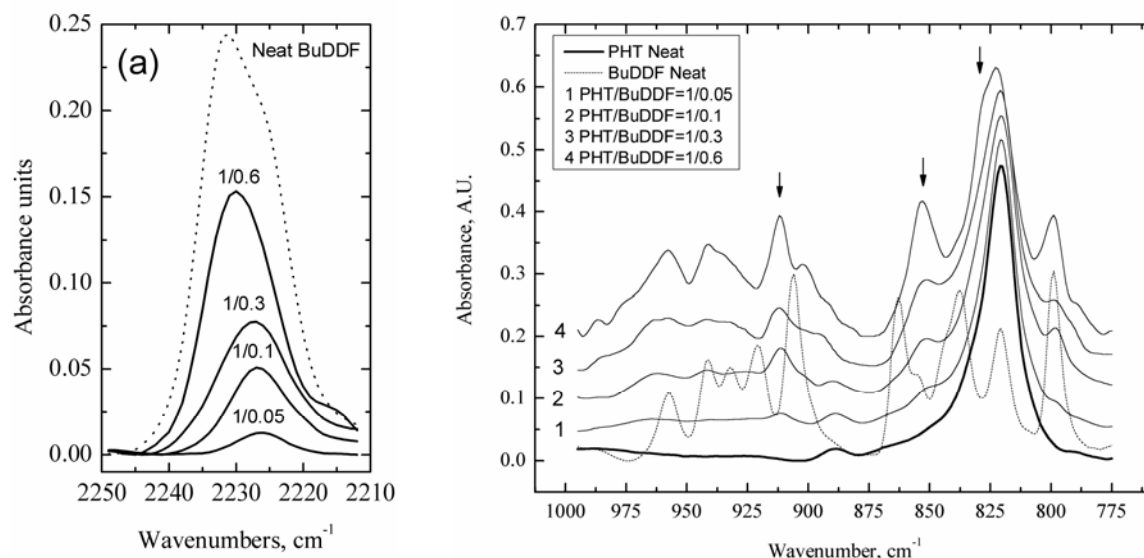


Fig. 54. FTIR data for PHT/BuDDF blends: (a)  $\text{C}\equiv\text{N}$  stretch vibration of the acceptor depending on the blend composition; (b) evolution of several new vibrations (indicated by arrows) in the deformational region.

Fig. 55 compares Raman spectra of neat PHT and 1:0.5 PHT/BuDDF blends. Two strongest bands at  $1380$  and  $1448\text{ cm}^{-1}$  belonging to PHT backbone vibrations are observed in the blend with essentially lower signal-to-noise ratio. We did not observe any shift of the PHT bands in the blend. It is worth of noting that, in contrast to the MEH-PPV/TNF blends, NIR-FT Raman spectroscopy (NIR-FTR) has turned out to be of little help in identification of partial CT in the PHT/BuDDF blends. In fact, both the neat PHT and BuDDF gave excellent NIR-FTR spectra, but those of blends have been invariably overwhelmed by fluorescence and thermal backgrounds.

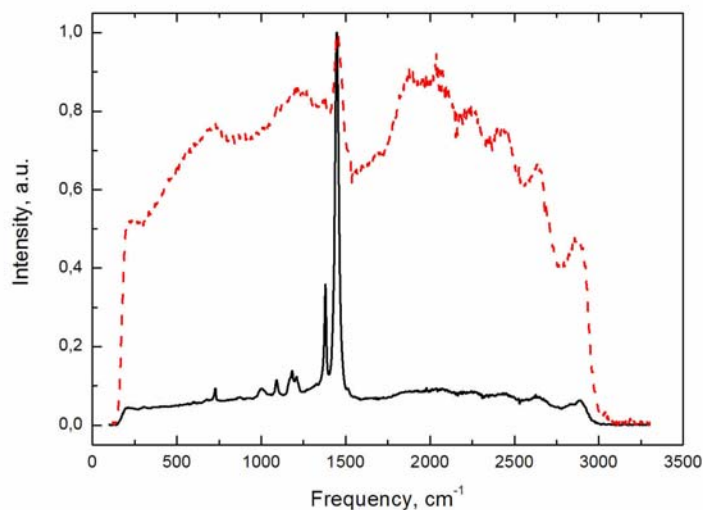


Fig. 55. Raman spectra of films of neat PHT (black solid) and blend with BuDDF (1:0.5) (red dashed) recorded at  $1064\text{ nm}$ .

### DSC

If a CTC is formed, it can give characteristic features in DSC traces. Fig. 56 presents our DSC results. It is seen that first heating DSC runs for neat PHT show two thermal transitions assigned to disordering the side chains (a broad endotherm peaking at  $\sim 90^{\circ}\text{C}$ ) and to melting the PHT crystallites (an endotherm peaking at  $235^{\circ}\text{C}$ ). As Fig. 56 illustrates, the DSC traces for the PHT/BuDDF blends reveal more complex thermal behavior. While the neat PHT and the blends with relatively low BuDDF content (e.g. that of 1/0.05, Fig. 56) exhibit similar behavior, the PHT/BuDDF blends with higher acceptor content (above 10% mol) show two additional transitions in the range of  $140\text{--}160^{\circ}\text{C}$  (Fig. 56). In addition, the PHT endotherm peaking at  $235^{\circ}\text{C}$  in the neat PHT gradually shifts to lower temperatures with increasing the BuDDF content in the blend (Fig. 56).

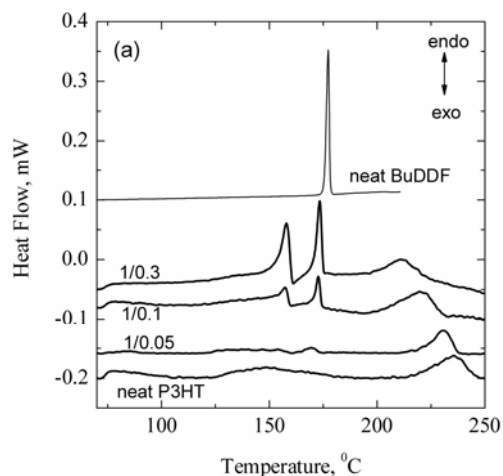


Fig. 56 Exemplary first heating DSC traces for the PHT:BuDDF blends with different molar ratios of the components.

The narrow endotherm always peaking at  $173^{\circ}\text{C}$  is a measure of free (i.e. not interacting with the P3HT matrix) BuDDF in the blends. By taking into account the melting enthalpy of the neat BuDDF ( $82.6\text{ J/g}$  or  $35.35\text{ kJ/mol}$ ), it has been evaluated that the free BuDDF content in the films has gradually increased as the initial acceptor loads in the blends increased. The other transition peaking around at  $158^{\circ}\text{C}$  is also characteristic of the blends with relatively high acceptor content (above 10% mol). One can suppose that the DSC feature at  $158^{\circ}\text{C}$  represents dissociation of the donor-acceptor bound species in the PHT/BuDDF blends.

Thus, the DSC traces of PHT/BuDDF blends certainly indicate noticeable interaction between the donor and the acceptor. Therefore the DSC data are consistent with the CTC hypothesis. However, since DSC is not specific to the nature of donor-acceptor interaction, it can not help to identify whether this interaction is CT in nature or not.

#### 3.4.4 Discussion

Our optical absorption, vibrational and DSC data are consistent with the concept of ground-state CT interaction in PHT/BuDDF films. These data strongly suggest that PHT and BuDDF noticeably interact in the electronic ground state of the blend. However, we could hardly claim that this interaction is the CT one in nature. Again, as in the case of blends of PHT with other acceptors (see above), other explanation of the observed non-additivity effects in the PHT/BuDDF blends is possible.

First of all, we did not observe any clear shift in PHT or acceptor vibrational bands to be unambiguously assigned to ground-state donor-acceptor CT. The red shift in the  $\text{C}\equiv\text{N}$  band observed in the PHT/BuDDF blends (Fig. 54a) can result from the different BuDDF phases, which may vary from the highly aggregated to the dispersed one in the PHT matrix. In this case, the red shifted  $\text{C}\equiv\text{N}$  band in the 1/0.05 blend (Fig. 54a) could be assigned to loosely bound BuDDF molecules being

present in the neat BuDDF film as well. The evidence for the latter can be a clear red shoulder observed in the neat BuDDF film in Fig. 54a.

As mentioned above, the observed non-additivity effects in the PHT/acceptor blends could stem from a modification of the regioregular domains of PHT as the result of acceptor addition. PHT crystalline domains may noticeably vary in size and concentration depending on details of the film preparation methods, and therefore addition of the acceptor to PHT films could change properties of the regioregular phase. Assuming that the interchain interaction in PHT increases in the presence of BuDDF molecules, the enhanced absorption tail in the PHT optical gap could be assigned to the PHT crystalline domains, which could give both the absorption and the scattering contribution in the measured absorption. On the other hand, the local environment of BuDDF molecules is evidently change in the PHT matrix as follows from our FTIR (Fig. 54) and DSC (Fig. 56) data.

At this stage, we conclude that PHT and BuDDF noticeably interact in the electronic ground state of the blend, and this interaction could be due to donor-acceptor CT interaction. However, other type of interaction is possible since we could not identify whether this interaction is CT in nature or not.

### 3.5 Polyfluorene as a possible donor for CTC

We have tried to find donor-acceptor blends with intermolecular CT interaction using other conjugated polymers. Poly(9,9-bis(2-ethylhexyl)-fluorene-2,7-diyl) (PF2/6) (Fig. 57) has been selected as a possible donor since the conjugated backbone of PF2/6 unit chain (Fig. 57) is the same as that of the fluorene acceptors (see Table 8) implying compatibility of the molecular orbital patterns of PF2/6 with them. According to the Mulliken model of CT interaction, this compatibility is essential for efficient ground-state CT interaction. Moreover, polyfluorenes have a wide bandgap, and a CTC could be a means to decrease the optical gap of the polyfluorene/acceptor blend. In addition, polyfluorenes have been attracting a lot of interest for recent years as promising conjugated polymers in optoelectronic applications. PF2/6 was obtained from American Dye Source, Canada (MW=40000–12000 g/mol, ADS131BE, [http://www.adsdyes.com/products/pdf/homopolymers/ADS131BE\\_DATA.pdf](http://www.adsdyes.com/products/pdf/homopolymers/ADS131BE_DATA.pdf)).

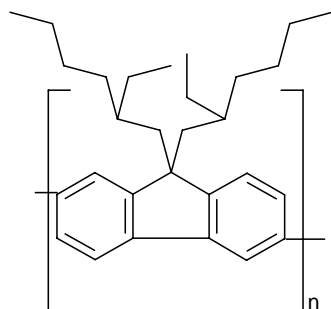


Fig. 57. Chemical structure of PF2/6.

#### Characterization of pristine PF2/6 films

Polymer was obtained from American Dye Source (Canada). Thin films of pristine PF2/6 were prepared by dip-coating, spin-casting, drop-casting and SSE methods. First, they were characterized by UV-vis absorption and PL spectroscopies. Typical PL and optical absorption spectra are presented in Fig. 58 and Fig. 59, respectively. PL spectra in PF2/6 films prepared by different methods show some differences (Fig. 58) but not as clear as in MEH-PPV films (Sec. 3.1.2). The absorption spectra of PF2/6 films prepared by different methods were also quite similar (Fig. 59).

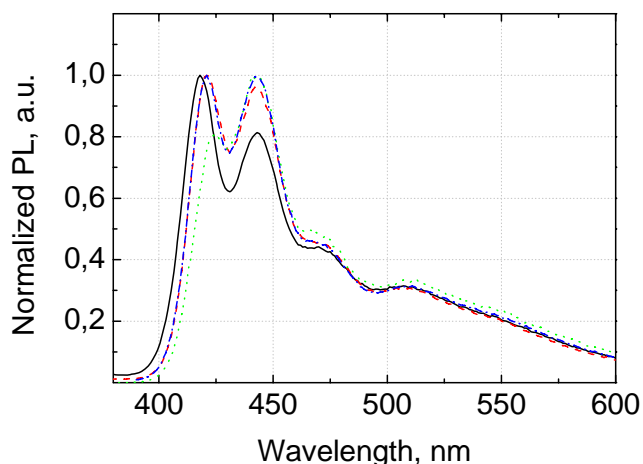


Fig. 58. PL spectra of PF2/6 films prepared by dip coating (black), spin casting (red), drop casting (green) and SSE (blue)

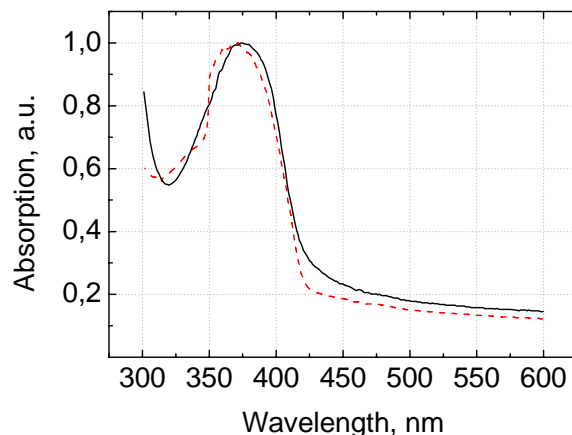


Fig. 59. Absorption spectra of PF2/6 films prepared by dip-coating (solid), and SSE (dashed).

### Blends of PF2/6 with different acceptors

We have tried to observe the signatures of ground-state CT interaction in PF2/6-acceptor blends. Blends of PF2/6 with TNF, DNAQ and DTeF were studied. Note that the latter is the strongest one from the acceptors of fluorene series (see Table 8). UV-vis spectra of the blends are presented in Fig. 60 possibly indicating sup-gap optical absorption tail in PF2/6:DTeF blend (dash-dotted line). However, our light scattering measurements using the method described in Sec. 2.2 have shown that this tail is due to light scattering. Furthermore, PL of PF2/6 is not quenched by even such a strong acceptor as DTeF. For comparison, MEH-PPV PL is deeply quenched by weaker acceptors (TNF or DNAQ).

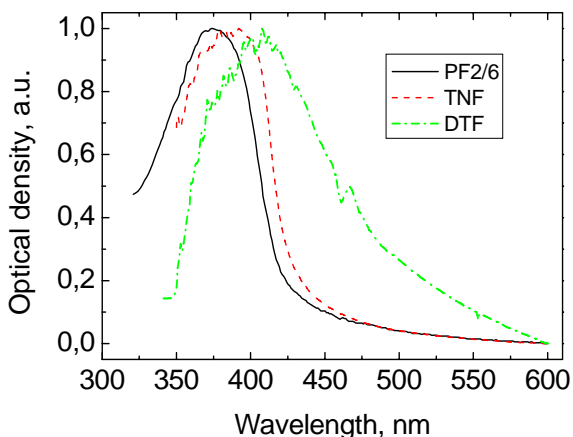


Fig. 60. UV-vis spectra of PF2/6 (solid), PF2/6:TNF=0,05 (dashed), and PF2/6:DTeF=1:1 (dash-dotted) blends.

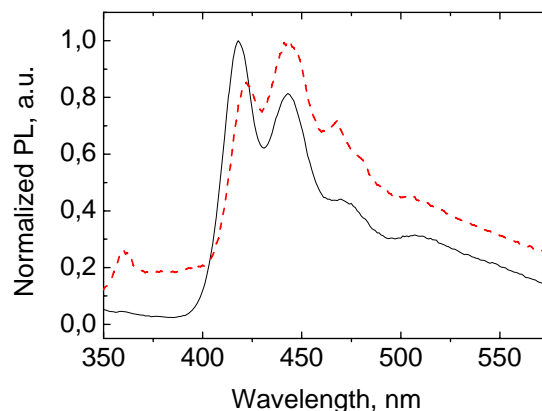


Fig. 61. Normalized PL spectra of PF2/6 (solid) and PF2/6:DteF (dashed) films.

Possibly, PF2/6 does not interact with the acceptors because of low miscibility of the blend components. If pristine PF2/6 films are quite homogeneous, PF2/6:DteF films are essentially inhomogeneous and show strong light scattering looking as mixture of green and orange-brown particles (Fig. 62).



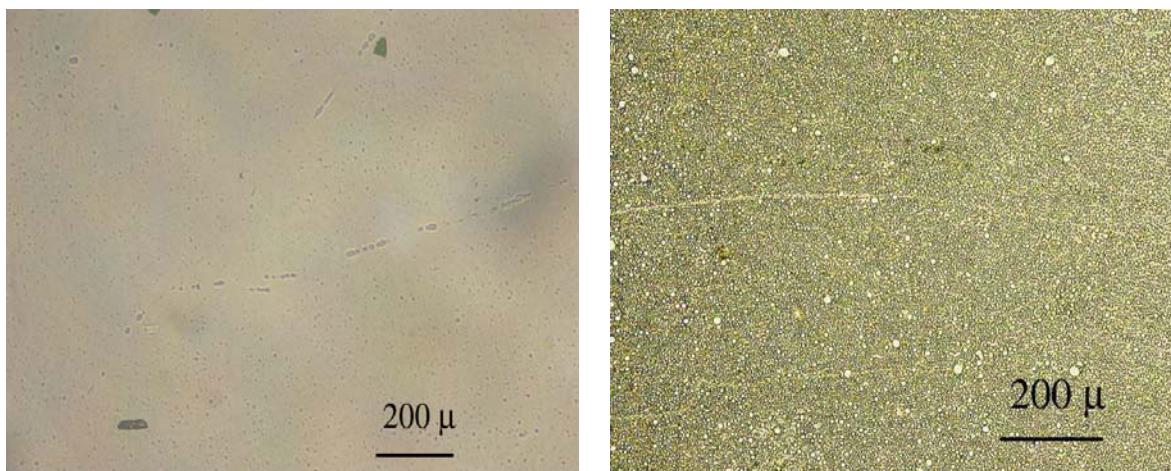
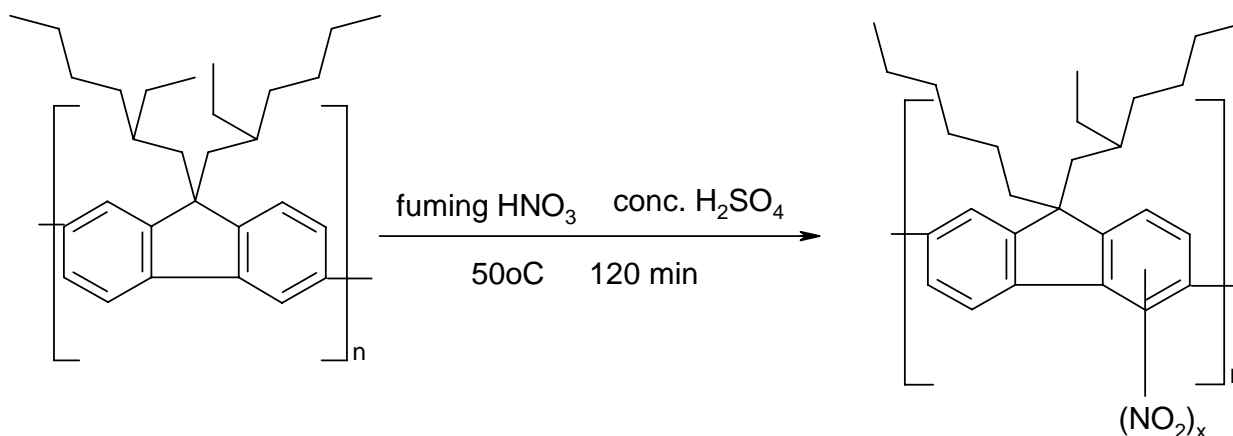


Fig. 62. Optical microscopic images of pristine PF2/6 film (left) and PF2/6:DTeF film (right).

### NitroPF2/6

Another approach has been tested for preparation of a PF2/6 CTC. The idea was to use as an acceptor the same polymer but with nitro groups introduced in the course of a special reaction. We were motivated by the following: (i) to use a “long” acceptor since we supposed that short organic molecules are not very favorable for CTC formation with conjugated polymers; (ii) to obtain highly miscible mixture of similar polymers; (iii) to have the interpenetrating networks of two polymers for the electron and hole transport. A part of the initial polymer was used in reaction with a mixture of sulfuric and fuming nitric acid according the scheme ( $x < n$ ):



The first attempt was made with concentrated HNO<sub>3</sub>, however the content of nitro groups (NO<sub>2</sub>) in the resulting polymer was too low according to its FTIR absorption spectra (Fig. 63). The second attempt with fuming HNO<sub>3</sub> has resulted in nitroPF2/6 that follows from FTIR spectra in Fig. 63 indicating two intensive bands of NO<sub>2</sub> groups at 1349 and 1532 cm<sup>-1</sup>. The FTIR data also show that (i) reaction of oxidation of PF2/6 occurs giving a noticeable C=O band at 1740 cm<sup>-1</sup>; (ii) nitration of the end fluorene fragments happens that follows from decreasing corresponding phenyl bands at 816 and 1000 cm<sup>-1</sup>.



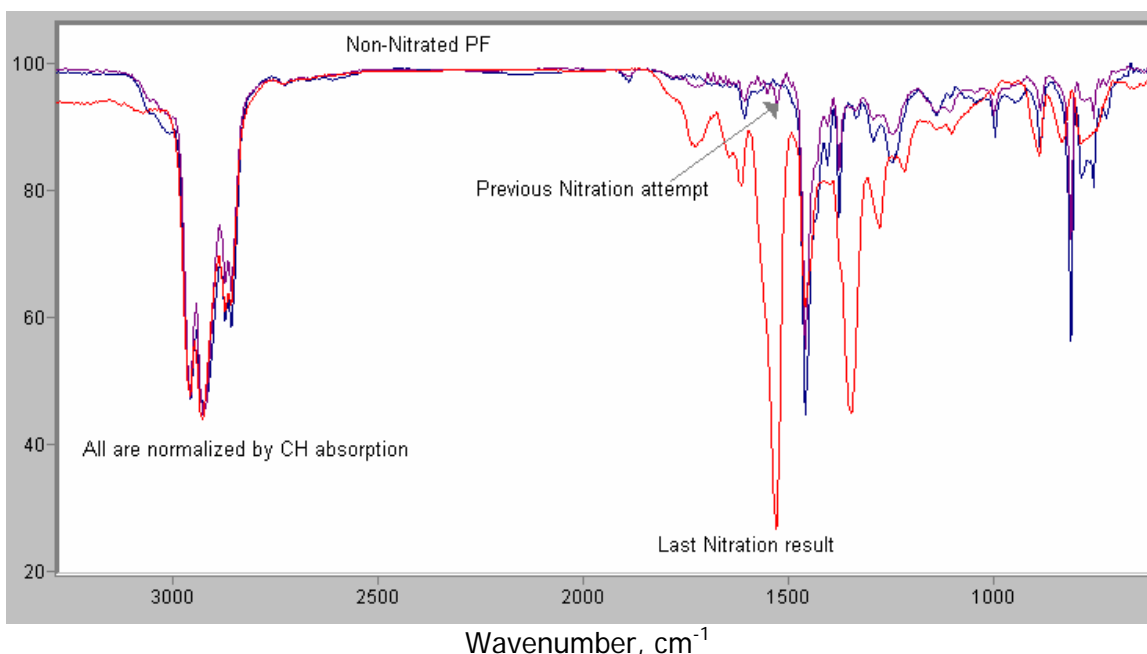


Fig. 63. IR-spectra of neat PF2/6 and samples obtained after reactions with concentrated  $\text{HNO}_3$  (blue) and fuming  $\text{HNO}_3$  (red).

UV-vis absorption and PL spectra of nitroPF2/6 and its mixture with PF2/6 are shown in Fig. 64 and Fig. 65, respectively. Again, we had the same situation as for the blends of PF2/6 with other acceptors studied: components are immiscible that gives optically inhomogeneous films (Fig. 66) with strong light scattering; PF2/6 PL is not quenched. Therefore, we have not observed any signatures of CT interaction in PF2/6:nitroPF2/6 blend.

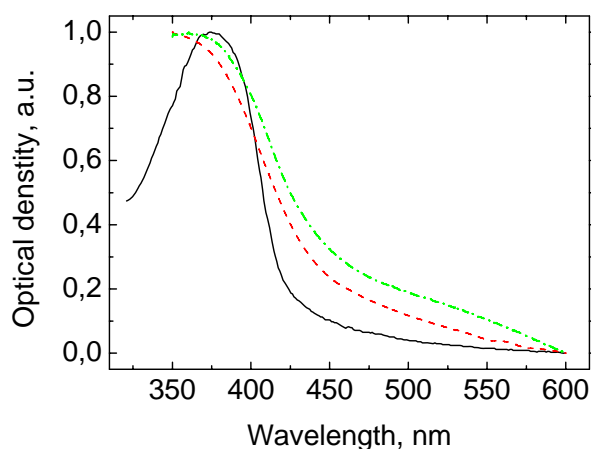


Fig. 64. UV-vis absorption spectra of PF2/6 (solid), nitroPF2/6 (dashed), and PF2/6:nitroPF2/6=1:1 (dash-dotted) blend.

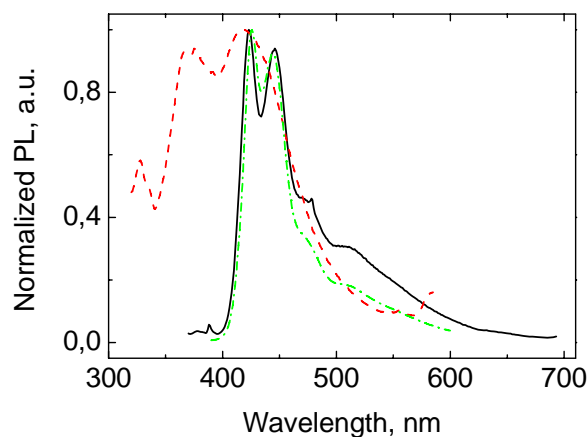


Fig. 65. Normalized PL spectra of PF2/6 (solid), nitroPF2/6 (dashed), and PF2/6:nitroPF2/6=1:1 (dash-dotted) films. Spectra were not corrected for the instrument response.

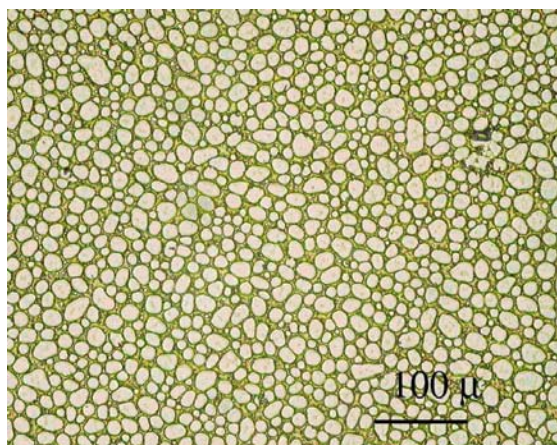


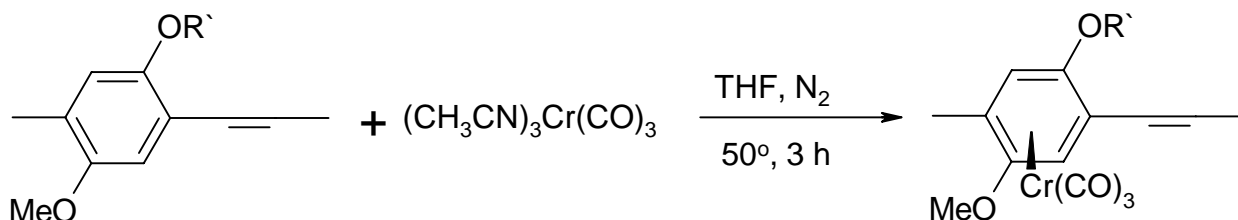
Fig. 66. Optical microscopic image of PF2/6:nitroPF=1:1 film.

## Conclusion

Thus, we have not found any signatures of CT interaction either in the ground or the excited electronic state of the PF2/6:acceptor blends from optical absorption and PL spectra, respectively. In all the blends studied clear phase separation was observed. Possibly, PF2/6 does not interact with the acceptors because of low miscibility of the blend components. Our analysis of possible donor-acceptor geometry given in Sec. 4.2.1 implies that the presence of  $sp^3$ -hybridized carbon atom with long aliphatic side groups in the PF2/6 backbone makes it hard to arrange any acceptors studied near the PF2/6 unit. This steric hindrance possibly impedes donor-acceptor interaction in the PF2/6 blends.

## 3.6 Other types of complexes with MEH-PPV

Various types of CTCs are known in particular coordination ones. To study such a possibility for conjugated polymers, we tried the following reaction of MEH-PPV:



The obtained product had the same color as the pristine MEH-PPV and was soluble in the same solvents. Its IR-spectra had two bands at 1952 and 1890  $\text{cm}^{-1}$  (Fig. 67) characteristic of coordination compounds [*J. Organometal. Chem.*, **338**, p. 357 and 19 (1988); *Organometallics*, **13**, 2284 (1994)]. These bands indicate the presence of  $\text{Cr}(\text{CO})_3$  fragments in the product of reaction. To best of our knowledge this is the first example of such a reaction with a PPV-type polymer.

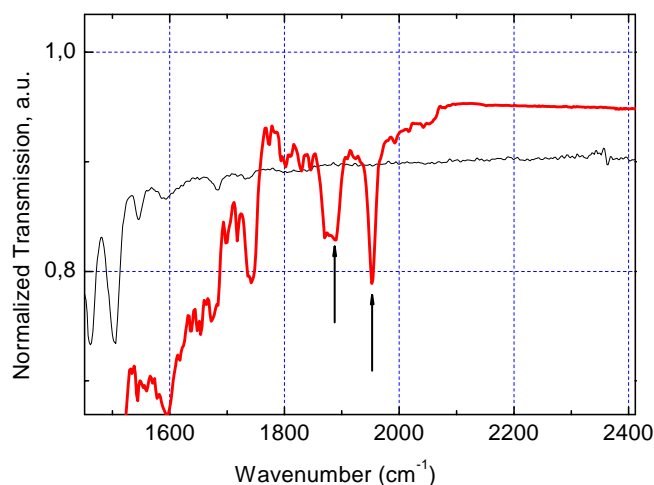


Fig. 67. IR-spectra of MEH-PPV (thin) and MEH-PPV-Cr(CO)<sub>3</sub> (thick) films. Arrows indicate the bands characteristic of the coordination compound.

UV-vis absorption, PL, and PIA spectra of MEH-PPV-Cr(CO)<sub>3</sub> films were recorded and compared with those of pristine MEH-PPV films. The optical absorption spectra were nearly the same. Fig. 68 compares the PL spectra of pristine MEH-PPV and MEH-PPV-Cr(CO)<sub>3</sub> films. The PL intensity in both films was about the same indicating the absence of quenching typical for donor-acceptor blends. Some blue shift of PL in the MEH-PPV-Cr(CO)<sub>3</sub> film could indicate shorter conjugation lengths. Also we did not observe any essential difference in PIA spectra (Fig. 69). Thus, our data show that properties of both the ground and the photoexcited states in MEH-PPV-Cr(CO)<sub>3</sub> do not differ essentially from those of pristine MEH-PPV.

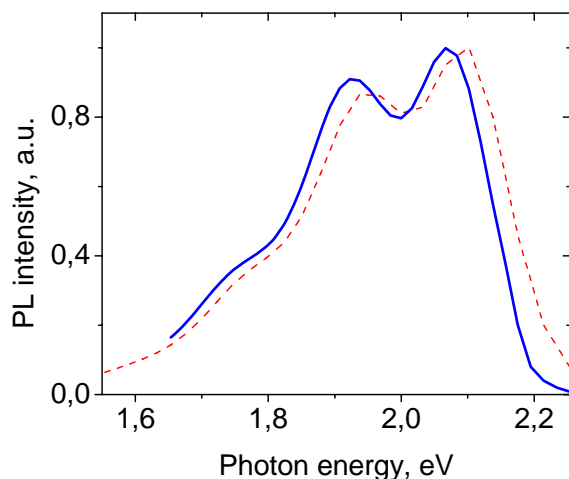


Fig. 68 Normalized PL spectra of MEH-PPV (solid) and MEH-PPV-Cr(CO)<sub>3</sub> (dashed) films prepared from toluene.

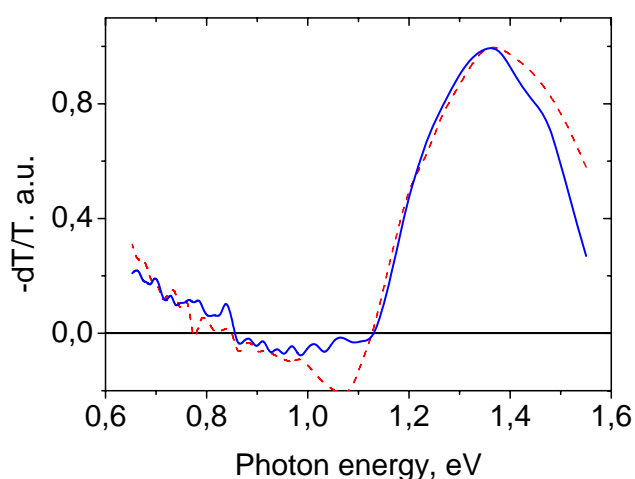


Fig. 69. Normalized PIA spectra of MEH-PPV (solid) and MEH-PPV-Cr(CO)<sub>3</sub> (dashed) films prepared from toluene, T=100K.

## 4 RESULTS

### 4.1 Evidence of conjugated polymer CTC

#### 4.1.1 MEH-PPV/TNF and MEH-PPV/DNAQ films

##### 4.1.1.1 Absorption spectra

MEH-PPV/DNAQ and MEH-PPV/TNF blended films had the different color as compared with pristine MEH-PPV films as seen in Fig. 70. Fig. 71 shows absorption spectra of MEH-PPV/DNAQ, MEH-PPV/TNF, and pristine MEH-PPV films. It is seen that the absorption spectra of the blended films are shifted to the red by 0.1–0.2 eV and show extended absorption tails compared with the pristine MEH-PPV film. Note that 1:1 MEH-PPV/DNAQ and MEH-PPV/TNF blends demonstrate essential phase separation (see Fig. 28) that can result in optical scattering contributing to the optical absorption spectra. This effect is discussed in Sec. 4.2.3 in detail. To evaluate a light scattering contribution to the measured optical transmission, we measured absorption and scattering separately using the technique described above (see Sec. 2.2). Fig. 72 demonstrates the results for 1:1 MEH-PPV/TNF blend. Although addition of the acceptor results in a noticeable increase of the scattering losses (Fig. 72), the latter gives the major contribution to the measured optical density only for energies below 1.5 eV. Note that the light scattering contribution to the measured optical density in MEH-PPV/DNAQ blends is much less than that of MEH-PPV/TNF blends (see Sec. 4.2.3). Since the optical absorption of both acceptors starts at  $\sim 3$  eV, the observed optical absorption below the absorption edge of pristine MEH-PPV could be a consequence of noticeable ground state interaction of MEH-PPV chains with the acceptor molecules resulting from CTC formation (Fig. 72, inset).

As TNF is a stronger acceptor, i.e., has higher EA, than DNAQ (see Table 2), the CTC band should be lower in energy in the MEH-PPV/TNF than in the MEH-PPV/DNAQ according to Mulliken's model. Indeed, this is in accordance with the spectra shown in Fig. 71. The quantitative relation between EAs of different acceptors and the CTC band energies is discussed below in Sec. 4.1.3.

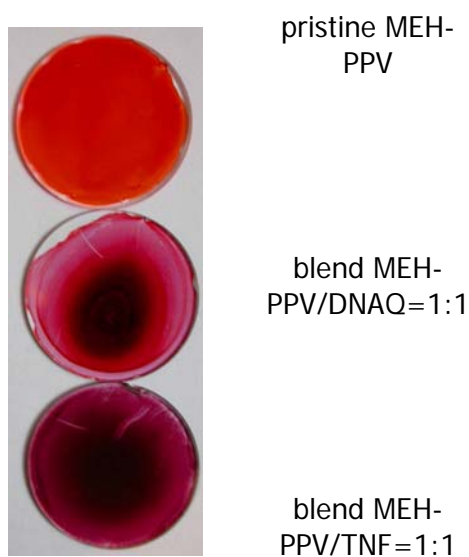


Fig. 70. Photos of polymer films drop-cast from cyclohexanone on a glass substrate with diameter 23 mm.

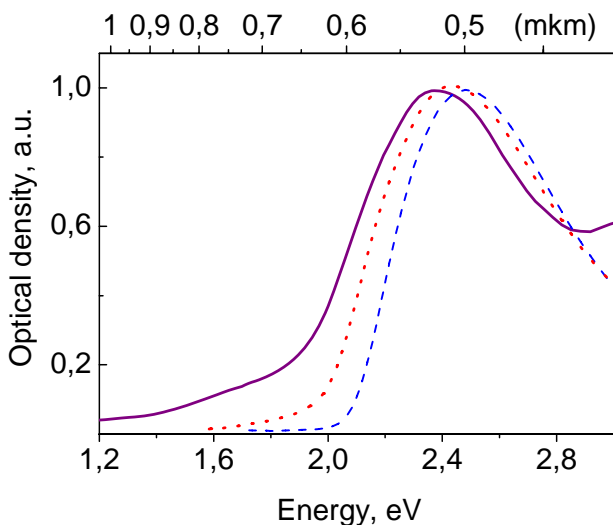


Fig. 71. Absorption spectra of pristine MEH-PPV (dashed), 1:1 MEH-PPV/DNAQ (dotted), and 1:1 MEH-PPV/TNF (solid) films drop-cast from chlorobenzene.

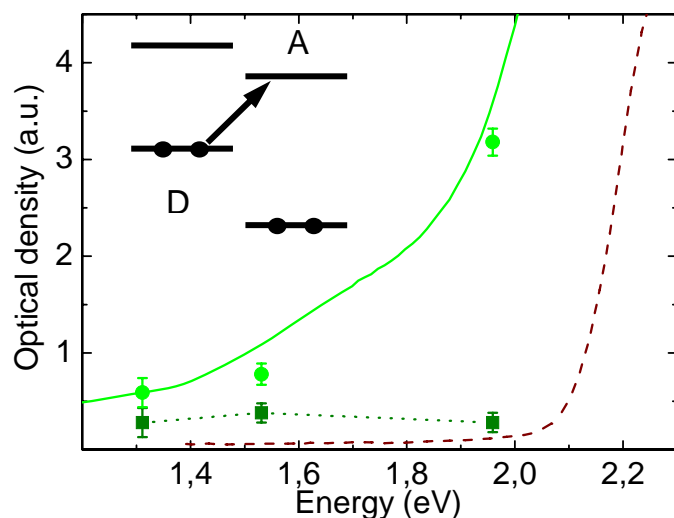


Fig. 72. Absorption spectra of 1:1 MEH-PPV/TNF (solid) and pristine MEH-PPV (dashed) drop-cast films prepared from chlorobenzene. Points show the sum of absorption and scattering (circles) and only the scattering (squares) contributing to the measured optical density of the 1:1 MEH-PPV/TNF film by using technique described above. Inset illustrates the donor and acceptor energy levels, the arrow indicates the CTC absorption corresponding to the electron transfer from the highest occupied orbital (HUMO) of the donor (D) to the lowest unoccupied orbital (LUMO) of the acceptor (A).

Note that appearance of a red shift and of an extended tail in the MEH-PPV spectrum upon adding the acceptor could be associated with two other effects: enhancing intermolecular interaction of polymer chains (i.e. aggregation) and/or increasing the concentration of relatively long conjugated chains. However, since the absorption tails observed for the blends are too intense and red shifted, it is difficult to suppose that either could result from blending of weakly non-interacting components.

#### 4.1.1.2 Vibrational spectroscopy data

Partial CT in the electronic ground state is expected to induce shifts in the vibrational frequencies of both the donor and the acceptor. Indeed, as Fig. 73 shows, Raman bands of MEH-PPV at 1551 and 1582  $\text{cm}^{-1}$ , corresponding to carbon-carbon (CC) stretching of the phenyl ring, are 3–4  $\text{cm}^{-1}$  red shifted in the 1:1 MEH-PPV/TNF blend. Fig. 74 compares the Raman band at 1582  $\text{cm}^{-1}$  in pristine MEH-PPV and MEH-PPV/DNAQ films. A smaller red shift of 2  $\text{cm}^{-1}$  of the 1582  $\text{cm}^{-1}$  band is observed in MEH-PPV/DNAQ blends as well. The observed red shifts support our assumption about partial CT from the MEH-PPV chain to the acceptor molecule (TNF or DNAQ) in the electronic ground state.

Furthermore, we have found that a number of other Raman and IR bands in the MEH-PPV/TNF blends are not just a superposition of the corresponding spectra of pristine MEH-PPV and TNF (see Sec. 3.3.3.2). Here we discuss frequency shifts relevant only to TNF carbonyl C=O vibration at the vicinity of  $\sim 1730 \text{ cm}^{-1}$  observed in both IR and Raman spectra (Fig. 75). The noticeable red shift of the C=O band in TNF by a few wavenumbers we explain by an increase of the electron density in the conjugated system of TNF resulting from partial ground-state CT. As is well documented for substituted fluorenones, introduction of electronegative substituents into a fluorenone molecule tends to increase the C=O frequency and this increase can amount up to 50  $\text{cm}^{-1}$  raising within the series from aminofluorenone to TNF (Fig. 76). The observed red shift of the C=O frequency in the MEH-PPV/TNF blend implies that electronegative action of nitro substituents could be partly compensated by extra electron density donated by the MEH-PPV.

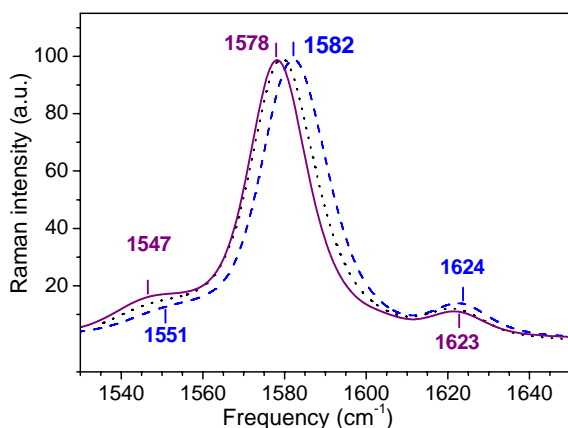


Fig. 73. Raman spectra of pristine MEH-PPV (dashed), 1:0.2 MEH-PPV/TNF (dotted), 1:1 MEH-PPV/TNF (solid) free-standing films in the region of the strongest Raman band of MEH-PPV. The excitation wavelength is 1064 nm.

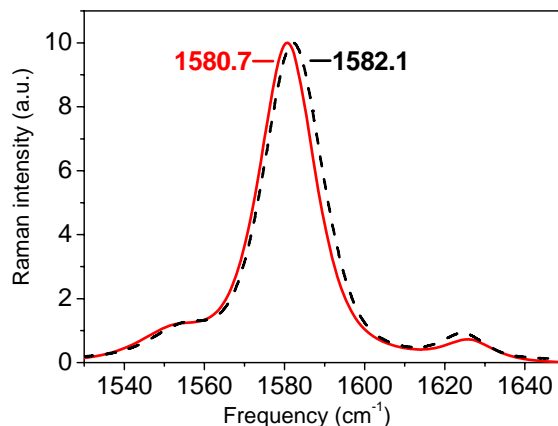


Fig. 74. Raman spectra of pristine MEH-PPV (dashed) and 1:1 MEH-PPV/DNAQ (solid) drop-cast films on glass substrates. The excitation wavelength is 670 nm.

It is known that *p*-doping MEH-PPV by  $\text{FeCl}_3$  results in full electron transfer from MEH-PPV that is accompanied by an approximately  $20 \text{ cm}^{-1}$  red shift of the MEH-PPV Raman band at  $1582 \text{ cm}^{-1}$  [13]. As one can see from the Raman spectra in Fig. 73 and Fig. 74, the Raman band shifts as a whole implying that all the MEH-PPV chains giving the Raman signal at  $1582 \text{ cm}^{-1}$  are involved in the CTC. The observed red shift amounting  $2\text{--}4 \text{ cm}^{-1}$  is much less than one in the doped polymer indicating a partial transfer of the electron density from the MEH-PPV to the TNF (or DNAQ) in the ground state. Accordingly, we conclude that the CTC in MEH-PPV/TNF and MEH-PPV/DNAQ blends is weak.

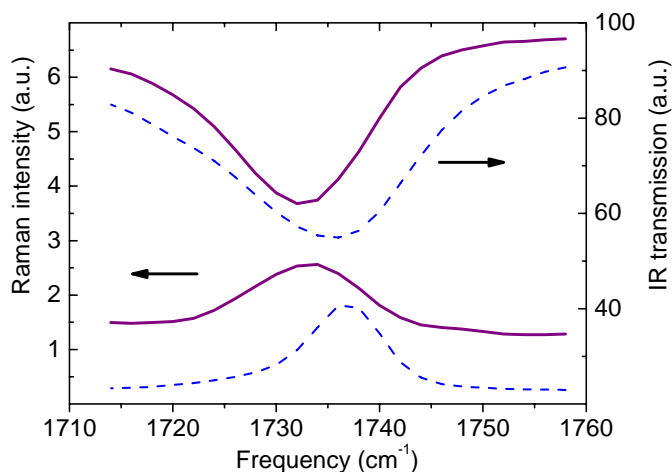


Fig. 75. Raman and IR spectra of pristine TNF (dashed) and 1:1 MEH-PPV/TNF (solid) free-standing films in the region of the TNF C=O stretch vibration. The spectra are offset vertically for clarity.

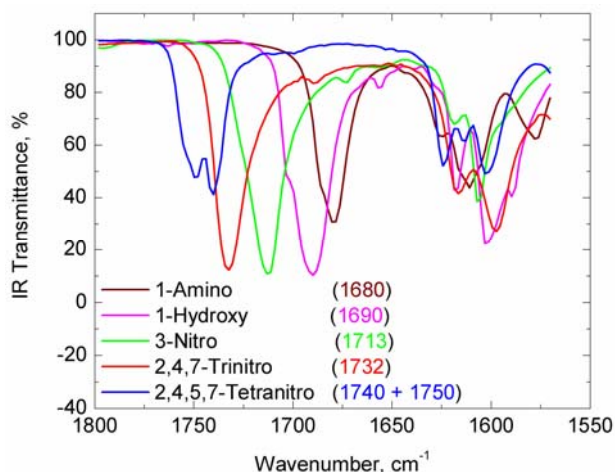


Fig. 76. IR spectra of different fluorenones in the range of C=O band observed between  $1680\text{--}1750 \text{ cm}^{-1}$ .



Thus, our vibrational studies indicate noticeable mixing of the ground state electronic wave functions of MEH-PPV and TNF or DNAQ providing partial CT from the donor to the acceptor. The observed a few wavenumbers shifts of the vibrational bands in the MEH-PPV/acceptor blends indicate relatively weak CT interaction typical of Mulliken CTCs.

#### 4.1.1.3 DSC data

If a CTC is formed, it could give an observable effect in the DSC traces. The detailed DSC data are given in Sec. 4.2.2.1. We have observed that a strong endotherm peak corresponding to the melting point of the crystalline TNF phase essentially decreases in 1:1 MEH-PPV/TNF blend and fully disappears in 1:0.2 MEH-PPV/TNF blend (Fig. 77). Thus, there is no evidence of the presence of the crystalline acceptor phase in the 1:0.2 MEH-PPV/TNF film, and therefore almost all the acceptor molecules are involved in some type of interaction with MEH-PPV. We interpret these observations as a direct consequence of intermolecular CT interaction between MEH-PPV and TNF.

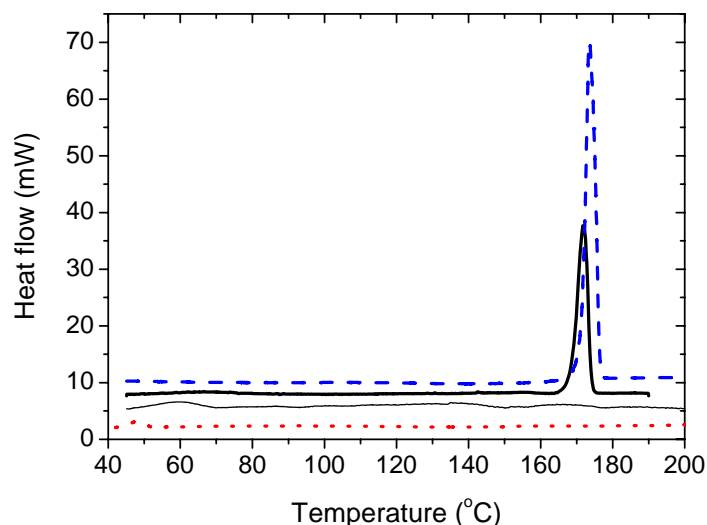


Fig. 77. DSC traces for neat TNF (dashed line), 1:1 MEH-PPV/TNF film (bold solid line), 1:0.2 MEH-PPV/TNF film (thin solid line) and pristine MEH-PPV polymer (dotted line). All curves are normalized to equal sample weight and are offset vertically for clarity.

#### 4.1.2 MEH-PPV/TNF solution

We observed that MEH-PPV/TNF solutions with concentration of the components in the blend higher than 0.5 g/l noticeably change their color as compared with pristine MEH-PPV solution. Fig. 78 compares absorption spectra of MEH-PPV/TNF and pristine MEH-PPV solutions. It is seen that analogously to the films the absorption spectrum of the blend shows an extended absorption tail as compared with the pristine MEH-PPV. As the light scattering contribution to the measured absorption in solutions is negligible, this tail is obviously due to absorption. Fig. 79 compares Raman spectra of the MEH-PPV/TNF and MEH-PPV solutions. Similar to the films, the strongest MEH-PPV Raman band at  $1585\text{ cm}^{-1}$  demonstrates a red shift of  $5\text{ cm}^{-1}$ . This red shift is no less than one in the film indicating that the intermolecular ground-state CT occurs in solution as well. Comparing our data for films (Fig. 73 and Fig. 74) and solutions (Fig. 78 and Fig. 79), we conclude that the observed absorption tail corresponds to the CTC absorption, and the Raman red shift results from partial CT in the electronic ground state. Our data suggest that the properties of the CTC are very similar both in films and solution. However, if the absorption of the MEH-PPV/TNF film demonstrates a 0.2 eV red shift of the whole MEH-PPV absorption band (Fig. 71), the latter does not show any shift in solution (Fig. 78). Therefore, the red shift of the MEH-PPV absorption band in the blended films is not a direct consequence of the ground-state CT. This red shift could result from changing interchain interactions of MEH-PPV chains involved in the CTC. This effect is discussed below in Sec. 4.2.5.

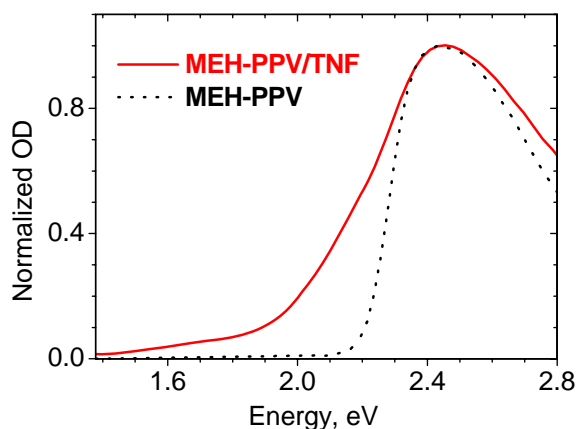


Fig. 78. Absorption spectra of 1:1 MEH-PPV/TNF and pristine MEH-PPV solutions in chlorobenzene with a concentration of 2.5 g/l for the each component.

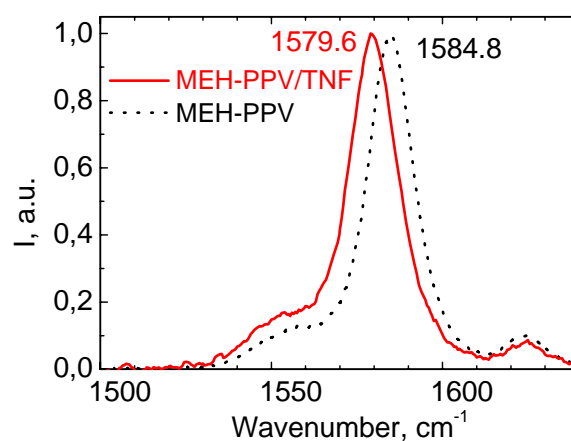


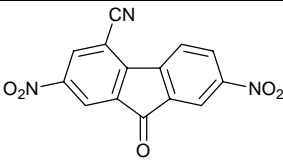
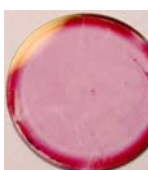
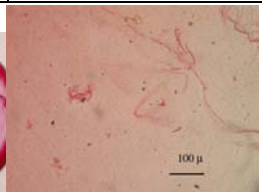
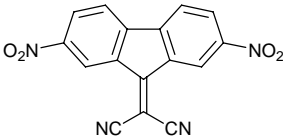
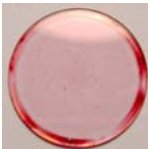
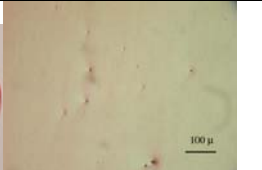
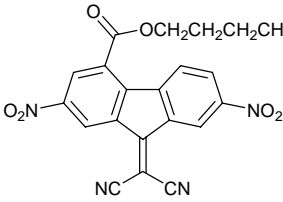
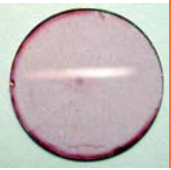
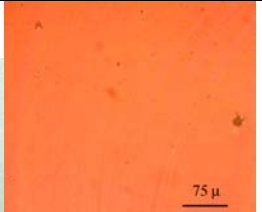
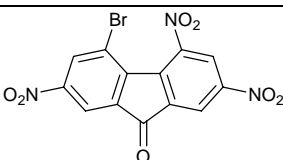
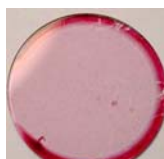
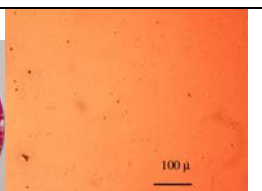
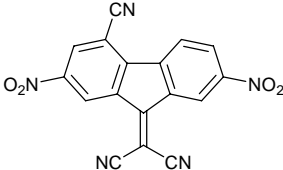
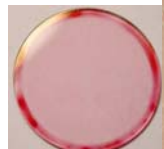
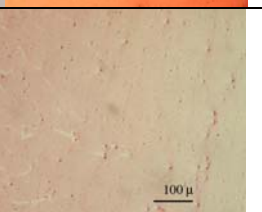
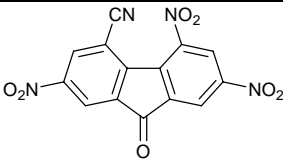

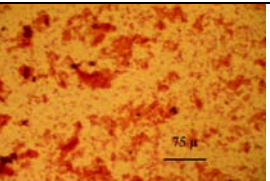
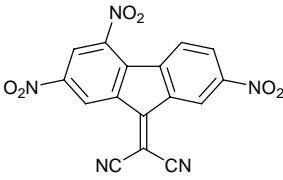
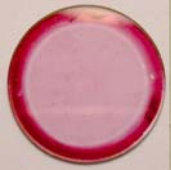
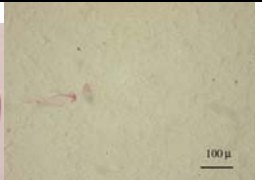
Fig. 79. Raman spectra of 1:1 MEH-PPV/TNF and pristine MEH-PPV solutions in chlorobenzene with a concentration of 2.5 g/l for the each component. The Raman excitation wavelength is 670 nm.

#### 4.1.3 CTCs of MEH-PPV with various fluorene acceptors

According to Mulliken's model of CTC, the higher the electron affinity (EA) of acceptor, the lower the CTC optical gap. Motivated by this point, we have studied blends of MEH-PPV with ten various acceptors of the fluorene series (Table 8), whose EAs is expected to be about or higher than the TNF EA (2.2 eV). Blends were prepared from chlorobenzene for MEH-PPV:acceptor molar ratio 1:0.4. As shown in Sec. 4.2, this ratio is optimal for MEH-PPV/TNF blends since for higher acceptor concentration a large number of acceptor microcrystals appear in the films. The MEH-PPV/acceptor films were prepared by spin-casting of the resulting mixture (with or without precipitate) on glass substrates of diameter 23 mm. All the studied films changed their color compared with neat MEH-PPV films that was a signature of CTC formation. Note that when tetrahydrofuran was used as a solvent instead of chlorobenzene, neat solutions (without precipitate) were obtained. The color of the films also changed compared with the pristine MEH-PPV. Table 8 presents formulas of acceptors, their EAs, qualitative characteristics of solution and films, and photos of the films.

Fig. 80 shows absorption spectra of good quality films described in Table 8, i.e., blends of MEH-PPV with CNDNFon, DDF, BuDDF, BrTNFon, and DTF. It is clearly seen that all the films demonstrate a 0.1–0.2 eV red shift of the main absorption band of pristine MEH-PPV at 2.4 eV and show an absorption tail extending down to 1.2 eV ( $\sim 1 \mu\text{m}$ ), which could be assign to the CTC band. These observations are in qualitative accordance with our studies of MEH-PPV/TNF and MEH-PPV/DNAQ blends. We have calculated the energy of the CTC band by deconvoluting the spectra in Fig. 80. Fig. 81 shows relation between the CTC band energy and the acceptor's EA calculated at PM3 level (see Table 8) for the blends showing a clear CTC band. The available experimental EAs from Table 8 are also plotted. As seen in Fig. 81, the CTC band energy varies in the range 1.5–1.75 eV, and it is well correlated with the acceptor EA. The latter is in accordance with Mulliken's model of CTC. Therefore, the fluorene acceptors form an intermolecular CTC with MEH-PPV. Importantly that the MEH-PPV PL was deeply quenched in all the samples indicating efficient photoinduced charge transfer. As a result, we conclude: (i) MEH-PPV can form CTCs with acceptors of the fluorene series, (ii) a number of acceptors allow us to prepare neat films of MEH-PPV/acceptor blends (see Table 8), (iii) position and intensity of the CTC band can be tuned (Fig. 80) in accordance with Mulliken's model.



Formula, Code	EA, eV	Peculiarities of		spin-cast films <sup>a</sup>	
		mixtures in chlorobenzene	spin-cast films	photos	micro photos
 <b>CNDNFon</b>	2.81 2.12c	moderate change in color, no precipitate	good quality		
 <b>DDF</b>	2.87 2.20b	no changes in color and no precipitate	color change, high quality		
 <b>BuDDF</b>	2.97	moderate change in color, no precipitate	excellent quality, homogeneous		
 <b>BrTNFon</b>	3.04	deep change in color, no precipitate	good quality		
 <b>CNDDF</b>	3.12	moderate change in color, no precipitate	visible defects		
 <b>CNTNFon</b>	3.25 2.34c	deep change in color, precipitate formation	low quality		
 <b>DTF</b>	3.26 2.45b 2.56c	deep change in color, no precipitate	high quality		

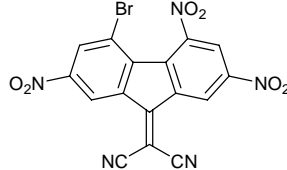
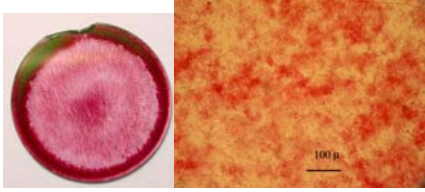
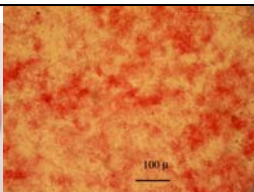
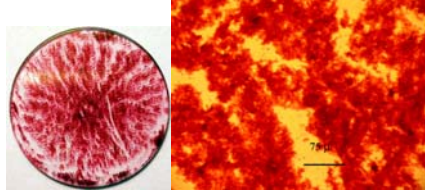

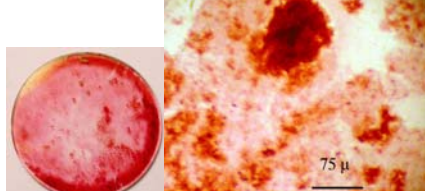
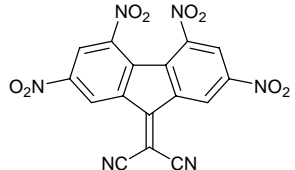

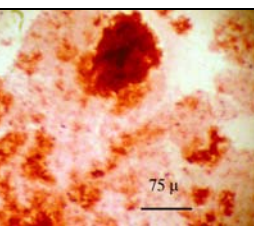
 <p><b>BrDTF</b></p>	3.34	deep change in color, precipitate formation	low quality	 
 <p><b>TeNFon</b></p>	3.41 2.20b 2.42c	deep change in color, precipitate formation	low quality	 
 <p><b>DTeF</b></p>	3.63 2.62b 2.77c	precipitate formation just after mixing solutions, gel formation after some time. very dark color	low quality film due to precipitate	 

Table 8. Acceptors and MEH-PPV/acceptors blends. EAs calculated at PM3 level are shown and experimental EAs are given if available.

<sup>a</sup> colors in photos do not fully correspond to the real film colors

<sup>b</sup> V.E. Kampars and O.Ya. Neilands Usp. Khim. **44** 945 (1977) (in Russian)

<sup>c</sup> I. F. Perepichka et al. J. Org. Chem. **63**, 6484 (1998)

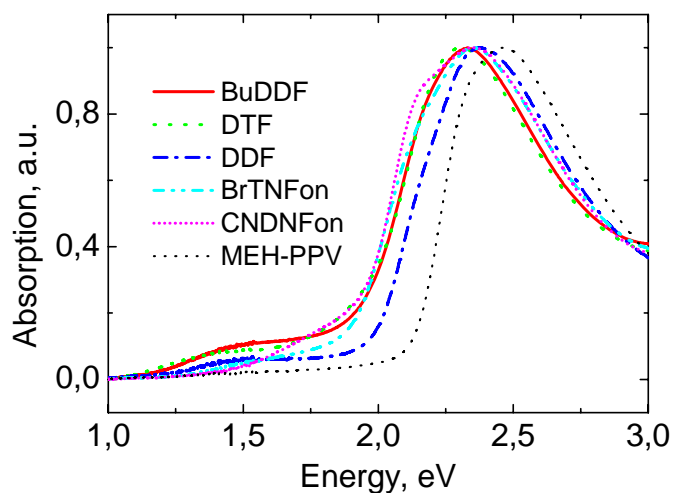


Fig. 80. Absorption spectra of spin-cast films of 1:0.4 MEH-PPV/acceptor blends. Spectra were corrected to zero at 1 eV and normalized.

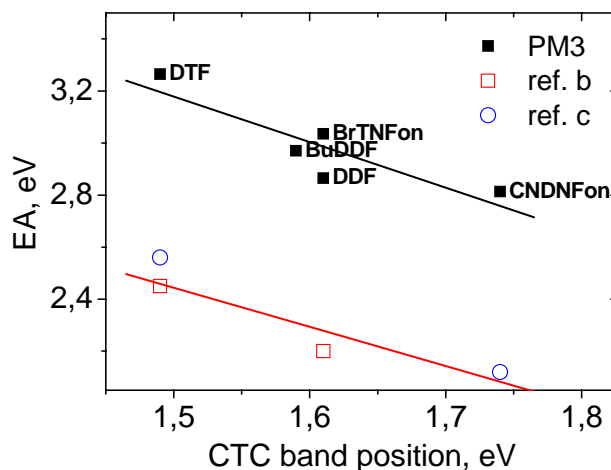


Fig. 81. Relation between the CTC band positions calculated from data in Fig. 80 and EAs of fluorene acceptors (Table 8). Linear fits to the data are also shown.

#### 4.1.4 Discussion

We have demonstrated that a conjugated polymer can form intermolecular ground-state state CTCs with molecular organic acceptors both in solutions and films. Using vibrational spectroscopy, we have found evidence that electron density from the  $\pi$ -conjugated system of the polymer donor partially transfers to the molecular acceptor. In other words, weak ground-state CT occurs. Furthermore, the

CTC band energy is correlated with the acceptor electron affinity (EA). These observations are in accordance with Mulliken's model of weak CTCs. The absorption (Fig. 71 and Fig. 80) and Raman (Fig. 73 and Fig. 74) spectra of MEH-PPV in the MEH-PPV/acceptor blended films shift *as a whole* indicating that all the polymer chains observed in these spectra are involved in the CTC.

As mentioned above in Sec. 1.2, despite a number of donor-acceptor blends of conjugated polymers have been studied by now, weak CT from a  $\pi$ -conjugated polymer chain in its electronic ground state has not been clearly observed. At the same time, from the very beginning of the field of  $\pi$ -conjugated polymers, they are well known to be easily doped by elements and inorganic compounds. Apparently, this doping corresponds to full CT. It is unclear why weak ground-state CT is not easy to observe in  $\pi$ -conjugated polymers. We discuss here main factors influencing weak CT from a  $\pi$ -conjugated chain. The important parameter controlling donor-acceptor intermolecular CT is the difference between the donor ionization potential and the acceptor electron affinity (EA). The EA of TNF is about 2.2 eV, which is within the range of EAs of acceptors studied earlier in blends with MEH-PPV by Heeger's team [14]. Therefore, the magnitude of EA alone does not determine the ground-state CT in  $\pi$ -conjugated chains. On the other hand, according to Mulliken's model, intermolecular CT in the electronic ground state depends on the overlapping of the HOMO donor and the LUMO acceptor wavefunctions. Since the wavefunction at an extended conjugated chain (donor) is strongly delocalized, noticeable overlapping of the donor and acceptor wavefunctions necessitates delocalization of the acceptor wavefunction as well. This could explain why such a strong acceptor as TCNQ does not lead to ground-state CT in MEH-PPV/TCNQ blends. However, ground-state CT was not observed for the acceptors both longer and shorter than TNF as well [14]. One can suppose that the molecular orbital pattern of fluorene acceptors (Table 8) provides better overlapping with corresponding MEH-PPV molecular orbitals. Note that DNAQ, which has a lower EA and a similar length compared with those of TNF, also forms a weak ground-state CTC in MEH-PPV/DNAQ blends. In these blends the CTC band is less intensive (Fig. 71) and the frequency shifts in the vibrational spectra are weaker than in the MEH-PPV/TNF blends (Fig. 74).

## 4.2 CTC properties in the ground-state

### 4.2.1 Modeling possible donor-acceptor geometry of CTCs

The ability of  $\pi$ -conjugated molecules and polymers to form CTC obviously depends on the geometry of donor and acceptor molecules. All molecules we used were investigated by calculation of their geometry by semi-empirical (AM1) method and molecular dynamics method (for polymers). Donor-acceptor pairs were examined in possible configurations to match their  $\pi$ -conjugated backbones. The combinations favoring the maximum overlapping of molecular orbitals of donor and acceptor are presented in Fig. 82–Fig. 84. The results of our analysis can be summarized as follows:

#### Donors:

- PF2/6 (Fig. 57): the presence of  $sp^3$ -hybridized carbon atom in the backbone and long aliphatic side groups covering  $\pi$ -conjugated backbone make it hard to arrange any acceptors exceeding benzene molecule near the PF2/6 unit.
- PT: pentagonal rings in the backbone suppose to be in good correspondence with fluorene-based acceptors.
- MEH-PPV: easy accessible (aliphatic side groups are connected to the backbone through oxygen atoms) conjugated backbone suits rather good both TNF and DNAQ molecules.

#### Acceptors:

- TNF: a plain molecule, which well suits both MEH-PPV and PT.
- DNAQ: the side groups bend the molecule around middle oxygen atoms ( $\sim 15$ – $30^\circ$ ) causing nonplanar structure. It could hamper CTC formation with the plain MEH-PPV backbone.

- polyDNAQ: nonplanar (possibly spiral or zigzag) structure of polymer is quite complicated. The monomer units form the polymer chain with rather big angles ( $\sim 60^\circ$ ) between their “planes”. A possible structure is shown in Fig. 85

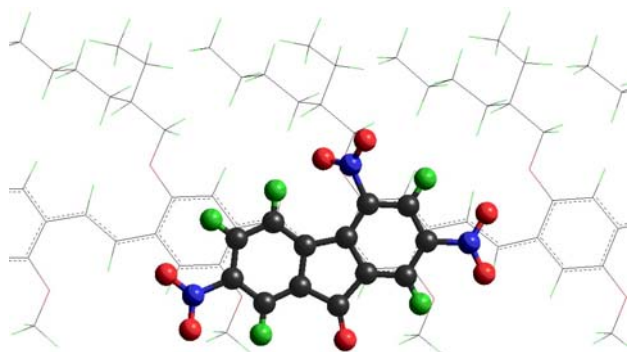


Fig. 82. MEH-PPV(thin)+TNF(bold).

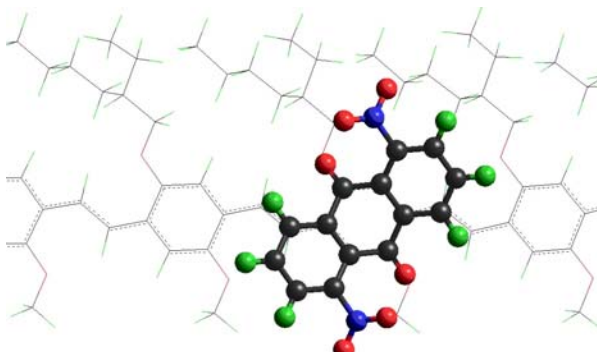


Fig. 83. MEH-PPV(thin)+DNAQ(bold).

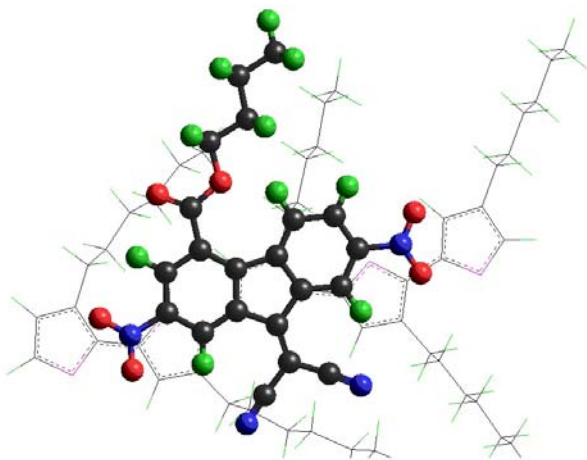


Fig. 84. PT(thin)+BuDDF(bold).

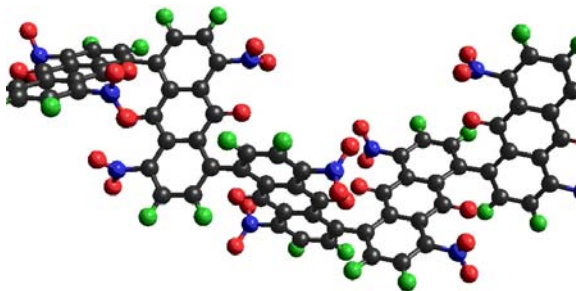


Fig. 85. Possible structure of polyDNAQ.

Thus, the above analysis is in good correlation with our experimental data. For example, the MEH-PPV/TNF pair is the most preferable because of the largest overlapping of  $\pi$ -conjugated backbones. Our failure to find CT interaction using PF2/6 and fluorene-type acceptors seems to be due to bulky aliphatic side groups of PF2/6 which impede close donor-acceptor configuration favoring overlapping of their molecular orbitals.

## 4.2.2 Thermal analysis of MEH-PPV/TNF blends

### 4.2.2.1 DSC of MEH-PPV, TNF, and MEH-PPV/TNF

Pristine MEH-PPV films, TNF powder, and MEH-PPV/TNF have been studied by the DSC method. It has been observed that pristine MEH-PPV has a low-temperature melting peak around  $46\text{--}48^\circ\text{C}$  (Fig. 86, left) presumably related to a melting of pendent substituents on phenylene rings of the macromolecule. Further heating of the neat MEH-PPV showed a non-linear transition of the sample to a new heat capacity level in the  $60\text{--}150^\circ\text{C}$  range which could be related to an intensification of molecular segments mobility within the polymer (or transition from a vitreous to viscous-elastic state) (Fig. 86, right).

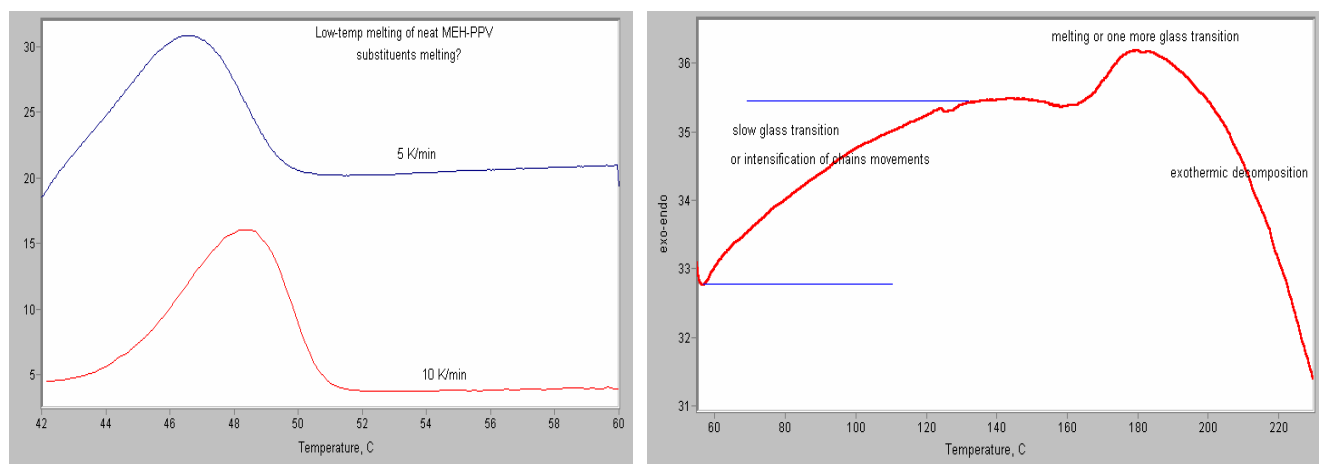


Fig. 86. Low-temperature (left) high-temperature (right) parts of the pristine MEH-PPV DSC curve.

This stage is accompanied by a second phase transition at the vicinity of 170–190°C which may be related to transition of the material to a viscous flow state (it could be interpreted as melting of the polymer chains, provided the latter has a measurable crystallinity degree). In any case, after this second transition MEH-PPV shows an intense exothermic feature of unknown origin. It could be a destruction of the polymer, but it could be related to evaporation of the low-molecular fraction from the sample too (see TGA data below).

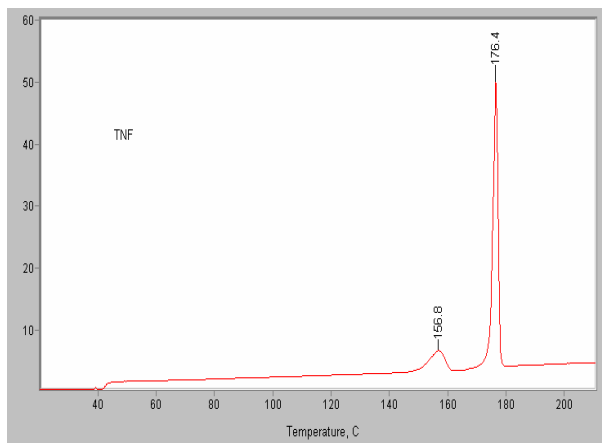


Fig. 87. DSC curve of pristine TNF.

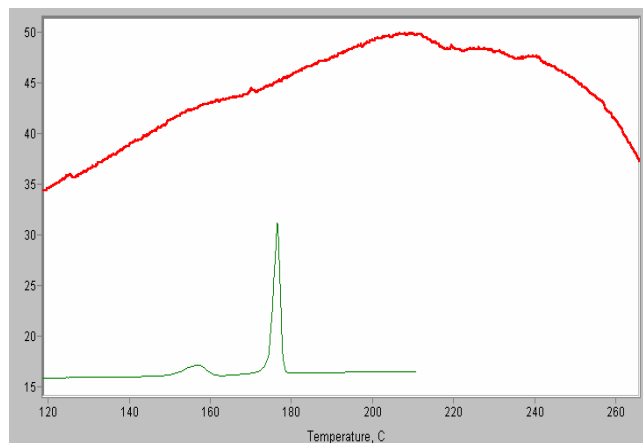


Fig. 88. DSC curves of TNF (lower curve) and 1:0.5 MEH-PPV/TNF film (upper curve).

Fig. 87 shows clear melting endotherms of TNF powder with the melting point at 176.4 °C. Notably, there is no evidence for presence of the crystalline TNF phase in the 1:0.5 MEH-PPV/TNF blend (Fig. 88). This implies that a major part of TNF turned out to be involved into some type of interaction with the MEH-PPV matrix. We suggest that this is intermolecular CT interaction between the MEH-PPV polymer chains and TNF molecules.

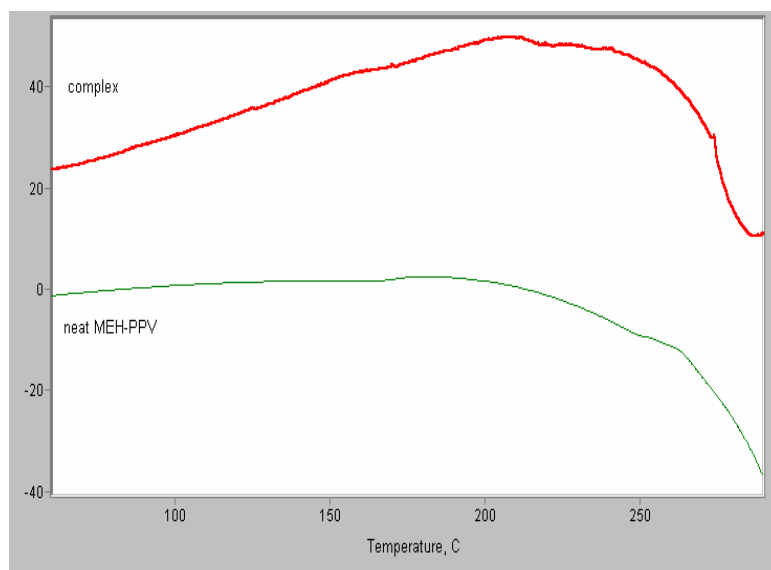


Fig. 89. DSC curves of pristine MEH-PPV (lower curve) and 1:1 MEH-PPV/TNF blend.

MEH-PPV/TNF films show thermal behavior resembling that of pristine MEH-PPV in terms of absence of clear, intense and/or well resolved thermal effects (Fig. 89). Instead, a couple of broad and weak endotherms are present on DSC trace at 150–160 and 200–220°C, which may belong to the CTC. Fig. 89 shows that, presumably, the thermal instability of the MEH-PPV matrix is responsible for the high temperature exotherm seen for the MEH-PPV/TNF film, which is very close by its nature to that observed for the pristine MEH-PPV film.

Fig. 90 shows DSC traces for MEH-PPV/TNF blends with various TNF content. Notable suppression of the lower temperature exotherm (180–240°C) of MEH-PPV is observed in MEH-PPV/TNF blends upon adding TNF (Fig. 90). This exotherm could be assigned to oxidation. At the same time, a clear exotherm is observed at higher temperature near 300°C. This MEH-PPV exotherm becomes progressively prevailing with increasing TNF content in the blends. Moreover, we observed that its intensity increases (not shown in Fig. 90). The latter circumstance is a clear indication to involvement of molten TNF in the process since it is reasonable to suggest that all sealed DSC pans contained approximately equal amount of atmospheric oxygen entrapped during the pan sealing procedure. It can be seen also that peak points of the exotherms progressively shift to higher temperatures in parallel with raising TNF content. (Perhaps at the highest TNF content studied (2:1) the oxidation/anti-oxidation mechanism changed once more in the system.) As was noted earlier, at TNF contents higher than 0.5:1 the presence of the crystalline TNF phase in the blends becomes obvious (see small features at 170°C in Fig. 90). It may be suggested that, when the crystalline TNF phase is present in the system from the very beginning of the heating process, molten TNF excess can induce a “premature” oxidation of the polymer matrix.



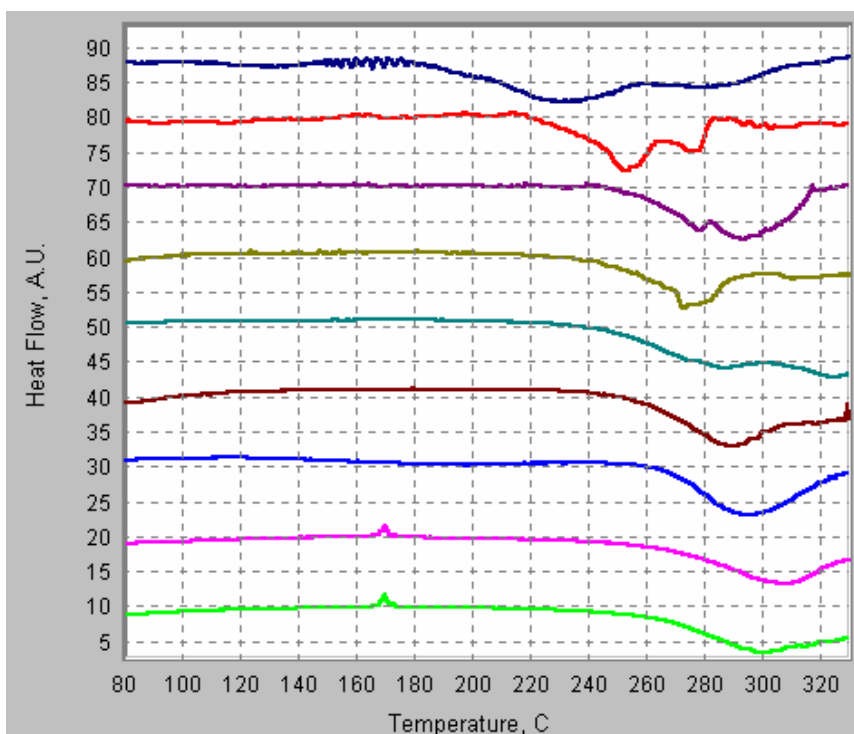


Fig. 90. DSC traces for a series of MEH-PPV/TNF blends with progressively increasing (from top to bottom) TNF molar content: 0:1 (pristine MEH-PPV), 0.025:1, 0.05:1, 0.1:1, 0.2:1, 0.3:1, 0.5:1, 1:1, 2:1.

#### 4.2.2.2 DSC of MEH-PPV/DNAQ blends

DSC traces shown in Figs 9 and 10 illustrate melting and crystallization behaviour of neat DNAQ. It can be seen that DNAQ demonstrates good thermal stability of its properties.

First of all, we recorded DSC traces of pristine DNAQ. They demonstrated melting and crystallization of DNAQ at 290°C. It melts and crystallizes with very good reproducibility in seemingly the same crystal modification. However, the DNAQ melting temperature is essentially higher than the temperatures inducing degradation of the MEH-PPV matrix. DSC traces of 1:1 MEH-PPV/DNAQ blend did not show any features distinct from those of individual components, i.e. MEH-PPV and DNAQ.

#### 4.2.2.3 Isothermal TGA analysis of MEH-PPV/TNF blends

TGA experiments have been undertaken in the isothermal regime to evaluate the content of volatile impurities (solvent) possibly entrapped by the solid blend material during the film formation process. The TGA instrument was rapidly ramped to a predetermined temperature with a rate of 100 K/min, and then the measurement was accomplished by following for the sample weight loss development with time. Since the series of the samples under investigation was prepared by using chlorobenzene (CB) as the common solvent for the blend components, 130-140°C (temperature close to or slightly above the CB boiling point) was chosen for these measurements. Fig. 91 shows the isothermal TGA trace of a pristine MEH-PPV film. As follows from Fig. 91, the pristine MEH-PPV film contained approximately 3% of entrapped CB that slowly left the solid at 130°C during 120 minutes.



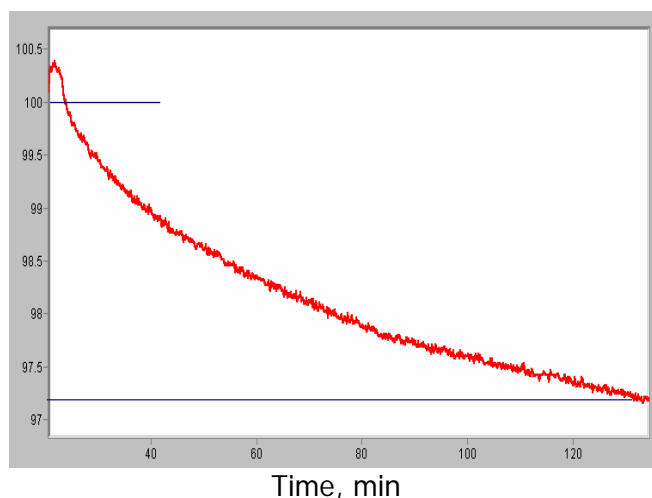


Fig. 91. Isothermal TGA trace of pristine MEH-PPV film drop-cast from chlorobenzene recorded at 130°C in air flow atmosphere.

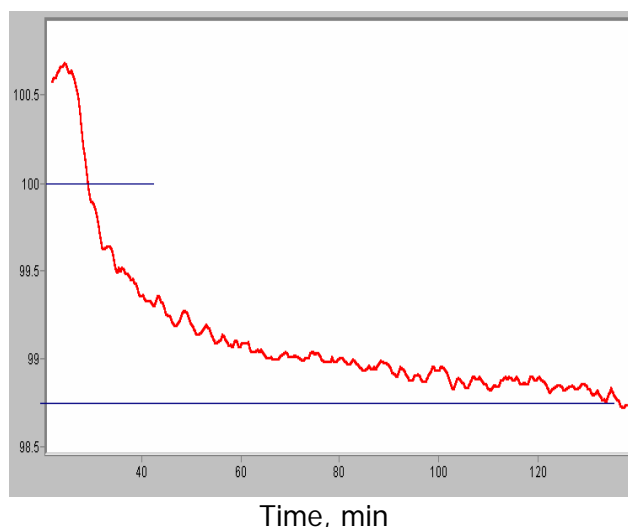


Fig. 92. Isothermal TGA trace for 1:0.3 MEH-PPV/TNF film recorded at 140°C.

Fig. 92 shows the isothermal TGA trace of a 1:0.3 MEH-PPV/TNF film. Similar curves in Fig. 91 and Fig. 92 indicate that the MEH-PPV/TNF blend also contains the entrapped solvent. It is of interest that the content of CB in the blend is lower than in the pristine MEH-PPV films suggesting that TNF perhaps is able to compete with CB molecules for the complexing sites within the MEH-PPV matrix during solidification. Fig. 91 and Fig. 92 demonstrate exothermic peaks within the first 10 min assignable to oxidative action of trace amounts of oxygen entrapped into the hermetically sealed DSC pans. It is obvious that in the presence of TNF the oxidative action of oxygen along with an oxidative action of TNF itself is rather complex and deserves thorough investigation.

#### 4.2.2.4 Dynamic TGA analysis: improving stability of donor/acceptor blends

Low stability of polymer solar cells is one of the main long-standing problems in the field. Because of this, it is very important to find approaches to a more stable working layer. Motivated by this, we studied thermal behavior of MEH-PPV/TNF blends. Fig. 93 compares TGA traces for MEH-PPV/TNF blends with those of pristine MEH-PPV and TNF. It is seen that addition of TNF to MEH-PPV essentially changes the MEH-PPV thermo-oxidative behavior. Our analysis of the TGA data could be summarized as follows:

1. Compounding of MEH-PPV with small amounts of TNF (e.g. 10 mol %, cf. Fig. 93) leads to a pronounced enhancement of MEH-PPV thermal-oxidative stability. The same is true for comparatively high loads of TNF in the composition (e.g. 50 mol %).
2. In very general terms, being present in small molar ratios, TNF tends to increase the MEH-PPV thermal-oxidative stability, while higher loads of TNF lead to a decrease of the stability of the composition at lower temperatures. In the light of the earlier findings that there is a "limiting" capacity of the MEH-PPV matrix in terms of its ability to bind the TNF molecules by complexation, the last result is not surprising. It is reasonable to suggest that excessive (uncomplexed) TNF persists in the blends in its own phase (cf. the DSC data above), and it is able to leave the matrix more easily as compared with that involved into the CTC.
3. The TGA traces shown in Fig. 93 evidence that thermal behavior of the blends is rather complex, being complex than that of the pristine MEH-PPV. The thermal-oxidative degradation process in the blends is a multistage one and indicates that a number of chemical reactions (transformations) are involved. Among these, e.g. splitting of aliphatic

pendants, depolymerization of MEH-PPV, oxidation and thermal degradation of the individual components, chemical addition of TNF residues to the polymer matrix sites, etc. can be envisaged. In any case, due to a series of chemical transformations taking place during the heating run, a TGA trace for a given blend can not be represented by a simple superposition of the TGA traces intrinsic for the individual components like, e.g., in the case of simple physical mixture.

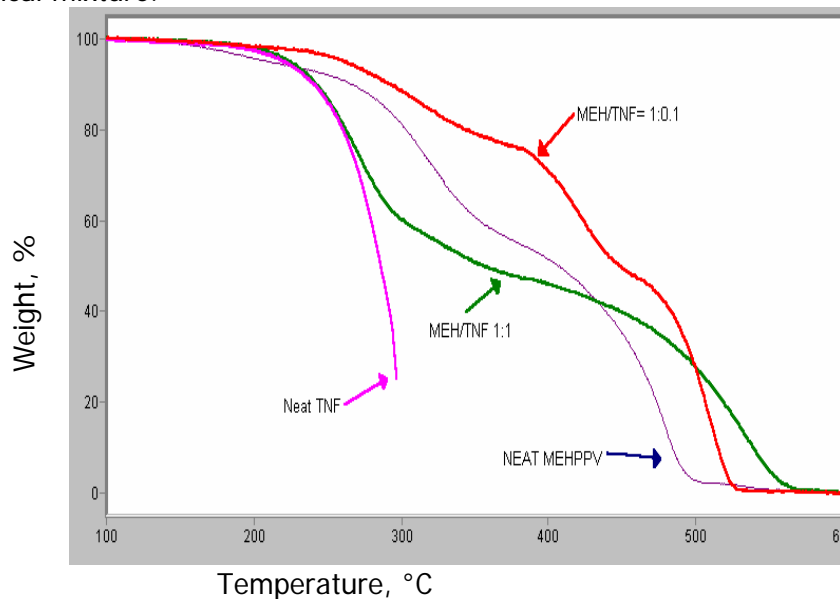


Fig. 93. Dynamic TGA traces for 1:0.1 and 1:1 MEH-PPV/TNF blends, pristine MEH-PPV and TNF.

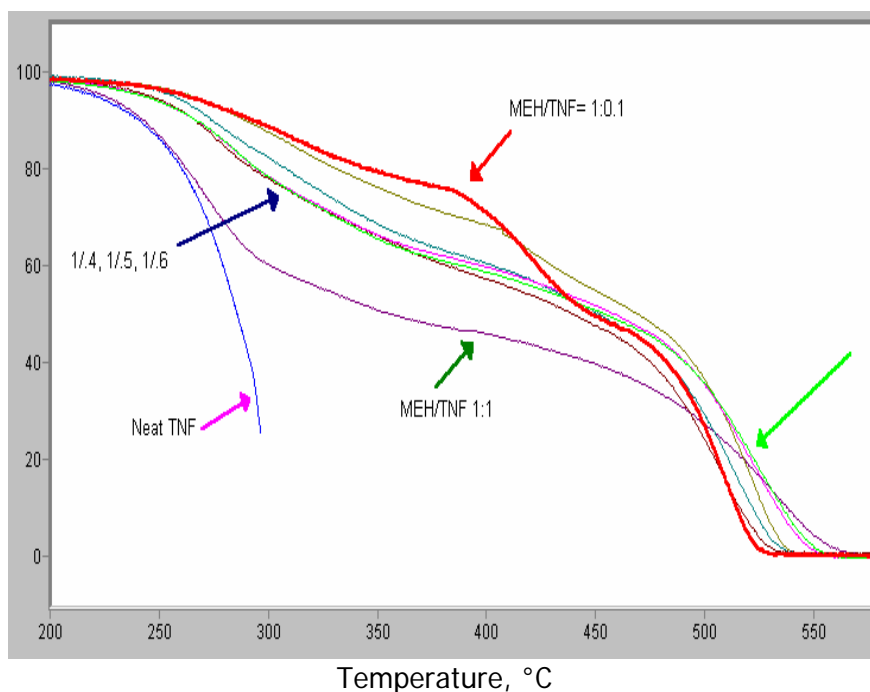


Fig. 94. TGA traces for a series of MEH-PPV/TNF blends and pristine components.

Fig. 94 shows TGA traces for MEH-PPV/TNF blends with various donor/acceptor ratio. These traces show rather a surprising result. Namely, the blend with a minimal TNF load investigated (1:0,1) shows the maximal thermal stability gain. Further increase of TNF content progressively leads

to a depression of the thermal stability. In other words, addition of one TNF molecule per 10 repeating units of the MEH-PPV chain is able to provide a material with drastically improved thermal-oxidative stability. These 10% of the acceptor are obviously bound by complexation with the corresponding MEH-PPV molecular units. The reason of the enhanced thermal stability in MEH-PPV/TNF blends is not clear at the moment. One might assume that CTC formation leads to noticeable modification of rigidity of the MEH-PPV matrix.

Thus, the most essential finding from our TGA studies is enhancement of the thermal-oxidative stability of MEH-PPV in MEH-PPV/acceptor blends. The gain can be approximately estimated as 100 K as seen in Fig. 93. The mechanism of this increasing is not clear and should be a subject of separate studies in view of its importance for polymer solar cells.

#### 4.2.2.5 Mass-spectra of pristine MEH-PPV and MEH-PPV/TNF blends

Taking into account the TGA results, we were interested in investigation of products delivered from MEH-PPV and MEH-PPV/TNF films at moderate thermal heating. It was expected that it should be side alkyl chains. In fact, alkyl chains compose ~43% of MEH-PPV molar mass. As follows from our TGA data, the weight loss of the pristine MEH-PPV under 350°C is practically the same. To check this hypothesis, samples of pristine MEH-PPV and 1:0.1 MEH-PPV/TNF have been analyzed using a MS-30 mass-spectrometer (Kratos, UK) in the temperature range from RT to 350°C ( $E_{\text{ion}}=70$  eV, temperature of ionic chamber was 210°C). Fig. 95 shows mass-spectra of pristine MEH-PPV and 1:0.1 MEH-PPV blends. Indeed, as seen in Fig. 95, fragments of MEH-PPV side chains form a major part of the total ionic current. It means that side chains elimination is a main process at temperatures up to 350°C. The mass-spectrum of 1:0.1 MEH-PPV/TNF blend (Fig. 95, bottom) also demonstrates that fragmentation of TNF was also represented in the mass-spectra. In general, we can resume that information obtained using both TGA and mass-spectra studies confirm that at temperatures not higher than 350°C the main process in both MEH-PPV and MEH-PPV/TNF is destruction of side chains.

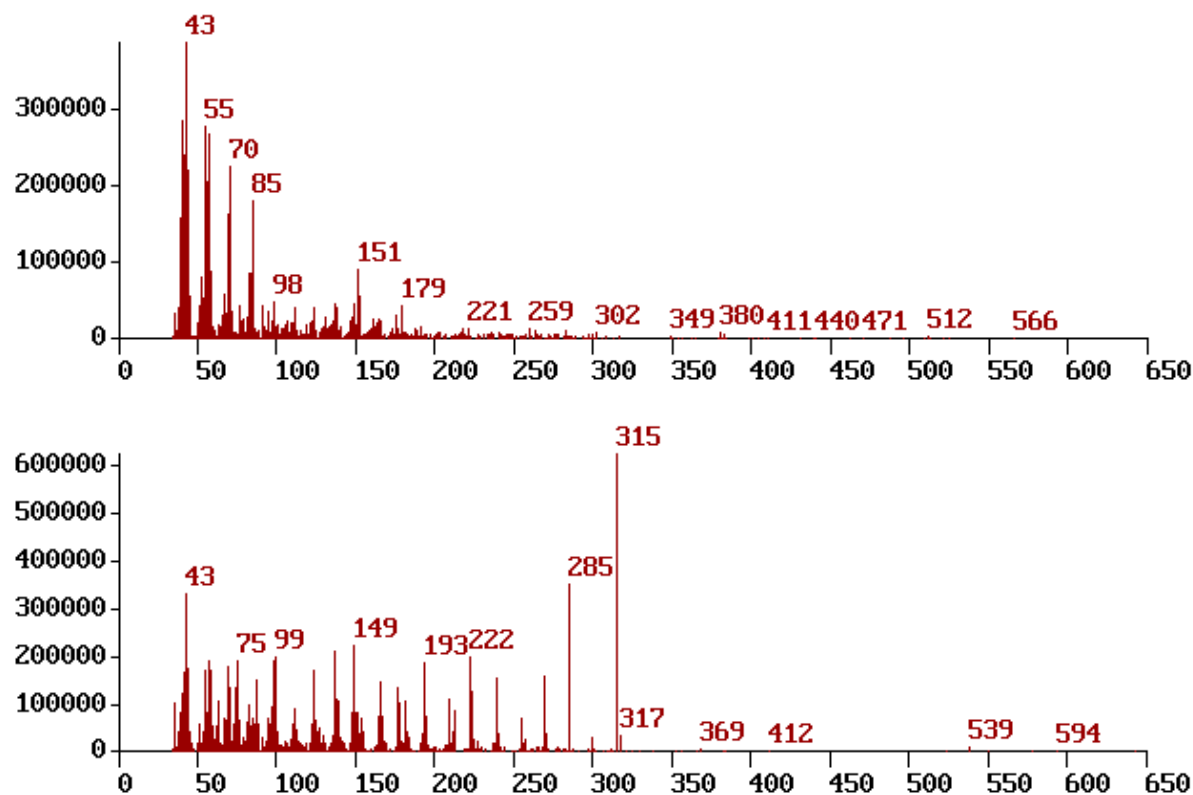


Fig. 95 Mass-spectra of pristine MEH-PPV (top) and 1:0.1 MEH-PPV/TNF blend (bottom).

### 4.2.3 Light absorption and scattering in MEH-PPV/acceptor blends

If the acceptor concentration in the donor-acceptor blend with ground-state CT interaction is higher than an optimum level, the excess of acceptor molecules that do not form intermolecular CTC could give their own phase. This uncomplexed acceptor could be a source of light scattering in films of MEH-PPV/acceptor blends and therefore contribute to the measured optical density to be determined from optical transmission of the films. On the other hand, the amount of light scattered in donor-acceptor blends might be used to characterize phase separation.

To evaluate the absorption and scattering losses in the measured optical density, i.e. extinction, separately we have elaborated a simple method, in which we measure the optical transmission of polymer films using a wide-aperture photodetector at a few laser wavelengths (see Sec. 2.2). Then making some assumptions about the scattering indicatrix, we calculate the scattering coefficient  $\sigma$  and absorption coefficient  $\alpha$ , which contribute to the extinction  $hd = \sigma d + \alpha d$  of the film with thickness  $d$ .

#### 4.2.3.1 MEH-PPV/TNF blends

Fig. 96 shows photomicrographs of MEH-PPV/TNF blends. At high acceptor concentration in the blend ( $X=1$  and 2), the acceptor molecules form their own tree-like phase visible in Fig. 96. The typical size of phase separated TNF species is 2–10  $\mu\text{m}$  as evaluated from the images in Fig. 96. In MEH-PPV/TNF films with  $X \leq 0.5$ , the optical microscopy does not reveal any phase separation.

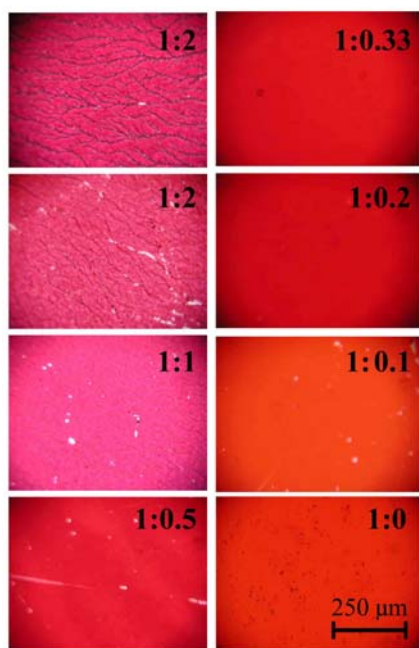


Fig. 96. Photomicrographs of MEH-PPV/TNF blends with different D:A ratio ( $1:X$ ). Two 1:2 MEH-PPV/TNF blends have different thicknesses; a thicker film at the upper image shows a clearer microcrystalline tree-like phase. The scale bar is shown in the right bottom corner.

As seen in Fig. 96, films of MEH-PPV/TNF blends essentially change their color compared with pristine MEH-PPV films. Fig. 97a shows absorption spectra of MEH-PPV/TNF blends for various D:A ratios ( $1:X$ ). The absorption spectra are shifted to the red and show extended absorption tails up to 800 nm (1.5 eV) compared with the pristine MEH-PPV film. Fig. 97b demonstrates the red shift of the MEH-PPV absorption peak maximum at  $\sim 500$  nm (from Fig. 97a) as a function of  $X$ . This shift begins to saturate at  $X \approx 0.33$  and reaches 30 nm (0.14 eV) for higher  $X$ .

As was discussed above, the observed spectral features in MEH-PPV/TNF blends indicate a noticeable ground-state interaction of the MEH-PPV chains with the TNF molecules, i.e., CTC formation. Therefore, the linear increase of the red shift for  $X < 0.33$  in Fig. 97b indicates that a part of the TNF molecules involved in the CT complex is proportional to  $X$ .

Thus, MEH-PPV/TNF blends exhibit an appreciable optical density in the MEH-PPV bandgap. However, the light scattering may give a contribution to the red absorption tails in Fig. 97a owing to the phase separation effect, which is seen in the photomicrographs in Fig. 96. To find that contribution, we have measured both the light scattering and absorption in MEH-PPV/TNF blends at several laser wavelengths.

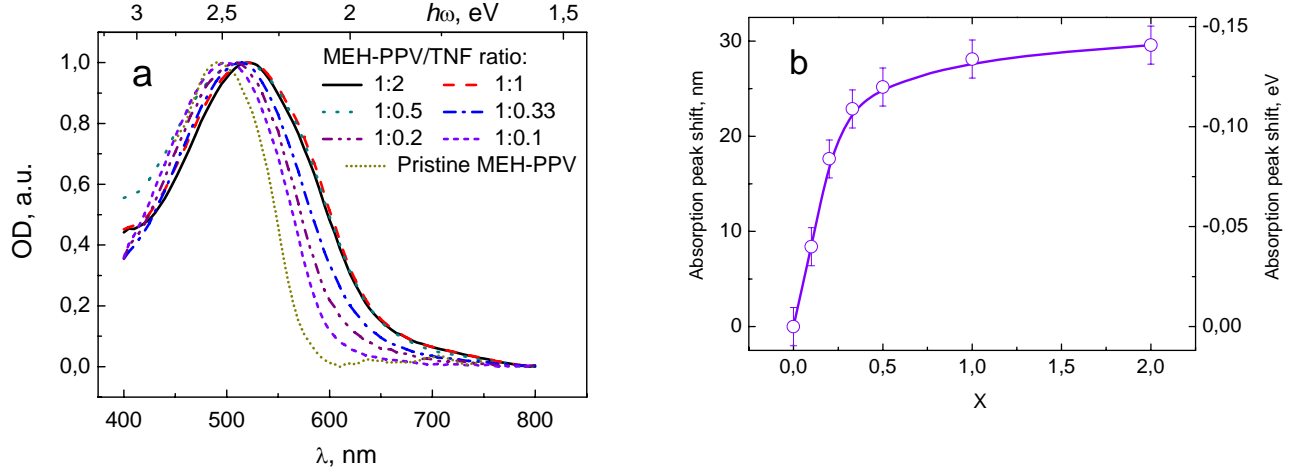


Fig. 97. (a) Normalized absorption spectra and (b) shifts of the absorption peak for MEH-PPV/TNF blends with different D:A ratio ( $1:X$ ). Lines are guide to the eye.

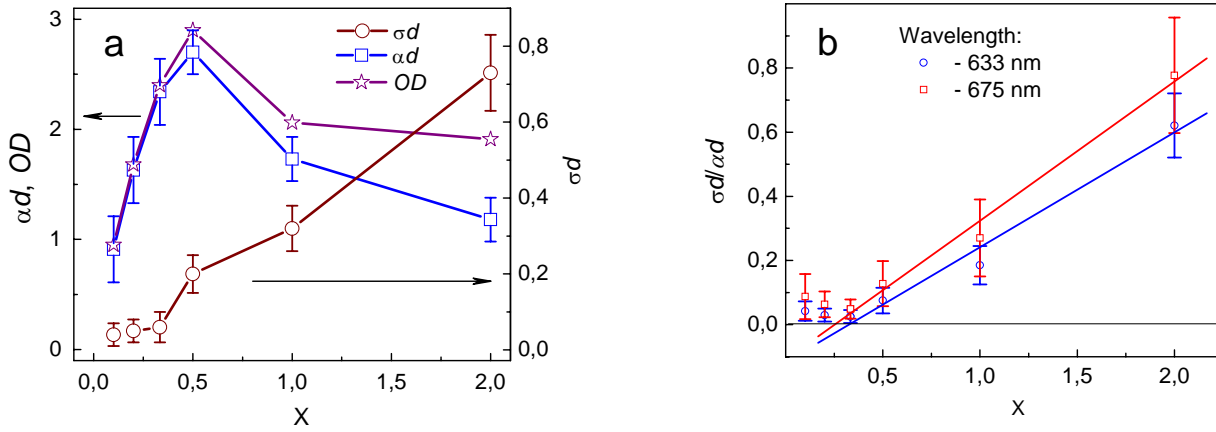


Fig. 98. (a) Absorption ( $\alpha d$ ), scattering ( $\sigma d$ ), and their sum ( $OD$ ) for MEH-PPV/TNF blends as a function of D:A ratio ( $1:X$ ) at 633 nm. Lines are guide to the eye. (b) Scattering normalized to absorption ( $\sigma d / \alpha d$ ) as calculated from the data in the left figure. Data points for  $X \geq 0.33$  are fitted by a straight line.

Fig. 98a shows the results for the wavelength 633 nm. As seen in Fig. 98a, the absorption increases proportionally to the acceptor concentration  $X$  for  $X \leq 0.33$ . This indicates that the TNF molecules are involved in the CT complex since the absorption at 633 nm is determined only by it (see Fig. 97a). Note that both pristine MEH-PPV and TNF are transparent at this wavelength. Fig. 98a also demonstrates that the light scattering is low (about the experimental error) and virtually constant at  $X \leq 0.33$ . However, as Fig. 98a shows, the scattering increases dramatically for  $X > 0.33$  since an essential part of TNF forms its own phase (see Fig. 96) resulting in growth of the scattered light. At the same time, the absorption decreases with increasing the TNF content in the blend for

$X > 0.5$  (Fig. 98a). This could be explained by the following. First, at  $X \approx 0.5$  almost all the MEH-PPV conjugated fragments that are able to interact with TNF are involved in the CTC as follows from the absorption saturation of the CTC (see Fig. 97). Second, the thickness of MEH-PPV/TNF films decreases with increasing TNF due to lowering the polymer concentration of in the solution from which the film is formed. To avoid the effect of film thickness, in Fig. 98b, we plot the scattering  $\sigma d$  normalized to the absorption  $\alpha d$  using the data in Fig. 98a.

Fig. 98b shows that for  $X \leq 0.33$  the  $\sigma d / \alpha d$  does not depend on  $X$  within our experimental error. This indicates that the  $\sigma d$  and  $\alpha d$  increase together proportionally to  $X$ . However, for  $X \geq 0.33$  the  $\sigma d / \alpha d$  increases linearly with  $X$ . We assign this growth mainly to the scattering ( $\sigma d$ ) since the normalized absorption is nearly saturated at  $X > 0.33$ , as seen in Fig. 97.

It is important to note that the absorption saturation in Fig. 97 and the threshold for growth of scattering in Fig. 98b occur at the same  $X \approx 0.33$ . This strongly suggests that, for  $X < 0.33$ , the most part of TNF molecules is involved in CT interaction with MEH-PPV, whereas, for  $X > 0.33$ , a noticeable part of TNF molecules gives its own phase. Therefore, our data indicate that one TNF molecule participates in the CT interaction with three MEH-PPV unit cells. TNF molecules added over this ratio (1:0.33) form their own phase observed in light scattering.

We have also measured the scattering and absorption data at wavelengths of 675, 810, and 946 nm. These data are analogous to those shown in Fig. 98. We have found that for each donor-acceptor ratio the magnitude of scattering ( $\sigma d$ ), remains virtually constant over the range 633–946 nm, where the absorption changes more than one order of magnitude. This implies that the light scattering occurs at large-scale inhomogeneities that are of the order or higher than the optical wavelength.

#### 4.2.3.2 MEH-PPV/DNAQ blends

Fig. 99 shows photomicrographs of MEH-PPV/DNAQ blends. It is seen that for the molar acceptor concentration  $X \geq 0.5$  the DNAQ molecules form their own grain-like phase. The typical size of DNAQ species is 20–50  $\mu\text{m}$ , which is approximately an order of magnitude larger than that in MEH-PPV/TNF blends (see Fig. 96). For  $X \leq 0.25$ , no phase separation was observed by optical microscopy in MEH-PPV/DNAQ blends (Fig. 99).

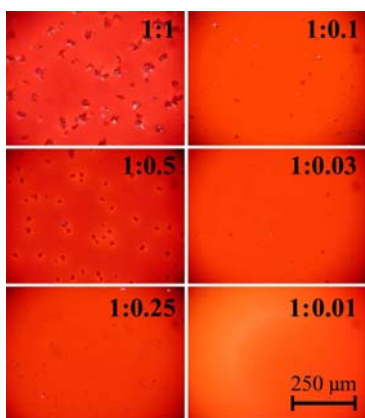


Fig. 99. Photomicrographs of MEH-PPV/DNAQ blends with different D:A ratio. The scale bar is shown in the right bottom corner.

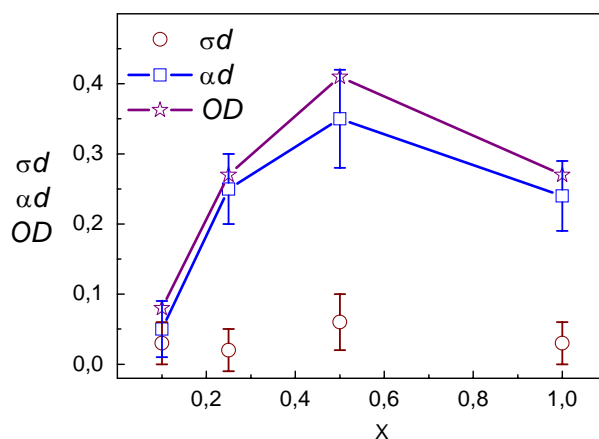


Fig. 100. Absorption ( $\alpha d$ ), scattering ( $\sigma d$ ), and their sum ( $OD$ ) for MEH-PPV/DNAQ blends as a function of D:A ratio (1: $X$ ) at 633 nm. Lines are guide to the eye.

Absorption spectra of the MEH-PPV/DNAQ blends are similar to those of the MEH-PPV/TNF blends (Fig. 97a) and are shown in Fig. 144. The MEH-PPV/DNAQ absorption spectra are also shifted



to the red and show extended absorption tails. However, as seen in Fig. 144, the maximum shift of the MEH-PPV absorption peak in MEH-PPV/DNAQ blends is about 20 nm (0.1 eV) that is 30% less than in the MEH-PPV/TNF blends (see Fig. 97b).

We have measured light scattering and absorption in the MEH-PPV/DNAQ blends at 633 nm for different donor-acceptor ratios. Fig. 100 shows the results. It is seen that the scattering is low and it is within the experimental error. Therefore, the optical density of the MEH-PPV/DNAQ blends at 633 nm is determined mainly by light absorption. We also assign this absorption to the CTC. As Fig. 100 demonstrates, for  $X < 0.5$ , the absorption increases monotonically with  $X$  indicating that the DNAQ molecules are involved in the CT interaction. For  $X > 0.5$ , the absorption drops that we attribute to saturation of MEH-PPV species involved in the CT interaction and to decrease in the film thickness. The similar behavior at high  $X$  was also observed for MEH-PPV/TNF blends (see above).

The light scattering in MEH-PPV/DNAQ blends is considerably lower than in MEH-PPV/TNF blends. This could be explained in the following way. Excess DNAQ molecules that are not involved in the CT interaction with MEH-PPV form larger and rarer species than those of TNF (cf. Fig. 96 and Fig. 99). This should result in less scattering in MEH-PPV/DNAQ blends than in MEH-PPV/TNF blends since, for both acceptors, the typical size of the acceptor species is larger than the optical wavelength.

#### **4.2.3.3 Conclusion**

We have found that the amount of scattered light in MEH-PPV/TNF blends does not depend smoothly on the TNF content. At the molar content of TNF below 0.33, the light scattering is low and depends on the TNF content only weakly, whereas the CTC absorption increases. At higher acceptor concentration, the scattered light begins to grow dramatically. We assign this growth to phase separation in the film owing to excess acceptor molecules that are not involved in the CT interaction with the donor. In MEH-PPV/DNAQ blends, the light scattering is within the experimental error for all the donor-acceptor ratios. We attribute this to the fact that the excess DNAQ molecules form phase separated species with size of 20–50  $\mu\text{m}$ . These DNAQ species seem too big to contribute noticeably to the measured light scattering. Thus, the CT interaction in the ground state of donor-acceptor polymer blends can influence phase separation and possibly could be used as a factor controlling it.

#### **4.2.4 Raman studies of blends with different MEH-PPV/acceptor ratio**

As an intermolecular CTC is formed in blends of MEH-PPV with a number of acceptors, it is important to find the maximum concentration of the complexed MEH-PPV in the films. As follows from our light scattering (see Sec. 4.2.3) and DSC (see Sec. 4.2.2.1) studies, the uncomplexed acceptor in the donor/acceptor blends gives its own phase. To find an optimal donor/acceptor ratio, we have studied MEH-PPV/acceptor blends with various donor/acceptor molar ratios (Sec. 4.2.3 and 4.2.2.1). Here we report on these studies using Raman spectroscopy. We used near-IR (1064 nm) and red (670 nm) Raman excitation initially expecting to realize either non-resonant or resonant excitation of the CTC, respectively. However, hardly Raman excitation at 1064 nm corresponds to the non-resonant conditions since the CTC absorption extends deeply in the optical gap of the polymer. In fact, as follows from our surface photovoltage studies (see Sec. 4.3.3, Fig. 127), the CTC absorption starts at  $\approx 1100$  nm indicating noticeable absorption. We have not managed to measure the absorption coefficient of the CTC below 1.5 eV, which we can only estimate as at least one order of magnitude less than at 670 nm. Because of this, it is more correct to refer the near-IR Raman excitation to weakly resonant, and the red one to strongly resonant. Note that for both we have observed very similar Raman spectra characteristic of MEH-PPV indicating that the strongly resonant CTC excitation gives neither any noticeable change in the relative Raman intensities nor new additional bands that could be associated with namely the CTC and not with the pristine polymer.

#### 4.2.4.1 MEH-PPV/TNF blends

As shown above in Sec. 4.1.1.2, the Raman strongest band of MEH-PPV at  $1582\text{ cm}^{-1}$  is red shifted in the MEH-PPV/TNF CTC (Fig. 73). Fig. 101 shows the Raman frequency of this band as a function of MEH-PPV/TNF molar ratio for near-IR (left) and red (right) excitation, respectively. It is seen that the maximum red shifts are about  $3\text{--}4\text{ cm}^{-1}$  and saturate at TNF mole fractions higher than 1:0.4. This ratio is correlated with that obtained from our light scattering studies (Sec. 4.2.3).

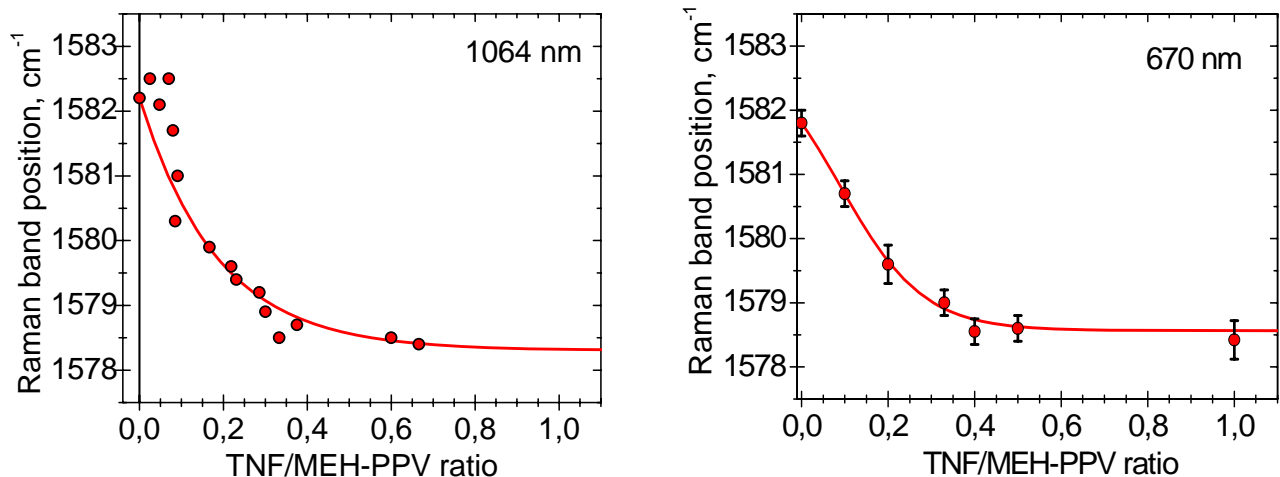


Fig. 101 Maximum of the  $1582\text{ cm}^{-1}$  band in MEH-PPV/TNF films vs. acceptor/donor molar ratio for excitation at 1064 nm (left) and 670 nm (right). The lines are guides to the eye.

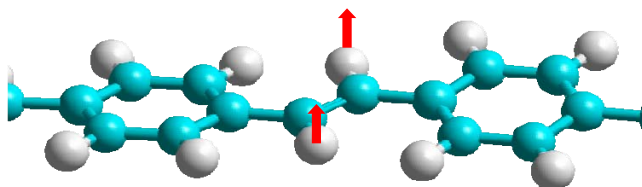


Fig. 102. Schematic representation of the  $966\text{ cm}^{-1}$  vibration in the planar PPV chain of  $C_{2h}$  symmetry. This vibration is active in the IR spectra but forbidden in the Raman ones.

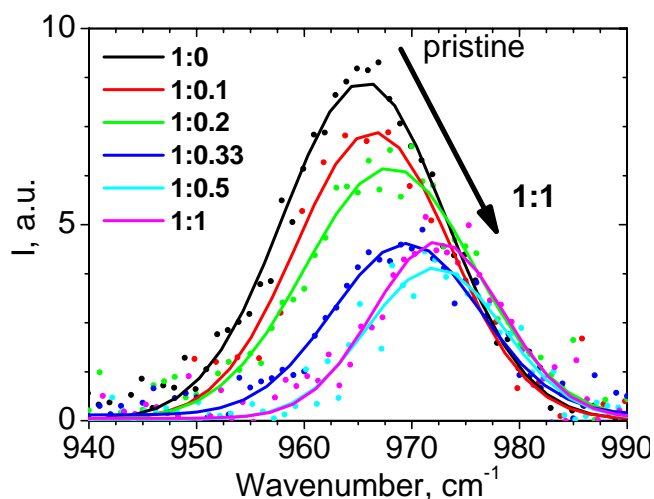


Fig. 103. Raman spectra of the  $966\text{ cm}^{-1}$  band in MEH-PPV/TNF blends with various donor/acceptor molar ratios indicated in the figure. The spectra are normalized to the intensity of the  $1582\text{ cm}^{-1}$  band. The excitation wavelength is 670 nm.

We have found that the MEH-PPV band at  $966\text{ cm}^{-1}$  is changed in frequency and intensity upon adding TNF. Fig. 102 schematically depicts this vibration corresponding to out-of-plane wag of vinylene CH. Fig. 103 plots Raman spectra of the  $966\text{ cm}^{-1}$  band recorded at 670 nm in blended films

with various donor/acceptor molar ratios. Note that this band shows a blue shift that monotonically depends on the TNF content reaching  $\approx 6 \text{ cm}^{-1}$ . Such a shift of the  $966 \text{ cm}^{-1}$  band was also observed in the IR transmission spectra of the blends (see Fig. 44 and Table 6). Note that this is the only Raman band observed demonstrating a clear dependence in intensity. Indeed, other Raman bands of MEH-PPV shown in Fig. 43 did not show any changes in the relative intensities upon blending with TNF or DNAQ. Fig. 104 plots the frequency of the  $966 \text{ cm}^{-1}$  band versus the TNF molar fraction in MEH-PPV/TNF films for excitation at  $1064 \text{ nm}$ . It is clearly seen that the shift in the CTC saturates at the MEH-PPV/TNF ratio 1:0.4 as was also observed for the  $1582 \text{ cm}^{-1}$  band (Fig. 101). Essentially that the same behavior of the  $966 \text{ cm}^{-1}$  band was observed in MEH-PPV/TNF solutions (Fig. 105) suggesting that this is an intrinsic property of the CTC. Interpretation of the Raman data on the  $966 \text{ cm}^{-1}$  band is given below in Sec. 4.2.5.2.

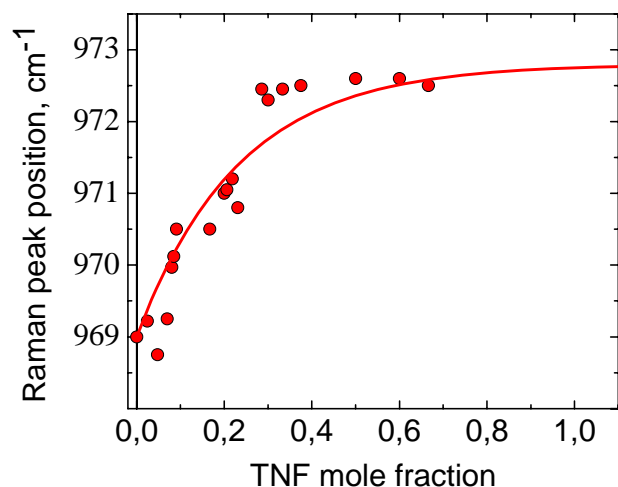


Fig. 104. Maximum of the  $966 \text{ cm}^{-1}$  Raman band vs mole fraction of TNF in MEH-PPV/TNF blends. The excitation wavelength is  $1064 \text{ nm}$ . The line is a guide to the eye.

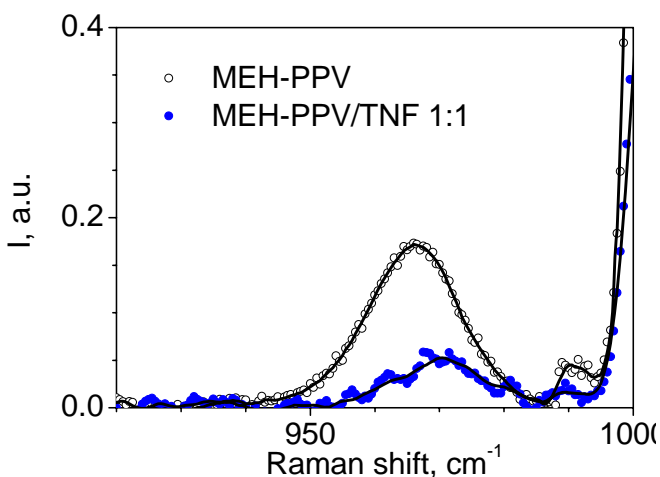


Fig. 105. Raman spectra of the  $966 \text{ cm}^{-1}$  band in 1:1 MEH-PPV/TNF and pristine MEH-PPV solutions. The concentration was  $2.5 \text{ g/l}$  for the each component. The spectra are normalized to the intensity of the  $1582 \text{ cm}^{-1}$  band. Excitation wavelength is  $670 \text{ nm}$ . An intensive band at  $\sim 1000 \text{ cm}^{-1}$  is of the solvent.

#### 4.2.4.2 MEH-PPV/DNAQ blends

We have observed a red shift of the  $1582 \text{ cm}^{-1}$  band of MEH-PPV in MEH-PPV/DNAQ blends as well. Fig. 106 shows that the maximum red shift is somewhat less ( $\sim 2 \text{ cm}^{-1}$ ) than in the MEH-PPV/TNF films. Note that the sub-gap absorption is less intensive in MEH-PPV/DNAQ films than in MEH-PPV/TNF films (see Fig. 71). We assign this fact to the lesser degree of ground-state CT in MEH-PPV/DNAQ blends. As follows from Fig. 106, the red shift in the MEH-PPV/DNAQ films saturates at MEH-PPV:DNAQ ratio 1:0.4 as in the case of MEH-PPV/TNF blends. Again, this ratio is supported by our absorption data (see Fig. 100 in Sec. 4.2.3.2).

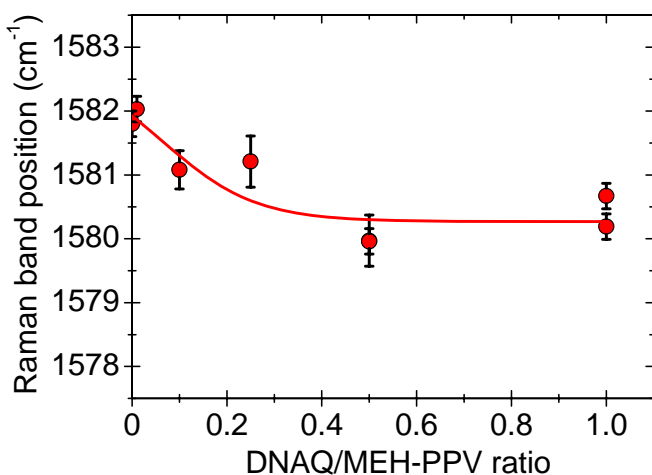


Fig. 106. The maximum of the 1582 cm<sup>-1</sup> band in MEH-PPV/DNAQ films vs acceptor/donor molar ratio. The line is a guide to the eye. The data were recorded for Raman excitation at 670 nm.

## 4.2.5 How are MEH-PPV properties changed in its CTC?

### 4.2.5.1 Optical absorption shift

As we noted in Sec. 4.1.1.1, the absorption spectrum of the 1:1 MEH-PPV/TNF film demonstrates a 0.2 eV red shift of the whole MEH-PPV absorption band (Fig. 71). This shift monotonically increases upon adding TNF to MEH-PPV saturating at the TNF molar content 0.4 (Fig. 97). Similar red shifts were observed in MEH-PPV/DNAQ films (Fig. 71 and Fig. 144), but the maximum shift was half of that in MEH-PPV/TNF amounting 0.1 eV. Remarkably that this red shift of the whole absorption spectrum was observed only in the films, whereas the solutions do not show any shift at all (Fig. 78). Therefore, the red shift of the MEH-PPV absorption band in the blended films is not a direct consequence of the ground-state CT. Below we discuss possible reasons of this red shift.

We suggest two possible reasons explaining the observed red shift. First, the longer the conjugated chain length, the lower its bandgap is. This is a well known fact for conjugated molecules and polymers. For oligo(p-phenylene vinylene)s, the bandgap energy  $E$  depends on the effective number of PPV conjugated monomer units  $N$  as [15]:

$$E \approx 2.5\text{eV} + 2.7\text{eV}/N. \quad (1)$$

$N$  is typically estimated as the length of 5–6 conjugated unit cells for PPV-type polymers. According to this  $E(N)$  dependence, the red shift in absorption (Fig. 71) would mean that the MEH-PPV conjugated length in the CTC increases in the film but not in the solution. Second, the absorption red shift in the CTC films could stem from a difference in the interchain interaction in the pristine polymer and in the polymer involved in the CTC. This can result in the different effective dielectric constants for the pristine polymer and the CTC due to local field effects.

### 4.2.5.2 Changes in vibrational spectra

Fig. 107 compares Raman spectra of MEH-PPV/TNF and MEH-PPV films in the range of the 1582 cm<sup>-1</sup> band recorded at 670 nm. Fig. 79 compares the corresponding spectra in solution. The spectra in Fig. 107 and Fig. 79 were recorded using the same experimental conditions. The Raman spectra show similar red shifts both in the film and the solution (cf. Fig. 79 and Fig. 107). The difference in the Raman band position between the film and the solution is assigned to different effective dielectric constants in them. On the other hand, the shift between the blend and the pristine polymer was assigned to the ground-state CT (see Sec. 4.1). Therefore, the following two changes in spectra are very similar in films and solutions: the appearance of the absorption tail and the red shift of the Raman 1582 cm<sup>-1</sup> band. However, the shift of the MEH-PPV absorption band in the CTC is a unique feature for the films.

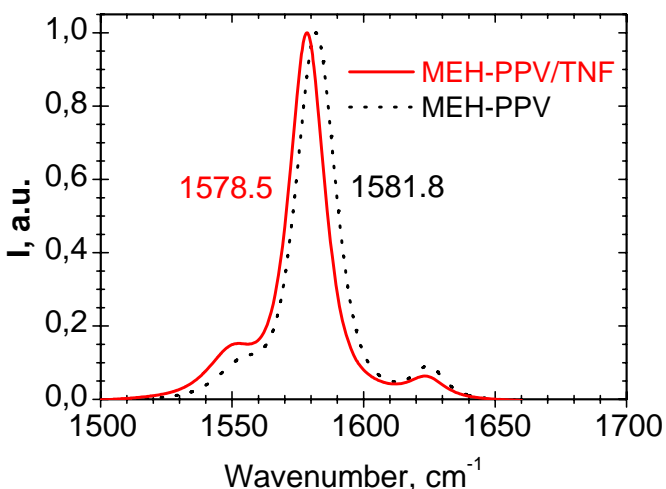


Fig. 107. Raman spectra of pristine MEH-PPV (dotted) and 1:1 MEH-PPV/TNF (solid) drop-cast films. The Raman excitation wavelength is 670 nm.

Another characteristic change in the Raman spectra of MEH-PPV/TNF blends is a blue shift and decrease in intensity of the band at  $966\text{ cm}^{-1}$  upon adding TNF to MEH-PPV (see Fig. 103, Fig. 104, and Fig. 105). This vibration is symmetrically forbidden in the Raman spectrum for the planar conformation of the MEH-PPV chain (Fig. 102). However, the  $966\text{ cm}^{-1}$  band of pristine MEH-PPV is clearly observed in the Raman spectra both in the solution (Fig. 103) and the film (Fig. 105). This indicates that the conformation of MEH-PPV chains is not planar. The non-planar conformation is also supported by the AFM data on MEH-PPV films [16] showing that MEH-PPV tends to form a spiral structure. Decreasing the  $966\text{ cm}^{-1}$  band intensity (see Fig. 103, Fig. 104, and Fig. 105) in the CTC suggests that the MEH-PPV chains become more planar in the CTC. This planarization might be a result of partial electron transfer from the HOMO of the polymer. In fact, it is generally accepted that the quinoid configuration is characteristic of the lowest excited state of the PPV-type conjugated chain in which an electron moves from the HOMO to the LUMO. The blue shift of the  $966\text{ cm}^{-1}$  vibration points to its different force constant characterizing a new equilibrium conformation of the MEH-PPV chain in the CTC. On the other hand, if a conjugated chain becomes more planar, one might expect increasing its conjugated length.

It is known that the conjugation length could influence the depolarization ratio of Raman bands corresponding to the conjugated backbone. We have measured the depolarization of the  $1582\text{ cm}^{-1}$  Raman band in solutions of 1:1 MEH-PPV/TNF and pristine MEH-PPV. Table 9 summarizes the results. It is seen that the depolarization ratio is reduced by 5% in the blend relative to the pristine MEH-PPV. The observed change in the depolarization is essentially higher than the experimental error ( $<1\%$ ) (Table 9). The details of the technique and the measurement procedure are described in [T.Sh. Makhmutov, M.Sc. thesis, MSU, 2005]. Note that the depolarization of pristine MEH-PPV does not depend on concentration of the components in solution (Table 9).

Sample,	Concentration, g/l	Frequency, $\text{cm}^{-1}$	Depolarization ratio
MEH-PPV	5	1584.8	$0.443 \pm 0.001$
MEH-PPV	2.5	1584.7	$0.446 \pm 0.004$
MEH-PPV/TNF	2.5/2.5	1579.7	$0.422 \pm 0.002$

Table 9. Depolarization ratio of the  $1582\text{ cm}^{-1}$  Raman band in MEH-PPV/TNF and pristine MEH-PPV solutions in chlorobenzene. The data were measured at Raman excitation wavelength 670 nm.

The observed depolarization decrease in the blend could be explained by an increase in the conjugated length by  $\sim 15\%$  [*Ibidem*]. At the same time, this increase should result in a noticeable red shift of the MEH-PPV absorption edge according to Eq. (1). However, we have not observed any shift in absorption of the MEH-PPV/TNF solution (Fig. 78). Therefore, the suggested increase in the MEH-PPV conjugation length does not explain the observed decrease of the depolarization ratio in the CTC. Other explanations of the latter might be as follows. For example, one can suppose that MEH-PPV chains involved in the CTC could be planarized without affecting their conjugation length. On the other hand, the depolarization could decrease due to a change in the components of the Raman scattering tensor characteristic of the Raman active chains. Analysis of these possibilities is beyond the scope of this project.

#### 4.2.5.3 Discussion

Table 10 summarizes the characteristic changes of observed MEH-PPV prosperities in the MEH-PPV/TNF CTC. They are as follows: (i) appearance of the CTC absorption band; (ii) red shift of the polymer absorption band; (iii) red shift of the Raman  $1582\text{ cm}^{-1}$  band; (iv) blue shift and decrease of the  $966\text{ cm}^{-1}$  Raman band; (v) decrease in the depolarization ratio. While the changes (i, iii, iv) are observed in both the films and the solutions, the change (ii) is observed only in the films. As mentioned above, the absorption band shift in films could result from increasing the conjugation length. In this case, it should increase by  $\sim 1\%$  for a red shift of  $0.15\text{ eV}$  according to Eq.(1). Therefore, we should expect different Raman shifts in the solution and the film. This difference in shifts is expected to be about  $2\text{ cm}^{-1}$  in the  $1582\text{ cm}^{-1}$  band corresponding to the  $0.15\text{ eV}$  shift in the absorption band [17]. As a result, we would observe a  $2\text{ cm}^{-1}$  larger red shift in the film. On the contrary, the observed Raman shifts are almost the same in the film and the solution. Accordingly, the suggestion of increasing the conjugated length in the CTC is not consistent with our observations. Because of this, we have to assign the absorption band shift of the MEH-PPV in the CTC to a increase in the effective dielectric constant,  $\epsilon$ . This increase is expected to occur mainly in films due to noticeably stronger interaction of a given chain with its local environment in film than in solution. In the latter, the local environment includes polymer chains, acceptor and solvent molecules, whereas, in the former, it includes only polymer chains and acceptor molecules. Consequently, the local environment is expected to be more polarizable in films due to essentially higher polarizability of conjugated chains. This should result in higher  $\epsilon$  in films. This hypothesis is in accordance with our suggestion that the MEH-PPV chains are more planar in the CTC permitting them to pack denser and hence to have a higher  $\epsilon$  as compared with pristine MEH-PPV chains. Thus, we conclude that conformation of MEH-PPV conjugated chains is noticeably changed in the CTC both in solutions and films. We suggest that the polymer chains become more planar in the CTC that might possibly result in their denser packing in films. At the same time, the polymer conjugation length probably does not change in the CTC. To arrive at more definite conclusions, further studies are necessary.

Observed change	Solution	Film
CTC absorption band	Yes	Yes
Shift in MEH-PPV absorption, eV	No	-0.2
$1582\text{ cm}^{-1}$ band frequency, $\text{cm}^{-1}$	-5	-4
$966\text{ cm}^{-1}$ band frequency, $\text{cm}^{-1}$	+6	+6
$966\text{ cm}^{-1}$ band intensity, %	-50	-50
Depolarization ratio, %	-5	Not available

Table 10. Changes in observable characteristics of the MEH-PPV/TNF CTC referenced to those of the pristine MEH-PPV.



### 4.2.6 Summary

Our optical absorption/scattering data, thermal analysis, and vibrational spectroscopy studies strongly suggest that ground-state CT interaction facilitates fine dispersion of the acceptor in the polymer matrix counteracting phase separating the blend components.

Using vibrational spectroscopy, we have found evidence that conformation of MEH-PPV conjugated chains is noticeably changed in the CTC both in solutions and films. Our data suggest that the polymer chains become more planar in the CTC that might possibly result in their denser packing in films. At the same time, the polymer conjugation length hardly changes in the CTC.

## 4.3 Photoexcited states in donor-acceptor blends with ground-state CT interaction

### 4.3.1 Photoluminescence

To study the potential of polymer CTCs for solar cells, the properties of the CTC photoexcited states should be investigated. First of all, we performed PL studies of MEH-PPV/TNF and MEH-PPV/DNAQ donor-acceptor blends with various donor/acceptor ratios. PL of MEH-PPV photoexcited at 532 nm is completely quenched (i.e. the PL signal drops by at least three orders of magnitude) in either MEH-PPV/TNF or MEH-PPV/DNAQ films with donor-acceptor molar ratio 1:1. The experimental details are given in Sec. 2.6.

#### 4.3.1.1 MEH-PPV/TNF and MEH-PPV/DNAQ films

Fig. 108 shows PL quenching in MEH-PPV/TNF films. It is seen that the PL spectra in the blends do not change their shape corresponding to that of the pristine MEH-PPV (Fig. 108 left). This suggests that the photoexcited MEH-PPV/TNF CTC relaxes only non-radiatively. Fig. 108 (right) compares PL quenching in MEH-PPV/TNF and MEH-PPV/C<sub>60</sub> blends. It is seen that for acceptor concentration 1% and below both the quenching curves are very close indicating that TNF is as strong as C<sub>60</sub> in quenching MEH-PPV PL. Remarkably that the TNF quenching curve at acceptor concentration more than 3% is dramatically steeper than that of C<sub>60</sub> as seen in Fig. 108 (right). We relate this difference

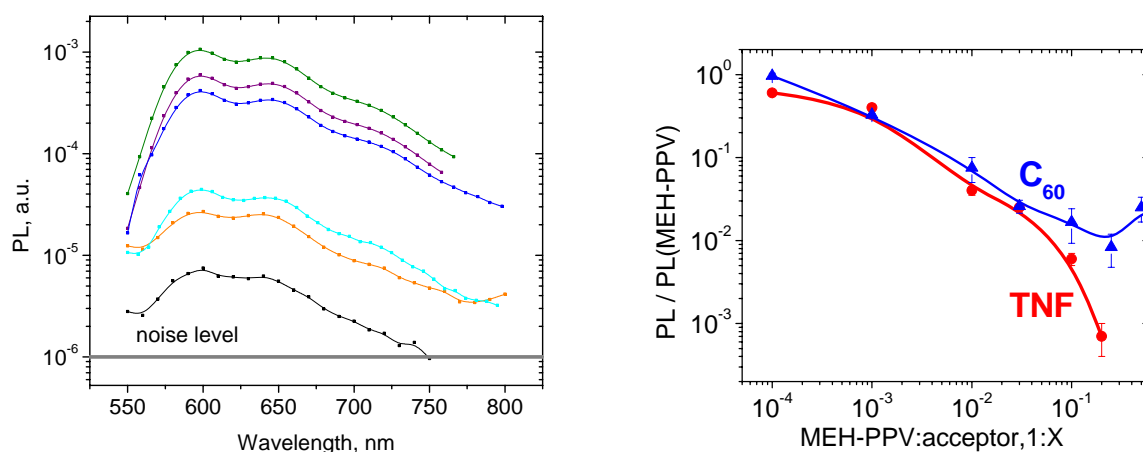


Fig. 108. PL quenching in MEH-PPV/TNF films drop-cast from chlorobenzene. Left: PL spectra for TNF concentration 0 (pristine MEH-PPV), 0.0001, 0.001, 0.01, 0.03, 0.1 (from top to bottom). The PL for the 1:0.2 MEH-PPV/TNF blend was within the noise level. Right: The corresponding peak intensities averaged on a few points on the sample, the data are normalized to the PL of pristine MEH-PPV. The PL quenching data for MEH-PPV/C<sub>60</sub> blends drop-cast from chlorobenzene are also shown. The lines are guide to the eye.

to aggregation of  $C_{60}$  resulting in very inhomogeneous distribution of  $C_{60}$  in the MEH-PPV matrix (see Sec.4.6). Moreover, this difference could be an illustration how CTC can help the acceptor being dispersed homogeneously in the polymer matrix. Note that for TNF concentration 20% and higher, the PL was quenched by at least three orders of magnitude and was below the noise level.

Fig. 109 presents PL quenching data in MEH-PPV/DNAQ blends. Again, the PL spectra in the blends reproduce that of the pristine MEH-PPV (Fig. 109 left) implying non-radiative relaxation of the photoexcited MEH-PPV/DNAQ CTC. Notably, that in the 1:0.01 blends the quenching efficiency is the same for both acceptors as seen in Fig. 109 (right). This suggests that the acceptor electron affinity is not a key parameter determining the PL quenching. However, as Fig. 109 (right) demonstrates, TNF is a more efficient quencher than DNAQ at acceptor concentration higher than 0.01. This difference could be assigned to more enhanced phase separation in the MEH-PPV/DNAQ blends than in the MEH-PPV/TNF ones. In fact, comparing the microphotographs in Fig. 96 and Fig. 99, it is seen that TNF species form smaller clusters in the blends, and therefore they are better dispersed in the MEH-PPV matrix than DNAQ ones. As a result, a more homogeneous distribution of quenching centers in MEH-PPV/TNF blends can result in a higher quenching efficiency.

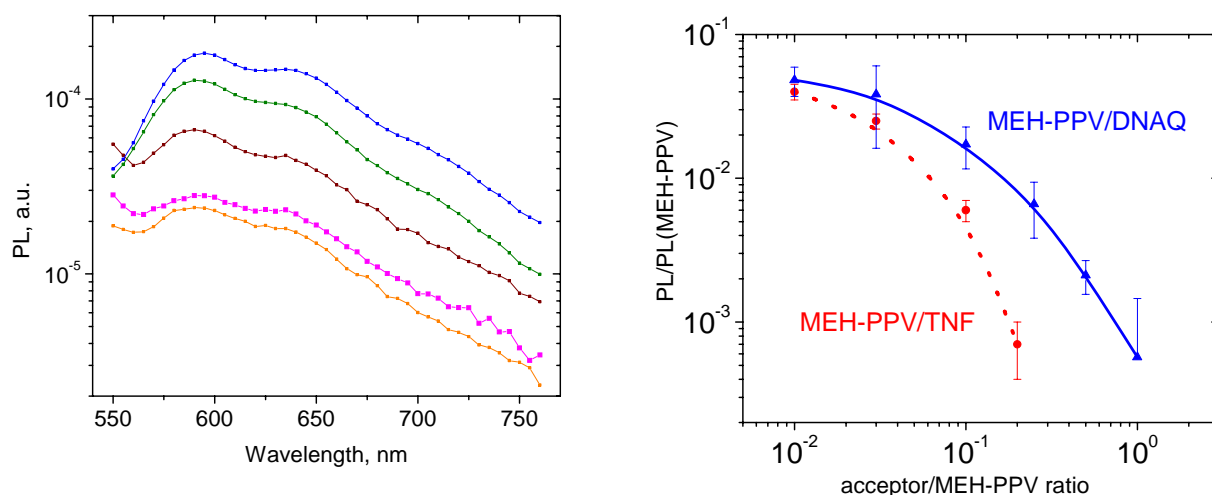


Fig. 109. PL quenching in MEH-PPV/DNAQ films drop-cast chlorobenzene. Left: Typical PL spectra for acceptor concentration 0.01, 0.03, 0.1, 0.25, and 0.5 (from top to bottom). Right: The peak PL intensity averaged on a few points for each sample and on the two different sample sets. The quenching data for MEH-PPV/TNF blends from Fig. 108 (right) are shown for comparison. The lines are guides to the eye.

#### 4.3.1.2 MEH-PPV/TNF solutions

We have observed that TNF is a strong quencher of MEH-PPV PL in solution as well. Fig. 110 shows PL quenching data in MEH-PPV/TNF solutions. As in the films, the PL spectra are almost invariable upon increasing the acceptor concentration. The quenching curve in Fig. 110 (right) could be used to evaluate the Stern-Volmer constant. Study of the temperature behavior of PL quenching could give the answer about the dynamic or static quenching mechanism to clarify the role of the CTC in PL quenching. However, we postponed a detailed study of PL quenching in solutions and concentrated our further work on films.

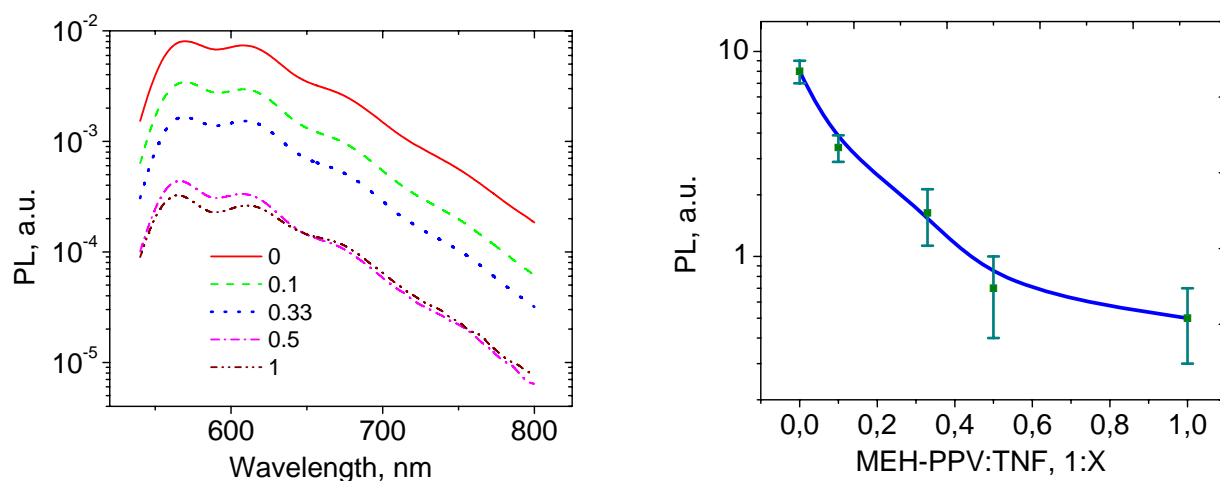


Fig. 110. PL quenching data in MEH-PPV/TNF chlorobenzene solution. Left: PL spectra; Right: the peak PL vs TNF:MEH-PPV molar ratio. The solution studied was a mixture of MEH-PPV solution (2 g/l) and TNF solution (2 g/l) with TNF:MEH-PPV molar ratio indicated in the left figure. The line in the right figure is a guide to the eye.

#### 4.3.1.3 Discussion

Our PL data show that both TNF and DNAQ are very efficient quenchers of MEH-PPV PL. The quenching efficiency at a few mol. % of acceptor is about that of  $C_{60}$ . Such a strong quenching efficiency suggests that the MEH-PPV singlet exciton disappears very fast after photoexcitation (probably within 100 fs). PL quenching in organic donor-acceptor blends upon photoexcitation of the donor (acceptor) is usually indicative of either energy or charge transfer from the donor to the acceptor (from the acceptor to the donor). Since the optical gap of the DNAQ and TNF is higher than 3 eV, their optical absorption spectra do not overlap with the MEH-PPV emission spectrum. Therefore, Forster energy transfer from the MEH-PPV to the acceptor can not be a reason for PL quenching. On the other hand, the MEH-PPV/acceptor CTC has a noticeable absorption in the optical gap of MEH-PPV, and hence the CTC could be an efficient energy funnel accumulating the MEH-PPV excitons via Forster energy transfer. Another possible mechanism of PL quenching could be photoinduced electron transfer from the MEH-PPV to the acceptor. The detailed analysis of the PL quenching data is out of the scope of this project.

Note that the measured PL quenching curves should be fitted by a model considering both the energy and the charge transfer. In addition, such a model should take into account acceptor aggregation that could be done by comparing the PL quenching data in films and solutions. After that a more substantial analysis of the quenching mechanisms in donor-acceptor blends with ground-state CTC will be possible.

#### 4.3.2 Photoinduced absorption spectroscopy

As follows from our PL study of the photoexcited states in MEH-PPV/TNF and MEH-PPV/DNAQ, these states relax non-radiatively. It is naturally to suggest that CTC excited states in the MEH-PPV optical gap play an essential role in relaxation of initial photoexcitations. We were interested in those that correspond to photoexcited either the MEH-PPV or the CTC. The issues addressed to photoinduced absorption (PIA) spectroscopy were determining the photoexcitation efficiency of long-lived charges and their lifetime.

We have done the most detailed PIA studies for MEH-PPV/TNF blends as the CTC in these blends is more pronounced than in MEH-PPV/DNAQ blends. As well-studied reference samples, we used MEH-PPV/C<sub>60</sub> and pristine MEH-PPV films. The details of our PIA technique are given in Sec. 2.8. The following three sections present visible and near-IR data recorded with pump modulation frequency in the range 5–2000 Hz (Sec. 2.8.1), and the last section reports on mid-IR data with pump modulation frequency at 1/64 or 1/32 Hz (Sec. 2.8.2).

#### 4.3.2.1 Identification of polaron states

Fig. 111 compares typical PIA spectra of MEH-PPV/TNF, MEH-PPV/C<sub>60</sub>, and pristine MEH-PPV films recorded at 100 K. It is seen that the most intensive PIA is observed in the range 1.1–1.4 eV for all the samples. A considerable increase of PIA in the MEH-PPV/C<sub>60</sub> blend compared with the pristine MEH-PPV is usually assigned to efficient photoinduced charge separation in the blend. In pristine MEH-PPV, the most intensive band is located at 1.35 eV, which is commonly assigned to triplet states. The PIA spectrum of the MEH-PPV/TNF blend is dominated by the band at 1.2 eV coinciding in shape with the low-frequency part of the band observed in the MEH-PPV/C<sub>60</sub> blend (Fig. 111, left). Moreover, the feature at 1.2 eV is clearly seen in all the three samples suggesting that it has the same origin. We assign this band in MEH-PPV/TNF to charged species at the MEH-PPV chains (polarons). This assignment is supported by frequency and temperature dependencies of PIA at 1.2 eV given below. In the MEH-PPV/C<sub>60</sub> blend, the PIA signals are the most intensive peaking at 1.2 and 1.35 eV with nearly the same intensity. These peaks are assigned to 0-0 and 0-1 vibrational sublevels of the polaron band [18]. In the MEH-PPV/C<sub>60</sub> blend, we also observed a wide PIA shoulder prolonging to the MEH-PPV absorption edge. This feature could be assigned to electroabsorption due to photoinduced charged excitations [18].

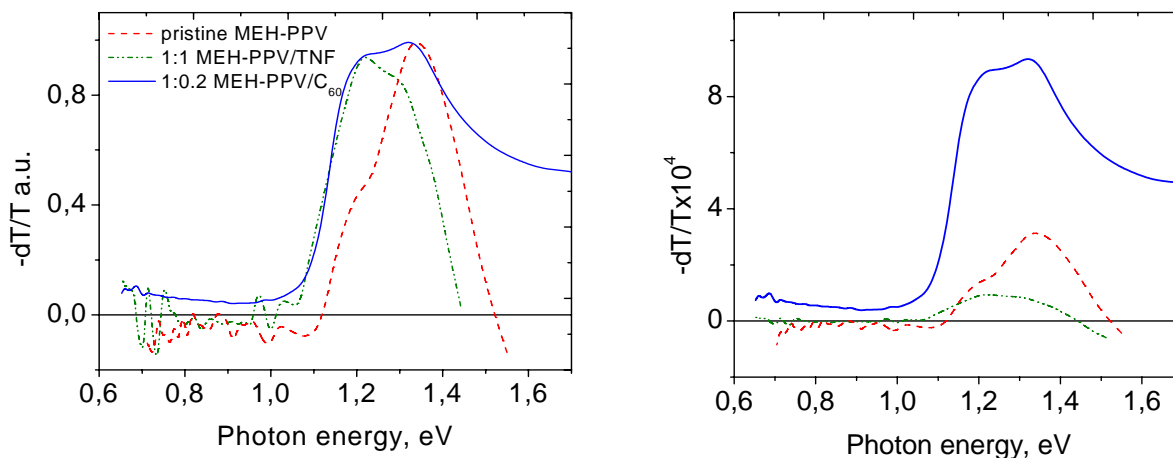


Fig. 111. Normalized (left) and in-scale (right) PIA spectra for pristine MEH-PPV, 1:1 MEH-PPV/TNF, and 1:0.2 MEH-PPV/C<sub>60</sub> blends recorded at  $T=100$  K for pump at 532 nm chopped at 75 Hz with intensity  $\approx 600$  mW/cm<sup>2</sup>. The pristine MEH-PPV and MEH-PPV/C<sub>60</sub> films were drop-cast from toluene, and the MEH-PPV/TNF film was drop-cast from cyclohexanone.

More definite assignment of the observed PIA bands can be made from their frequency and temperature dependences. Fig. 112, Fig. 113 and Fig. 114 compare these dependences for MEH-PPV/TNF, MEH-PPV/C<sub>60</sub>, and pristine MEH-PPV. These dependences were measured in maximums of the PIA spectrum for each sample. The frequency dependence for the pristine MEH-PPV exactly follows the monomolecular recombination kinetics (Fig. 112) with a decay time of 15  $\mu$ s at 100 K. Moreover, the PIA signal in pristine PPV has strong temperature dependence different from those of the blends (Fig. 114). These frequency and temperature dependencies of the PIA at 1.35 eV for pristine MEH-PPV are usually considered as signatures of neutral states, namely triplet excitons. The

shoulder at 1.2 eV in the pristine MEH-PPV spectrum (Fig. 111) polymer is reasonably to assign to charged states appearing at defects. In fact, addition of  $C_{60}$  enhances this feature as seen in Fig. 111 (right). In the MEH-PPV/ $C_{60}$  blend, both the 1.2 and 1.35 eV bands demonstrate the same frequency dependence different from that of the triplet states (Fig. 112). Also, the temperature dependencies in the pristine MEH-PPV and MEH-PPV/ $C_{60}$  are different as seen in Fig. 114. These observations are commonly considered as characteristics allowing assignment of the 1.2 and 1.35 eV bands in MEH-PPV/ $C_{60}$  to MEH-PPV polaron states.

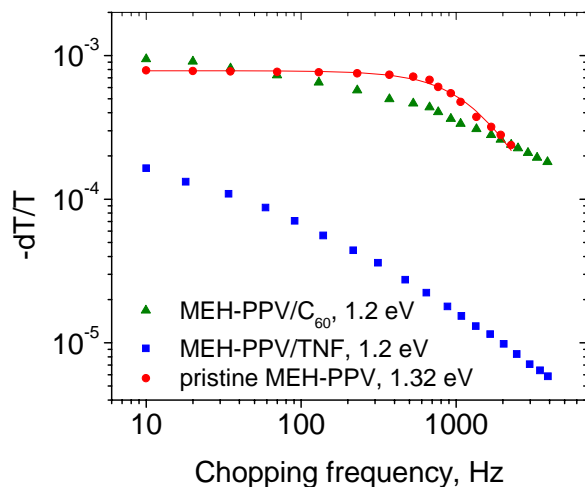


Fig. 112. Frequency dependence of PIA bands at 1.2 and 1.32 eV for the samples and conditions indicated in Fig. 111. The solid line shows a monomolecular kinetics fit.

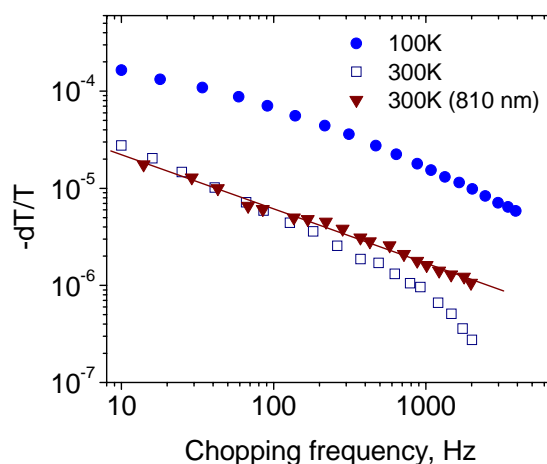


Fig. 113. The same as in Fig. 112 but only for the PPV/TNF blend. The data were recorded at 100 and 300 K for pump wavelengths 532 and 810 nm. The line is a power-law fit with exponent 0.55.

The frequency dependence for the MEH-PPV/TNF blend in Fig. 112 is close to a power function and is similar to that observed in MEH-PPV/ $C_{60}$  blend. Such an approximately power dependence was also observed in the MEH-PPV/TNF blend at different temperatures and pump wavelengths (Fig. 113). As Fig. 114 shows, the temperature dependencies for the 1.2 eV band in the MEH-PPV/TNF and MEH-PPV/ $C_{60}$  blends are close in the range 100–180 K and are different from that of pristine MEH-PPV.

Fig. 115 demonstrates PIA dependencies on pump intensity. These dependencies are very similar for all the three types of films implying that the density of photoexcitations probed by PIA spectroscopy is driven by the same mechanism.

The initial photoexcitation in MEH-PPV/ $C_{60}$  blends, i.e., an exciton, is generally accepted to dissociate quickly into a pair of positive and negative charges localized at the MEH-PPV and  $C_{60}$ , correspondingly. In other words, efficient photoinduced charge transfer occurs. The observed similarities of PIA features (i.e. the spectra, the temperature and frequency dependencies) in the MEH-PPV/TNF and MEH-PPV/ $C_{60}$  blends strongly suggest that photoinduced charge transfer takes place in MEH-PPV/TNF films as well.

However, the PIA intensity in the MEH-PPV/TNF blend is one order of magnitude less than in the MEH-PPV/ $C_{60}$  blend (Fig. 111, right) indicating that, in the former, the initial charge generation is less efficient or/and the charge recombination is more efficient than in the latter. Note that the PIA intensities of polarons at 1.2 eV are very similar in the MEH-PPV/TNF blend and the pristine MEH-PPV (Fig. 111, right) implying that TNF does not help in generation of long-lived charges as compared with pristine MEH-PPV. On the other hand, the PL quenching efficiency of TNF is no less than that of  $C_{60}$  as seen in Fig. 108. Therefore, we conclude that recombination of photoinduced

charges is responsible for the lower density of separated charges in the MEH-PPV/TNF blends. It is reasonable to suggest that the geminate recombination limits the charge generation efficiency in the CTC as the initial charge separation can be very high in it.

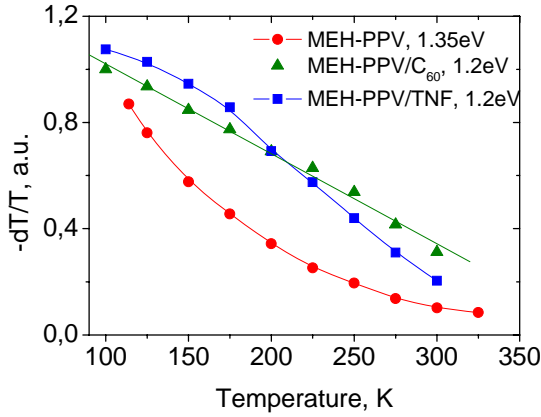


Fig. 114. Temperature dependencies of the PIA bands for the samples and conditions indicated in Fig. 111. The lines are guides to the eye.

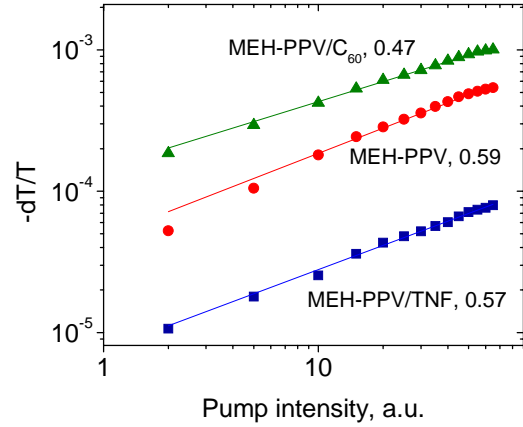


Fig. 115. Pump intensity dependencies of the PIA bands indicated in Fig. 114 for the samples and conditions described in Fig. 111,  $T=115$  K. Solid lines are power-law fits with exponents indicated in the figure.

We have found that the PIA features in MEH-PPV/TNF and MEH-PPV/DNAQ blends are very similar. Fig. 116, Fig. 117, and Fig. 118 compare the corresponding PIA data measured at pump wavelength 532 nm. These data strongly suggest that the charge generation mechanism is the same in MEH-PPV/TNF and MEH-PPV/DNAQ blends. A difference in the PIA spectra in Fig. 116 at probe energies higher than 1.4 eV could be assigned to the effect of absorption tail, which is essentially longer for MEH-PPV/TNF blends. Indeed, bleaching the CTC excited states below the MEH-PPV absorption edge could be responsible for a negative contribution to the PIA spectrum. Note that this negative contribution is absent in the MEH-PPV/ $C_{60}$  blend (Fig. 111).

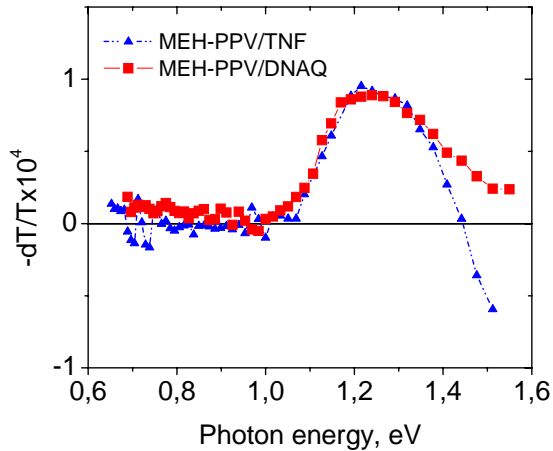


Fig. 116. PIA spectra of 1:1 MEH-PPV/DNAQ and 1:1 MEH-PPV/TNF (from Fig. 111) films prepared from cyclohexanone and chlorobenzene, respectively. The MEH-PPV/DNAQ spectrum was recorded at 110 K, pump intensity  $\approx 0.83$  W/cm<sup>2</sup> at 532 nm and chopping frequency 75 Hz.

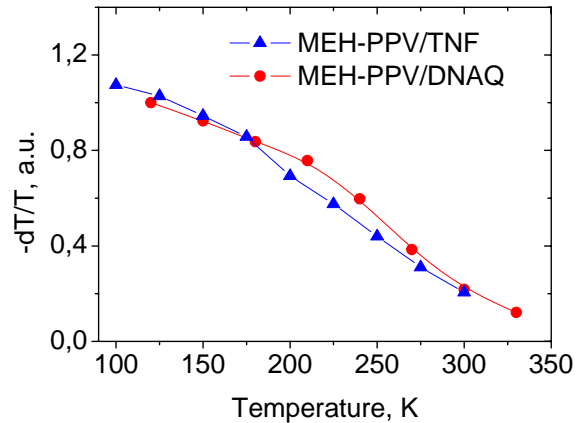


Fig. 117. Normalized temperature dependencies of the 1.2 eV band for the blends mentioned in Fig. 116. The data for the MEH-PPV/TNF blend are taken from Fig. 114. The pump intensity for the MEH-PPV/DNAQ blend was  $\approx 2.9$  W/cm<sup>2</sup>.



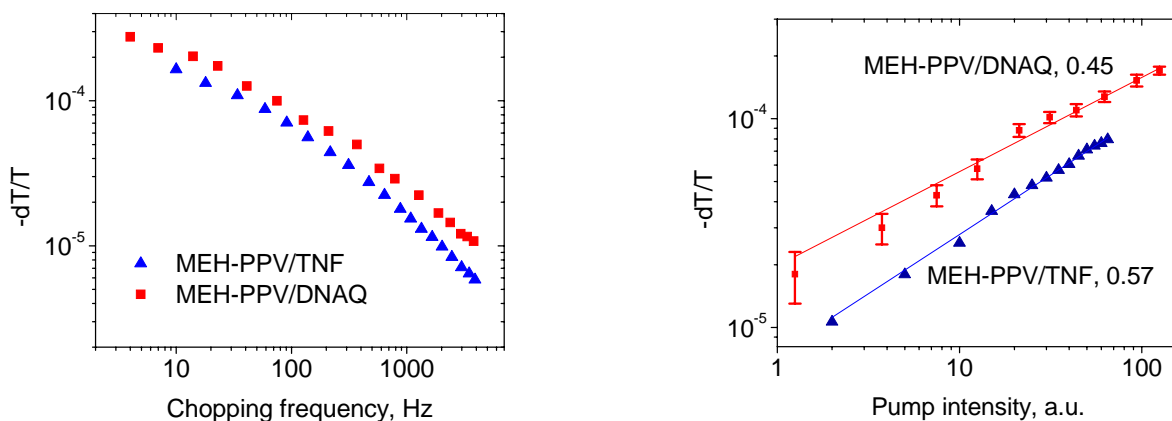


Fig. 118. Frequency (left) and pump intensity (right) dependencies of the 1.2 eV band for the blends mentioned in Fig. 116. The data for the MEH-PPV/TNF blend are taken from Fig. 112 and Fig. 115. Lines in the right figure are power-law fits with exponents shown in it. For the MEH-PPV/DNAQ blend, the frequency dependence was recorded at pump intensity  $\approx 2.9 \text{ W/cm}^2$ , and the pump intensity dependence was measured at 30 Hz.

#### 4.3.2.2 Direct photoexcitation of CTC

As was shown above, MEH-PPV/TNF and MEH-PPV/DNAQ blends have a long absorption tail prolonging to the near IR range in contrast to pristine MEH-PPV. It is important to found the relaxation pathways of these low-energy excited states that we assign to the CTC states. We studied PIA for red and infra-red pump with wavelengths corresponding to the MEH-PPV optical gap.

Fig. 119 shows PIA spectra of 1:1 MEH-PPV/TNF blend recorded at different pump wavelengths corresponding to the MEH-PPV absorption band (532 nm) and the CTC band (670 and 810 nm). For the latter pump wavelengths, pristine MEH-PPV films do not show any PIA signal at all. At the same time, the MEH-PPV/TNF blend gives nearly the same spectra for all the three pump wavelengths (Fig. 119) indicating that photoexcitation of either the MEH-PPV or the CTC results in the same charged species.

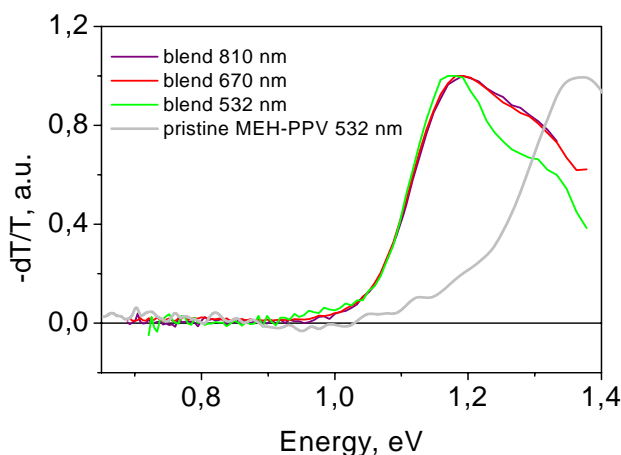


Fig. 119. Normalized PIA spectra of 1:1 MEH-PPV/TNF film drop-cast from chlorobenzene recorded for different pump wavelengths;  $T=100 \text{ K}$ ,  $f=75 \text{ Hz}$ . PIA spectrum of pristine MEH-PPV is shown for comparison.

Fig. 120 demonstrates PIA excitation spectrum of the 1.25 eV band for 1:1 MEH-PPV/TNF blend measured at room temperature. This spectrum was calculated by dividing the PIA signal

$|dT/T|$  by the absorbed pump photon flux  $F = I_0(1 - \exp(-OD))/h\nu$ . Here  $I_0$  is the incident pump intensity, and  $OD$  is the film's optical density at probe energy  $h\nu$ . Therefore, the PIA excitation spectrum is proportional to the charge generation efficiency (CGE) per absorbed pump photon. As follows from Fig. 120, within the absorption range of MEH-PPV and CTC, the CGE does not depend on pump wavelength within our experimental error amounting 50%. In addition, the absorbed pump flux varied for the different pump wavelengths; it was minimal at 629 nm ( $\approx 7$  mW/cm<sup>2</sup>), moderate at 532 nm ( $\approx 40$  mW/cm<sup>2</sup>), and maximal ( $\approx 70$  mW/cm<sup>2</sup>) at 810 nm. As the pump intensity dependence of PIA is sub-linear (Fig. 115), this should make the curve in Fig. 120 more flat. In view of our experimental error, it is safer to conclude that the CGE does not change more than twice in the range 532–810 nm. Note that we did not observe any PIA signal for pump wavelength 946 nm (Fig. 120). We measured very similar PIA excitation spectra for 1:1 MEH-PPV/TNF films prepared from toluene or chlorobenzene. Therefore, photoexcitation of either the MEH-PPV or the CTC results in the same charged species with efficiency weakly depending on photon energy. These results suggest that CTCs could be used to extend the spectral sensitivity of polymer solar cells into the red and near IR spectral ranges.

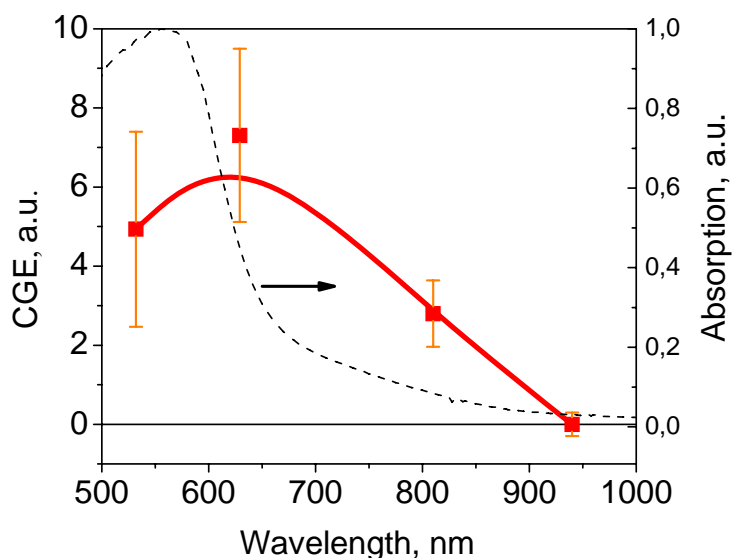


Fig. 120. Photoexcitation spectrum of the 1.25 eV band (CGE) for 1:1 MEH-PPV/TNF film drop-cast from cyclohexanone. The solid line is a guide to the eye. The dashed line shows the MEH-PPV/TNF absorption. The data were recorded at room temperature and chopping frequency 40 Hz. Large errors are due to uncertainty in the absorbed pump flux for different pump wavelengths (532, 629, 810, 946 nm).

#### 4.3.2.3 Varying donor-acceptor ratio, solvents, and temperature

Using PIA spectroscopy, we studied MEH-PPV/TNF and MEH-PPV/DNAQ blended films prepared from different solvents (chlorobenzene, toluene, and cyclohexanone) with various donor-acceptor ratios. We tried to find conditions influencing the charge generation efficiency (CGE) which is proportional to the intensity of the polaron band at 1.2 eV per absorbed pump photon. In all the cases, the PIA spectra of the blends were very similar.

We have observed that the PIA intensity in 1:1 MEH-PPV/TNF films drop-cast from chlorobenzene is strongly inhomogeneous over the sample area changing more than one order of magnitude. The maximum signal was observed only in a spot of the film seen in Fig. 121. This spot is formed upon evaporation of the residue solvent during solidification, and it has a lower concentration of the uncomplexed TNF phase giving the scattered light. Such a spot is formed only for TNF/MEH-PPV ratio higher than 0.5:1. One might guess that mechanical stress is present in the spot increasing the CGE. As follows from our light scattering data, the scattering level in this spot is half of that of the remaining film making this spot visible in the image in Fig. 121. The PL in this spot was completely quenched, and the optical absorption was the same as in the remaining film.



Fig. 121. Photo of the 1:1 MEH-PPV/TNF film drop-cast from chlorobenzene in the reflected light. The substrate diameter is 23 mm.

In the sample shown in Fig. 121 the maximum CGE was about half of that of MEH-PPV/C<sub>60</sub> blends both at room and liquid nitrogen temperatures indicating that the long-lived charges can indeed be generated in the CTC with quite a high efficiency. Our PIA data on MEH-PPV/TNF blends suggest that the CGE in MEH-PPV/TNF films is strongly dependent on the details of film's morphology. However, we have not managed to control the CGE varying the film preparation conditions. For example, we did not find any smooth dependence of the CGE on the donor/acceptor ratio. The maximum CGE we observed in the 1:1 MEH-PPV/TNF films drop-cast from chlorobenzene. In toluene and cyclohexanone films, the maximum CGE typically was two times and ten times lower, respectively. Note that these films did not have a characteristic spot similar to that shown in Fig. 121.

The CGE in MEH-PPV/DNAQ blends did not depend strongly on the point on the sample as in MEH-PPV/TNF blends. Moreover, a monotonic dependence of the CGE on DNAQ concentration was measured (Sec. 4.5.3, Fig. 153). PIA in MEH-PPV/DNAQ films was observed at pump wavelength 532 and 670 nm, but not at 810 nm. For the latter, the MEH-PPV/DNAQ blends have negligible optical absorption (Fig. 71).

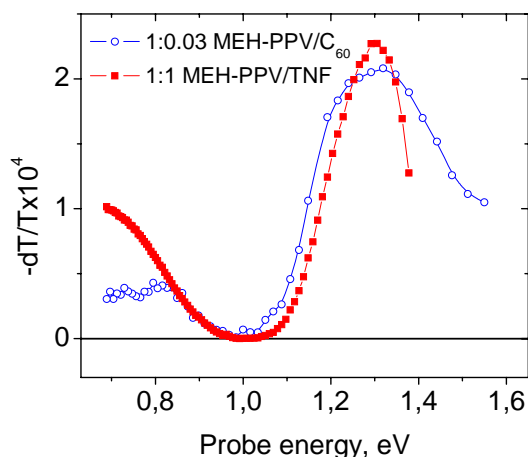


Fig. 122. Room-temperature PIA spectra for chlorobenzene MEH-PPV/TNF and MEH-PPV/C<sub>60</sub> films recorded at pump wavelength 532 nm (0.8 W/cm<sup>2</sup>) and 810 nm (30 W/cm<sup>2</sup>), respectively. The optical density of the MEH-PPV/TNF film at 810 nm evaluated from its optical transmission was 1. The chopping frequency was 75 Hz.

Note that photoexcited charged species in blends of soluble PPVs with fullerenes are commonly observed in PIA spectra as low-energy (LE) and high-energy (HE) bands peaking at 0.4 and 1.3 eV, respectively. As we can not record PIA spectra below 0.65 eV, the LE band could be observed only as its high-energy shoulder (Fig. 111). However, in MEH-PPV/TNF and MEH-PPV/DNAQ blends, we did not observe any traces of the LE band at low temperature (~100 K) as clearly seen in Fig. 119. On the other hand, the LE band can be observed in these blends at room temperature. Fig. 122 compares room-temperature PIA spectra of MEH-PPV/TNF and MEH-PPV/C<sub>60</sub> blends recorded at 810 and 532 nm, correspondingly. Both the HE and the LE bands in Fig. 122

showed typical dispersive frequency dependencies analogous to those shown in Fig. 113. The similar PIA spectra and intensity in Fig. 122 indicate that the density of photoexcited charged species in the MEH-PPV/TNF blend can be as high as in MEH-PPV/C<sub>60</sub> blends. However, the absence of the LE band at low temperature and its appearance at room temperature in the MEH-PPV/acceptor blends with CT interaction is not clear at the moment. These observations may suggest that the LE and HE bands can stem from different charged species in MEH-PPV. One can expect that generation and recombination of long-lived charges in MEH-PPV chains involved in the CTC occur in a different way as compared with the pristine ones.

Fig. 123 compares room-temperature PIA spectra of pristine MEH-PPV and MEH-PPV/TNF films for excitation at 532 nm. Although the PIA signals are low, the polaron bands at 1.3–1.4 eV and below 0.8 eV are clearly observed in both films. The polaron assignment is also supported by their characteristic “dispersive” dependences on chopping frequency plotted in Fig. 124. Note that the 1.4 eV polaron band is essentially broader in the pristine MEH-PPV. A narrower high-frequency tail in the MEH-PPV/TNF could be explained by interference with a more intensive positive signal assigned to bleaching the CTC absorption band (see above). Nevertheless, the 1.3 eV polaron band in the blend is also narrower at its low-frequency side. This could be assigned to a narrower distribution in the polaron energies in the blend than that of the pristine polymer. This is another indication that the CTC can change the properties of pristine conjugated chains.

The charge generation efficiency (CGE) at room temperature in the MEH-PPV/DNAQ CTC is typically similar to that of the pristine MEH-PPV as follows from close PIA intensities observed in pristine MEH-PPV (Fig. 123) and MEH-PPV/DNAQ (Fig. 151). Note again that the CGE in MEH-PPV/TNF CTC strongly varied for different samples.

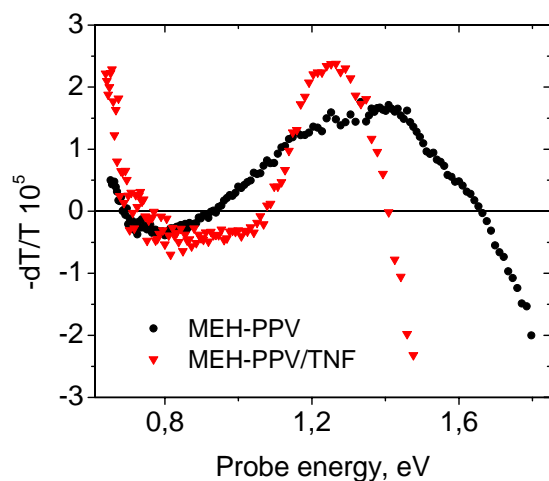


Fig. 123. Room-temperature PIA spectra of pristine MEH-PPV and 1:1 MEH-PPV/TNF films drop-cast from cyclohexanone. Photoexcitation was at 532 nm chopped at 35 Hz with intensity  $\sim 1 \text{ W/cm}^2$ .

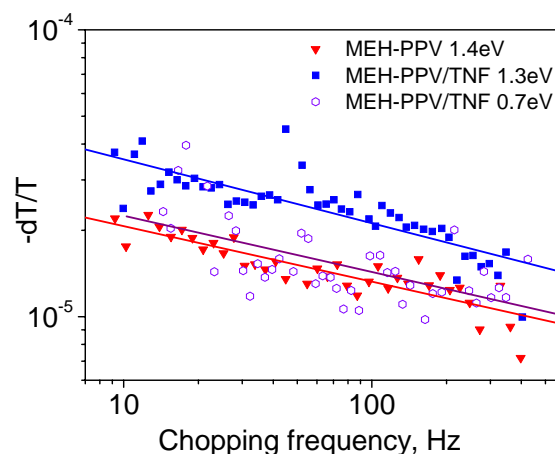


Fig. 124. PIA signal as a function of chopping frequency for samples and conditions indicated in Fig. 123. The signals were recorded in the peaks of the bands indicated in the figure. The lines are power-law fits with exponents 0.19–0.22.

#### 4.3.2.4 Photoinduced absorption FTIR spectroscopy

It is commonly accepted that a direct consequence of the formation of self-localized charged excitation in conjugated polymers is the development of infrared-active vibrational (IRAV) modes with associated electronic state(s) in the  $\pi$ - $\pi^*$  energy gap. Due to the electron-phonon interaction, a

charged excitation in the system causes a localized distortion of the  $\pi$ -electron charge density, which distorts the lattice in the vicinity of the carrier. This structural distortion breaks the local symmetry of the lattice, splitting off localized phonon modes (IRAV's) which represent the normal modes of the structural distortion. Each mode corresponds to one of the Raman-active optical-phonon bands of the polymer and appears with enhanced infrared oscillator strength due to coupling to the  $\pi$ -electron system. As a result of this distortion, the  $\pi$ -electron system forms localized electronic states in the gap giving rise to new sub-gap absorptions, in particular the LE polaron band. Consequently, the IRAV modes and the sub-gap electronic absorptions provide a "fingerprint" of the charged excitations of the polymer system. Photoinduced IR measurements allow study of the most long-lived charged states whose lifetime is in the range of tens of seconds supplementing our PIA studies presented above in the three preceding sections.

Photoinduced FTIR absorption (PIA-FTIR) measurements were performed on blends of MEH-PPV with DNAQ, TNF,  $C_{60}$ , and  $Pt_{0.75}C_{60}$ . The donor/acceptor molar ratios were the following: MEH-PPV:DNAQ (1:1, 1:0.25, 1:0.03), MEH-PPV:TNF (1:0.4, 1:0.03, 1:0.001), MEH-PPV: $C_{60}$  (1:0.05), and MEH-PPV:  $Pt_{0.75}C_{60}$  (1:0.05). Blended films were prepared by drop casting on  $BaF_2$  substrates from chlorobenzene. All the measurements were carried out at ambient laboratory conditions. The PIA-FTIR technique is described in Sec. 2.8.2.

Fig. 125 (left) shows PIA-FTIR spectra of a pristine MEH-PPV film and MEH-PPV/TNF films with different TNF content. Characteristic signatures of a charged separated state resulting from photoinduced charge transfer from MEH-PPV are seen only for the pristine MEH-PPV and the blend with the lowest TNF concentration (1:0.001): both the photoinduced IRAV bands are observed in the range 800–1500  $cm^{-1}$  and the in-gap absorption around 3000–3500  $cm^{-1}$  ( $\sim 0.4$  eV). The latter we assign to the LE polaron band whose shoulder at  $\sim 0.7$  eV was observed in our near-IR PIA studies (see the preceding sections). At the same time, for MEH-PPV:TNF films with higher TNF content (the 1:0.03 and 1:0.4 curves in Fig. 125, left) we have not observed any signatures of photoinduced charged states at our signal-to-noise ratio.

Fig. 125 (right) demonstrates PIA-FTIR spectra of MEH-PPV/DNAQ films with different molar ratios of the components. The PIA-FTIR spectrum of pristine MEH-PPV from the same batch of samples is also plotted for comparison. It is seen that addition of DNAQ to MEH-PPV decreases all the MEH-PPV PIA bands as in the case of TNF. Nevertheless, both the IRAV modes and the in-gap absorption are seen Fig. 125 (right) even for the highest content of DNAQ.

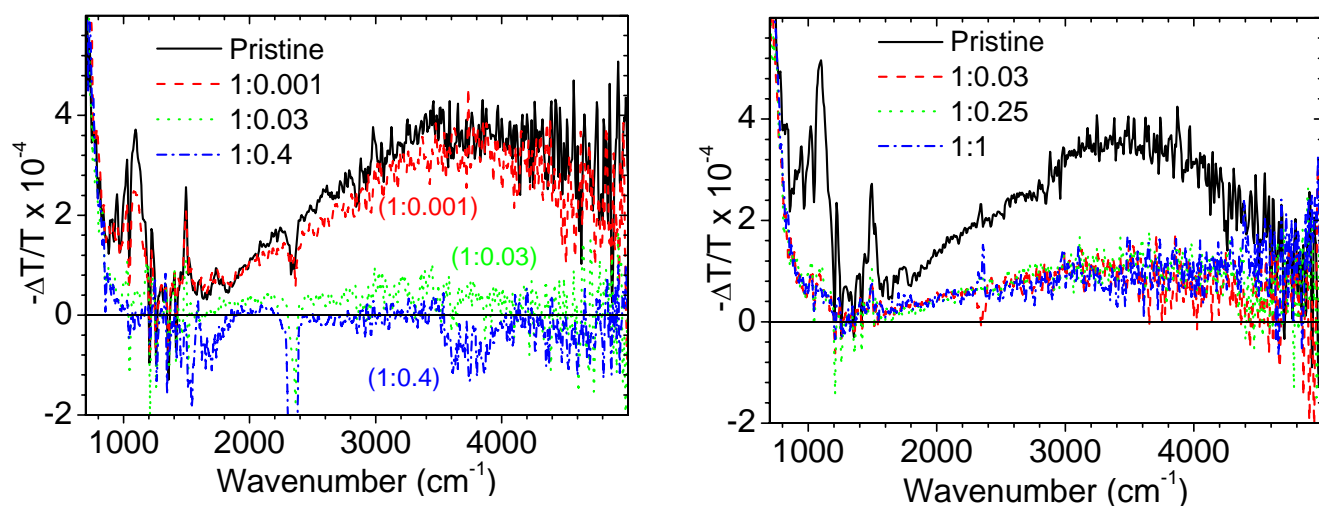


Fig. 125. Left: PIA-FTIR spectra of MEH-PPV/TNF films with different acceptor molar concentration. Negative values of PIA signal for 1:0.4 blend in the 1600 and 3600  $cm^{-1}$  region are due to the

ambient water vapor. Right: PIA IR spectra of the MEH-PPV:TNF film with different acceptor concentration. Features at  $\sim 2350\text{ cm}^{-1}$  are due to the ambient  $\text{CO}_2$ .

As reference data, we recorded PIA-FTIR for a 1:0.05 MEH-PPV/ $\text{C}_{60}$  film. Fig. 126 (left) demonstrates the result. It is seen that the spectra for MEH-PPV/ $\text{C}_{60}$  and pristine MEH-PPV (Fig. 125) are almost the same in shape and intensity. This is in contrast with literature data at low temperatures ( $<100\text{ K}$ ). Indeed, doping of MEH-PPV by  $\text{C}_{60}$  (5% wt.) results in a strong increase of PIA-FTIR MEH-PPV bands by almost two orders of magnitude [19]. Accordingly, almost the same spectra in the MEH-PPV/ $\text{C}_{60}$  (Fig. 126, left) and the pristine MEH-PPV (Fig. 125) suggest that the deepest trapped charges probed by PIA-FTIR at room temperature have the same characteristics in both materials. Indeed, the near-IR PIA spectroscopy at millisecond pump modulation in pristine MEH-PPV reveals long-lived photoinduced charges at room temperature (see Fig. 123). This implies that  $\text{C}_{60}$  remains intact MEH-PPV chains that result in room-temperature PIA signals.

Fig. 126 (right) depicts PIA-FTIR spectrum for a 1:0.05 MEH-PPV/ $\text{Pt}_{0.75}\text{C}_{60}$  film. Again, the spectrum is very similar to those of the MEH-PPV/ $\text{C}_{60}$  and MEH-PPV films suggesting that  $\text{Pt}_{0.75}\text{C}_{60}$  also does not influence MEH-PPV chains active in room-temperature FTIR-PIA. The detailed comparative study of MEH-PPV/ $\text{C}_{60}$  and MEH-PPV/ $\text{Pt}_{0.75}\text{C}_{60}$  blends is presented below in Sec. 4.6.

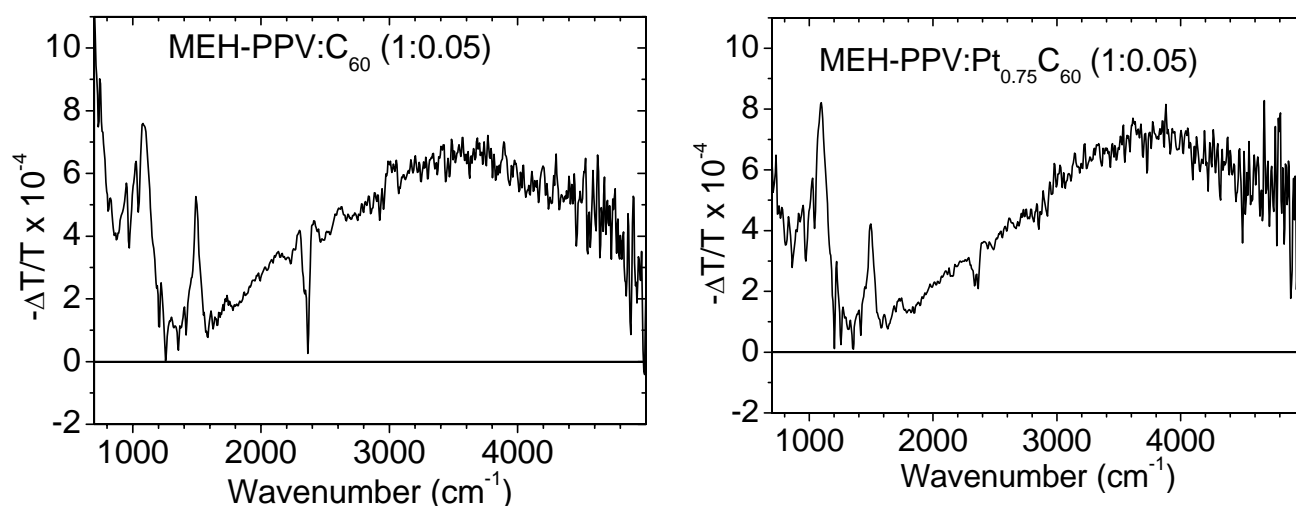


Fig. 126. PIA-FTIR spectra for 1:0.05 MEH-PPV/ $\text{C}_{60}$  (left) and 1:0.05 MEH-PPV/ $\text{Pt}_{0.75}\text{C}_{60}$  (right) films. A negative band at  $\sim 2350\text{ cm}^{-1}$  is due to the ambient  $\text{CO}_2$ .

Thus, our room-temperature FTIR-PIA data show that addition of an acceptor forming a CTC with MEH-PPV results in strong suppression of both the IRAV and the electronic bands of MEH-PPV. If in MEH-PPV:DNAQ blends PIA signals can be observed even at 1:1 ratio of the components, in MEH-PPV:TNF blends 3% mol. of TNF suppresses all the MEH-PPV FTIR-PIA bands below our signal-to-noise ratio.

It is reasonable to associate this suppression with an effect of CTC. Indeed, as we have shown above, TNF results in a more pronounced ground-state CT interaction with MEH-PPV than DNAQ, and an effect of the CTC on FTIR-PIA can be expected to be higher. It seems that TNF results in more thorough mixing of the blend components. This is in accordance with our PL quenching data (see Sec. 4.3.1.1). Therefore, a part of MEH-PPV chains remaining intact in the CTC is higher in MEH-PPV:DNAQ blends than in MEH-PPV:TNF ones. We suggest that these intact chains contribute mainly to the FTIR-PIA spectra.



#### 4.3.2.5 Summary

We have established that long-lived photoinduced charges can be generated in the MEH-PPV/TNF and MEH-PPV/DNAQ blends at the millisecond time scale. Photoexcitation either of the MEH-PPV or the CTC, i.e., in the spectral range 500–800 nm, results in the same charged species with efficiency weakly depending on photon energy. We have observed that the density of long-lived photoinduced charges in MEH-PPV/TNF blends can be as high as in MEH-PPV/fullerene blends. However, the generation efficiency of long-lived charges in the CTC is typically one order of magnitude lower than that in MEH-PPV/fullerene blends. Despite the fact that the initial charge separation in the CTC can be as efficient as in polymer/fullerene blends as follows from our PL quenching data, geminate recombination in the CTC possibly impedes efficient generation of long-lived charges.

On the other hand, the most long-lived charges probed by FITR-PIA are deeply suppressed in the CTC. We suggest that, at room temperature, these long-lived charges appear at MEH-PPV chains remaining intact in MEH-PPV/acceptor blends. Our FTIR-PIA data imply that the CTC facilitates intimate donor-acceptor mixing as compared with MEH-PPV/acceptor blends without noticeable ground-state interaction of the components, for example with MEH-PPV/C<sub>60</sub>.

#### 4.3.3 Surface photovoltage spectroscopy

We have done surface photovoltage (SPV) spectroscopy studies on MEH-PPV/TNF and pristine MEH-PPV films. We were motivated to study photoinduced charge separation in conjugated polymer CTCs. The SPV technique is described in Sec. 2.11.

Fig. 127 compares SPV spectra of pristine MEH-PPV and 1:0.6 MEH-PPV/TNF films. It is seen that the SPV spectrum of the pristine MEH-PPV film follows the edge of its absorption spectrum. Hence the absorbed photons generate spatially separated charges. As Fig. 127 shows, at higher photon energy (>2.1 eV), the SPV in pristine MEH-PPV does not follow its absorption spectrum decreasing by two orders of magnitude. Therefore, the SPV spectrum is antibatic with the absorption spectrum. We observed that for thinner samples the SPV spectrum is less antibatic, i.e., the SPV is higher in the spectral region of strong optical absorption of MEH-PPV.

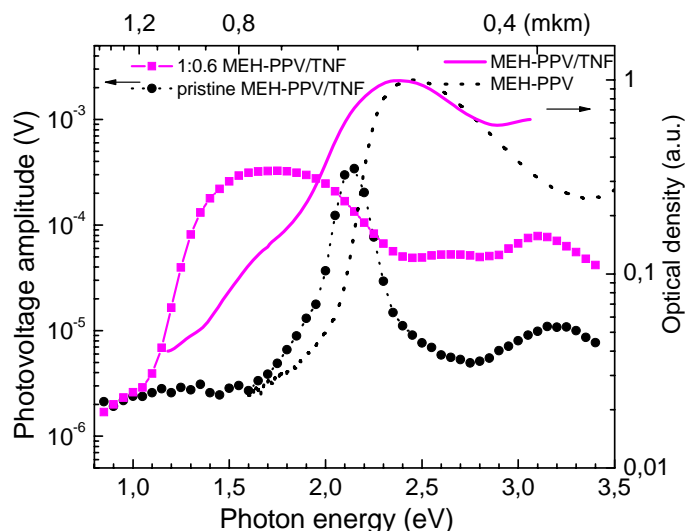


Fig. 127. SPV spectra of pristine MEH-PPV and MEH-PPV/TNF films (points) and their absorption spectra (lines). The SPV spectra were recorded for drop-cast films in ambient conditions at a chopping frequency of 8 Hz. The SPV spectra are shown without correction to the incident spectrum.

On the other hand, for illumination of the sample through the glass substrate (Fig. 9), the SPV spectrum was symbatic with the absorption spectrum. These observations indicate that spatial charge separation in pristine MEH-PPV occurs mainly at the ITO/film interface. The antibatic behavior of the SPV spectrum we assign mainly to the internal filter effect, i.e., the effect of optically thick film absorbing photons before they reach the ITO/film interface. In the 1:0.6 MEH-PPV/TNF film, the SPV spectrum rises at 1.2 eV indicating that absorption in the CTC band generates spatially separated

charges. The SPV spectrum of the MEH-PPV/TNF film shows a broad band at 1.7 eV as compared with the narrow band at 2.15 eV for the pristine MEH-PPV (Fig. 127). This difference in width can be assigned to a broad and less intensive CTC absorption spectrum resulting in the internal filter effect only for photon energy higher than 1.9 eV. As follows from the SPV spectra in the range 2–3.5 eV (Fig. 127), the internal filter effect is less pronounced in the blend than in the pristine MEH-PPV despite both films were optically thick. Moreover, we have observed that the shape of the SPV spectra does not evolve monotonically with addition of TNF. These observations probably suggest that the mechanism of charge generation in MEH-PPV/TNF blends is different from that of the pristine polymer. To identify the charge separation mechanism in the blend, more detailed studies are needed.

The most important result of our SPV studies is that MEH-PPV/TNF blends can generate mobile charges upon the red and near-IR photoexcitation with photon energies 1.2 eV and higher.

#### 4.3.4 Charge drift mobilities in MEH-PPV/TNF and MEH-PPV/DNAQ films

An efficient photovoltaic material should have relatively high drift mobility of charges of both signs. Because of this, the drift mobility of both electrons and holes photoexcited in a CTC is an important issue to be studied. Drift mobility in 1:0.2 MEH-PPV:TNF and 1:0.2 MEH-PPV:DNAQ films prepared by drop casting was measured using the time-of-flight (TOF) technique described above (Sec. 2.10). Fig. 128 shows the results. It is well known that charge transport in conjugated polymers is dominated by holes. However, as seen in Fig. 128, even for 1:0.2 MEH-PPV:acceptor ratio the electron mobility becomes higher than the hole one. One can suggest that the CTC acts as a trap for holes decreasing their mobility. The latter decreases in a few times compared with the pristine MEH-PPV (Fig. 24). Decreasing the hole mobility upon adding the acceptor was observed more than 30 years ago in poly-*n*-vinylcarbazole (PVK)/TNF blends in which a ground-state CTC forms [20]. At the same time, the electron mobility increased in PVK/TNF and the hole and electron mobilities became equal at 1:0.5 PVK:TNF molar ratio. Possibly, similar behavior of the electron and hole mobilities could occur in the MEH-PPV CTC. Fig. 128 demonstrates that the MEH-PPV/TNF blend shows higher both the electron and hole mobilities than those of the MEH-PPV/DNAQ. Note that the difference between the electron and hole mobility is stronger in MEH-PPV/DNAQ.

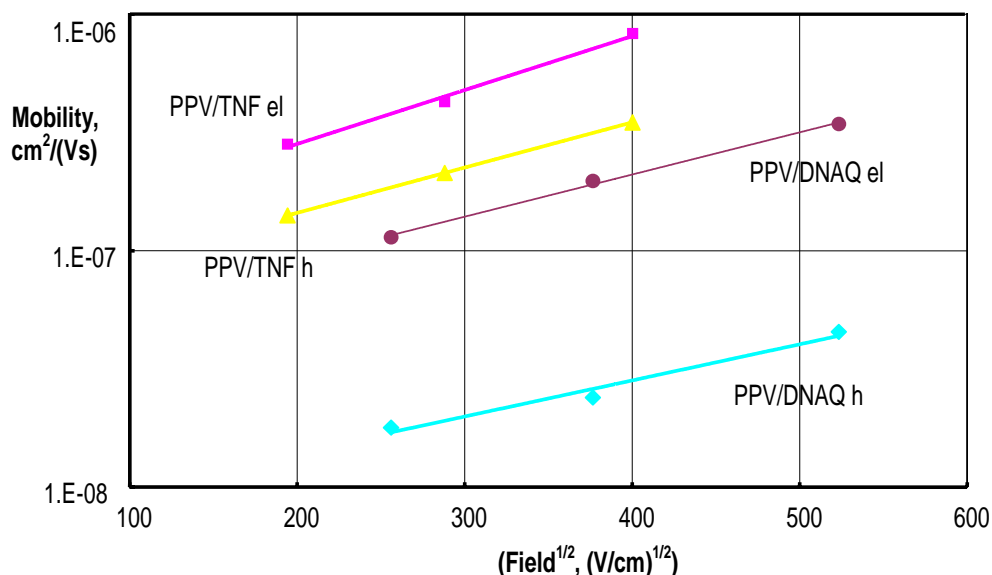


Fig. 128. Hole (h) and electron (el) drift mobilities in 1:0.2 MEH-PPV:TNF and 1:0.2 MEH-PPV:DNAQ films at room temperature.

Both the electron and the hole mobilities in MEH-PPV/TNF and MEH-PPV/DNAQ are too low for efficient charge transport in solar cells (below  $10^{-6}$  cm<sup>2</sup>/V s). The low mobilities and their strong field dependence (Fig. 128) imply intermolecular hopping transport mechanism in a disordered system. Note that the best working layer compositions for polymer solar cells must contain no less than 50% wt. of fullerene derivative (PCBM) and namely it provides efficient charge transport. Because of this, we have studied ternary blends (Sec. 4.4) to combine the attractive properties of fullerenes and CTCs.

#### 4.3.5 Photoelectric data

Our PIA studies demonstrate that the photoexcited CTC can relax into a charged-separated state (Sec. 4.3.2). Our surface photovoltage spectroscopy data indicates that these photogenerated charges can be mobile (Sec. 4.3.3). An important question to be addressed: how effectively do photoinduced charges contribute to the photocurrent? To study this question, we measured the photocurrent action spectra and current-to-voltage characteristics of solar cells prototypes (photodiodes) with the active layer consisting of MEH-PPV/TNF, MEH-PPV/DNAQ, pristine MEH-PPV and MEH-PPV/C<sub>60</sub> blends. The two latter were used as a reference. The experimental methods are given in Sec. 2.12, and the sample preparation details are presented in Sec. 3.3.4. The optical density of the active layer was below unity allowing us to neglect the internal filter effect, i.e., any essential influence of the active layer thickness on the shape of the photocurrent spectra.

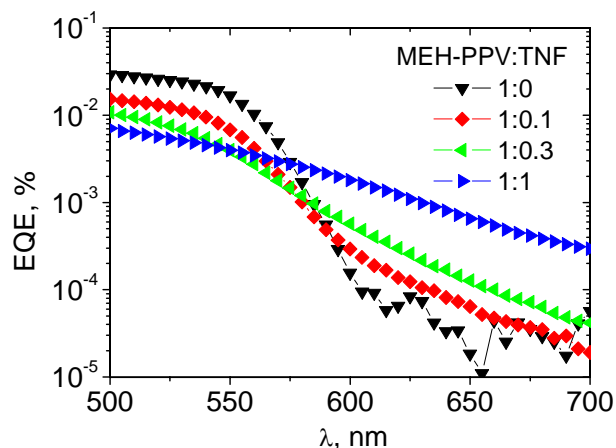


Fig. 129 Photocurrent action spectra of MEH-PPV/TNF photodiodes for different donor/acceptor ratios.

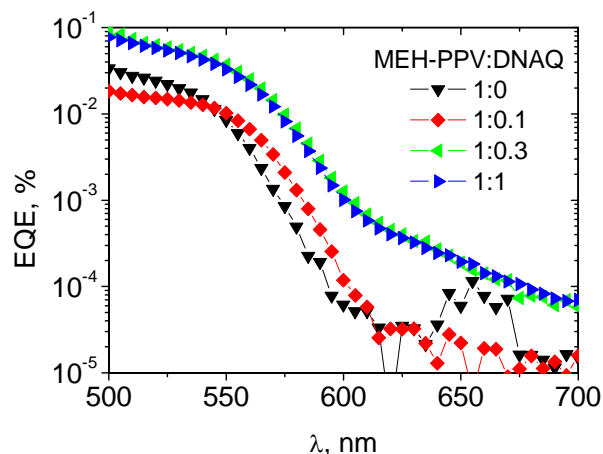


Fig. 130 Photocurrent action spectra of MEH-PPV/DNAQ photodiodes for different donor/acceptor ratios.

Fig. 129 and Fig. 130 show photocurrent action spectra of MEH-PPV/TNF and MEH-PPV/DNAQ photodiodes, respectively. It is seen that addition of TNF to MEH-PPV leads to decreasing the external quantum efficiency (EQE) in the region of MEH-PPV absorption and increasing the EQE in the MEH-PPV optical gap. Meanwhile, the MEH-PPV/DNAQ photodiodes demonstrate an increase in EQE both in the absorption and the transparency ranges of MEH-PPV.

Considerable EQE increasing in the MEH-PPV optical gap with adding the acceptors evidences for mobile charges generated in the CTC. Nevertheless, the photocurrent action spectra clearly correlate with the absorption spectra only for MEH-PPV/TNF blends implying the same charge collection efficiency over the entire investigated spectral region (our PIA studies indicate approximately the same efficiency of generation of long-lived charges in this spectral region, see Sec. 4.3.2.2). At the same time, the charge collection efficiency tends to decrease with increasing

the TNF content indicating lower charge mobilities or/and higher recombination rate as compared with the pristine MEH-PPV device. On the contrary, DNAQ enhances the photocurrent in both the absorption and the transparency ranges of MEH-PPV yet acting obviously different within them.

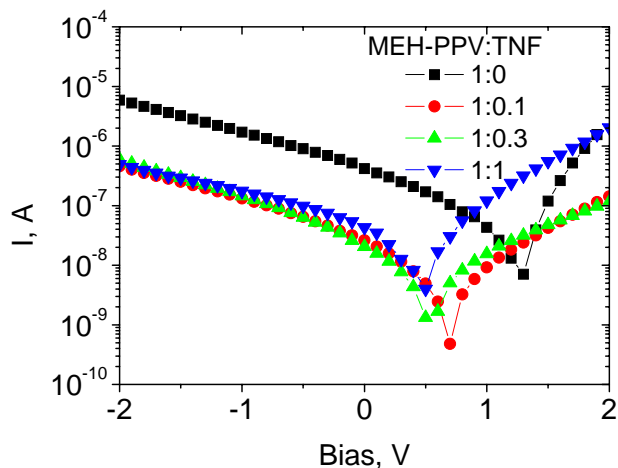


Fig. 131 Current-to-voltage characteristics of MEH-PPV/TNF photodiodes for different donor/acceptor ratios.

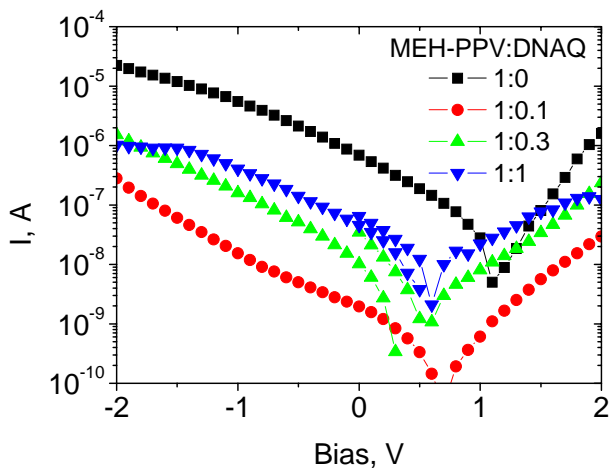


Fig. 132 Current-to-voltage characteristics of MEH-PPV/DNAQ photodiodes for different donor/acceptor ratios.

Characteristics of MEH-PPV/TNF and MEH-PPV/DNAQ photodiodes are summarized in Table 11. Our data for pristine MEH-PPV and MEH-PPV/C<sub>60</sub> devices are also given for comparison. Current-to-voltage characteristics under white light illumination ( $\sim 100 \text{ mW/cm}^2$ ) of MEH-PPV/TNF and MEH-PPV/DNAQ photodiodes (Fig. 131 and Fig. 132) show a considerable decrease in the photocurrent as compared with the pristine MEH-PPV devices. For the MEH-PPV/TNF photodiodes, it could be explained by EQE decrease in the spectral range giving the maximum contribution to the photocurrent, i.e., in the range 500–550 nm as seen in Fig. 129. For MEH-PPV/DNAQ photodiodes, the photocurrent increases within this range (Fig. 130), and therefore one could expect increasing the short circuit current  $I_{sc}$  with adding DNAQ compared with the pristine MEH-PPV devices. However, the  $I_{sc}$  in the MEH-PPV/DNAQ photodiodes is essentially lower than that in the pristine MEH-PPV photodiode as seen in Fig. 132 and Table 11. The absence of correlation between the photocurrents excited at monochromatic and white light illumination in the MEH-PPV/TNF and MEH-PPV/DNAQ devices makes us suppose different dependencies of the photocurrent on the light intensity in them. In fact, the TOF mobilities are essentially lower in the MEH-PPV/DNAQ blend than in the MEH-PPV/TNF blend (see Fig. 128) implying a less efficient charge collection network in the former. Probably, the conductive pathways in the MEH-PPV/DNAQ bulk heterojunction are saturated at lower current densities than in the MEH-PPV/TNF one. The observed low EQE and energetic efficiency (Table 11) in MEH-PPV/TNF and MEH-PPV/DNAQ blends can be explained by combination of two factors: the low generation efficiency of long-lived charges in the CTC (see Sec. 4.3.2) and their low mobility (see Sec. 4.3.4).

Current-to-voltage characteristics under illumination also show different acceptor concentration dependences for the MEH-PPV/TNF and MEH-PPV/DNAQ photodiodes (cf. Fig. 131 and Fig. 132). Increasing the TNF content results in decreasing  $V_{oc}$  at approximately constant  $I_{sc}$  (Table 11). At that, the forward currents rise, and the backward currents remain almost the same (Fig. 131). On the contrary, increasing the DNAQ content raises all the currents while the  $V_{oc}$  does not change considerably. A stronger decrease of the  $V_{oc}$  in MEH-PPV/TNF photodiodes than in MEH-PPV/DNAQ ones could be assigned to a higher electron affinity (EA) of TNF. In fact, the TNF EA is

expected to be  $\approx 0.4$  eV higher (Table 2). This difference in EA is similar to that in  $V_{oc}$  as seen in Table 11.

Active layer (numbers show donor/acceptor molar ratio)	$I_{sc}$ , $\mu A/cm^2$	$V_{oc}$ , V	$FF$ , %	$EQE$ at 500 nm, %	Energetic efficiency $\eta$ , %
MEH-PPV:TNF 1:1	0.87	0.47	22.1	$8.4 \cdot 10^{-03}$	$9.0 \cdot 10^{-05}$
MEH-PPV:TNF 1:0.3	0.41	0.54	21.7	0.01	$4.8 \cdot 10^{-05}$
MEH-PPV:TNF 1:0.1	0.52	0.68	19.6	0.02	$6.9 \cdot 10^{-05}$
MEH-PPV:DNAQ 1:1	1.14	0.77	16.1	0.08	$1.4 \cdot 10^{-04}$
MEH-PPV:DNAQ 1:0.3	0.7	0.54	14.2	0.10	$5.4 \cdot 10^{-05}$
MEH-PPV:DNAQ 1:0.1	0.04	0.67	19.5	0.02	$5.2 \cdot 10^{-06}$
Pristine MEH-PPV	8.35	1.26	16.2	0.03	$1.7 \cdot 10^{-03}$
MEH-PPV:C <sub>60</sub> 1:0.4	738	0.68	23.1	2.7	0.12

Table 11. Characteristics of MEH-PPV/TNF and MEH-PPV/DNAQ photodiodes. Data for pristine MEH-PPV and MEH-PPV/C<sub>60</sub> devices are also given for comparison.

Note that our reference devices, i.e., the pristine MEH-PPV and MEH-PPV/C<sub>60</sub> photodiodes, showed typical characteristics that are very similar to the literature data (for example, [21]). This indicates that our low magnitudes of EQE,  $I_{sc}$  etc. observed for the CTCs are not due to any flaw in the device preparation or measurement procedure.

In summary, we have observed that the photoexcited CTC in MEH-PPV/TNF and MEH-PPV/DNAQ blends generates mobile charges. As a result, the photosensitivity spectral range of MEH-PPV/TNF photodiodes is extended in the optical gap of MEH-PPV. However, the studied photodiodes with the CTC show very low photocurrents under white illumination of solar intensity, which are even lower than those of pristine MEH-PPV devices. We suggest that the low mobility of charges in the blends with CTC is one of the main reasons of this behavior.

#### 4.3.6 Enhancing photooxidation stability of MEH-PPV in donor-acceptor blends

One of the basic drawbacks of conjugated polymers is their poor photooxidation stability in ambient conditions. Encapsulation techniques are currently used to reduce photooxidation in polymer devices, but they are insufficient to block oxygen contamination completely and are incompatible with devices fabricated on flexible substrates. Moreover, encapsulation increases the cost of the polymer devices. Therefore, intrinsically photostable conjugated polymers are strongly demanded. Excited triplet states (excitons) are considered to be a key intermediate in photooxidation of conjugated PPV-type polymers. The triplet excitons are precursors for highly reactive singlet oxygen resulting from energy transfer from the polymer triplet to an oxygen molecule or for a direct attack of ground state oxygen upon the conjugated chain in the triplet state. Triplet quenching is a well-known approach for improving photostability of molecules and materials.

It was observed earlier that the photooxidation rate in oxygen atmosphere of a soluble PPV derivative in the donor-acceptor blend with fullerene slows down by an order of magnitude as compared with the pristine polymer [22]. The fast electron transfer from the photoexcited polymer to C<sub>60</sub> was suggested to result in quenching triplet excitons on the polymer that are formed from singlet ones via intersystem crossing. Note that the polymer photooxidation rate in the blend was about that of C<sub>60</sub>, and it is unclear whether the polymer photooxidation stability could be further improved.

We have found that the photooxidation rate of MEH-PPV in a donor-acceptor blend can be suppressed by a few orders of magnitude. This allows us to expect that the polymer in the blend could be stable to visible radiation of solar intensity for thousands of hours without encapsulation.

#### 4.3.6.1 FTIR data

To study the photooxidation stability of MEH-PPV/TNF and MEH-PPV/DNAQ films in ambient conditions, we have recorded evolution of their FTIR spectra under green laser irradiation with an intensity of 330 mW/cm<sup>2</sup>. Films of MEH-PPV/TNF and MEH-PPV/DNAQ blends with different molar donor/acceptor ratio were prepared by drop-casting from chlorobenzene solution on BaF<sub>2</sub> substrates. Also we recorded photooxidation in a 1:0.05 MEH-PPV/C<sub>60</sub> blend.

Fig. 133 shows results for pristine MEH-PPV film. The right figure demonstrates difference absorption spectra, i.e. the spectra for the gradually oxidized film minus the spectrum of the unirradiated film. The photooxidation effect is clearly seen in Fig. 133 resulting in decreasing intensity of a number of narrow MEH-PPV bands below 1550 cm<sup>-1</sup> and appearing carbonyl bands in the range 1550-1800 cm<sup>-1</sup> indicating photooxidation of MEH-PPV.

We have found that addition of acceptor essentially slows down the photooxidation rate, i.e. decreasing the MEH-PPV bands and increasing the carbonyl bands. Fig. 134 shows difference FTIR spectra of MEH-PPV/TNF blends. Fig. 134 (left) illustrates that small addition of TNF (3% mol.) to MEH-PPV essentially slows down intensity changes for all the observed bands. The MEH-PPV bands (966 and 1506 cm<sup>-1</sup>) decrease slower, and the bands of photooxidation products (1730, 1000–1500, 1550–1850 cm<sup>-1</sup>) increase slower as well (Fig. 134). Moreover, for 1:0.4 MEH-PPV:TNF blend Fig. 134 (right) does not show any signatures of photooxidation at all during about 6 hours of irradiation. Note that the MEH-PPV/C<sub>60</sub> blend did not show any noticeable increase in the photooxidation stability as compared with the pristine MEH-PPV.

From the experimental data, we calculated changes in the area of a few characteristic bands at 966, 1506, and 1730 cm<sup>-1</sup> as a function of irradiation time. We analyze below the only mode of the MEH-PPV backbone at 966 cm<sup>-1</sup> assigned to the out-of-plane wagging vibration of vinylene CH. This mode is very sensitive to  $\pi$ -conjugation and its decreasing is usually attributed to the loss of  $\pi$ -conjugation. Moreover, we noted that, during irradiation, the 966 cm<sup>-1</sup> band decreases faster than phenyl ring modes of MEH-PPV observed at 1415 and 1506 cm<sup>-1</sup> (Fig. 133). To monitor the photooxidation products, we followed the 1730 cm<sup>-1</sup> band, which is a characteristic of the carbonylic structures.

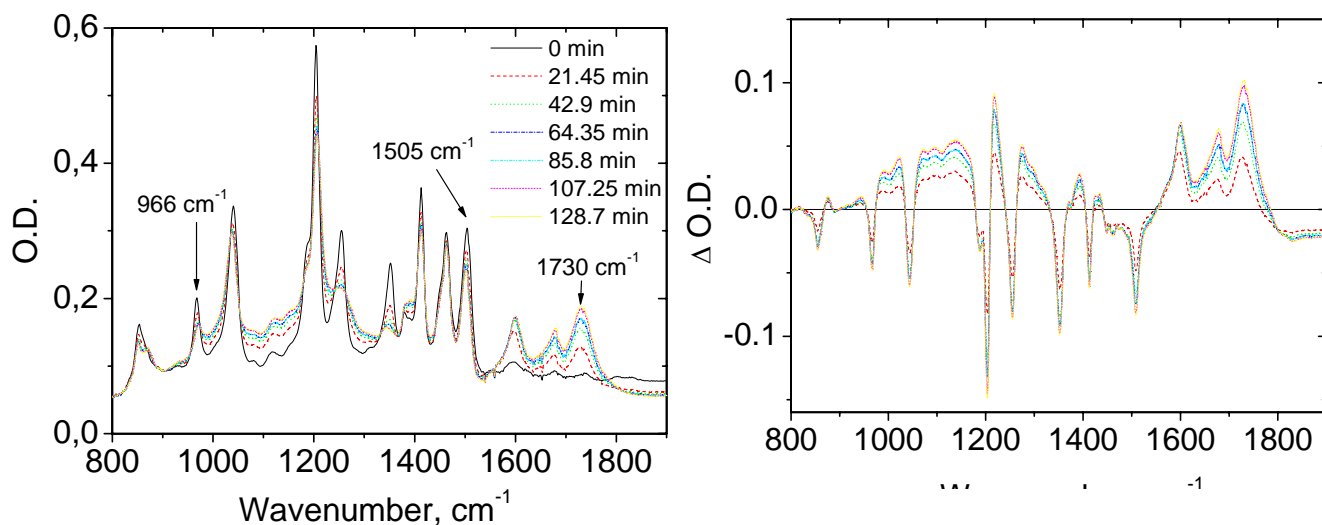


Fig. 133. Left: IR absorption spectra of pristine MEH-PPV under irradiation. Right: the difference spectra (referenced to the unirradiated MEH-PPV film) calculated from the spectra in the left figure. The cumulative irradiation time is indicated in the figures.



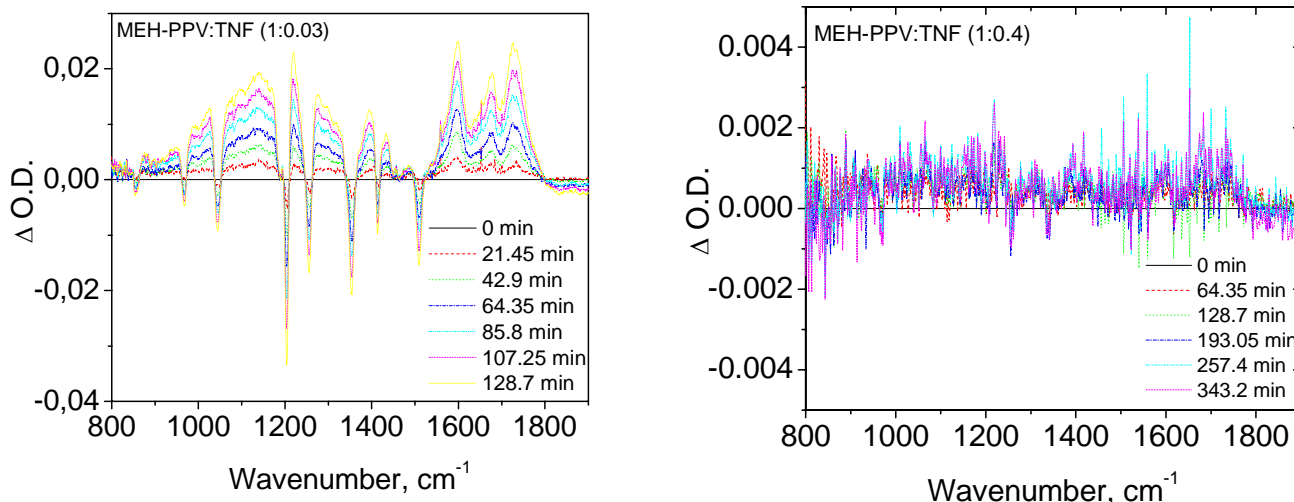


Fig. 134. Differential IR absorption spectra of 1:0.03 (left) and 1:0.4 (right) MEH-PPV/TNF blends under irradiation.

Fig. 135 presents relative changes in the area under the bands at 966 and 1730  $\text{cm}^{-1}$  as a function of irradiation time for different TNF concentration. As seen in Fig. 135, even 0.1% mol. of TNF noticeably slows down the photooxidation rate, and 3% mol. of TNF decreases it by an order of magnitude: the 966  $\text{cm}^{-1}$  band decreases slower, and the 1730  $\text{cm}^{-1}$  band increases slower as well. Moreover, for 1:0.4 MEH-PPV:TNF blend we did not observe any changes for the band at 966  $\text{cm}^{-1}$  within our experimental error after 6 hours of irradiation (exposure 7  $\text{kJ}/\text{cm}^2$ ). On the other hand, the 1730  $\text{cm}^{-1}$  band shows a very slowly increase as seen Fig. 135 (right).

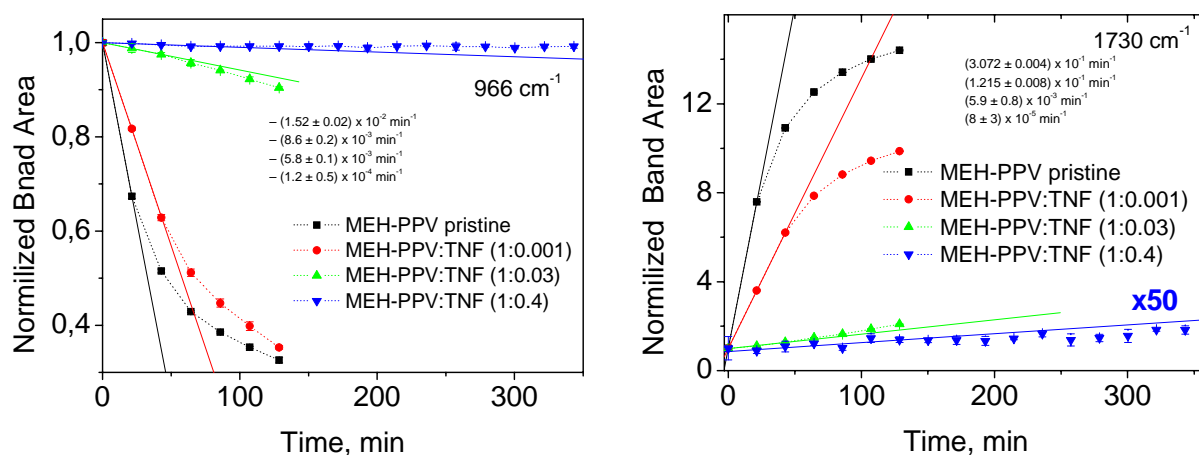


Fig. 135 Normalized area under the bands at 966  $\text{cm}^{-1}$  (left) and 1730  $\text{cm}^{-1}$  (right) as a function of irradiation time for MEH-PPV:TNF blends. The data for the 1:0.4 blend in the right figure are scaled by a factor of 50. Solid lines show the initial degradation rate, i.e., the slope of the curves calculated at the beginning of irradiation.



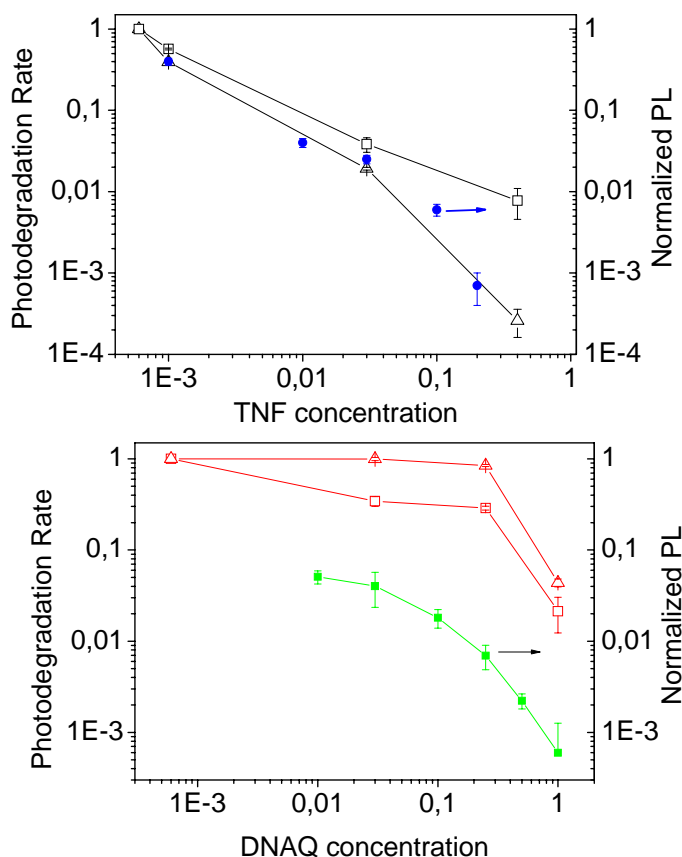


Fig. 136. Normalized initial photooxidation rate rate (empty points,  $\square$  – 966,  $\Delta$ – 1730  $\text{cm}^{-1}$ ) and the PL efficiency (filled points) in and MEH-PPV/TNF (top) and MEH-PPV/DNAQ (bottom) blends. The data are referenced to the pristine MEH-PPV. The first left point in both graphs corresponds to the pristine MEH-PPV. The data on photooxidation rate are taken from Fig. 135. The PL data are taken from Sec. 4.3.1.1. The rightmost points in the PL quenching curves correspond to the noise level.

We have found that the photooxidation rate is correlated with the PL intensity in the blends. Fig. 136 demonstrates correlation between the normalized initial photooxidation rate for the 966 and 1730  $\text{cm}^{-1}$  bands and the normalized PL intensity in MEH-PPV/TNF (top) and MEH-PPV/DNAQ (bottom) blends for different acceptor concentration. The initial degradation rates were calculated as a slope of the curves in Fig. 2 at the beginning of irradiation. As seen in Fig. 136 (top) for MEH-PPV/TNF blends, the photooxidation rate is closely follows the PL intensity with variation of TNF concentration, and both decrease by more than two orders of magnitude as compared with pristine MEH-PPV. Note that the point for the 966  $\text{cm}^{-1}$  band at the MEH-PPV/TNF ratio 1:0.4 in Fig. 136 (top) is close to the experimental error and therefore gives the upper limit of the photooxidation rate. As seen in Fig. 136 (bottom), MEH-PPV/DNAQ blends also demonstrate correlation between the photooxidation rate and the PL intensity. However, the photooxidation rate depends on DNAQ concentration far slower than the PL intensity: if the latter is quenched by 1000 times, the former decreases only by 40 and 20 times for the 966 and 1730  $\text{cm}^{-1}$  bands, respectively, upon increasing the DNAQ:MEH-PPV ratio up to 1:1.

Thus, the less the PL in the blends, the less the photooxidation rate of MEH-PPV. It is reasonably to assume that the observed stabilization effect in the blends, i.e., decreasing the photooxidation rate, is mainly associated with efficient quenching of MEH-PPV triplet excitons. In fact, MEH-PPV singlet excitons relax into triplet ones via relatively slow intersystem crossing competing with radiative relaxation (PL) and dissociation. The latter pathway becomes dominant with increasing acceptor concentration nearly blocking the two others and therefore the singlet-triplet pathway. This is supported by our photoinduced absorption data showing the absence of triplet-triplet absorption in both the MEH-PPV/TNF and MEH-PPV/DNAQ blends (see Sec. 4.3.2). The complete correlation between the PL intensity and photooxidation rate in MEH-PPV/TNF blends Fig. 136 (top)) suggests that MEH-PPV triplet excitons are the sole intermediate for photooxidation in these blends. However, in MEH-PPV/DNAQ blends the concentration dependence of the

photooxidation rate is smoother than that of PL indicating that not only MEH-PPV triplet excitons are responsible for photooxidation.

The faster photooxidation rate in MEH-PPV/DNAQ blends could be explained as follows. Photoexcitation of this blend results in a long lived charged separated state  $\text{MEH-PPV}^+/\text{DNAQ}^-$  as our photoinduced absorption data indicate. Subsequently, a radical anion  $\text{DNAQ}^-$  can reduce molecular oxygen to superoxide (anion  $\text{O}_2^-$ ). This electron transfer is shown to be efficient for anions of dicyanoanthracene, whose reduction potential is close to that of DNAQ ( $-0.7$  eV). Superoxide is shown to be responsible for photooxidation of model compounds of PPV and probably can react with  $\text{MEH-PPV}^+$ . Note that as TNF has a  $\sim 0.5$  V lower reduction potential than oxygen, therefore the above mechanism of oxygen reduction in photoexcited MEH-PPV/TNF blend should be far less efficient.

Our data support earlier findings that quenching of excited triplet states could be an effective means to slow down photooxidation of conjugated polymer chains. Note that photoexcited triplets in donor/acceptor blends apparently should be quenched at both the donor and acceptor. Indeed, it is reasonable to suppose that photooxidation of MDMO-PPV/ $\text{C}_{60}$  blends is mainly controlled by triplet states forming at  $\text{C}_{60}$ . Noticeably absorbing visible light,  $\text{C}_{60}$  is known to be an efficient photosensitizer of singlet oxygen, which oxidizes the conjugated polymer.

#### 4.3.6.2 Optical absorption

Films of MEH-PPV/TNF blends with different molar donor/acceptor ratio were prepared by spin-casting from chlorobenzene solution on glass substrates. Evolution of the absorption spectra of MEH-PPV/TNF films was evaluated under irradiation with broad-band light by using a collimated beam from a 1000 W xenon lamp.

Fig. 137 shows photobleaching a pristine MEH-PPV film. It is seen that the lowest absorption band of MEH-PPV at  $\sim 500$  nm completely disappears after 30 min of irradiation. The observed photobleaching is obviously a direct result of photooxidation observed in the FTIR spectra as well (Fig. 133). Fig. 138 illustrates decreasing in the photobleaching rate in MEH-PPV/TNF blends. It is seen that addition of TNF to MEH-PPV considerably slows down the photobleaching rate.

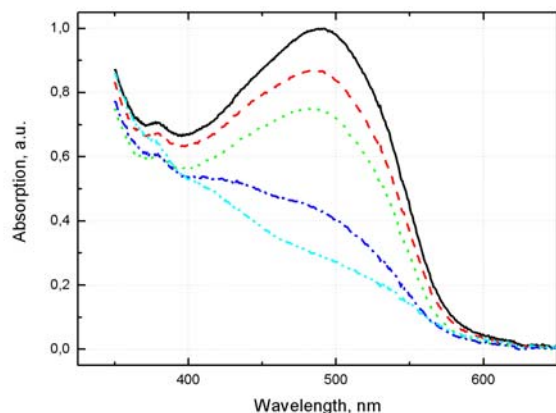


Fig. 137. Absorption spectra of a spin-cast MEH-PPV film recorded for different times of irradiation: 0, 1, 3, 15, and 30 min (from top to bottom).

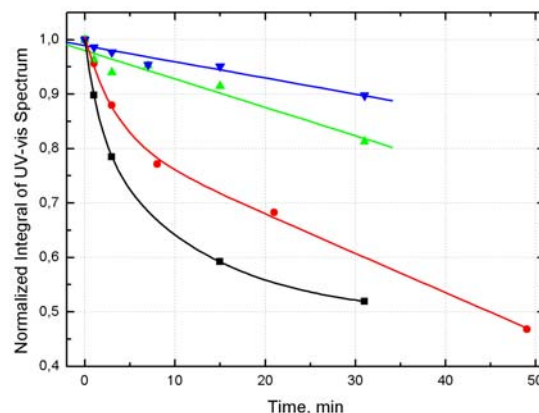


Fig. 138. Integral intensity of UV-vis spectrum of MEH-PPV/TNF blends as a function of irradiation time; pristine MEH-PPV (black); MEH-PPV:TNF = 1:0,3 (red); MEH-PPV:TNF = 1:0,6 (green); MEH-PPV:TNF = 1:1 (blue) (from bottom to top). The lines are a guide to the eye.

However, comparing Fig. 135 and Fig. 138 one can see that the photobleaching rate for MEH-PPV/TNF blends is essentially higher under the broad-band irradiation than their photooxidation rate under the monochromatic green irradiation of similar intensity. This suggests that mainly UV light results in photodegradation of MEH-PPV/TNF. Note that for correct comparison of the photooxidation and photobleaching rates an adequate model should be developed. Such a model should take into account the effect of film thickness and analyze the data in terms of the photooxidation rate parameter calculated as the number of absorbed photons per MEH-PPV monomer resulting in its oxidation [23]. Development of this model is beyond of the scope of this project.

#### **4.3.6.3 Discussion**

In our studies of MEH-PPV/TNF and MEH-PPV/DNAQ blends under green monochromatic irradiation, the triplets at the acceptor can not be populated by its direct light absorption as the absorption edge of these acceptors is around 400 nm. On the other hand, we observed that the photooxidation rate was noticeably higher in the blends irradiated by a broad-band radiation from a Xe lamp as compared with green irradiation. Assuming that the photooxidation rate does not strongly depend on the irradiation wavelength in films of PPV-type polymers [23], one could suppose that the acceptor absorption results in singlet oxygen generation via acceptor's triplets states. The triplet quantum yield in photoexcited TNF is expected to be as high as that of nitrofluorenone for which the quantum yield about unity was reported [24].

In conclusion, we have demonstrated a dramatic increase in photostability of MEH-PPV/TNF and MEH-PPV/DNAQ blends under monochromatic green radiation in ambient conditions. This suggests that a PPV-type polymer in an appropriate donor-acceptor blend could have the lifetime reaching thousands of hours under visible radiation of solar intensity in ambient conditions. However, the photostability of MEH-PPV/TNF blends under broad-band radiation containing UV light is less pronounced. To clarify photooxidation mechanisms and their dependence on light wavelength, a more detailed study is necessary.

### **4.4 Ternary blends**

The MEH-PPV CTCs have essential absorption in the red spectral range, but they give low photocurrents as compared with polymer/fullerene blends. For efficient polymer solar cells, it would be important to combine the important properties of conjugated polymer CTCs such as strong absorption in the red and enhanced photooxidation stability with the indispensable properties of fullerenes such as efficient generation of charge-separated states and relatively high charge mobilities. This combination might be realized in ternary blends consisting of a polymer donor and two acceptors: one of which forms a CTC with the donor, and the other is fullerene accepting the photoexcited electrons and providing their transport. For realization of efficient photoinduced electron transfer to the fullerene, to a first approximation, one needs to have the LUMO of fullerene lower than the LUMO of the acceptor forming the CTC (Fig. 139). According to the literature electrochemical data, the LUMO of  $C_{60}$  is lower than the LUMO of DNAQ but higher than the LUMO of TNF. Therefore, one could expect the photoinduced charge transfer from CTC to  $C_{60}$  to occur in the MEH-PPV/DNAQ/ $C_{60}$  blend. We also have tried a soluble fullerene derivative (PCBM) as the second acceptor in MEH-PPV/DNAQ/PCBM blend. The LUMO of PCBM is higher by 0.1 eV than that of  $C_{60}$ , and is close to that of DNAQ.

#### **4.4.1 Photoinduced charge generation**

We have studied ternary blends MEH-PPV/TNF/ $C_{60}$  and MEH-PPV/DNAQ/ $C_{60}$ . Each component was individually dissolved in chlorobenzene with concentration 2 g/l. Then the solutions were mixed with

the molar ratio of components MEH-PPV:acceptor:fullerene=1:0.3:0.05 (acceptor=TNF or DNAQ). Films were prepared by drop-casting on glass substrates. The ratio MEH-PPV/DNAQ and MEH-PPV/TNF was 1:0.3 to provide the maximum CTC concentration in the films. The absorption spectra of MEH-PPV/TNF/C<sub>60</sub> and MEH-PPV/DNAQ/C<sub>60</sub> were almost the same as those of MEH-PPV/TNF and MEH-PPV/DNAQ, respectively. To identify photoinduced charge transfer in ternary blends, we used photoinduced absorption (PIA) spectroscopy with red excitation at 670 nm below the absorption edge of pristine MEH-PPV. Therefore, only the photoexcited states of the CTC could contribute to the PIA spectra.

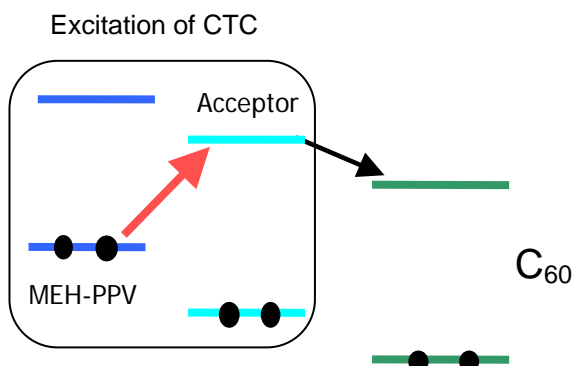


Fig. 139. Photoinduced charge transfer in the ternary blend.

#### *MEH-PPV/TNF/C<sub>60</sub> blend*

Phase separation characteristic of the TNF phase was strongly enhanced in the ternary blend compared with the binary one (MEH-PPV/TNF) as was seen in an optical microscope. We observed that PIA spectra of the PPV/TNF/C<sub>60</sub> blend were the same both in shape and magnitude as those of MEH-PPV/TNF blends. This indicates that C<sub>60</sub> hardly has any influence on charge separation in the ternary blend. Indeed, according to the electrochemical data, the reduction potential in TNF is 0.28 eV higher than in C<sub>60</sub> (−0.6 V) (Table 2). Therefore, TNF as a stronger electronic acceptor should retain the photoexcited electron that is supported by our PIA data.

#### *MEH-PPV/DNAQ/fullerene blend*

Phase separation features characteristic of the DNAQ phase were nearly the same in the binary and ternary blends as was observed in an optical microscope. Fig. 140 compares optical absorption spectra of MEH-PPV/DNAQ and MEH-PPV/DNAQ/C<sub>60</sub> blends. It is seen that the red shift of the MEH-PPV absorption edge is less in the ternary blend upon addition of 5 % mol. of C<sub>60</sub>. This indicates that C<sub>60</sub> influences the MEH-PPV/DNAQ CTC. Fig. 141 (left) compares PIA spectra in MEH-PPV/DNAQ/C<sub>60</sub> and MEH-PPV/DNAQ blends. It is seen that addition of C<sub>60</sub> to MEH-PPV/DNAQ results in a twentyfold increase of the MEH-PPV polaron band at 1.2 eV. Therefore, C<sub>60</sub> facilitates generation of long-lived charges in the photoexcited CTC implying that the LUMO of C<sub>60</sub> is lower than the LUMO of DNAQ. This is in accordance with the electrochemical data showing that the reduction potential in C<sub>60</sub> is 0.14 eV higher than in DNAQ (Table 2). Fig. 141 (right) compares the PIA spectra in MEH-PPV/DNAQ/C<sub>60</sub> and MEH-PPV/C<sub>60</sub> blends photoexcited at 670 nm and 532 nm, respectively. The spectra have nearly the identical shape and the intensities of both polaron bands (at ~1.3 eV and below 0.8 eV) are close in both blends for the similar photoexcitation conditions. Almost the same PIA spectra were measured for MEH-PPV/DNAQ/PCBM blend. This indicates that the photoinduced charge transfer efficiency in the ternary blend is close to that in the binary blend. For the latter, the efficiency about 100% is commonly suggested.

Thus, our PIA data show that long-lived holes are efficiently generated in the MEH-PPV/DNAQ/C<sub>60</sub> and MEH-PPV/DNAQ/PCBM blends for photon energy below the optical gap of MEH-PPV. Therefore, polymer CTCs could be used as a red absorber in polymer/fullerene solar cells. Our

PIA studies also suggest that tuning the difference between the LUMOs of the acceptor forming the CTC and fullerene, one can achieve efficient generation of long-lived charges in ternary blends. Given the enhanced photostability of the CTC, ternary blends might be a promising approach in polymer solar cells.

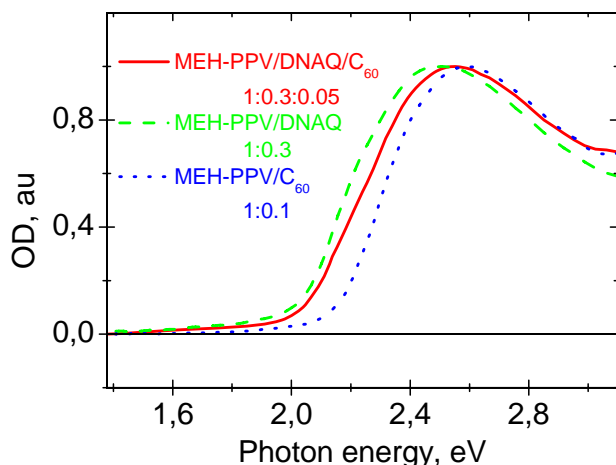


Fig. 140. Normalized absorption spectra of MEH-PPV/DNAQ and MEH-PPV/DNAQ/C<sub>60</sub> blends.

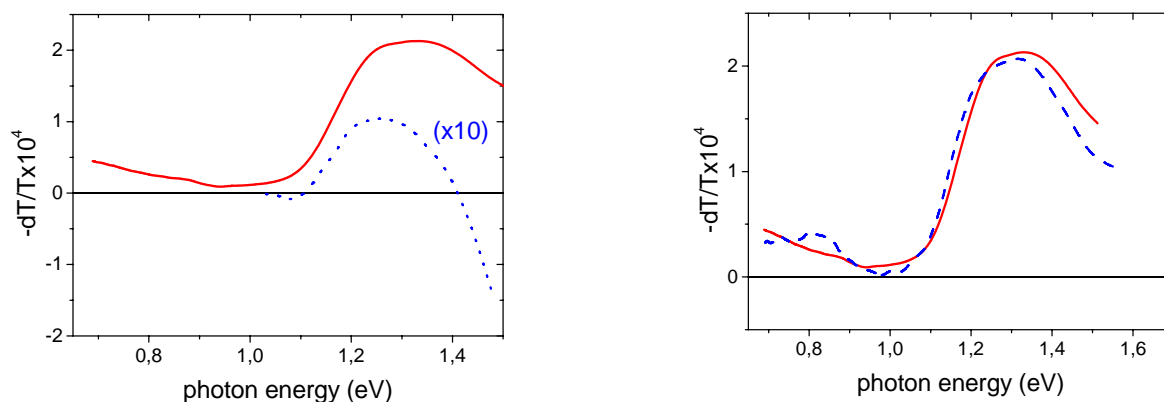


Fig. 141. PIA spectra in ternary and binary blends measured at room temperature and chopping frequency 75 Hz. Left: PIA in 1:0.3:0.05 MEH-PPV/DNAQ/C<sub>60</sub> (solid) and 1:0.3 MEH-PPV/DNAQ (dashed, x10) blends excited at 670 nm. Right: PIA in MEH-PPV/DNAQ/C<sub>60</sub> blend (solid) excited at 670 nm and MEH-PPV/C<sub>60</sub> blend (dashed) excited at 532 nm; the fluxes of absorbed pump photons were approximately the same for both wavelengths.

#### 4.4.2 Photoelectric data

We have performed comparative photoelectric studies of photodiodes with ternary blends (MEH-PPV/DNAQ/C<sub>60</sub> and MEH-PPV/TNF/C<sub>60</sub>) as active layers. As reference devices, we used photodiodes with binary blends MEH-PPV/DNAQ, MEH-PPV/TNF, and MEH-PPV/C<sub>60</sub>. We tried to keep the device preparation steps (Sec. 3.3.4) and the measurement procedures (Sec. 2.12) as close as possible. The optical density of the active layer was below unity allowing us to neglect the internal filter effect. We expected to obtain higher EQE in the MEH-PPV/DNAQ/C<sub>60</sub> blend as the photoinduced charge

transfer from the CTC to  $C_{60}$  is very efficient as follows from our PIA data (see the preceding section).

Fig. 142 compares photocurrent action spectra of photodiodes with ternary and binary blends. Addition of  $C_{60}$  seems to affect the EQE of MEH-PPV/DNAQ and MEH-PPV/TNF blends analogously for both acceptors increasing the EQE by  $\sim 1.5$  order of magnitude in the MEH-PPV absorption range and by almost 3 orders in the MEH-PPV optical gap (Fig. 142). This observation allows us to suppose that  $C_{60}$  affects both blends via the same mechanism regardless of the acceptor's electron affinities or CTC properties. One can suggest that the main contribution to photocurrent in the ternary blends stems from MEH-PPV species that are not involved in the CTC.

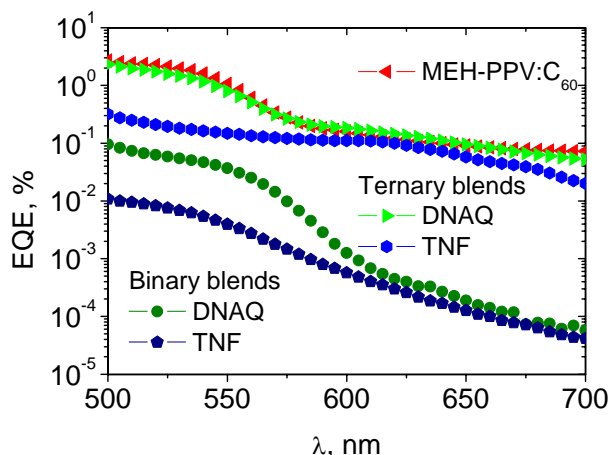


Fig. 142 Photocurrent action spectra of MEH-PPV/acceptor/ $C_{60}$  photodiodes for TNF and DNAQ as an acceptor. Spectra of MEH-PPV/ $C_{60}$ , MEH-PPV/TNF, and MEH-PPV/DNAQ photodiodes are given for comparison.

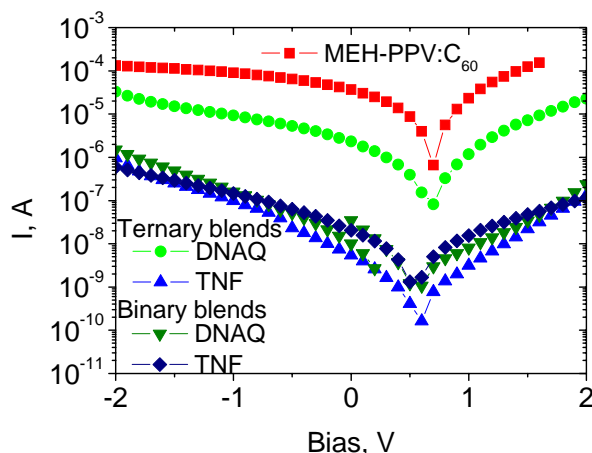


Fig. 143 Current to voltage characteristics of MEH-PPV/acceptor/ $C_{60}$  blend photodiodes for TNF and DNAQ as acceptor. Curves for MEH-PPV/ $C_{60}$ , MEH-PPV/TNF, and MEH-PPV/DNAQ photodiodes are given for comparison.

From our PIA studies of the ternary blends we expected that the ternary blend with DNAQ could result in increasing the photocurrent below the absorption edge of MEH-PPV, whereas the blend with TNF should not. However,  $C_{60}$  has noticeable absorption in the MEH-PPV optical gap as seen in the photocurrent spectra of MEH-PPV and MEH-PPV/ $C_{60}$  (see below Fig. 165). Probably  $C_{60}$  absorption hinders in observation of the possible contribution to the photocurrent CTC in the MEH-PPV/DNAQ/ $C_{60}$  device in the optical gap of MEH-PPV. In addition,  $C_{60}$  in the ternary blend could result in decreasing the concentration of MEH-PPV complexed species as follows from the absorption spectra in Fig. 140.

Fig. 143 presents current-to-voltage characteristics of photodiodes with the ternary and binary blends under white light illumination. Table 12 summarizes the corresponding parameters. It is seen that the MEH-PPV/ $C_{60}$  blend shows the highest photocurrent. The photocurrent in the MEH-PPV/DNAQ/ $C_{60}$  blend is about one order lower than that in the MEH-PPV/ $C_{60}$  blend. In the MEH-PPV/TNF/ $C_{60}$  blend,  $C_{60}$  does not result in any increase in the photocurrent (Fig. 143). One can suppose that the morphology of the bulk heterojunction in the ternary blends is not optimal for charge collection as compared with the binary MEH-PPV/fullerene blends.

Thus, we have not managed to observe any increase in photocurrent in the ternary blends as compared with the binary ones. Photocurrents in the MEH-PPV/ $C_{60}$  and MEH-PPV/DNAQ/ $C_{60}$  blends were almost the same under weak monochromatic illumination and by one order of magnitude less in the ternary blend under intensive white light illumination. Whether the photocurrent could be

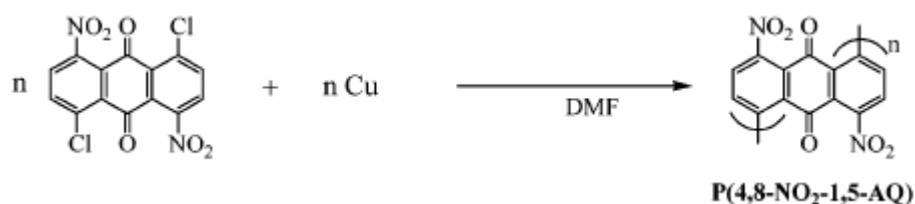
increased in polymer solar cells by using red absorption of the CTC is not clear at the moment. In the project, we have studied only a few samples, and possibly optimization of the ternary blends (for example, using PCBM, varying the ratio of the components etc.) is necessary to arrive to more definite conclusions.

Active layer (numbers show donor/acceptor molar ratio)	$I_{sc}$ , $\mu A/cm^2$	$V_{oc}$ , V	$FF$ , %	$EQE$ at 500 nm, %	Energetic efficiency $\eta$ , %
MEH-PPV:TNF 1:0.3	0.41	0.54	21.7	0.012	$4.8 \cdot 10^{-05}$
MEH-PPV:TNF:C <sub>60</sub> 1:0.3:0.4	0.11	0.57	17.2	0.32	$1.1 \cdot 10^{-05}$
MEH-PPV:DNAQ 1:0.3	0.7	0.54	14.2	0.096	$5.4 \cdot 10^{-05}$
MEH-PPV:DNAQ:C <sub>60</sub> 1:0.3:0.4	46.4	0.66	19.6	2.3	$6.0 \cdot 10^{-03}$
MEH-PPV:C <sub>60</sub> 1:0.4	738	0.68	23.1	2.7	0.12

Table 12. Characteristics of photodiodes on ternary and binary blends.

## 4.5 MEH-PPV/DNAQ and MEH-PPV/polyDNAQ blends

As showed above, blends of MEH-PPV forms a CTC with 1,5-dinitroanthraquinone (DNAQ). One can suppose that for a quasi one-dimensional conjugated chain one needs an acceptor with similar structure in order to realize efficient CT interaction. Furthermore, for solar cells it is essential to have conductive both the donor and acceptor networks to allow the photoinduced charges to be transported. Therefore, a polymeric acceptor might be the optimal one. Motivated by these points, we have studied donor-acceptor blends of MEH-PPV with a polymer form of DNAQ (polyDNAQ). The first question to be studied was: can polyDNAQ form a CTC with MEH-PPV? Below we compare our data for MEH-PPV/DNAQ and MEH-PPV/polyDNAQ blends from absorption, vibrational, light scattering, PL, and PIA spectroscopies. Then we compare photoelectric data for these blends. The polymeric acceptor poly[4,8-dinitro-1,5-anthraquinone] (polyDNAQ) was obtained from Prof. T. Yamamoto (Tokyo Institute of Technology). Polymer was synthesized according the following reaction:



A number of its properties are described in *Chem. Mater.* **15** 4384 (2003). At the first stage, we have searched for a common solvent for MEH-PPV and polyDNAQ. polyDNAQ has MW~10000 and dissolves in N-methyl-pyrrolidone, DMFA and other polar solvents in which MEH-PPV does not dissolve. It was found that both components dissolve in cyclohexanone, CCl<sub>4</sub>, dichloroethane, and THF with polyDNAQ dissolving only partly (40–80%). MEH-PPV/polyDNAQ films were prepared from these solutions by spin-casting, drop-casting, and SSE.

### 4.5.1 Absorption, light scattering, and Raman data

Fig. 144 and Fig. 145 compare optical absorption spectra of MEH-PPV/DNAQ and MEH-PPV/polyDNAQ for different donor-acceptor ratios, respectively. If the 1:1 MEH-PPV/DNAQ film demonstrates noticeable absorption beyond 600 nm (Fig. 144), i.e., below the MEH-PPV absorption



edge, absorption of MEH-PPV/polyDNAQ in this spectral range is questionable (Fig. 145). In fact, light scattering is a typical feature in films of donor-acceptor blends resulting from phase separation of non-interacting donor and acceptor (e.g. MEH-PPV/C<sub>60</sub>). To establish the origin of the long-wavelength tails observed in the optical transmission spectra of the films, we have applied our absorption/scattering technique described in Sec. 2.2.

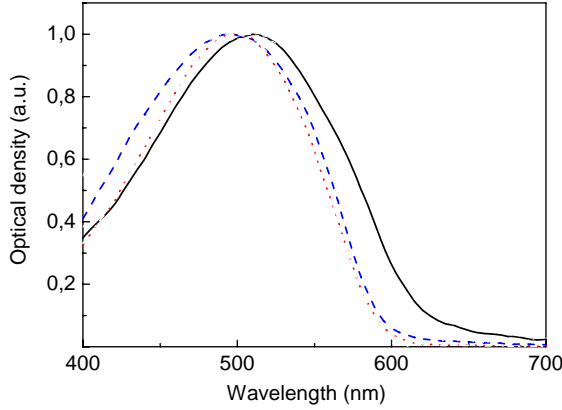


Fig. 144. Normalized absorption spectra MEH-PPV/DNAQ drop-cast films for molar MEH-PPV:DNAQ ratio 1:0.03 (dotted), 1:0.1 (dashed), and 1:1 (solid). The films were prepared from chlorobenzene.

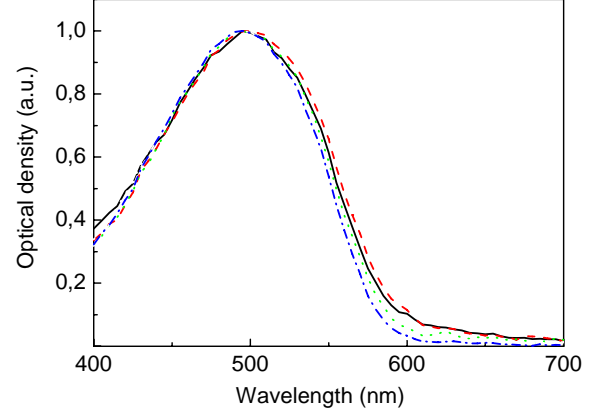


Fig. 145. Normalized absorption spectra MEH-PPV/polyDNAQ drop-cast films for molar MEH-PPV:polyDNAQ ratio 1:0.01 (dash-dotted), 1:0.25 (dotted), 1:0.5 (dashed), and 1:1 (solid). The films were prepared from dichloroethane.

Fig. 146 shows absorption ( $\alpha d$ ), scattering ( $\sigma d$ ), and their sum at 633 nm for MEH-PPV/DNAQ films with different donor/acceptor ratio. Essentially that almost all the measured optical density at 633 nm, i.e.,  $hd = \alpha d + \sigma d$ , results from the optical absorption (see Fig. 144).

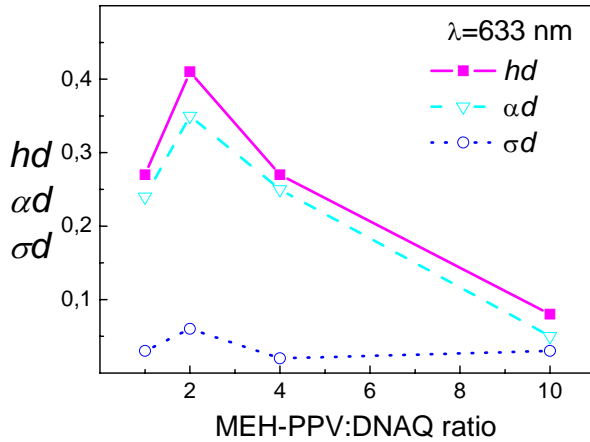


Fig. 146. Absorption ( $\alpha d$ ), scattering ( $\sigma d$ ) and their sum ( $hd = \alpha d + \sigma d$ ) at 633 nm for MEH-PPV/DNAQ drop-cast films prepared from chlorobenzene.

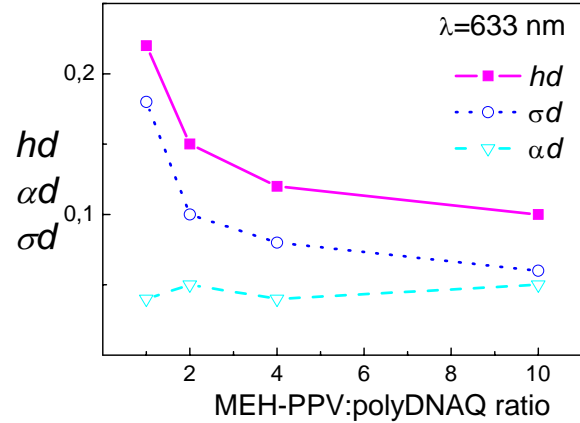


Fig. 147. Absorption ( $\alpha d$ ), scattering ( $\sigma d$ ) and their sum at 633 nm for MEH-PPV/polyDNAQ drop-cast films prepared from dichloroethane.

Fig. 145 demonstrates that MEH-PPV/polyDNAQ films do not significantly change their optical absorption spectra with increasing the acceptor content as we have observed for MEH-PPV/DNAQ and MEH-PPV/TNF blends. Fig. 147 shows absorption ( $\alpha d$ ), scattering ( $\sigma d$ ), and their sum at 633 nm for MEH-PPV/polyDNAQ films with different donor/acceptor ratio. In contrast to MEH-PPV/DNAQ films (Fig. 146), the absorption in MEH-PPV/polyDNAQ films is much less than the scattering. Moreover, for MEH-PPV/polyDNAQ films the absorption loss ( $\alpha d$ ) is comparable with our experimental error. Therefore we can not assign the observed tails in the optical transmission spectra in Fig. 145 to the light absorption. As follows from Fig. 146 and Fig. 147, the light scattering level in the MEH-PPV/polyDNAQ films is higher than in MEH-PPV/DNAQ films. This possibly indicates that the characteristic scale of phase separation is much closer to the optical wavelength as compared with that of MEH-PPV/DNAQ. In fact, DNAQ in MEH-PPV/DNAQ drop-cast films forms features with a typical size of 20–50  $\mu\text{m}$  (Sec. 4.2.3.2).

Ground-state CT results in a red shift of the strongest MEH-PPV Raman band at 1582  $\text{cm}^{-1}$  (see Sec. 4.1.1.2). Fig. 148 compares Raman spectra of MEH-PPV/polyDNAQ, MEH-PPV/DNAQ, and pristine MEH-PPV drop-cast films. It is seen that the MEH-PPV/polyDNAQ does not show any red shift of the 1582  $\text{cm}^{-1}$  band compared with the pristine MEH-PPV. On the other hand, the red shift is clearly seen in the MEH-PPV/DNAQ film (Fig. 148).

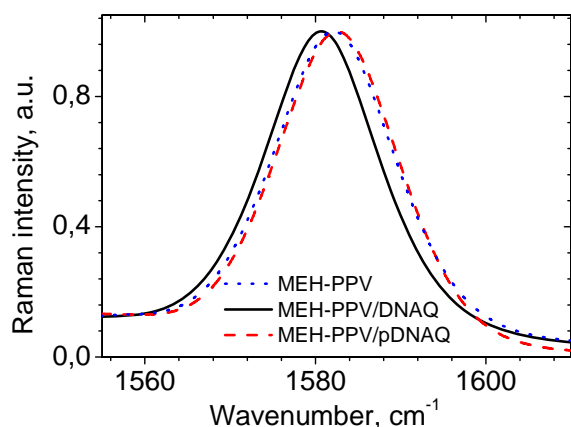


Fig. 148. Raman spectra of 1:1 MEH-PPV/polyDNAQ, 1:1 MEH-PPV/DNAQ, and pristine MEH-PPV drop-cast films. The pristine MEH-PPV and MEH-PPV/DNAQ films were prepared from chlorobenzene, and the MEH-PPV/polyDNAQ film was prepared from dichloroethane. The excitation wavelength was 670 nm.

Thus, we have not observed any evidence of ground-state CT in MEH-PPV/polyDNAQ films. This could be explained in the following way. DNAQ monomers are expected to be readily dispersed within the MEH-PPV matrix forming close contacts with MEH-PPV chains as illustrated in Fig. 149 (left). On the other hand, two polymers hardly would intermix at the molecular scale (Fig. 149, right) as a polymer and small molecules. CT interaction could occur at the interface between the two polymers as shown in Fig. 149 (right). It seems that the effective area of this interface is too small, and therefore the density of possible CT sites is too low to be detected.

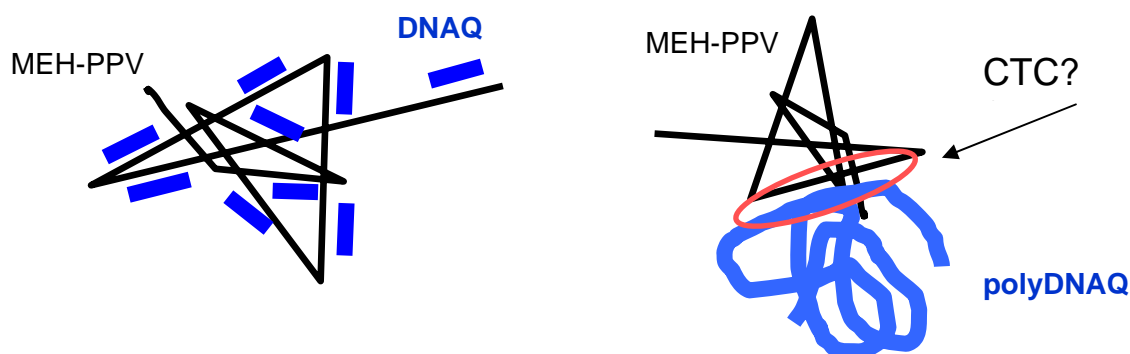


Fig. 149. Possible schematic structure of MEH-PPV/DNAQ (left) and MEH-PPV/pDNAQ (right) blends.

### 4.5.2 Photoluminescence

At the next stage, we have studied the properties of the photoexcited states of MEH-PPV/polyDNAQ films. First of all, we have observed that polyDNAQ is quite an efficient quencher of MEH-PPV PL as well as DNAQ. Note that pristine polyDNAQ has a very weak PL band at  $\sim 380$  nm, therefore for 532-nm excitation of MEH-PPV/polyDNAQ blends only the MEH-PPV PL is essential. To reveal the difference between the monomer and polymer forms of DNAQ, we have studied PL quenching in MEH-PPV/DNAQ and MEH-PPV/polyDNAQ films varying the acceptor content. Fig. 150 summarizes the results. It is seen that both acceptors quench PL very efficiently and their concentration dependencies are nearly the same. In terms of absolute values, the monomer DNAQ quenches the MEH-PPV PL by 1.5–2 times more efficient than the polyDNAQ (Fig. 150).

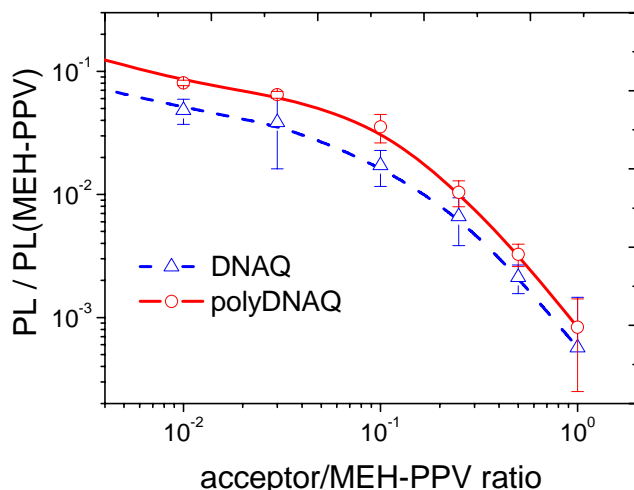


Fig. 150. Peak PL signal in MEH-PPV/DNAQ and MEH-PPV/polyDNAQ films normalized to the PL from pristine MEH-PPV. PL excited at 532 nm in optically thick drop-cast films was recorded at the backscattering geometry in ambient room conditions. The effect of PL degradation during the measurement was less than 10%. Each data point is a result of averaging out over two films of different thicknesses. The PL absorption was evaluated as no more than 10–15%.

This could be associated with more thorough donor-acceptor mixing of MEH-PPV chains with DNAQ monomers than with polyDNAQ. In fact, the ground-state CT was reliably observed only in MEH-PPV/DNAQ implying noticeable attractive interaction between the donor and the acceptor. This CT interaction seems to compete with phase separation. The latter is expected to be more pronounced for MEH-PPV/polyDNAQ films at the nanoscale as could be suggested from our light scattering data (see the preceding section). On the other hand, the efficiency of PL quenching in donor-acceptor blends depends on the average exciton diffusion length (time) from the point of its excitation to the donor-acceptor interface. Therefore, the less the phase separation scale, the more efficient the PL quenching. Essentially that if a photon is absorbed by the CTC, there is no stage of exciton diffusion at all and this case should correspond to the maximum PL quenching efficiency. At the same time, we observe that the difference in PL quenching by DNAQ and polyDNAQ is not very high implying that the exciton diffusion time over the typical phase separation scale ( $\sim 10$  nm) is quite short compared with the lifetime of singlet exciton at MEH-PPV.

### 4.5.3 Photoinduced absorption spectroscopy

We have done comparative studies of photoexcited states in MEH-PPV/polyDNAQ and MEH-PPV/DNAQ films using our PIA technique, which can probe the long-lived charged states. We kept the film preparation and experimental conditions as close as possible. Note that MEH-PPV/polyDNAQ blends do not show any noticeable PIA signal for red pump at 670 nm, at which the blends are almost transparent. Because of this, only the pump at 532 nm was used.

Fig. 151 compares PIA spectra in 1:0.5 MEH-PPV/DNAQ and 1:1 MEH-PPV/polyDNAQ films. It is seen that the intensity of the polaron peak is a few times higher in MEH-PPV/polyDNAQ than in

MEH-PPV/DNAQ despite the pump absorption in the former was somewhat less in the latter. This difference in PIA intensity was typically observed for different experimental conditions (temperature, pump chopping frequency, pump intensity) and donor-acceptor ratios (see below). Fig. 152 compares normalized PIA spectra of MEH-PPV/DNAQ, MEH-PPV/polyDNAQ, and 1:0.2 MEH-PPV/C<sub>60</sub> films. We use the latter blend as a reference that according to the literature data provides nearly 100% charge separation efficiency for a singlet exciton photoexcited in MEH-PPV. It is seen that the MEH-PPV/polyDNAQ blend demonstrates almost the same PIA shape as the MEH-PPV/C<sub>60</sub> blend. This is again in accordance with our above observations that MEH-PPV does not form a CTC with polyDNAQ. The PIA signal in the MEH-PPV/C<sub>60</sub> blend was ~2 times higher than in the MEH-PPV/polyDNAQ blend taking into account the optical densities of the films at the pump wavelength.

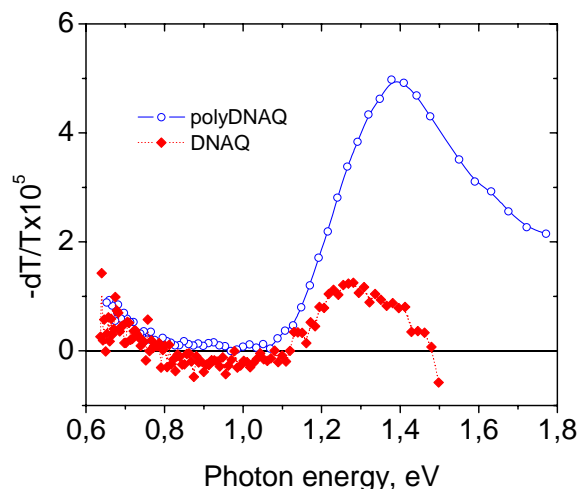


Fig. 151. PIA spectra of 1:1 MEH-PPV/DNAQ and 1:0.5 MEH-PPV/polyDNAQ drop-cast films photoexcited at 532 nm. The chop frequency was 75 Hz, pump intensity ~300 mW/cm<sup>2</sup>, T≈300 K.

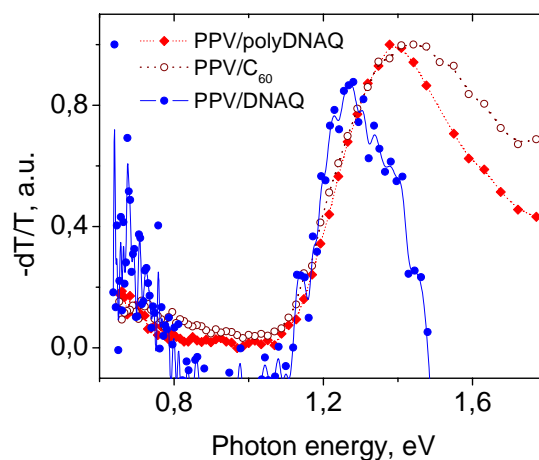


Fig. 152. Normalized PIA spectra of 1:0.2 MEH-PPV/C<sub>60</sub>, 1:1 MEH-PPV/DNAQ and 1:0.5 MEH-PPV/polyDNAQ films. For other parameters see the caption of Fig. 151.

We have investigated the effect of acceptor concentration on the PIA spectra of MEH-PPV/DNAQ and MEH-PPV/polyDNAQ films varying the acceptor/donor ratio from 0.01 to 1. All the spectra for a given acceptor had similar shapes with only the PIA signal magnitude changing. Fig. 153 shows the polaron peak intensity at 1.3 eV as a function of acceptor/donor ratio. It is seen that the PIA in MEH-PPV/polyDNAQ films is systematically higher than in MEH-PPV/DNAQ films. Note that the PIA signal tends to saturate at the acceptor/donor ratio about 0.2–0.4 (Fig. 153) indicating saturation in the charge separation efficiency.

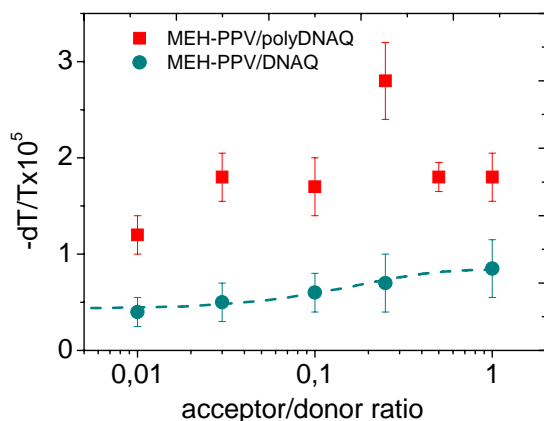


Fig. 153. PIA peak intensity at 1.3 eV vs molar acceptor/donor ratio for MEH-PPV/DNAQ and MEH-PPV/polyDNAQ films prepared from chlorobenzene and dichloroethane, respectively. The data were normalized to the absorbed pump intensity. Experimental conditions are indicated in Fig. 151

We conclude that singlet excitons in MEH-PPV/polyDNAQ dissociate quite efficiently in long-lived charged-separated states with the CGE being a few times lower in MEH-PPV/DNAQ films. On the other hand, the PL quenching data in Fig. 150 indicate that the initial charge separation is more efficient in MEH-PPV/DNAQ blends. Therefore, one can suggest that the charge separation at the millisecond time scale in MEH-PPV/DNAQ films is less efficient due to relatively higher probability of geminate recombination in the CTC.

#### 4.5.4 Photoelectric data

We have performed comparative photoelectric studies of MEH-PPV/DNAQ and MEH-PPV/polyDNAQ blends. We tried to keep the device preparation steps (Sec. 3.3.4) and the measurement procedures (Sec. 2.12) as close as possible. The optical density of the active layer was below unity allowing us to neglect the internal filter effect.

Fig. 154 and Fig. 155 show photocurrent action spectra of photodiodes with monomer and polymer form of DNAQ as an acceptor, respectively. It is seen that MEH-PPV/polyDNAQ photodiodes demonstrate EQE increase in 600–700 nm region but less than for the photodiodes with DNAQ. PolyDNAQ also slightly increases the EQE for wavelength less than 550 nm leaving it unchanged at the absorption edge. The 1:1 MEH-PPV:polyDNAQ photodiode gives a considerably lower EQE within all the examined spectral range that possibly reflects the peculiarities of this sample.

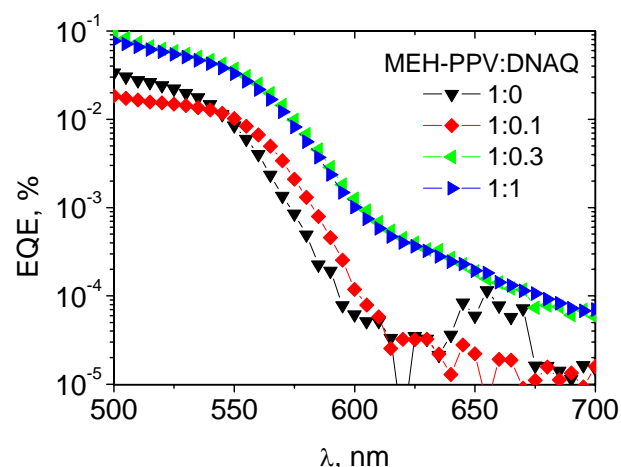


Fig. 154 Photocurrent action spectra of MEH-PPV/DNAQ photodiodes for different donor/acceptor ratios.

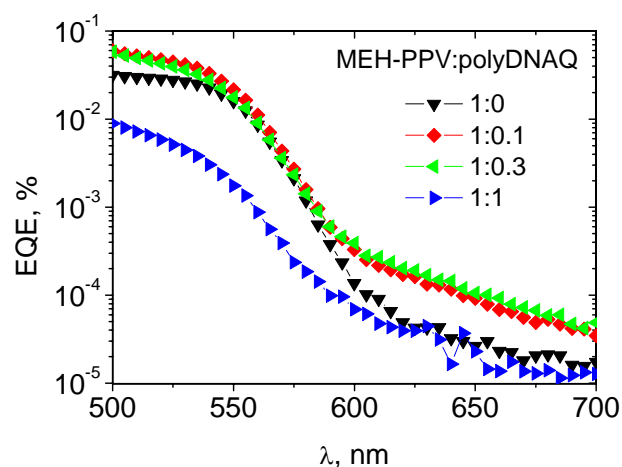


Fig. 155 Photocurrent action spectra of MEH-PPV/polyDNAQ photodiodes for different donor/acceptor ratios.

Fig. 156 and Fig. 157 show current-to-voltage characteristics of MEH-PPV/DNAQ and MEH-PPV/polyDNAQ photodiodes. Table 13 summarizes characteristics of MEH-PPV/DNAQ and MEH-PPV/polyDNAQ photodiodes. One can see that the MEH-PPV/polyDNAQ bulk heterojunction has a very low efficiency of charge collection despite our PIA studies indicated a few times higher efficiency of charge generation in MEH-PPV/polyDNAQ blends than in MEH-PPV/DNAQ ones (see the preceding section). Unfortunately, the observed photocurrents were too low and hardly showed any systematic behavior to arrive to any definite conclusions. Possibly, the device preparation procedure was not optimal for MEH-PPV/polyDNAQ devices.

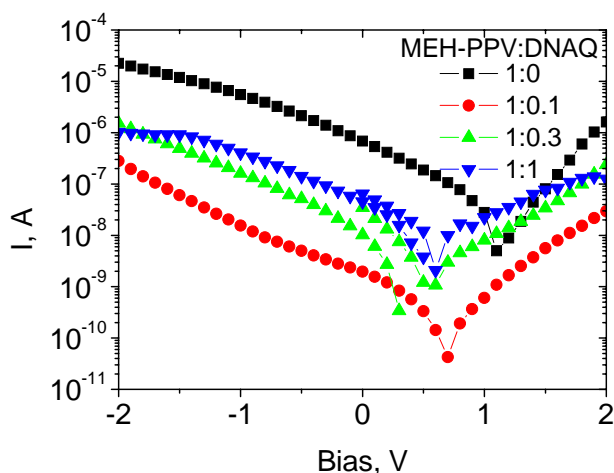


Fig. 156 Current-to-voltage characteristics of MEH-PPV/DNAQ photodiodes for different donor/acceptor ratios.

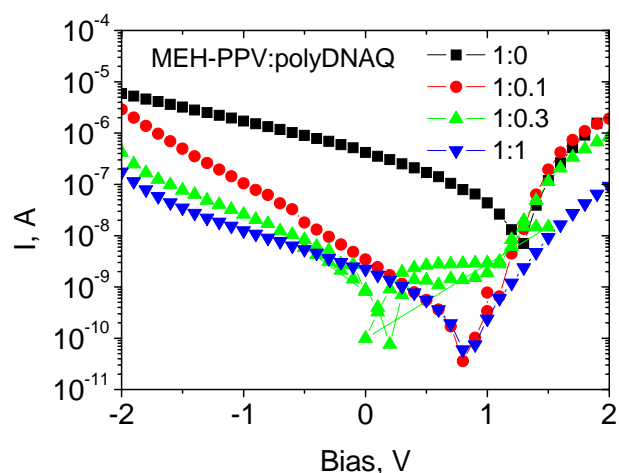


Fig. 157 Current-to-voltage characteristics of MEH-PPV/polyDNAQ photodiodes for different donor/acceptor ratios. The curve for the 1:0.3 MEH-PPV/polyDNAQ device in the bias range 0..1 V is incorrect due to measurement bugs

Active layer (numbers show donor/acceptor molar ratio)	$I_{sc}$ , $\mu\text{A}/\text{cm}^2$	$V_{oc}$ , V	$FF$ , %	$EQE$ at 500 nm, %	Energetic efficiency $\eta$ , %
MEH-PPV:DNAQ 1:1	1.14	0.77	16.1	0.08	$1.4 \cdot 10^{-04}$
MEH-PPV:DNAQ 1:0.3	0.7	0.54	14.2	0.10	$5.4 \cdot 10^{-05}$
MEH-PPV:DNAQ 1:0.1	0.04	0.67	19.5	0.02	$5.2 \cdot 10^{-06}$
MEH-PPV:polyDNAQ 1:1	0.04	0.84	16.8	0.01	$5.7 \cdot 10^{-06}$
MEH-PPV:polyDNAQ 1:0.3	-	-	-	0.06	-
MEH-PPV:polyDNAQ 1:0.1	0.07	0.82	12.7	0.06	$7.3 \cdot 10^{-06}$
Pristine MEH-PPV	8.35	1.26	16.2	0.03	$1.7 \cdot 10^{-03}$
MEH-PPV:C <sub>60</sub> 1:0.4	738	0.68	23.1	2.7	0.12

Table 13. Characteristics of MEH-PPV/DNAQ and MEH-PPV/polyDNAQ photodiodes.

#### 4.5.5 MEH-PPV/DNAQ and MEH-PPV/polyDNAQ: summary

Table 14 summarizes the results of our comparative studies. We have observed that the monomer DNAQ forms a weak ground-state CTC in MEH-PPV/DNAQ films, whereas any signatures of CTC in MEH-PPV/polyDNAQ films have not been found. Light scattering in MEH-PPV/DNAQ blends is noticeably lower than that in MEH-PPV/polyDNAQ blends reflecting a difference in phase separation in them. The exciton singlet states in MEH-PPV are efficiently quenched by either DNAQ or polyDNAQ with the quenching efficiency being 1.5–2 times higher in MEH-PPV/DNAQ blends. At the same time, the polaron band in MEH-PPV/DNAQ films is a few times less intensive possibly indicating a higher recombination rate of separated charges. Our comparative photoelectric studies of MEH-PPV/DNAQ and MEH-PPV/polyDNAQ blends did not show any essential difference between them. The photocurrents in both blends were considerably lower than that of the pristine MEH-PPV.

Property	DNAQ	polyDNAQ
CT in the ground state	Yes	No
CT in the excited state	Yes	Yes
Photoinduced CT efficiency	higher	lower
Charge recombination rate	higher	lower

Table 14. Summary of comparative studies of MEH-PPV/DNAQ and MEH-PPV/polyDNAQ blends.

## 4.6 MEH-PPV/Pt<sub>0.75</sub>C<sub>60</sub> composites

Fullerenes and their derivatives in blends with conjugated polymers are well known to be the most efficient acceptors in photoinduced charge transfer reaction. In addition, fullerenes in these blends can form a highly conductive network for collection of photoinduced charges that makes fullerenes indispensable in polymer solar cells. However, the active layer of such an optimized cell contains from 45 to 80% of methanofullerene by weight, which weakly absorbs the solar light. In this project, we study a recently synthesized fullerene-based coordination oligomer (Pt<sub>0.75</sub>C<sub>60</sub>)<sub>n</sub> (Fig. 158) as an acceptor for the photoinduced charge separation in the bulk heterojunction. We were motivated that (Pt<sub>0.75</sub>C<sub>60</sub>)<sub>n</sub> chains could facilitate the charge transport in the bulk heterojunction allowing decreasing the fullerene content in it. Moreover, we supposed that Pt might form a coordination complex with MEH-PPV chain.

We characterized MEH-PPV/Pt<sub>0.75</sub>C<sub>60</sub> composite films by using optical absorption and scattering technique, and then investigated their photophysical properties by using photoluminescence (PL), photoinduced absorption (PIA), and photocurrent spectroscopy methods. We also studied MEH-PPV/C<sub>60</sub> blends and compare their properties with those of MEH-PPV/Pt<sub>0.75</sub>C<sub>60</sub>.

### 4.6.1 Samples

(Pt<sub>0.75</sub>C<sub>60</sub>)<sub>n</sub> was synthesized by reaction of C<sub>60</sub> with Pt(dba)<sub>2</sub> (dba=dibenzylideneacetone) at molar ratio Pt(dba)<sub>2</sub>/C<sub>60</sub>=3/4. The compound was characterized by elemental analysis, IR and Raman spectroscopies. Fig. 159 shows Raman spectra of C<sub>60</sub> and (Pt<sub>0.75</sub>C<sub>60</sub>)<sub>n</sub>. It is seen that the strongest Raman band of C<sub>60</sub> is red shifted by 7 cm<sup>-1</sup> in (Pt<sub>0.75</sub>C<sub>60</sub>)<sub>n</sub>. This indicates that a charge of ~1.5 e is transferred from Pt to C<sub>60</sub>. Therefore, the electron affinity of (Pt<sub>0.75</sub>C<sub>60</sub>)<sub>n</sub> must be somewhat lower than C<sub>60</sub>.

Drop-cast films of MEH-PPV/Pt<sub>0.75</sub>C<sub>60</sub> and MEH-PPV/C<sub>60</sub> were prepared from chlorobenzene for various molar donor-acceptor ratio. Drop-cast films of MEH-PPV/Pt<sub>0.75</sub>C<sub>60</sub> and MEH-PPV/C<sub>60</sub> blends were prepared from chlorobenzene for molar acceptor:donor ratios in the range 0.0001–1. The mixtures were treated in ultrasonic bath before film preparation.



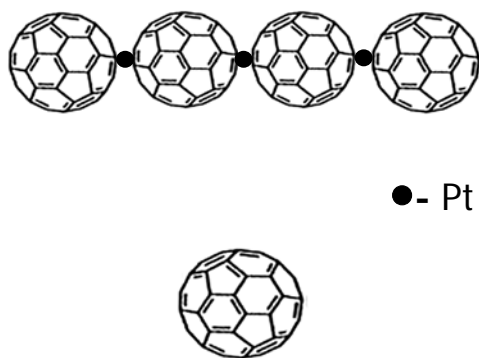


Fig. 158. Chemical structure of  $(\text{Pt}_{0.75}\text{C}_{60})_n$  (top) and  $\text{C}_{60}$  (bottom).

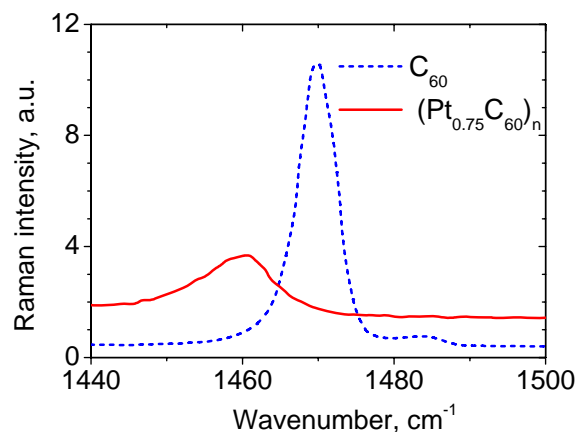


Fig. 159. Raman spectra of  $\text{C}_{60}$  and  $(\text{Pt}_{0.75}\text{C}_{60})_n$ . The excitation wavelength was 514 nm.

#### 4.6.2 Microscopy, absorption, and scattering data

Fig. 160 shows microphotographs of MEH-PPV/ $\text{Pt}_{0.75}\text{C}_{60}$  and MEH-PPV/ $\text{C}_{60}$  films. It is seen that for acceptor concentration higher than 10% both  $(\text{Pt}_{0.75}\text{C}_{60})_n$  and  $\text{C}_{60}$  form their own phase in the blends resulting in a more inhomogeneous film. For acceptor concentration higher than 20%, film's orangish red color resulting from MEH-PPV absorption weakened and fully disappeared in the 1:1 blends. At low acceptor concentration ( $<10\%$ ), optical absorption spectra of MEH-PPV/ $\text{Pt}_{0.75}\text{C}_{60}$  blends were similar to those of MEH-PPV/ $\text{C}_{60}$ . Fig. 161 plots absorption spectrum of a 1:0.1 MEH-PPV/ $\text{Pt}_{0.75}\text{C}_{60}$  drop-cast film. A clear absorption tail below tail can be assigned to absorption of  $(\text{Pt}_{0.75}\text{C}_{60})_n$  (see next paragraph). For higher  $(\text{Pt}_{0.75}\text{C}_{60})_n$  concentration, light scattering gave a noticeable contribution to the optical transmission of the films impeding the optical absorption measurement.

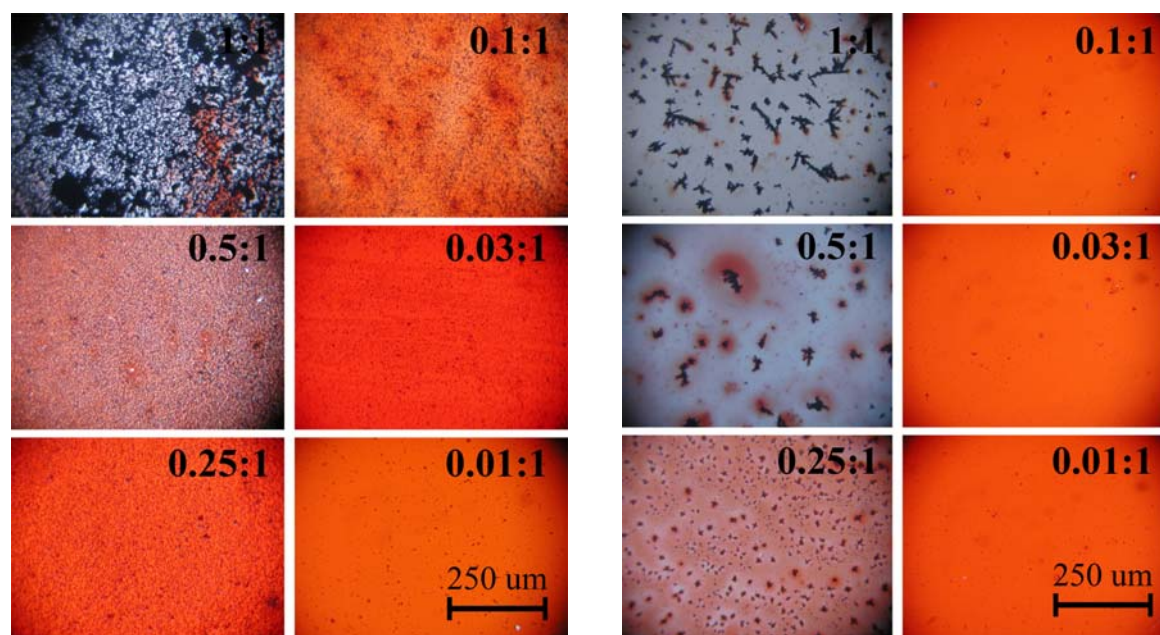


Fig. 160. Microphotographs of MEH-PPV/ $\text{Pt}_{0.75}\text{C}_{60}$  (left) and MEH-PPV/ $\text{C}_{60}$  (right) blends with different acceptor:donor ratio shown in each photo.

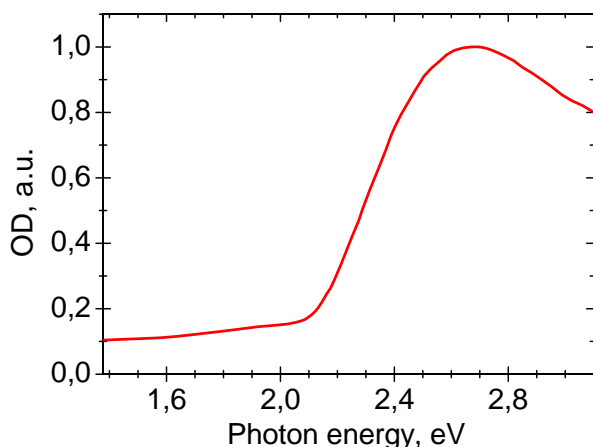


Fig. 161. Normalized absorption spectrum of 1:0.1 MEH-PPV/Pt<sub>0.75</sub>C<sub>60</sub> film drop-cast from chlorobenzene. The spectrum was recorded on the spectrometer collecting light scattered in  $2\pi$  sr (see Sec. 2.1).

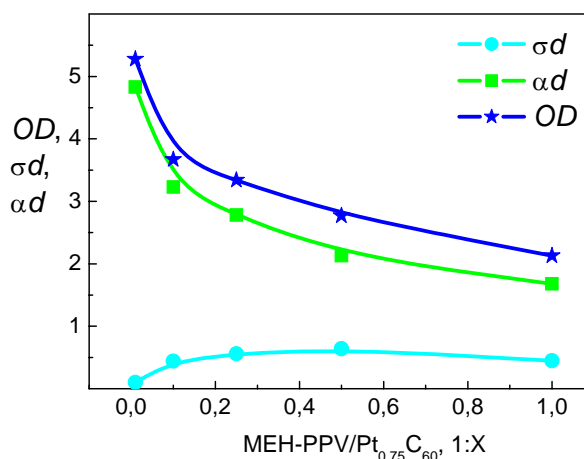


Fig. 162. Scattering ( $\sigma d$ ) and absorption ( $\alpha d$ ) contributions to the measured optical density ( $OD = \sigma d + \alpha d$ ) for MEH-PPV/Pt<sub>0.75</sub>C<sub>60</sub> films vs acceptor:donor ratio at 532 nm. The lines are guides to the eye.

We evaluated both optical absorption ( $\alpha d$ ) and Rayleigh scattering ( $\sigma d$ ) to the measured optical density ( $OD$ ) of a blended film with thickness  $d$  by using the technique described above. Fig. 162 shows the results at 532 nm. It is seen that the contribution of  $\sigma d$  to the  $OD$  gradually increases with (Pt<sub>0.75</sub>C<sub>60</sub>)<sub>n</sub> concentration, whereas the  $\alpha d$  decreases. Similar dependencies were measured at 633 nm, but both the  $\alpha d$  and  $\sigma d$  curves were close to each other monotonically increasing with (Pt<sub>0.75</sub>C<sub>60</sub>)<sub>n</sub> concentration from zero. However, for MEH-PPV/C<sub>60</sub> blends, both the  $\alpha d$  and  $\sigma d$  at 633 nm were below the experimental error ( $\sim 0.1$ ). It seems that the noticeable absorption of MEH-PPV/Pt<sub>0.75</sub>C<sub>60</sub> at 633 nm is due to (Pt<sub>0.75</sub>C<sub>60</sub>)<sub>n</sub> species.

Thus, our light scattering and microscopy data suggest that the characteristic size of optical inhomogeneity in MEH-PPV/Pt<sub>0.75</sub>C<sub>60</sub> blends is considerably closer to the optical wavelength than that in MEH-PPV/C<sub>60</sub> blends. Fullerene molecules form large separated features observed optically at high fullerene concentration (Fig. 160, right). Therefore, we suppose that essentially different morphologies of MEH-PPV/Pt<sub>0.75</sub>C<sub>60</sub> and MEH-PPV/C<sub>60</sub> blends at the microscale can lead to their different photophysical properties.

#### 4.6.3 Photoluminescence quenching data

We have observed that (Pt<sub>0.75</sub>C<sub>60</sub>)<sub>n</sub> strongly quenches MEH-PPV PL. Fig. 163 compares photoluminescence (PL) quenching efficiency in MEH-PPV/Pt<sub>0.75</sub>C<sub>60</sub> and MEH-PPV/C<sub>60</sub> blends. One can see that both acceptors display strong PL quenching at less than 0.01% acceptor content; however, the quenching efficiency in MEH-PPV/Pt<sub>0.75</sub>C<sub>60</sub> is 5–8 times less than in MEH-PPV/C<sub>60</sub> at acceptor concentrations  $\leq 20\%$ . We suggest that the most possible reason of this difference is due to more pronounced phase separation in MEH-PPV/Pt<sub>0.75</sub>C<sub>60</sub> blends as compared with MEH-PPV/C<sub>60</sub>. In fact, (Pt<sub>0.75</sub>C<sub>60</sub>)<sub>n</sub> is insoluble and can form relatively large aggregates at the nanoscale, whereas fullerene molecules are expected to give more intimate mixing with MEH-PPV chains. As a result, a singlet exciton photoexcited at MEH-PPV has to travel a longer path to the donor/acceptor interface in the MEH-PPV/Pt<sub>0.75</sub>C<sub>60</sub> than in MEH-PPV/C<sub>60</sub>. In addition, (Pt<sub>0.75</sub>C<sub>60</sub>)<sub>n</sub> has a lower electron affinity than C<sub>60</sub> as follows from their Raman spectra in Fig. 159. This also could result in a lower charge separation efficiency for (Pt<sub>0.75</sub>C<sub>60</sub>)<sub>n</sub>.

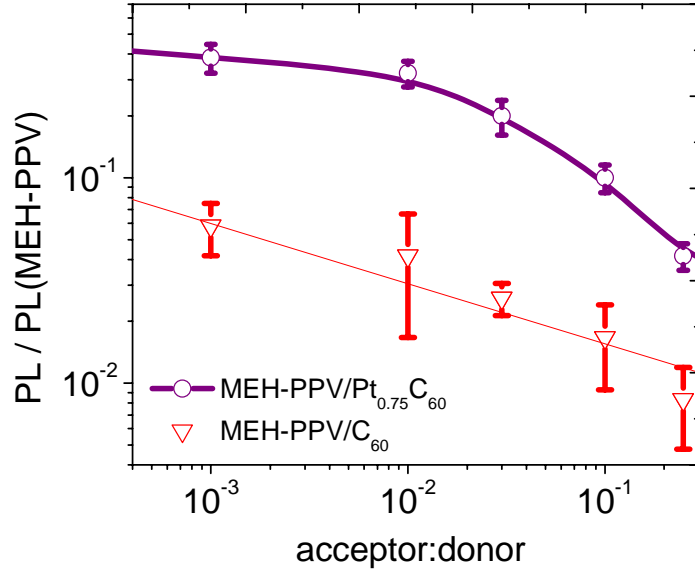


Fig. 163. PL quenching in MEH-PPV/Pt<sub>0.75</sub>C<sub>60</sub> and MEH-PPV/C<sub>60</sub> blends vs acceptor:donor molar ratio referenced to pristine MEH-PPV PL. All values are normalized to absorbed pump power at 532 nm. Solid lines are a guide to the eye.

The shape of the PL quenching curves in is essentially different for C<sub>60</sub> and (Pt<sub>0.75</sub>C<sub>60</sub>)<sub>n</sub> that can also be attributed mainly to the difference in characteristic phase separation lengths at different donor/acceptor ratios in both types of blends. Note that MEH-PPV/C<sub>60</sub> blends demonstrate some increase in normalized PL at acceptor concentration >20% (Fig. 163). The reasons of this are unclear. We believe that this is not an artifact of PL normalization to the absorbed pump since the unnormalized PL also increased with C<sub>60</sub> content. Moreover, we rather overestimate the pump power absorbed by MEH-PPV in both types of blends mainly because of dropping MEH-PPV absorption at high acceptor content.

#### 4.6.4 Photoinduced absorption data

Fig. 164 summarizes our photoinduced absorption (PIA) data for 1:0.03 MEH-PPV/Pt<sub>0.75</sub>C<sub>60</sub> and MEH-PPV/C<sub>60</sub> blends measured under the same experimental conditions. Fig. 164a demonstrates PIA spectra of both. One can see that PIA absorption spectra have nearly the same shape. Both spectra show high (1.3 eV) and low (<0.8 eV) energy bands assigned to polarons at MEH-PPV. As Fig. 164a shows, long-lived charge separated states are efficiently excited in both blends; meanwhile, the PIA signal at 1.3 eV is ~2 times higher in MEH-PPV/C<sub>60</sub> than in MEH-PPV/Pt<sub>0.75</sub>C<sub>60</sub>. This ratio was nearly the same for all the pump intensities and chopping frequencies studied.

The frequency dependence of the PIA signal can provide information about the lifetime of photoexcitations. If they follow a monomolecular kinetics with lifetime  $\tau$ , the frequency dependence of the PIA is

$$\frac{dT}{T} \propto \frac{\tau}{1 + i2\pi f\tau}. \quad (2)$$

In pristine MEH-PPV, triplet excitons are known to dominate in PIA at low temperature (~100 K) giving a band at 1.35 eV with the monomolecular kinetics. On the other hand, polarons in PPV-type conjugated polymers show a power-law frequency dependence  $1/f^\alpha$  with  $\alpha \sim 0.5$ . This dependence is usually interpreted as “dispersive” recombination implying a broad distribution in polaron lifetimes as a result of sample inhomogeneity and can be fit by the empirical Cole-Cole model

$$\frac{dT}{T} \propto \frac{1}{1 + i(2\pi f\tau)^\alpha}. \quad (3)$$

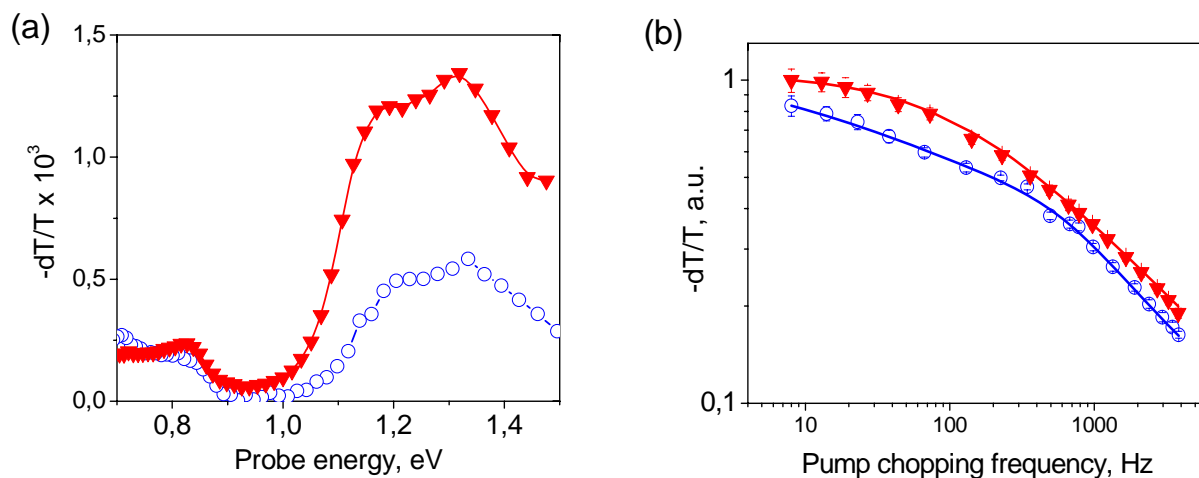


Fig. 164. PIA data for 1:0.03 MEH-PPV/(Pt<sub>0.75</sub>C<sub>60</sub>)<sub>n</sub> (○) and MEH-PPV/C<sub>60</sub> (▼) blends photoexcited at 532 with pump intensity 1 W/cm<sup>2</sup> at 110 K. Almost all the pump power was absorbed in the films. (a) PIA spectra for chopping frequency 70 Hz. (b) Normalized frequency dependences for the 1.3 eV band. Solid lines are fits to the data (see the text).

Since the PIA signal is proportional to the density of photoexcitations whose lifetime is longer than  $1/f$  (Eq. (2)), we can suggest that the generation efficiency of long-lived polarons is approximately two times lower in MEH-PPV/Pt<sub>0.75</sub>C<sub>60</sub> blends. Fig. 164b compares frequency dependences of the peak at 1.3 eV for 1:0.03 MEH-PPV/Pt<sub>0.75</sub>C<sub>60</sub> and MEH-PPV/C<sub>60</sub> blends. "Dispersive" kinetics according to Eq. (3) with  $\alpha=0.44$  and  $\tau=12$  ms gave a good fit to the experimental data for MEH-PPV/C<sub>60</sub> (Fig. 164b, solid line). For MEH-PPV/Pt<sub>0.75</sub>C<sub>60</sub> blends, the frequency dependence had a characteristic knee (Fig. 164b), and any single "dispersive" kinetics (Eq. (2)) did not give a satisfactory fit for all the donor/acceptor ratios studied. We relate this to the contribution of MEH-PPV triplet excitons in the PIA band at 1.3 eV. A superposition of "dispersive" and monomolecular kinetics gave a good approximation to the frequency dependence for all the MEH-PPV/Pt<sub>0.75</sub>C<sub>60</sub> blends. The lower line in Fig. 164b shows such a bimodal fit by the sum of "dispersive" ( $\alpha=0.35$ ,  $\tau=11$  ms) and monomolecular ( $\alpha=1$ ,  $\tau=1.5$  ms) kinetics (Eq. (2)). Therefore, our PIA data suggest that MEH-PPV triplet excitons in MEH-PPV/Pt<sub>0.75</sub>C<sub>60</sub> blends are not completely quenched in contrast to MEH-PPV/C<sub>60</sub> blends. This is also supported by the PL quenching data in Fig. 163 showing that the PL in the 1:0.03 MEH-PPV/Pt<sub>0.75</sub>C<sub>60</sub> blend is quenched only by a factor of 5 indicating that a part of singlet excitons lives a sufficient time to be converted into triplet excitons via intersystem crossing.

Using the temperature dependencies of photoinduced absorption at 1.4 eV in MEH-PPV/Pt<sub>0.75</sub>C<sub>60</sub> and MEH-PPV/C<sub>60</sub>, we have modeled the characteristic binding energies of long-lived charged states, i.e., trap depths. Our analysis has shown that at low acceptor concentrations ( $<0.1$ ) the characteristic trap depth in MEH-PPV/Pt<sub>0.75</sub>C<sub>60</sub> composites is lower than in MEH-PPV/C<sub>60</sub> blends. We suggest that these deep traps have longer lifetimes giving higher photoinduced absorption signals in MEH-PPV/C<sub>60</sub> than in MEH-PPV/Pt<sub>0.75</sub>C<sub>60</sub>.

Comparative PIA-FTIR data on PPV/Pt<sub>0.75</sub>C<sub>60</sub> and MEH-PPV/C<sub>60</sub> are presented above in Sec. 4.3.2.4. It was observed that very long-lived charge states with a lifetime of  $\sim 10$  sec have the same characteristic features in both blends.

#### 4.6.5 Photoelectric data

We performed comparative photoelectric studies of MEH-PPV/ $\text{Pt}_{0.75}\text{C}_{60}$  and MEH-PPV/ $\text{C}_{60}$  blends. We tried to keep the device preparation steps (Sec. 3.3.4) and the measurement procedures (Sec. 2.12) as close as possible. The optical density of the active layer was below unity allowing us to neglect the internal filter effect. Two types of  $(\text{Pt}_{0.75}\text{C}_{60})_n$  samples were used for preparation of bulk heterojunction photodiodes: powder and liquid composition (3.4 g/l in toluene with traces of dibenzylideneacetone) as it was obtained after the synthesis reaction.

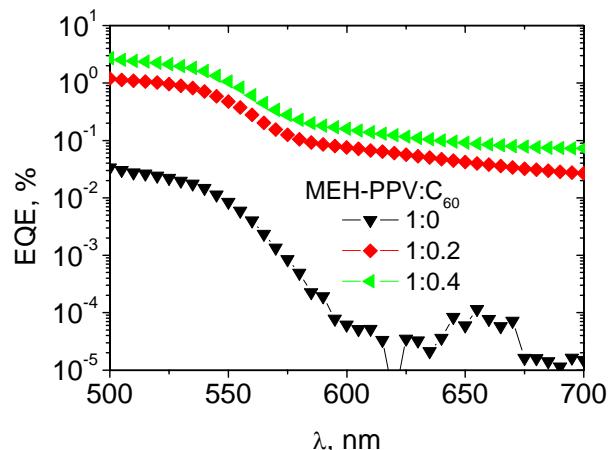


Fig. 165 Photocurrent action spectra of MEH-PPV/ $\text{C}_{60}$  photodiodes for different donor/acceptor ratios.

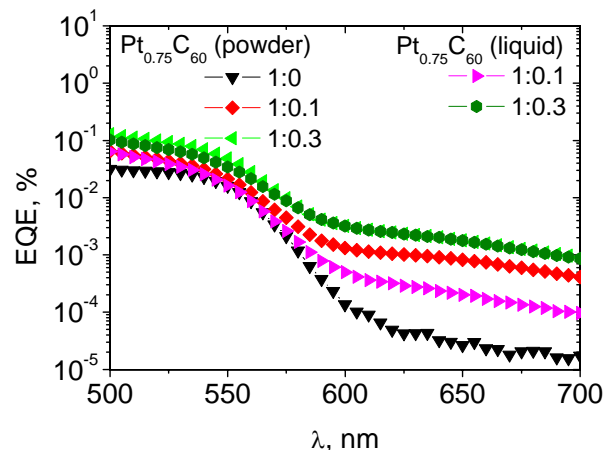


Fig. 166 Photocurrent action spectra of MEH-PPV/ $\text{Pt}_{0.75}\text{C}_{60}$  photodiodes for different donor/acceptor ratios.

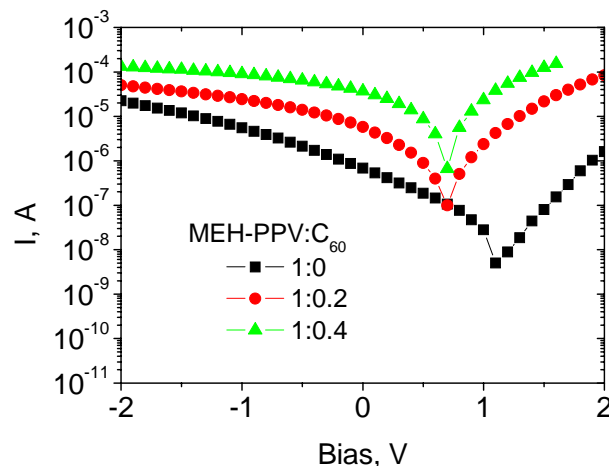


Fig. 167 Current-to-voltage characteristics of MEH-PPV/ $\text{C}_{60}$  photodiodes for different donor/acceptor ratios.

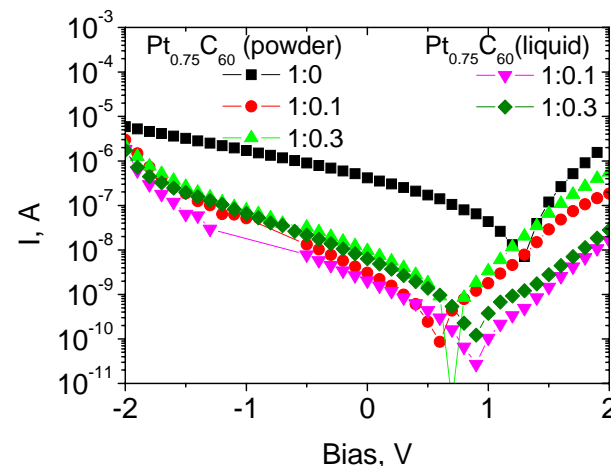


Fig. 168 Current-to-voltage characteristics of MEH-PPV/ $\text{Pt}_{0.75}\text{C}_{60}$  photodiodes for different donor/acceptor ratios.

Fig. 165 and Fig. 166 plot photocurrent action spectra for MEH-PPV/ $\text{C}_{60}$  and MEH-PPV/ $\text{Pt}_{0.75}\text{C}_{60}$  photodiodes, respectively, with different acceptor content. Fig. 167 and Fig. 168 demonstrate the corresponding current-to-voltage characteristics. Data for the referenced pristine MEH-PPV device are also shown for comparison. Table 15 summarizes characteristics for both types of photodiodes. As follows from Fig. 165 and Fig. 167 (see also Table 15), the MEH-PPV/ $\text{C}_{60}$  blends show a typical behavior very close to that reported in the literature, i.e., the photocurrent strongly rises with increasing the  $\text{C}_{60}$  content both at monochromatic (weak) and white light (intensive) illumination. In contrast,  $(\text{Pt}_{0.75}\text{C}_{60})_n$  results in a strong drop of the photocurrent under white light illumination (Fig. 168) compared with the reference pristine MEH-PPV device.

At the same time, under monochromatic illumination, the photocurrent triples in the spectral range of MEH-PPV absorption (Fig. 166) that is in accordance with our PIA data (Sec. 4.6.4). Note that photocurrent increases in the MEH-PPV optical gap in both blends due to absorption of C<sub>60</sub> (Fig. 165) or (Pt<sub>0.75</sub>C<sub>60</sub>)<sub>n</sub> (Fig. 166). Therefore, if under weak illumination addition of (Pt<sub>0.75</sub>C<sub>60</sub>)<sub>n</sub> to MEH-PPV increases the photocurrent, then under intensive illumination the photocurrent drops essentially. Therefore, charge collection is expected to be very inefficient in the MEH-PPV/Pt<sub>0.75</sub>C<sub>60</sub> bulk heterojunction possibly due to low density of the conductive network in it. However, we can not exclude that something was wrong at the device interfaces.

Active layer (numbers show donor/acceptor molar ratio)	$I_{sc}$ , $\mu A/cm^2$	$V_{oc}$ , V	$FF$ , %	$EQE$ at 500 nm, %	Energetic efficiency $\eta$ , %
MEH-PPV:Pt <sub>0.75</sub> C <sub>60</sub> (powder) 1:0.1	0.06	0.57	18.4	0.07	$6.3 \cdot 10^{-06}$
MEH-PPV:Pt <sub>0.75</sub> C <sub>60</sub> (powder) 1:0.3	0.19	0.71	17.9	0.13	$2.4 \cdot 10^{-05}$
MEH-PPV:Pt <sub>0.75</sub> C <sub>60</sub> (liquid) 1:0.1	0.04	0.73	16.7	0.06	$4.8 \cdot 10^{-06}$
MEH-PPV:Pt <sub>0.75</sub> C <sub>60</sub> (liquid) 1:0.3	0.13	0.87	14.6	0.10	$1.7 \cdot 10^{-05}$
MEH-PPV	8.35	1.26	16.2	0.03	$1.7 \cdot 10^{-03}$
MEH-PPV:C <sub>60</sub> 1:0.2	115	0.68	17.8	1.2	0.014
MEH-PPV:C <sub>60</sub> 1:0.4	738	0.68	23.1	2.7	0.12

Table 15. Characteristics of MEH-PPV/C<sub>60</sub> and MEH-PPV/ Pt<sub>0.75</sub>C<sub>60</sub> photodiodes.

#### 4.6.6 Summary

We have done comparative studies of optical and photophysical properties of MEH-PPV/Pt<sub>0.75</sub>C<sub>60</sub> and MEH-PPV/C<sub>60</sub> films. Their optical characterization has shown that the morphology of the blends is essentially different at the microscale. By using PL and PIA spectroscopy, we have found that the efficiency of photoinduced charge transfer in MEH-PPV/Pt<sub>0.75</sub>C<sub>60</sub> is about 2 times lower than in MEH-PPV/C<sub>60</sub>. We attribute this difference to higher phase separation in MEH-PPV/Pt<sub>0.75</sub>C<sub>60</sub> at the nanoscale. Our photoelectric studies suggest that charge collection is inefficient in the MEH-PPV/Pt<sub>0.75</sub>C<sub>60</sub> bulk heterojunction.



## 5 DISCUSSION AND IMPLICATIONS

One of the most important results of the project is a demonstration that conjugated polymers can form intermolecular ground-state charge-transfer complexes (CTC) with molecular organic acceptors both in solutions and films. At least one conjugated polymer (MEH-PPV) forms a CTC with different organic acceptors. Probably, PHT can also form a CTC with a fluorene-type acceptor; however, we have not found clear evidence, namely, for CT ground-state interaction although signatures of ground-state interaction of the components in this blend have been observed.

Using vibrational spectroscopy, we have found evidence that electron density from the  $\pi$ -conjugated system of the polymer donor partially transfers to the molecular acceptor. In other words, weak ground-state CT occurs. Furthermore, the CTC band energy is correlated with the acceptor's electron affinity. These observations are in accordance with Mulliken's model of weak CTCs.

The next issues relating to conjugated polymer CTCs were addressed in the project:

- (i) How can CTCs influence the ground- and excited-state properties of donor/acceptor blends?
- (ii) Do CTCs have a potential for solar cells?

### (i) Ground state

Our results suggest that CT interaction facilitates fine dispersion of the acceptor in the polymer matrix counteracting phase separating the blend components. Our reasoning is as follows:

- If the acceptor content in the blend is below an optimal level ( $\sim 30\%$  mol. for MEH-PPV/TNF), the film's structure at the microscale is very similar to that of the pristine polymer, i.e., highly homogeneous films can be formed. At the nanoscale, AFM studies reveal that the acceptor is aggregated in its own phase starting from the acceptor content  $20\%$  mol. Our AFM and optical data imply that if the acceptor content is not higher than the optimal level, a major part of the acceptor is involved in the CTC. On the other hand, almost all the polymer chains observed in Raman and optical absorption spectra are involved in the CTC.
- Dramatic enhancement of the photostability of MEH-PPV/acceptor blends with CTC (see below) can also be assigned to the very intimate mixing of the blend components, which is hardly reachable in polymer/acceptor blends without their noticeable attraction. The latter occurs, for example, in soluble PPV/fullerene blends. Moreover, our comparative FTIR-PIA data on MEH-PPV CTCs, pristine MEH-PPV, and MEH-PPV lightly doped by  $C_{60}$  also suggest that the CTC essentially facilitates intimate donor-acceptor mixing compared with the MEH-PPV/ $C_{60}$  blend.

Using vibrational spectroscopy, we have found evidence that the conformation of MEH-PPV conjugated chains is noticeably changed in the CTC both in solutions and films. Our data suggest that the polymer chains become more planar in the CTC that might possibly result in their denser packing in films. At the same time, the polymer conjugation length hardly changes in the CTC.

### (i) Excited state

We have found that polymer photoluminescence (PL) is quenched very efficiently in blends of MEH-PPV with acceptors forming the CTC with the quenching efficiency about that of  $C_{60}$ . As the acceptors used have a larger bandgap than that of the polymer, the PL quenching indicates fast dissociation of MEH-PPV singlet excitons. However, the generation efficiency of long-lived charges in the CTC is

typically one order of magnitude lower than that in MEH-PPV/fullerene blends. This could be explained by geminate recombination in the CTC impeding efficient generation of long-lived charges.

Remarkably that long-lived charges can be generated in the CTC under its direct photoexcitation, i.e., under red or infrared light corresponding to the CTC absorption band. Photoexcitation of either the MEH-PPV or the CTC results in the same charged species with efficiency weakly depending on photon energy. Moreover, the density of long-lived photoinduced charges in MEH-PPV/TNF blends can be as high as in MEH-PPV/fullerene blends.

We have shown a proof-of-concept demonstration that mobile charges can be generated in the MEH-PPV CTC under red or infrared excitation. The photosensitivity of the MEH-PPV/TNF CTC extends deeply in the polymer optical gap down to 1 eV.

One of the basic drawbacks of conjugated polymers is their poor photooxidation stability in ambient conditions. We have found that the photooxidation rate under visible irradiation of MEH-PPV doped by TNF or DNAQ can be deeply suppressed. Although it is well known that such acceptors as fullerenes improve the photostability of the blend essentially, the observed photostability enhancement in MEH-PPV/TNF blends is considerably higher. It is reasonable to assume that the ground-state CT interaction facilitates dispersion of the acceptor in the polymer matrix. The finely dispersed acceptor provides deep quenching the MEH-PPV singlet excitons that in turn blocks formation of triplet excitons. The latter are known to sensitize highly reactive singlet oxygen.

Thus, as follows from our studies, ground-state CT interaction can noticeably modify both the ground and the excited states of the donor/acceptor blend. The CTC obviously influences the photophysics including charge generation and recombination processes in the blend as the lowest excited states in it are the CTC ones. On the other hand, one might expect that ground-state CT in conjugated polymer/acceptor blends is a more general phenomena than was thought previously. In fact, recent absorption data on a MDMO-PPV/PCBM blend obtained with the use of photothermal deflection spectroscopy have revealed noticeable non-additivity of the MDMO and PCBM spectra [25]. The authors have suggested a weak CTC as a possible reason of this non-additivity. A recent study of OC1C10-PPV/PCBM blends have shown that the hole mobility of the polymer in the blend increases by more than two orders of magnitude from its pure polymer value [26]. These data indicate a ground-state interaction between the polymer and PCBM, and it could be CT one.

(ii) This question was addressed at the beginning of the project. Potentialities of CTCs for solar cells were summarized in Fig. 3 (Sec. 1.1.). First, we have shown that a polymer CTC can have essential red and infrared absorption in the optical gap of the polymer. We have demonstrated that the CTC bandgap can be tuned by varying the electron affinity of acceptor. Second, charge separation seems to start nearly at the moment of photon absorption by the CTC (although we did not performed time-resolved studies, our PL quenching data imply this). Third, our studies by using different techniques indicate that the CTC can be a factor counteracting donor-acceptor phase separation. Probably ground-state CT interaction could be used to modify phase separation peculiarities of the bulk heterojunction in the desired direction. Forth, possible anisotropy in properties of CTCs has not been studied at all. In addition, another unexpected benefit of CTC is that it can essentially improve the photooxidation stability of the blend.

Nevertheless, the studied CTCs have two obvious drawbacks. The first is that the charge collection efficiency is too low as compared with that of polymer/fullerene blends. On one hand, the intrinsic electron mobility of the studied acceptors is strongly less than that of fullerenes. On the other hand, the hole mobility in the blend with CTC decreases essentially compared with that of pristine polymer. The second is low efficiency of generation of long-lived charges compared with polymer/fullerene blends. To enhance separation and collection of charges photoexcited in the CTC, we have tried to combine red absorption of the CTC with fullerenes by using ternary blends

consisting of the polymer and two acceptors. We have shown that the photoinduced charge transfer from the photoexcited CTC to the fullerene can be highly efficient. However, we have not managed to demonstrate any increase of photocurrent in the ternary blends versus the binary polymer/fullerene blends. Possibly, optimization of the composition and preparation routine is necessary.

Finally, can CTCs help in improving the performance of organic solar cells? It is still an open question. We have shown that the conjugated polymer CTC can be a photostable red and infra-red absorber; however, charge separation and collection in the studied blends with CTC are not efficient. Possibly, a more optimized acceptor could improve charge separation and collection.

#### *Conjugated polymer CTCs for photonics?*

One might expect that such properties of conjugated polymer CTCs as the bandgap in the range 1-1.5 eV, high optical homogeneity, and enhance photostability to visible irradiation are very desirable for photonics applications, for example, as efficient nonlinear optical materials. In fact, the lower bandgap of a material  $E_g$ , the higher optical nonlinearity  $\chi^{(3)}$  is expected. As was shown in the 1970s,  $\chi^{(3)}$  scales as  $1/E_g^6$  in a one-dimensional semiconductor within the simple one-electron model. Therefore, a two fold decrease in  $E_g$  is expected to increase  $\chi^{(3)}$  up to two orders of magnitude. Moreover, a possibility of varying the CTC  $E_g$  near 1.6 eV that was demonstrated in the project could be useful for nonlinear optic devices operating at  $\sim 1.5 \mu\text{m}$  to tune the  $E_g$  near the CTC two-photon resonance.

## 6 CONCLUSIONS

The main results of the project are summarized as follows:

Although blends of conjugated polymers with various organic acceptors usually do not show any clear signatures of ground-state charge transfer (CT) interaction, we have found for the first time, to the best of our knowledge, that a ground-state charge transfer complex (CTC) is formed in donor-acceptor blends of MEH-PPV with a number of organic acceptors, in particular with 2,4,7-trinitrofluorenone (TNF) or 1,5-dinitroantraquinone (DNAQ). Optical absorption spectra of the blended films are non-additive: a CTC band appears in the optical gap of MEH-PPV extending down to the near-IR region. Vibrational spectra of the blends are also indicative of the ground-state CT: characteristic vibrational donor (acceptor) bands demonstrate frequency shifts both in the Raman and the IR spectra. The optimal donor-acceptor molar ratio corresponding to the maximum CTC concentration in the blend has been found. It comprises about 1:0.4 both for MEH-PPV/TNF and MEH-PPV/DNAQ films as follows from our optical absorption, light scattering, and vibrational studies. The acceptor added above this ratio forms mainly its own phase separated features in the blend. As follows from our optical spectroscopy data, the MEH-PPV chains involved in the CTC change their conformation. We suggest that the chains become more planar in the CTC; however, the polymer conjugated length hardly changes.

We have established that long-lived photoinduced charges can be generated in the MEH-PPV/TNF and MEH-PPV/DNAQ blends. Photoexcitation of either the MEH-PPV or the CTC, i.e., in the spectral range 500–800 nm, results in the same charged species with efficiency weakly depending on photon energy. We have observed that the density of long-lived photoinduced charges in MEH-PPV/TNF blends can be as high as in MEH-PPV/fullerene blends. However, the generation efficiency of long-lived charges in the CTC is typically one order of magnitude lower than that in MEH-PPV/fullerene blends. Despite the fact that initial charge separation in the CTC can be as efficient as in polymer/fullerene blends as follows from our photoluminescence (PL) quenching data, geminate recombination in the CTC possibly impedes efficient generation of long-lived charges.

We have shown that the MEH-PPV CTC can generate mobile charges under visible or near-IR photoexcitation starting from 1 eV. The photocurrent spectra of MEH-PPV/TNF and MEH-PPV/DNAQ blends are correlated with their absorption. However, charge mobilities are too low in these blends. In spite of increasing the electron mobility of the blends with CTC upon addition of acceptor, the hole mobility decreases below that of the pristine polymer.

To enhance separation and collection of charges photoexcited in the CTC, we have studied ternary blends consisting of MEH-PPV, TNF or DNAQ, and fullerene ( $C_{60}$  or PCBM). Using photoinduced absorption spectroscopy, we have found that the photoinduced charge transfer from the photoexcited CTC to the fullerene is highly efficient in MEH-PPV/DNAQ/fullerene blends and is inefficient in MEH-PPV/TNF/ $C_{60}$  blends. These observations are in accordance with the acceptor LUMO energies increasing in the following sequence: DNAQ, fullerene, TNF. Therefore, tuning the difference between the LUMOs of the acceptor forming the CTC and fullerene, one can achieve efficient generation of long-lived charges in ternary blends. However, we have not managed to demonstrate higher photocurrents in the ternary blends versus the binary polymer/fullerene blends.

We have found that the photooxidation rate of MEH-PPV in the MEH-PPV/TNF blend under visible irradiation can be three orders of magnitude lower than that of pristine MEH-PPV. Observing that the photoluminescence intensity and the photooxidation rate in the MEH-PPV/acceptor blends are correlated, we suppose that MEH-PPV triplet excitons are a sole intermediate for photooxidation in these blends. Our findings suggest that a PPV-type polymer in a donor-acceptor blend could have the lifetime reaching thousands of hours under visible radiation of solar intensity in ambient conditions without encapsulation.

To find whether a ground-state CTC between two polymers can be formed, we have performed comparative studies of donor-acceptor blends MEH-PPV/DNAQ and MEH-PPV/polyDNAQ, where polyDNAQ is a polymer form of DNAQ (poly(4,8-dinitroanthraquinone-1,5-diyl)). We have found that if the monomer DNAQ forms a CTC in MEH-PPV/DNAQ blend, the MEH-PPV/polyDNAQ blends do not show any clear signatures of CTC. Remarkably that MEH-PPV singlet excitons are efficiently quenched by either DNAQ or polyDNAQ with the quenching efficiency being 1.5–2 times higher in MEH-PPV/DNAQ blends. At the same time, the generation efficiency of long-lived charges in the MEH-PPV/DNAQ blends is a few times less than in the MEH-PPV/polyDNAQ blends. These findings support our suggestion that the geminate recombination is an essential factor limiting charge separation in the CTC.

We have studied a fullerene-based coordination oligomer  $(\text{Pt}_{0.75}\text{C}_{60})_n$  as an acceptor for polymer solar cells. We have not found any clear signatures of ground-state interaction between MEH-PPV and  $(\text{Pt}_{0.75}\text{C}_{60})_n$ . In the photoexcited state,  $(\text{Pt}_{0.75}\text{C}_{60})_n$  demonstrates a few times lower efficiency of photoinduced charge transfer than  $\text{C}_{60}$ . We attribute this difference to higher phase separation in MEH-PPV/ $\text{Pt}_{0.75}\text{C}_{60}$  at the nanoscale. However, our photoelectric studies suggest that charge collection is inefficient in the MEH-PPV/ $\text{Pt}_{0.75}\text{C}_{60}$  bulk heterojunction.

We have investigated a slow solvent evaporation (SSE) method for preparation of conjugated polymer films in comparison with spin-casting, drop-casting, and dip-coating. Our studies suggest that the SSE films of MEH-PPV can have longer conjugated chains, their narrower distribution, and more effective charge transport as compared with the other methods. Note that unwanted aggregation in SSE films seems not to increase as follows from their PL properties. In addition, by varying the evaporation conditions, the SSE method allows preparation of MEH-PPV films with very different absorption and PL spectra usually not observed in films prepared by the other methods.

**In summary**, we have found that conjugated polymers can form ground-state CTCs with appropriate organic acceptors. The polymer CTC can have extended optical absorption down to the near-IR spectral range far beyond the absorption edge of the pristine polymer. The photoexcited CTC can relax in long-lived separated charges. However, the efficiency of charge collection in the studied polymer CTCs is too low to be used in polymer solar cells. To provide efficient charge separation and collection, we have tried to combine the polymer CTCs with fullerenes. Although efficient photoinduced charge transfer from the CTC to fullerene has been demonstrated, we have not observed any noticeable gain in photocurrent. We have found that the photooxidation rate of MEH-PPV in the CTC under visible irradiation can be a few orders of magnitude lower than that of pristine MEH-PPV. This suggests that a PPV-type polymer in a donor-acceptor blend could have a lifetime sufficient for applications. Thus, polymer CTCs possibly could be used as a highly stable red absorber in solar cells and maybe in other photonic devices.

## 7 ACKNOWLEDGMENT

We thank for collaboration the following people:

- T. Yamamoto, Tokyo Institute of Technology, for polyDNAQ;
- Th. Dittrich, Hahn-Meitner-Institute, Berlin, for surface photovoltage spectroscopy data;
- I.F. Perepichka, Durham University, for fluorene acceptors;
- A.S. Shchegolikhin, Institute of Biochemical Physics, Moscow, for DSC and some FTIR data;
- Yu.N. Novikov, Institute of Organoelement Compounds, Moscow, for  $(\text{Pt}_{0.75}\text{C}_{60})_n$ ;
- A.R. Tameev, Institute of Physical Chemistry and Electrochemistry, Moscow, for time-of-flight mobility measurements;
- J.C. Hummelen, University of Groningen, for PCBM.

## 8 REFERENCES

1. M. S. A. Abdou, F. P. Orfino, Y. Son, and S. Holdcroft, "Interaction of Oxygen With Conjugated Polymers: Charge Transfer Complex Formation With Poly(3-Alkylthiophenes)", *Journal of the American Chemical Society*, **119**, 19, 4518-4524, 1997
2. P. J. Skabara, I. M. Serebryakov, I. F. Perepichka, N. S. Sariciftci, H. Neugebauer, and A. Cravino, "Toward Controlled Donor-Acceptor Interactions in Noncomposite Polymeric Materials: Synthesis and Characterization of a Novel Polythiophene Incorporating Pi-Conjugated 1,3-Dithiole-2- Ylidenefluorene Units as Strong D-a Components", *Macromolecules*, **34**, 7, 2232-2241, 2001
3. B. Xu, D. Fichou, G. Horowitz, and F. Garnier, "Preparation of Charge-Transfer Complexes Based on Thiophene and Paraphenylene Oligomers as Electron-Donors", *Synthetic Metals*, **42**, 3, 2319-2322, 1991
4. M. Ichida, T. Sohda, and A. Nakamura, "Optical transition and ionicity of C<sub>60</sub>/amine charge-transfer complexes studied by optical spectroscopy.", *Chemical Physics Letters*, **310**, 3-4, 373-8, 1999
5. G. Ruani, C. Fontanini, M. Murgia, and C. Taliani, "Weak Intrinsic Charge Transfer Complexes: a New Route for Developing Wide Spectrum Organic Photovoltaic Cells", *Journal of Chemical Physics*, **116**, 4, 1713-1719, 2002
6. A. A. Bakulin, S. G. Elizarov, A. N. Khodarev, D. S. Martyanov, I. V. Golovnin, D. Y. Paraschuk, M. M. Triebel, I. V. Tolstov, E. L. Frankevich, S. A. Arnautov, and E. M. Nechvolodova, "Weak charge-transfer complexes based on conjugated polymers for plastic solar cells", *Synthetic Metals*, **147**, 1-3, 221-225, 2004
7. G. Li, V. Shrotriya, J. S. Huang, Y. Yao, T. Moriarty, K. Emery, and Y. Yang, "High-Efficiency Solution Processable Polymer Photovoltaic Cells by Self-Organization of Polymer Blends", *Nature Materials*, **4**, 11, 864-868, 2005
8. T. Q. Nguyen, V. Doan, and B. J. Schwartz, "Conjugated Polymer Aggregates in Solution: Control of Interchain Interactions", *Journal of Chemical Physics*, **110**, 8, 4068-4078, 1999
9. T. Q. Nguyen, I. B. Martini, J. Liu, and B. J. Schwartz, "Controlling Interchain Interactions in Conjugated Polymers: the Effects of Chain Morphology on Exciton-Exciton Annihilation and Aggregation in MEH-PPV Films", *Journal of Physical Chemistry B*, **104**, 2, 237-255, 2000
10. D. Moses, A. Feldblum, E. Ehrenfreund, A. J. Heeger, T. C. Chung, and A. G. MacDiarmid, "Pressure dependence of the photoabsorption of polyacetylene.", *Physical Review B-Condensed Matter*, **26**, 6, 3361-9, 1982
11. A. R. Inigo, H. C. Chiu, W. Fann, Y. S. Huang, U. S. Jeng, T. L. Lin, C. H. Hsu, K. Y. Peng, and S. A. Chen, "Disorder controlled hole transport in MEH-PPV", *Physical Review B*, **69**, 7, 075201-1-8, 2004
12. L. Forro and L. Mihaly, "Electronic properties of doped fullerenes", *Reports on Progress in Physics*, **64**, 5, 649-699, 2001
13. S. Lefrant, J. P. Buisson, and H. Eckhardt, "Raman spectra of conducting polymers with aromatic rings ", *Synthetic Metals*, **37**, 1-3, 91-98, 1990
14. R. A. J. Janssen, M. P. T. Christiaans, C. Hare, N. Martin, N. S. Sariciftci, A. J. Heeger, and F. Wudl, "Photoinduced Electron-Transfer Reactions in Mixed Films of Pi-Conjugated Polymers and a Homologous Series of Tetracyano-P-Quinodimethane Derivatives", *Journal Of Chemical Physics*, **103**, 20, 8840-8845, 1995



15. Janssen, R. A. J. Photoexcitations in Conjugated Oligomers. In: *Primary Photoexcitations in Conjugated Polymers: Molecular Exciton versus Semiconductor Band Model*, ed. Sariciftci, N. S. Singapore : World Scientific Publ., 1997.pp. 524-558.
16. M. Kemerink, J. K. J. vanDuren, P. Jonkheijm, W. F. Pasveer, P. M. Koenraad, R. A. J. Janssen, H. W. M. Salemink, and J. H. Wolter, "Relating Substitution to Single-Chain Conformation and Aggregation in Poly(p-phenylene Vinylene) Films", *Nano Lett.*, **3**, 9, 1191-1196, 2003
17. F. A. C. Oliveira, L. A. Cury, A. Righi, R. L. Moreira, P. S. S. Guimaraes, F. M. Matinaga, M. A. Pimenta, and R. A. Nogueira, "Temperature effects on the vibronic spectra of BEH-PPV conjugated polymer films.", *Journal of Chemical Physics*, **119**, 18, 9777-82, 2003
18. X. Wei, Z. V. Vardeny, N. S. Sariciftci, and A. J. Heeger, "Absorption-Detected Magnetic-Resonance Studies of Photoexcitations in Conjugated-Polymer/C<sub>60</sub> Composites", *Physical Review B-Condensed Matter*, **53**, 5, 2187-2190, 1996
19. K. H. Lee, N. S. Sariciftci, and A. J. Heeger, "Infrared Photoexcitation Spectroscopy in Soluble Derivatives of Poly(P-Phenylenevinylene) and Composites with C-60", *Synthetic Metals*, **69**, 1-3, 445-446, 1995
20. W. D. Gill, "Drift mobilities in amorphous charge-transfer complexes of trinitrofluorenone and poly-n-vinylcarbazole", *Journal of Applied Physics*, **43**, 12, 5033-5040, 1972
21. F. C. Krebs, J. E. Carle, N. Cruys-Bagger, M. Andersen, M. R. Lilliedal, M. A. Hammond, and S. Hvidt, "Lifetimes of Organic Photovoltaics: Photochemistry, Atmosphere Effects and Barrier Layers in Ito-Mehppv: Pcbm-Aluminium Devices", *Solar Energy Materials and Solar Cells*, **86**, 4, 499-516, 2005
22. H. Neugebauer, C. Brabec, J. C. Hummelen, and N. S. Sariciftci, "Stability and Photodegradation Mechanisms of Conjugated Polymer/Fullerene Plastic Solar Cells", *Solar Energy Materials and Solar Cells*, **61**, 1, 35-42, 2000
23. E. G. J. Staring, A. J. M. Berntsen, S. T. R. Romme, Rikken Gija, and P. Urbach, "On the Photochemical Stability of Dialkoxy-Ppv; a Quantitative Approach", *Philosophical Transactions of the Royal Society of London Series a-Mathematical Physical and Engineering Sciences*, **355**, 1725, 695-706, 1997
24. L. Biczok, T. Berces, and H. Inoue, "Effects of Molecular Structure and Hydrogen Bonding on the Radiationless Deactivation of Singlet Excited Fluorenone Derivatives", *J. Phys. Chem. A*, **103**, 20, 3837-3842, 1999
25. L. Goris, K. Haenen, M. Nesladek, P. Wagner, D. Vanderzande, L. De Schepper, J. D'Haen, L. Lutsen, and J. V. Manca, "Absorption phenomena in organic thin films for solar cell applications investigated by photothermal deflection spectroscopy", *Journal of Materials Science*, **40**, 6, 1413-1418, 2005
26. V. D. Mihailetschi, L. J. A. Koster, P. W. M. Blom, C. Melzer, B. De Boer, J. K. J. Van Duren, and R. A. J. Janssen, "Compositional Dependence of the Performance of Poly(P-Phenylene Vinylene): Methanofullerene Bulk-Heterojunction Solar Cells", *Advanced Functional Materials*, **15**, 5, 795-801, 2005

## 9 PUBLICATIONS

### 9.1 Published papers

1. Bakulin A.A., Elizarov S.G., Khodarev A.N., Martyanov D.S., Golovnin I.V., Paraschuk D.Yu., Triebel M.M., Tolstov I.V., Frankevich E.L., Arnautov S.A., and Nechvolodova E.M. *Weak charge-transfer complexes based on conjugated polymers for plastic solar cells*. Synth. Met. **147**, 221-225 (2004).

As known for short conjugated molecules, the absorption band of a weak (Mulliken) charge-transfer complex (CTC) can be tuned in the region where both the donor and acceptor are transparent. This can be used for tailoring low-band gap absorbing materials to match the solar spectrum. We studied donor/acceptor blends of poly[2-methoxy-5-(2'-ethyl-hexyloxy)-1,4-phenylene vinylene] (MEH-PPV) with 2,4,7-trinitrofluorenone or 2,6-dinitroantraquinone by a number of optical and photoelectric methods. From optical and vibrational IR absorption spectra, we found that the donor/acceptor blends demonstrate noticeable ground-state interaction indicating CTC formation. The CTC is characterized by a long absorption tail extending to the near-IR region. The blends also show strong quenching of photoluminescence (PL) and a near-IR photoinduced absorption (PIA) band, indicating donor/acceptor charge-transfer. Essentially, this band appears for both visible and IR pump wavelengths. In addition, to probe the charge photogeneration mechanisms, a magnetic field spin effect technique was applied. This technique shows that the charge photogeneration mechanism is essentially different in the blends compared to pristine MEH-PPV. Furthermore, photoconductivity in the blends strongly increases compared to pristine MEH-PPV and the photocurrent action spectrum closely follows to the extended absorption tail. We discuss photoinduced charge-transfer and relaxation of photoexcited CTC as possible mechanisms of mobile charge generation.

2. Arnautov S.A., Nechvolodova E.M., Bakulin A.A., Elizarov S.G., Khodarev A.N., Martyanov D.S., and Paraschuk D.Yu. *Properties of MEH-PPV films prepared by slow solvent evaporation*. Synth. Met. **147**, 287-291 (2004).

Because of various macromolecules conformations, solution-casted conjugated polymers films demonstrate a wide spectrum of intermolecular interactions which strongly influence essential electronic properties. Using poly[2-methoxy-5-(2'-ethyl-hexyloxy)-1,4-phenylene vinylene] (MEH-PPV) and different solvents, we studied polymer films prepared by dip-coating, spin/drop-casting and by a method based on slow solvent evaporation (SSE) from solution. The SSE films exhibit some redder photoluminescence (PL) and optical absorption edge indicating longer conjugated lengths and better film morphology. At the same time, the PL quantum yield for the SSE films is no less than that of the dip-coated films. Furthermore, the SSE films show a distinct evolution of their PL spectra during long-term storing compared with other preparation methods. This indicates different film morphologies evolving after preparation in distinct ways. We speculate about correlation between the preparations methods, morphology, interchain interaction and optical properties of the studied MEH-PPV films.

3. Bakulin, A.A., Khodarev, A.N., Martyanov, D.S., Elizarov, S.G., Golovnin, I.V., Paraschuk, D.Yu., Arnautov, S.A., and Nechvolodova, E.M. *Charge transfer complexes of a conjugated polymer*. Doklady Chemistry **398**, 204-206 (2004).

Without Abstract

4. Paraschuk D.Yu., Elizarov S.G., Khodarev A.N., Shchegolikhin A.N., Arnautov S.A., and Nechvolodova E.M. *Weak intermolecular charge transfer in the ground state of a  $\pi$ -conjugated polymer chain*, JETP Lett **81**, Iss.9, 583-586 (2005).

We show that a  $\pi$ -conjugated polymer chain can demonstrate weak intermolecular charge transfer in the electronic ground state. Poly[2-methoxy-5-(2'-ethyl-hexyloxy)-1,4-phenylene vinylene]/2,4,7-trinitrofluorenone (MEH-PPV/TNF) donor-acceptor films have been studied by optical absorption, Raman, infrared spectroscopy, and differential scanning calorimetry. The factors influencing weak intermolecular charge transfer in  $\pi$ -conjugated chains are discussed.

5. Arnautov S.A., Nechvolodova E.M., Bakulin A.A., Elizarov S.G., Khodarev A.N., Martyanov D.S., and Paraschuk D.Yu. *Influence of the preparation procedure on the optical properties of conjugated-polymer thin films*, Polymer Science, Ser. A **47**, 711-715 (2005) (Translated from Vysokomolekulyarnye Soedineniya, Ser. A **47**, 1153–1159 (2005)).

Because of various macromolecules conformations, solution-casted conjugated polymers films demonstrate a wide spectrum of intermolecular interactions which strongly influence essential electronic properties. Using poly[2-methoxy-5-(2'-ethyl-hexyloxy)-1,4-phenylene vinylene] (MEH-PPV) and different solvents, we studied polymer films prepared by dip-coating, spin/drop-casting and by a method based on slow solvent evaporation (SSE) from solution. The SSE films exhibit some redder photoluminescence (PL) and optical absorption edge indicating longer conjugated lengths and better film morphology. At the same time, the PL quantum yield for the SSE films is no less than that of the dip-coated films. Furthermore, the SSE films show a distinct evolution of their PL spectra during long-term storing compared with other preparation methods. This indicates different film morphologies evolving after preparation in distinct ways. We speculate about correlation between the preparations methods, morphology, interchain interaction and optical properties of the studied MEH-PPV films.

6. Bakulin A.A., Elizarov S.G., Ozimova A.E., Paraschuk D.Yu., Novikov Yu.N., Arnautov S.A., Nechvolodova E.M., *Photoinduced charge transfer in MEH-PPV/(Pt<sub>0.75</sub>C<sub>60</sub>) in donor-acceptor blends*, Functional Materials 2006 (in press).

Photoinduced charge transfer (PCT) in donor-acceptor blends of poly[2-methoxy-5-(2'-ethyl-hexyloxy)-1,4-phenylene vinylene] (MEH-PPV) with coordination oligomer (Pt<sub>0.75</sub>C<sub>60</sub>)<sub>n</sub> has been studied and compared with that in MEH-PPV/C<sub>60</sub> blends. The blends were investigated by using optical absorption, scattering, photoluminescence (PL), photoinduced absorption (PIA), and photocurrent action spectroscopies. We have found that as an electron acceptor (Pt<sub>0.75</sub>C<sub>60</sub>)<sub>n</sub> demonstrates the efficiency of PCT somewhat less than C<sub>60</sub>. This difference is attributed to more enhanced phase separation in MEH-PPV/Pt<sub>0.75</sub>C<sub>60</sub> at the nanoscale. Meanwhile, our photocurrent data suggest that (Pt<sub>0.75</sub>C<sub>60</sub>)<sub>n</sub> can provide an effective network for collection of photoinduced charges.

7. Elizarov S.G., Ozimova A.E., Paraschuk D.Yu., Arnautov S.A., Nechvolodova E.M. *Laser light scattering as a probe of phase separation in conjugated polymer films of donor-acceptor blends*, Proc. SPIE, v. **6257**, 293-302 (2006).

Light scattering and absorption in the visible and near-infrared ranges were studied in films of donor-acceptor blends of poly[2-methoxy-5-(2'-ethyl-hexyloxy)-1,4-phenylene vinylene] (MEH-PPV) with 2,4,7-trinitrofluorenone (TNF) or 1,5-dinitroantraquinone (DNAQ). Charge-transfer interaction in the electronic ground state of MEH-PPV/TNF and MEH-PPV/DNAQ blends results in optical absorption in the bandgap of MEH-PPV. At the same time, because of donor-acceptor phase separation, light scattering can grow with increasing the acceptor content in the blends contributing to their optical transmission. To evaluate the amount of absorbed and scattered light separately, we have elaborated a simple method in which the optical transmission of the films is measured at several laser wavelengths using a wide-aperture photodetector with or

without a dump blocking the straight laser beam. Making some assumptions about the scattering indicatrix, the scattering and absorption coefficients of the blends can be evaluated. We have found that the amount of scattered light in MEH-PPV/TNF blends does not depend smoothly on the acceptor content. At the molar acceptor concentration MEH-PPV:TNF below 1:0.33, the light scattering is low and depends on the TNF content only weakly, whereas at higher ratios, the scattered light begins to grow dramatically. We assign this growth to phase separation in the blend owing to excess acceptor molecules that are not involved in charge-transfer interaction with the donor. In MEH-PPV/DNAQ blends, the phase separated DNAQ forms large species, which weakly contribute to the observed light scattering.

## 9.2 Conference presentations

8. Arnautov S.A., Nechvolodova E.M., Ryzkova K.A., Zhidkova N.V., Bakulin A.A., Khodarev A.N., Martyanov D.S., and Paraschuk D.Yu., *Optical properties of MEH-PPV films prepared by slow solvent evaporation*. 11th Conference on Unconventional Photo-active Systems (UPS-2003), September 14-18, 2003, Leuven, Belgium, Abstracts, p.210-213.

Conjugated polymers are very attractive for a wide variety of photonics applications. Soluble phenylene-based conjugated polymers are in the focus of research activity mainly because of their luminescent properties and simple processability. It is well known that solution-prepared polymers films demonstrate a wide distribution of intramolecular conformations and intermolecular interactions. The latter are generally considered to be detrimental, for example, to LED applications as they favour formation of non-emissive or weakly emissive states. In this work, we show that efficient interchain interactions can be compatible with intensive luminescence. Using poly[2-methoxy-5-(2'-ethyl-hexyloxy)-1,4-phenylene vinylene] (MEH-PPV), we prepared polymer films by two different methods — by dip-coating and by an original method based on slow solvent evaporation (SSE) from the solution, and reported their photoluminescence properties.

MEH-PPV with molecular weight ca. 125 000 g/mol from Sigma-Aldrich was dissolved in toluene or chlorobenzene under stirring for 60-90 min at 50°C to give 0.5–2% (w/v) solutions. Films were prepared on glass substrates by dip-coating and by slow evaporation of large amount of solution. The SSE films show a broader main absorption peak at ~500 nm compared with the dip-coated films indicating a wider distribution of conjugation lengths. At the same time, the PL spectra of SSE films are not wider than that of the dip-coated films and show a ~15 nm red shift. Such a red shift is about that of the dip-coated films compared with the MEH-PPV solution. Furthermore, the measured PL quantum yield for the SSE films is no less than that of the dip-coated films and is about 10%. We discuss the observed optical features of the SSE films as a manifestation of enhanced interchain organization leading to effective energy funneling to the emissive species.

9. S.G. Elizarov, A.N. Khodarev, D.Yu. Paraschuk, *VIS/NIR Raman spectrometer for study of polymer's films and solutions*. International scientific and practical conference Spectroscopy in Special Applications (SSA 2003), June 18-21, 2003, Kyiv, Ukraine, Book of abstracts, p. 175.

We report on development a Raman spectrometer on the basis of opto-mechanics of a commercial double monochromator DFS-52 (LOMO, St. Petersburg) for studying conjugated polymers by the Raman spectroscopy method. We have developed the control electronics for positioning diffraction gratings, an optical illumination unit with zero-degree light collection scheme, three different photodetection systems, and the corresponding LabView-based software. The spectrometer was connected to a computer via serial interface or a twisted-pair Ethernet adapter. As a photodetector, we used a photomultiplier with multialkaline

photocathode. Two photodetection systems were based on lock-in technique. The first works as a digital lock-in employed on the basis of a computer sound card and an original interface unit. In the second, we used a commercial lock-in amplifier. In the third photodetection system, we used the photon counting method. In our original implementation the dead time was less than five nanoseconds for operating in the box-car mode. We discuss the sensitivity of the three photodetection systems.

We have developed the LabView-based software for visualization of the Raman band allowing us to account the luminescence, light absorption, and background radiation.

We compare the parameters of our Raman spectrometer with those of best commercial devices, discuss the advantages and disadvantages of different Raman spectrometer types such as an infrared Fourier-transform spectrometer, diffraction gratings monochromator, polychromator with CCD array etc.

10. Martyanov D.S. , Bakulin A.A. , Khodarev A.N. , Elizarov S.G., Golovnin I.V., Paraschuk D.Yu., Triebel M.M., Tolstov I.V. , Frankevich E.L. , Arnautov S.A. , Nechvolodova E.M., Ryzkova K.A., and Zhidkova N.V. , *Potentialities of weak charge-transfer complexes based on conjugated polymers in plastic solar cells* (oral), 16th Workshop on Quantum Solar Energy Conversion (QUANTSOL) Bad Gastein, Austria, March 14-20, 2004 ([http://www.quantisol.unibe.ch/pub/pub\\_235.pdf](http://www.quantisol.unibe.ch/pub/pub_235.pdf)).

Conjugated polymers combine optical absorption, conductivity, mechanical flexibility, and ease of processing promising applications in photovoltaics especially in large-scale low-cost solar cells. The spectral range of photosensitivity of such devices is determined by the optical gap of a conjugated polymer used. However, they usually have the optical gap about 2 eV, while it needs to be considerably lower to match the solar spectrum. We use intermolecular charge-transfer complexes of soluble poly(*p*-phenylene vinylene) derivative (MEH-PPV) with low-molecular organic acceptors (trinitrofluorenone or dinitroantraquinone) that has allowed us to extend the range of photosensitivity down to the near infrared. Moreover, we show that the ground state interaction between the donor and acceptor can be a factor controlling the donor/acceptor phase separation. The results of studies of MEH-PPV/acceptor films using optical and vibrational spectroscopy, AFM, different scanning calorimetry, photoinduced absorption spectroscopy, and photocurrent measurements are discussed.

11. Triebel M.M. , Tolstov I.V. , Belov A.V., Frankevich E.L. , Arnautov S.A., and Nechvolodova E.M., *Magnetic field spin effect on photoconductivity of MEH-PPV with acceptors*, accepted as oral paper to 16th Workshop on Quantum Solar Energy Conversion (QUANTSOL) Bad Gastein, Austria, March 14-20, 2004.

Magnetic field spin effect (MFSE) on photoconductivity of MEH-PPV films is variation of photoconductivity value ( $\sigma$ ) by switching on an external magnetic field (B). MFSE is connected with spin evolution of intermediate species called polaron pairs, which are two polarons of opposite sign connected by Coulomb field. Polaron pairs have the lifetime of about ns and mainly recombine geminately. MFSE levels off in a weak field, and  $B = 10$  mT increases  $\sigma$  on a few percent typically. It has been found that MFSE is very sensitive to procedure of the sample preparation, and this fact permits to use MFSE as a test for very existence of geminate recombination, which heavily competes with formation of free charge carriers. Experiments were performed with surface-like samples as well as with sandwiches with typical thickness of about 100 nm. The results obtained were similar for both types of the samples.

Trinitrofluorenone (TNF) insertion in MEH-PPV was found to increase  $\sigma$  dramatically and decrease the relative value of MFSE to about zero. We have used concentrations of TNF from 0.01 to 1 by weight.

This fact suggests that a new channel of charge generation arises. If in pristine MEH-PPV the dissociation of polaron pairs, which is the main channel of charge generation, is slow in

comparison with geminate recombination of the pairs, in the case of MEH-PPV/TNF blend the transfer of electron from MEH-PPV to TNF provides significant charge separation. There is a reason to believe that TNF molecules form nanosize particles at high enough TNF concentration, so the electron transfer takes place on the MEH-PPV/TNF interface. On condition that TNF concentration is large enough the percolation effect may occur and, consequently, electron may achieve anode moving in the TNF nanoparticles space. Holes move to cathode, as it usually is, through MEH-PPV space.

Reduction of MFSE in the blend indicates that electrons are effectively intercepted by TNF nanoparticles, and a short lifetime of the pairs in respect to dissociation does not permit them to recombine geminately and to show MFSE.

12. Arnautov S.A. , Nechvolodova E.M. , Bakulin A.A. , Elizarov S.G., Golovnin I.V., Khodarev A.N., Martyanov D.S. , Triebel M.M., Tolstov I.V., Frankevich E.L., and Paraschuk D.Yu. , *Possibilities of weak charge-transfer complexes based on conjugated polymers for photovoltaic applications*, 15th International Conference on Photochemical Conversion and Storage of Solar Energy, Paris, France, July 4-9, 2004. Books of abstracts, oral presentation, W1-O-14.

Combination of conductivity, optical properties, mechanical flexibility, and ease of processing of conjugated polymers make them promising materials for large-scale solar cells. It is generally accepted that photoinduced charge transfer from a conjugated polymer acting as a donor to an acceptor is an effective way to generate mobile charges. On the other hand, it is possible a more direct way from an incident photon to mobile charges using weak charge-transfer complexes (CTC) of Mulliken type. CTC optical absorption formally implies donor-acceptor electron transfer and as a result a pair of separated charges can be formed. As known for short conjugated molecules, the CTC absorption band can be tuned in the region where both the donor and acceptor are transparent. This can be used for extending the photosensitivity to match the solar spectrum. Furthermore, a CTC implies donor-acceptor attraction; it may be used to obtain a homogeneous working layer avoiding phase separation. In this work we were motivated by attractive potentialities of weak CTCs for using in plastic photovoltaics.

We studied blends of poly[2-methoxy-5-(2'-ethyl-hexyloxy)-1,4-phenylene vinylene] (MEH-PPV) with 2,4,7-trinitrofluorene (TNF) or 1,5-dinitroantraquinone (DNAQ) by a number of optical and photoelectric methods. Drop-cast films of MEH-PPV/TNF and MEH-PPV/DNAQ blends were prepared from different solvents. For photocurrent studies we fabricated single layer diodes in the sandwich structure on ITO-coated glass substrates. First, the donor-acceptor blends demonstrate considerable changes in the region of the MEH-PPV optical absorption band and below it. Furthermore, the vibrational IR absorption spectra of the blends do not show additivity of those of MEH-PPV and the acceptor. These observations indicate noticeable interaction between MEH-PPV and the acceptor in their ground electronic states and therefore CTC formation. Second, the photoluminescence efficiency of MEH-PPV is strongly quenched in the blends. Third, the blends demonstrate the photoinduced absorption bands in the near-infrared range indicating charge generation in the presence of the acceptor. Essentially, these bands appear for both visible and infrared pump wavelengths. Fourth, the photocurrent in the blends strongly increases compared to pristine MEH-PPV and its spectrum closely follows to the absorption of the blend. We discuss photoinduced charge transfer and relaxation of photoexcited CTC as possible mechanisms of mobile charge generation.

13. Arnautov S.A., Nechvolodova E.M., Bakulin A.A., Elizarov S.G., Golovnin I.V., Martyanov D.S., Khodarev A.N., Paraschuk D.Yu., *Weak charge-transfer complexes of a conjugated polymer* (poster). World polymer congress MACRO 2004, 40th International Symposium on Macromolecules. Paris, July 4-9, 2004. Congress Proceedings on CD-ROM, Pt.5-1-5.

Combination of conductivity, optical properties, mechanical flexibility, and ease of processing of conjugated polymers make them promising materials for large-scale solar cells. It is generally

accepted that photoinduced charge transfer from a conjugated polymer acting as a donor to an acceptor, for example, a fullerene molecule, is an effective way to generate mobile charges. On the other hand, it is possible a more direct way from an incident photon to mobile charges using weak charge-transfer complexes (CTC) of Mulliken type. CTC optical absorption formally implies donor-acceptor electron transfer and as a result a pair of separated charges can be formed. Furthermore, as known for short conjugated molecules, the CTC absorption band can be tuned in the region where both the donor and acceptor are transparent. This can be used for tailoring low-band gap absorbing materials to match the solar spectrum. Note that a promising approach in plastic photovoltaics is using a bulk heterojunction in which photoexcitations dissociate into mobile charges throughout a donor-acceptor blend. On the other hand, the bulk heterojunction approach perturbs the working layer morphology lowering the device efficiency due to, for example, donor-acceptor phase segregation. As a CTC implies donor-acceptor attraction, it may be used to obtain a homogeneous working layer avoiding phase separation. In this work we were motivated by attractive potentialities of weak CTCs for using in plastic photovoltaics. In the present work, results of studies of blends of poly[2-methoxy-5-(2'-ethyl-hexyloxy)-1,4-phenylene vinylene] (MEH-PPV) MEH-PPV with 2,4,7-trinitrofluorene (TNF) or 1,5-dinitroantraquinone (DNAQ) are reported.

14. Arnautov S.A., Nechvolodova E.M., Shchegolikhin A.N., Bakulin A.A., Elizarov S.G., Khodarev A.N., Martyanov D.S., Paraschuk D.Yu. *Low-gap photovoltaic materials based on charge-transfer complexes of a conjugated polymer* (oral). 17th Workshop on Quantum Solar Energy Conversion (QUANTSOL 2005), Rauris, Austria, March 13-19, 2005, ([http://www.esqsec.unibe.ch/pub\\_275.pdf](http://www.esqsec.unibe.ch/pub_275.pdf)).

Conjugated polymers combine optical absorption, conductivity, mechanical flexibility, and ease of processing promising applications in photovoltaics especially in large-scale low-cost solar cells. The spectral range of photosensitivity of such devices is determined by the optical gap of a conjugated polymer used. However, they usually have the optical gap about 2 eV, while it needs to be considerably lower to match the solar spectrum. We use intermolecular charge-transfer complexes of soluble poly(*p*-phenylene vinylene) derivative (MEH-PPV) with low-molecular organic acceptors (trinitrofluorenone or dinitroantraquinone) that has allowed us to extend the range of photosensitivity down to the near infrared. Moreover, we show that the ground state interaction between the donor and acceptor can be a factor controlling the donor/acceptor phase separation. The results of studies of MEH-PPV/acceptor films using optical and vibrational spectroscopy, AFM, differential scanning calorimetry, photoinduced absorption spectroscopy, and photocurrent measurements are discussed.

15. Arnautov S.A., Nechvolodova E.M., Bakulin A.A., Elizarov S.G., Khodarev A.N., Martyanov D.S., and Paraschuk D.Yu. *Charge-transfer complexes of conjugated polymers as photoelectric materials with near-IR photosensitivity* (oral). International Conference on Coherent and Nonlinear Optics. St. Petersburg, May 11-15, 2005, in ICONO/LAT 2005 Technical Digest on CD-ROM, IWH2, <http://congress.phys.msu.ru/icono-lat-2005/>.

Conjugated polymers combine optical absorption, conductivity, mechanical flexibility, and ease of processing promising ubiquitous applications in electronic and photonic devices. However, most promising conjugated polymers are not photosensitive below 2 eV that is determined by their optical gap. As known for short conjugated molecules, the absorption band of a weak (Mulliken) charge transfer complex (CTC) can be tuned in the region where both the donor and acceptor are transparent. This can be used for tailoring low-band gap photoelectric materials. We studied donor-acceptor films of blends of poly[2-methoxy-5-(2'-ethyl-hexyloxy)-1,4-phenylene vinylene] (MEH-PPV) with 2,4,7-trinitrofluorene or 2,6-dinitroantraquinone by a number of optical and photoelectric methods. We found that a ground state CTC is formed characterizing by a long absorption tail extending down to the near IR. Photoluminescence in the films is strongly quenched indicating donor-acceptor photoinduced charge transfer. The



photoinduced absorption and photocurrent action spectra of the films point the effective generation of long-lived mobile charges under near-IR photoexcitation. The mechanisms of photoinduced charge transfer in conjugated polymer CTCs are discussed.

16. Elizarov S.G., Ozimova A.E., Paraschuk D.Yu., Arnautov S.A., and Nechvolodova E.M. *Laser light scattering as a probe of phase separation in donor-acceptor conjugated polymer films* (poster). Ibidem, IFO10.

A promising approach in organic photosensitive materials based on conjugated polymers is using a bulk heterojunction concept formed in a film of donor-acceptor blend. The well-known problem in such films is donor-acceptor phase separation resulting, specifically, in optical inhomogeneity and, therefore, light scattering. Using an original Rayleigh light scattering technique we show that if the donor and acceptor interact in their electronic ground states, phase separation could be controlled. Light scattering and absorption in soluble polyparaphenylenevinylene/trinitrofluorenone (MEH-PPV/TNF) films with various donor-acceptor molar ratio were measured at several laser wavelengths corresponding to the charge-transfer complex absorption. We have found that the level of light scattering is strongly correlated with the acceptor content that is not involved in the charge-transfer interaction.

17. Bruevich V.V., Elizarov S.G., and Paraschuk D.Yu. *External cavity red diode laser for Raman spectroscopy of conjugated polymers* (poster). Ibidem, IFO12.

External cavity diode lasers can provide a narrow linewidth and contrast, which are indispensable for Raman spectroscopy. Red excitation is very convenient in Raman studies of conjugated polymers as it gives a possibility to realize non-resonant sub-gap excitation for the most promising pristine conjugated polymers and, on the other hand, permits resonant excitation in the charge-transfer bands of their donor-acceptor compositions. We have designed an external cavity GaInP/AlGaInP diode laser in the Littrow configuration based on a multimode commercial laser diode and diffractive grating with the output power more than 50 mW at the wavelength 670 nm and the FWHM linewidth less than  $3 \text{ cm}^{-1}$ . We have studied charge transfer interaction in blends of poly[2-methoxy-5-(2'-ethyl-hexyloxy)-1,4-phenylene vinylene] (MEH-PPV) with 2,4,7-trinitrofluorene (TNF) resulting in frequency shifts of some characteristic vibrational MEH-PPV bands with adding the acceptor. The origin of these shifts are discussed.

18. Arnaudov S.A., Nechvolodova E.M. Paraschuk D.Yu., Elizarov S.G., Bakulin A.A., Shchegolikhin A.N. *Conjugated polymer based intermolecular charge transfer complexes as low bandgap photovoltaic media with enhanced thermal and photo stability*. European polymer congress, Moscow, June 27-30, 2005 (oral), p.41.

As we have shown recently, poly[2-methoxy-5-(2'-ethyl-hexyloxy)-1,4-phenylene vinylene] (MEH-PPV) is capable of forming CTC with organic acceptors. It has been found that photovoltaic response of such donor-acceptor blends is extended into the red and near infrared (NIR) where the solar spectrum peaks. It has been found also that these blends revealed a remarkable enhancement of thermooxidative stability. Merits of exploiting intermolecular polymeric CTCs for plastic photovoltaics will be reported and discussed.

19. Arnaudov S.A., Nechvolodova E.M., Paraschuk D.Yu., Bakulin A.A., Vannikov A.V., Tameev A.R. *Slow solvent evaporation as a promising method of solidification of polymers*, ibidem (poster), p.214.

Films of poly[2-methoxy-5-(2'-ethyl-hexyloxy)-1,4-phenylene vinylene] prepared by dip-coating, spin/drop-casting and by slow solvent evaporation (SSE) were studied. The SSE films exhibit redder photoluminescence (PL) with distinct evolution during long-term storage; redder

optical absorption edge; the PL quantum yield no less than that of the dip-coated films; the essentially higher hole drift mobility compared to that of the drop-cast films and non-dispersed behavior of transient currents. We discuss morphologies of the films prepared by the different methods.

20. Tameev A.R., Vannikov A.V., Arnautov S.A., Nechvolodova E.M. *Hole drift mobility in MEH-PPV films prepared by various methods*, ibidem (poster), p.139.

Hole drift mobility in films of poly[2-methoxy-5-(2'-ethyl-hexyloxy)-1,4-phenylene vinylene] (MEH-PPV) was investigated by conventional time-of-flight method. Samples were obtained by drop casting and by slow solvent elimination (SSE) method. Values of the hole drift mobility in SSE films are more than in drop-cast films by a factor of 4-5, transient currents show non-dispersed behavior. Taking into consideration relevant data on MEH-PPV morphology changes, feasible reasons of the observed mobility enhancement in the SSE films are suggested.

21. Arnautov S.A., Nechvolodova E.M., Yamamoto T., Muramatsu Y., Bakulin A.A., Elizarov S.G., Khodarev A.N., Bruevich V.V., Paraschuk D.Yu. *Ground-state and excited-state charge transfer in donor-acceptor blends of MEH-PPV with 1,5-dinitroanthraquinone and poly(4,8-dinitroanthraquinone-1,5-diyl)*, ibidem (oral), p.46.

We have found that 1,5-dinitroanthraquinone (DNAQ) forms a weak ground-state charge-transfer complex with poly[2-methoxy-5-(2'-ethyl-hexyloxy)-1,4-phenylene vinylene] (MEH-PPV) whereas poly(4,8-dinitroanthraquinone-1,5-diyl) (pDNAQ) does not show signatures of the ground-state interaction. At the same time, singlet excitons in MEH-PPV are deeply quenched by either DNAQ or pDNAQ. Furthermore, photoinduced charge transfer is more efficient in MEH-PPV/pDNAQ as evidenced by photoinduced absorption spectroscopy.

22. Arnautov S.A., Nechvolodova E.M., Novikov Yu.N., Bakulin A.A., Elizarov S.G., Paraschuk D.Yu. *Photoinduced charge transfer in MEH-PPV/(Pt<sub>0.75</sub>C<sub>60</sub>)<sub>n</sub> donor-acceptor blends*, ibidem (oral), p.47.

Donor-acceptor blends of poly[2-methoxy-5-(2'-ethyl-hexyloxy)-1,4-phenylene vinylene] (MEH-PPV) with a coordination oligomer Pt-C60 have been studied by photoluminescence, photoinduced absorption spectroscopy, and photoelectric methods. We show that as an electronic acceptor Pt-C60 demonstrates quite efficient photoinduced charge transfer compared to C60. The features of photoinduced charge transfer and photoelectric response in MEH-PPV/PtC60 and MEH-PPV/C60 are discussed.

23. Tameev A.R., Vannikov A.V., Arnautov S.A., Nechvolodova E.M. *Hole drift mobility in MEH-PPV films prepared by drop casting and slow solvent evaporation methods* (poster) EUROMAT` 2005, Prague, Czech Republic, September 5-9, 2005 (<http://www.euromat2005.fems.org/>), A11-377.

In poly[2-methoxy-5-(2'-ethyl-hexyloxy)-1,4-phenylene vinylene] (MEH-PPV) films prepared by various methods, hole drift mobility was investigated by conventional time-of-flight (TOF) techniques at room temperature. The polymer films were obtained by drop casting from solution onto ITO coated glass substrates and by new method named as slow solvent elimination (SSE). The SSE films exhibit some redder photoluminescence (PL) and optical absorption edge indicating longer conjugated lengths and better film morphology. At the same time, the PL quantum yield for the SSE films is no less than that of the dip-coated films. Furthermore, the SSE films show a distinct evolution of their PL spectra during long-term storing compared with other preparation methods. This indicates different film morphologies evolving after preparation in distinct ways. Transient currents are found to show non-dispersed and dispersed behavior in SSE and drop-casted films respectively. Values of the hole drift mobility in SSE films range from  $2.2 \cdot 10^{-6}$  to  $7.0 \cdot 10^{-6} \text{ cm}^2 \text{V}^{-1} \text{s}^{-1}$  rising as applied electric field

increases from  $4.2 \cdot 10^4$  to  $2.9 \cdot 10^5$  Vcm<sup>-1</sup>. These values are more than in drop-cast films by a factor of 4-5 in the mentioned range of electric field. The both results are in favour of that in SSE films 1) charge carrier transport sites are more uniform distributed, and 2) the sites form a net of pathways for effective charge transport without deep trapping of holes. Such a charge transport behavior indicates the difference in the morphology of the MEH-PPV films obtained by various methods. Feasible mechanisms of the observed mobility enhancements in the SSE films are suggested and discussed in combination with other data concerning morphology changes.

24. Bruevich V.V., Paraschuk D.Yu., Arnautov S.A., Nechvolodova E.M. *Raman spectroscopy of MEH-PPV intermolecular charge transfer complexes* (oral), Ibidem, A35.

It has been recently shown that a conjugated polymer can form ground-state intermolecular charge transfer complexes (CTC) with low-molecular acceptors. Partial charge transfer in the CTC electronic ground state should result in change in vibrational spectra of both the donor and acceptor. In this work we have studied Raman bands of poly[2-methoxy-5-(2'-ethyl-hexyloxy)-1,4-phenylene vinylene] (MEH-PPV) in MEH-PPV/2,4,7-trinitrofluorene and MEH-PPV/2,6-dinitroantraquinone donor-acceptor films with noticeable ground-state charge transfer interaction. We have used an external cavity GaInP/AlGaInP diode laser in the Littrow configuration based on a multimode commercial laser diode and diffractive grating giving the output power 50mW at 670 nm and the linewidth less than 3 1/cm. Red excitation is very convenient here as it provides non-resonant sub-gap excitation of pristine MEH-PPV and, at the same time, permits resonant excitation of its CTCs. We have found that adding of the acceptor result in a monotonic redshift of the strongest Raman band of MEH-PPV at ca. 1582 1/cm. The maximum shift of a few inverse wavenumbers was observed for the molar acceptor/donor ratio higher than ca. 0.3. This shift might be explained as a result of partial electron transfer from MEH-PPV to the acceptor. On the other hand, we suggest that the MEH-PPV conjugated chains in the CTC acquire more planar geometry. In this geometry the conjugation length is longer than that of pristine MEH-PPV giving the observed redshift. This suggestion is supported, in particular, by the observed behaviour of the out-of-plane MEH-PPV mode at ca. 766 1/cm upon adding of the acceptor. These two contributions to the observed redshift are discussed. In addition, we discuss essentially different temporal behaviour of the 1582-1/cm band observed in pristine and donor-acceptor films under long-term exposure by the pump beam.

25. Arnautov S.A., Nechvolodova E.M. Paraschuk D.Yu., Elizarov S.G., Bakulin A.A., Shchegolikhin A.N. *Conjugated polymer based intermolecular complexes as low band-gap photovoltaic media with enhanced thermal and photo stability* (poster), Ibidem, A12-376.

As we have shown recently, poly[2-methoxy-5-(2'-ethyl-hexyloxy)-1,4-phenylene vinylene] (MEH-PPV) is capable of forming peculiar intermolecular charge-transfer complexes (CTC) with such organic acceptors as, e. g., 2,4,7-trinitrofluorenone (TNF) or 1,5-dinitroantraquinone (DNAQ) in electronic ground states of the components. It has been found that photovoltaic response of such donor-acceptor blends is extended into the red and near infrared (NIR) where the solar spectrum peaks. Photoinduced absorption spectroscopy measurements showed that photoexcited CTCs in these materials could effectively relax into a charged separated state. Notably, the efficiency of the charge separation was only weakly dependent on the excitation wavelength in the spectral range 500–800 nm. Moreover, the photocurrent excitation spectra in the spectral region of the CTC absorption (600–800 nm) closely followed the CTC absorption curves thus indicating that the photoexcited CTC relaxed into mobile charges giving the photocurrent. It has been found also that, in a specific range of molar ratios of the components, MEH-PPV/TNF based CTCs revealed a remarkable enhancement of thermooxidative stability as compared to that of pristine conjugated polymer matrix. Photostability of these CTC films have been evaluated in a wide range of NIR laser excitation

(1064 nm) powers. In particular, it has been found that such photovoltaic films are capable of tolerating high excitation powers of, e.g., up to 70 W/cm<sup>2</sup> in the NIR without noticeable degradation of their characteristics. Merits of exploiting intermolecular polymeric CTCs for plastic photovoltaics as well as the problems intrinsic for this approach will be reported and discussed.

26. Elizarov S.G., Bakulin A.A., Paraschuk D.Yu., Arnautov S.A., Nechvolodova E.M. *Photogeneration of separated and mobile charges in ground-state charge transfer complex of MEH-PPV* (poster), Ibidem, A12-856.

It is generally accepted that effective photogeneration of mobile charges in pi-conjugated polymers occurs in an appropriate donor-acceptor blend without interaction of the components in the electronic ground state, for example in polyparaphenylenevinylene/fullerene films. Here, an exciton photogenerated at the polymer chain has to diffuse to the donor-acceptor interface and dissociate there into the separate charges. By employing an intermolecular charge transfer (CT) complex with essential donor-acceptor interaction in the electronic ground state, a more direct way from an incident photon to separate charges becomes feasible since the CT complex optical absorption formally implies donor-acceptor electron transfer and as a result a pair of separated charges can be formed. Here we show that intermolecular CT complexes of poly[2-methoxy-5-(2'-ethyl-hexyloxy)-1,4-phenylene vinylene] (MEH-PPV) with 2,4,7-trinitrofluorenone (TNF) can relax quite effectively into charged states. First, photoluminescence of MEH-PPV is strongly quenched in MEH-PPV/TNF films indicating effective dissociation of singlet excitons photoexcited at MEH-PPV. Second, in MEH-PPV/TNF films, photoexcitation of MEH-PPV results in appearance of a photoinduced absorption band at 1.2 eV characteristic of long-lived charged states, whereas the only triplet photoinduced absorption band appears in pristine MEH-PPV films. Essentially, that photoexcitation of CT band in the optical gap of MEH-PPV gives only photoinduced charged states as well. Moreover, the efficiency of charge separation per absorbed photon is weakly dependent on the excitation wavelength in the spectral range 500–800 nm. Third, the photocurrent excitation spectra of ITO/MEH-PPV:TNF/Al photodiodes closely follow the CT complex absorption spectrum indicating that the photoexcited CT complex can relax into mobile charges giving the photocurrent. The efficiency of charge separation and mobile charge photogeneration in MEH-PPV/TNF films is discussed.

27. Arnautov S.A., Nechvolodova E.M., Paraschuk D.Yu., Elizarov S.G., Bakulin A.A., Shchegolikhin A.N. *Conjugated polymer based intermolecular charge transfer complexes* (poster). 8th International Symposium "Polymers for Advanced Technologies", Hungary, Budapest, September 13-16, 2005 (<http://www.bme.hu/pat2005/>).

Poly[2-methoxy-5-(2'-ethyl-hexyloxy)-1,4-phenylene vinylene] (MEH-PPV) is capable of forming peculiar intermolecular charge-transfer complexes (CTC) with such organic acceptors as, e. g., 2,4,7-trinitrofluorenone (TNF) or 1,5-dinitroantraquinone (DNAQ) in electronic ground states of the components. It has been found that photovoltaic response of such donor-acceptor blends is extended into the red and near infrared (NIR) where the solar spectrum peaks. Photoinduced absorption spectroscopy measurements showed that photoexcited CTCs in these materials could effectively relax into a charged separated state. Notably, the efficiency of the charge separation was only weakly dependent on the excitation wavelength in the spectral range 500–800 nm. Moreover, the photocurrent excitation spectra in the spectral region of the CTC absorption (600–800 nm) closely followed the CTC absorption curves thus indicating that the photoexcited CTC relaxed into mobile charges giving the photocurrent. It has been found also that, in a specific range of molar ratios of the components, MEH-PPV/TNF based CTCs revealed a remarkable enhancement of thermooxidative stability as compared to that of

pristine conjugated polymer matrix. Perspectives of exploiting intermolecular polymeric CTCs for plastic photovoltaics as well as the problems intrinsic for this approach will be reported and discussed.

28. Bakulin A.A., Elizarov S.G., Paraschuk D.Yu., Novikov Yu. N., Arnautov S.A., Nechvolodova E.M. *Long-lived charge-separated states in MEH-PPV/(Pt<sub>0.75</sub>C<sub>60</sub>)<sub>n</sub> donor-acceptor blends* (poster), International Conference "Functional Materials" (ICFM-2005), abstracts, p. 298, Ukraine, Crimea, Partenit, October 3–8, 2005 (<http://www.ccssu.crimea.ua/tnu/conference/icfm/>).

Fullerenes and their derivatives in blends with conjugated polymers are well known to be the most effective acceptors in photoinduced charge transfer reaction. In addition, fullerenes in these blends can form a highly conductive network for collection of photoinduced charges (electrons) that makes fullerenes indispensable in bulk-heterojunction polymer solar cells. However, the active layer of such a cell comprises about 80% of fullerene, which almost does not absorb the solar light. In this work, we study a recently synthesized fullerene-based coordination polymer (Pt<sub>0.75</sub>C<sub>60</sub>)<sub>n</sub> as an acceptor for bulk-heterojunction solar cells. (Pt<sub>0.75</sub>C<sub>60</sub>)<sub>n</sub> could facilitate electron transport in the bulk heterojunction allowing decreasing the fullerene content in it. Moreover, such a polymer is expected to influence phase separation peculiarities, which are very important for the device efficiency. We have investigated donor-acceptor blends of poly[2-methoxy-5-(2'-ethyl-hexyloxy)-1,4-phenylene vinylene] (MEH-PPV) with (Pt<sub>0.75</sub>C<sub>60</sub>)<sub>n</sub> using photoluminescence, photoinduced absorption spectroscopy, and photoelectric methods. The properties of MEH-PPV/Pt<sub>0.75</sub>C<sub>60</sub> blends are compared with those of MEH-PPV/C<sub>60</sub>.

Drop-cast films of MEH-PPV/Pt<sub>0.75</sub>C<sub>60</sub> and MEH-PPV/C<sub>60</sub> blends were prepared from chlorobenzene for various molar donor-acceptor ratio. For photoelectric studies we fabricated single layer diodes in the sandwich structure on ITO-coated glass substrates. A top Al-electrode was deposited on films of thickness about 200 nm. The active area of the device was ≈0.1 cm<sup>2</sup>.

Optical absorption spectra of MEH-PPV/Pt<sub>0.75</sub>C<sub>60</sub> blends are similar to those of MEH-PPV/C<sub>60</sub> indicating the absence of essential donor-acceptor interaction in the electronic ground state. We have observed that (Pt<sub>0.75</sub>C<sub>60</sub>)<sub>n</sub> strongly quenches MEH-PPV photoluminescence (PL). For both acceptors strong PL quenching was observed at less than 0.01% acceptor content. We have found that PL quenching at acceptor content ≤10% is more efficient in MEH-PPV/C<sub>60</sub> blends. This could be due to lower electron affinity of (Pt<sub>0.75</sub>C<sub>60</sub>)<sub>n</sub> or/and more pronounced phase separation in MEH-PPV/Pt<sub>0.75</sub>C<sub>60</sub> blends as compared with C<sub>60</sub>. However, at higher acceptor content, the PL quenching efficiencies in both blends are very similar. This implies that the characteristic exciton diffusion lengths over MEH-PPV to the MEH-PPV/acceptor interface are close in both blends indicating similar phase separation lengths.

ITO/MEH-PPV:Pt<sub>0.75</sub>C<sub>60</sub>/Al photodiodes showed strongly asymmetric current-voltage curves typical of photodiodes. We have found that the photocurrent action spectrum closely follows the absorption edge of MEH-PPV indicating that (i) MEH-PPV and (Pt<sub>0.75</sub>C<sub>60</sub>)<sub>n</sub> do not interact essentially in the electronic ground state and (ii) photoexcitations at MEH-PPV dissociate into free carriers in the bulk heterojunction as it occurs in MEH-PPV/C<sub>60</sub> blends. Essentially that the 1:0.2 MEH-PPV/Pt<sub>0.75</sub>C<sub>60</sub> blend provided higher photocurrent than the 1:0.6 MEH-PPV/C<sub>60</sub> blend. In summary, we conclude that (Pt<sub>0.75</sub>C<sub>60</sub>)<sub>n</sub> is less effective in photoinduced charge transfer, but it provides better charge transport.

29. Bakulin A.A., Elizarov S.G., Ozimova A.E., Paraschuk D.Yu., Tsikalova M.V., Novikov Yu.N., Arnautov S.A., Nechvolodova E.M., *Photoinduced charge separation in blends of MEH-PPV with*

( $Pt_{0.75}C_{60}$ )<sub>n</sub> (oral). 18th Workshop on Quantum Solar Energy Conversion (QUANTSOL 2006), March 20–24, Rauris, Austria, 2005, ([http://www.esqsec.unibe.ch/pub\\_327.pdf](http://www.esqsec.unibe.ch/pub_327.pdf)).

Fullerene and its derivatives in blends with conjugated polymers are well known to be the most effective acceptors for photoinduced charge transfer. In addition, fullerene molecules in these blends can form a highly conductive network for collection of photoinduced charges making fullerenes indispensable in bulk heterojunction polymer solar cells. However, the active layer of such an optimized cell comprises about 80% of fullerene, which weakly absorbs the solar light. In this work, we study a recently synthesized fullerene-based coordination oligomer ( $Pt_{0.75}C_{60}$ )<sub>n</sub> as an acceptor for the photoinduced charge separation and charge transport in bulk heterojunction devices. We were motivated that ( $Pt_{0.75}C_{60}$ )<sub>n</sub> chains could facilitate electron transport in the bulk heterojunction allowing decreasing the fullerene content in it. We have done comparative studies of optical and photophysical properties of MEH-PPV/ $Pt_{0.75}C_{60}$  and MEH-PPV/ $C_{60}$  blends by using optical absorption, scattering, photoluminescence, photoinduced absorption spectroscopies, and photoelectric methods. We have found that as an electron acceptor ( $Pt_{0.75}C_{60}$ )<sub>n</sub> demonstrates the efficiency of photoinduced charge transfer somewhat less than  $C_{60}$ . We discuss this difference and relate it to more enhanced phase separation in MEH-PPV/ $Pt_{0.75}C_{60}$  blends. Meanwhile, our photoelectric studies possibly suggest that ( $Pt_{0.75}C_{60}$ )<sub>n</sub> could provide an effective network for collection of photoinduced charges. Potentialities of fullerene-based coordination oligomers for bulk-heterojunction devices are discussed.

### 9.3 Theses and Dissertations

The following qualification works were done and defended at MSU as a result of the work on the project:

1. V.V. Bruevich, M.Sc. thesis, "External-cavity diode laser for Raman spectroscopy of conjugated polymers", December 2004;
2. V.V. Kuzmin, M.Sc. thesis, "Photovoltaic properties of solar cells prototypes based on charger-transfer complexes of soluble PPV", December 2004.
3. V.M. Kasatkin, M.Sc. thesis, "IR Fourier-spectroscopy of photoinduced absorption of donor-acceptor blends based on soluble PPV", June 2005.
4. A.A. Bakulin, M.Sc. thesis, "Photoinduced absorption and photoluminescence spectroscopy of donor-acceptor blends based on soluble PPV", June 2005.
5. T.Sh. Mahmutov, M.Sc. thesis, "Depolarization of Raman scattering in intermolecular CTC based on PPV", December 2005.
6. S.G. Elizarov, Ph.D. thesis, "Raman scattering spectroscopy of nanopolyacetylene and donor-acceptor CTCs based on PPV", March 2006.

Director of leading Institute:

V.A. Makarov

Project manager:

D. Yu. Paraschuk